Experimental and numerical study of 2G HTS tapes to develop high-performance R-SFCL conductors

Alexandre Zampa

Université Grenoble Alpes

THÈSE

Pour obtenir le grade de

DOCTEUR DE L'UNIVERSITE GRENOBLE ALPES

Spécialité : **Génie électrique**

Arrêté ministériel : 25 mai 2016

Présentée par

Alexandre ZAMPA

Thèse dirigée par **Pascal TIXADOR**
, et co-encadrée par **Arnaud BADEL,**

préparée au sein du **Laboratoire de Génie Electrique de Grenoble (G2ELab) et de l'Institut Néel**
dans **l'École Doctorale Electrotechnique, Electronique, Automatique et Traitement du Signal**

Experimental and numerical study of 2G HTS tapes to develop high-performance R-SFCL conductors

Thèse soutenue publiquement le **21 octobre 2021**,
devant le jury composé de :

M. Daniel BOURGAULT
Directeur de recherche au CNRS, Président
M. Marco BRESCHI
Professeur associé à l'Università di Bologna, Rapporteur
M. Jean LEVEQUE
Professeur à l'Université de Lorraine, Rapporteur
M. Xavier OBRADORS
Professeur à l'Institut de Ciència de Materials de Barcelona, Examinateur
M. Philippe VANDERBEMDEN
Professeur à l'Université de Liège, Examinateur
M. Arnaud BADEL
Chargé de recherche au CNRS, Encadrant de thèse
M. Pascal TIXADOR
Professeur à Grenoble INP – UGA, Directeur de thèse

Ai miei Nonni

Acknowledgments

C'est avec un grand plaisir que j'écris ces quelques lignes pour remercier les personnes que j'ai cotoyées durant ces trois années. Tout d'abord, je remercie les membres du jury d'avoir accepté d'évaluer mes travaux de thèse. J'en suis honoré et reconnaissant.

Débuter un doctorat est un ensemble de paris. Le plus risqué est certainement celui de l'encadrement. Dans mon cas, il a été gagnant. Pascal, merci pour ton accompagnement au quotidien et pour avoir mis tout en oeuvre pour me soutenir dans les projets que j'ai entrepris. Arnaud, malgré la distance, merci pour m'avoir aidé à mettre en évidence la valeur et la cohérence de mes travaux. Il aurait été difficile de tomber sur un duo plus investi et équilibré.

Dans les personnes qui m'ont accompagnées au quotidien, je pense bien sûr à Julien et Blandine. Julien, malgré le fait que tu factures tes conseils, merci pour l'aide précieuse que tu m'as apportée à chaque fois que je t'ai sollicité. Blandine, merci pour l'initiation à la modélisation et pour avoir été une co-bureau au top. Je ne me suis pas lassé de partager ces journées avec vous.

Ces travaux ont été menés au sein du G2ELAB et de l'Institut Néel. Je remercie les directions de ces deux laboratoires pour leur accueil. Un remerciement chaleureux aux membres des pôles cryogénie et électronique de Néel pour l'aide apportée et pour avoir accompagné mes premiers pas (médiocres) en usinage. Une pensée pour les personnes croisées au quotidien dans le bâtiment V, particulièrement pour Daniel et Laureline, qui ont toujours accueilli mes questions. Merci à mes voisins de la menuiserie, Jérémy, Emeric et Mathieu, qui, en plus d'être sympathiques, m'ont considérablement aidé pour les expériences. Au G2ELAB, merci à Alexis et Benoit pour la rapidité avec laquelle le switch DC a été développé.

Une partie importante de ce doctorat s'inscrit dans le projet européen Fastgrid. Parmis les collaborations qui en sont issues, j'ai une pensée particulière pour les journées de manips passées avec Amir (Tel-Aviv University) et Pedro (ICMAB). Je remercie chaleureusement

Christian et Frédéric (EPM) pour m'avoir accueilli à Montréal. Une partie significative des résultats présentés ici découle de ce séjour.

Hemant, Louise, Pauline et Timothé, en plus d'être des personnes exceptionnelles, vous avez accepté de relire ce manuscrit (presque) sans juger mon anglais perfectible. Je vous en suis très reconnaissant.

L'une de mes grandes chances est celle d'être si bien entouré. Mes parents, merci pour votre accompagnement et les efforts que vous avez faits pour que votre "chtit" étudie toutes ces années. Mami, Papi, merci pour votre soutien infaillible et pour toute la tendresse que vous avez à mon égard. Vanessa, merci d'être toujours présente pour m'épauler et d'être si dédiée aux autres. Angéline et Eddy, merci pour tout ce que vous faites pour moi, rares sont les personnes qui, à vos places, en auraient fait autant. Augustine et Marius, merci pour l'ambiance et les chants endiablés. Lina et Lisio, merci pour vos sourires qui font tout oublier.
Aux copains de Digoin, merci pour toutes ces années.

Durant les années passées à Grenoble, j'ai eu le plaisir de rencontrer des personnes qui mettent très peu de limites à leurs rêves. Votre accompagnement m'a sans aucun doute rendu plus enthousiaste. Merci à la famille Duf, à mes bro du ch'Nord, à mes deux bongs, à mes ancien.ne.s colocs. Je n'aurais jamais vécu autant d'aventures sans vous !

Pour terminer, Amélia, Etienne, Hemant, Julie, Nelly, Pacco, Pierre, Quentin, Sacha, Zoé, merci pour les petites soirées, les découvertes culturelles et votre bienveillance. Ces trois années n'auraient pas été aussi belles sans vous.

Contents

Introduction

To mitigate the very negative impacts of the acceleration of climate change, governments all around the World announce new energy policies in the framework of the energy transition to reduce the use of fossil fuels. The electricity, as an energy vector, will play a major part in the energy transition coming from the possibility to produce it thanks to primary sources poor in carbon emissions such as nuclear energy or renewable energies. This implies the electrification of many technologies such as vehicles or individual heating. In 2018, the final energy consumption was 9938 MToe* and the share of the electricity was 1919 MToe, almost 20 % of this total [1]. To reach net-zero carbon emissions by 2050, the International Energy Agency (IEA) foresees a final energy consumption equals to 8121 MToe in 2050 with a share of electricity around 50 % ($\sim$ 4000 MToe) [2]. These predictions are based on energy efficiency measures. Energy sobriety should be the key element to reach net-zero carbon emissions from the point of view of the author.

Energy infrastructures must respond to these objectives. A significant increase in the electricity generation capacity will be observed with a large development of the renewable electricity sources. Nevertheless, the addition of distributed generation sources to an already overburdened system coupled with the multiplication of the network interconnections is already causing fault current levels approaching the limiting values of the network [3]. Indeed, the grid components are selected according to the maximum fault current, not to be damaged if such current occurs. The increase of the maximum fault current may lead in a near future to costly updates of the grid components to withstand more severe fault currents. As a consequence, the utilities will face in the upcoming years stronger constraints than the ones currently existing in order to limit the maximum fault current. One response to this issue is the fault current limitation to limit the fault current levels.

The property of superconducting materials which consists in transporting current without Joule loss under certain conditions is well-known. In a Resistive-type Superconducting Fault Current Limiter (R-SFCL), this property is suddenly lost when a fault occurs. The technology which was almost invisible in normal conditions, from an electrical point of view, becomes resistive. In the framework of power grids, this appears as a very interesting solution to limit the fault current levels.

The use of the second generation of high-temperature superconductors (2G HTS) profoundly impacts the applied superconductivity community. Indeed, with these conductors, liquid nitrogen can be used as a cryogenics fluid which is not possible with low-temperature superconductors (LTS) leading to smaller cryogenics costs. Among other outstanding performances, they show a higher critical current and a higher critical magnetic field than the LTS. The recent advances in the production of long lengths of these 2G HTS tapes with a high critical current [4] position them as very good candidates for power applications and particularly for R-SFCL. Indeed, their high resistance per unit length makes them well adapted to fault current limitation.

The R-SFCL using 2G HTS tape responds to an increasing need to limit fault current levels in power grids. Indeed, some examples are already installed in power grids like the three-phase 12 kV-2310 A R-SFCL successfully operating since 2014 in Essen (Germany) [5] and the three-phase 220 kV-1.5 kA R-SFCL operating in a high-voltage substation in Moscow (Russia) since 2019 [6]. Nevertheless, the technology is not widely spread in power grids. Indeed, it is a breakthrough technology not presenting a long history of field experiences. This does not comfort the utilities to promote its development but the two successes in Germany and Russia may remove these concerns. In addition, the cost of the 2G HTS conductors remains a large barrier to the development of the R-SFCL as a commercial product. The high performances of the 2G HTS conductor are generally not fully use which drives the cost up. The recent project Fastgrid funded by the European Union through the program Horizon 2020 addresses precisely these issues.

This thesis falls within this large context and within Fastgrid. Here, "tape" refers to the commercial "bare" tape sold by the manufacturers and "conductor" refers to the architecture based on a 2G HTS tape wound in a R-SFCL. This work aims to contribute, at the local scale, to a better understanding of the behavior of the 2G HTS tapes over any fault current, focusing particularly on the inhomogeneous quench, to gain confidence in the conductor design approach based on the critical current inhomogeneity and, at a higher scale, to gradually use them closer to their full performances to develop cost-effective conductors for R-SFCL applications. Modeling effort of 2G HTS conductors, collaborations with other institutions and experimental tests are used together to achieve these objectives. The approach adopted starts at the scale of the system introducing the R-SFCL as a response to the today's pressing needs of power grids in chapter 1 and focusing on the conductor design in chapter 2, then the local behavior of 2G HTS tapes is studied to assess the validity of the conductor design approach, in chapters 3 and 4, and the study comes back to the conductor scale with the development of architectures with high performances in chapters 5 and 6.

In this scope, the **first chapter** presents a review of the fault current limiter technologies based on the sudden impedance increase occurring during a fault, focusing particularly on the existing superconducting fault current limiters (SFCL) and on the advantages of the R-SFCL. It also introduces the 2G HTS tapes highlighting their high performances particularly well adapted to fault current limitation. The high-cost of the conductor in a

R-SFCL is presented as the main difficulty to take the step from prototypes to commercial products. It concludes on the objectives of this PhD thesis.

The **second chapter** presents the operation of the 2G HTS tapes on a wide range of prospective currents through simulation using a 1D electro-thermal model of these tapes which considers their specificities and particularly the critical current variations given by characterization machines such as Tapestar® [7]. The study makes appear two extreme cases which are the limitation regime and the hot-spot regime. The formalization of these regimes with analytic expressions is a powerful tool to design R-SFCL conductor.

The **third chapter** focuses on the experimental study of the hot-spot regime. A dedicated set-up is developed to observe the behavior of the tape through optical observation and electrical measurements. The study of the heat dissipation is realized through the analysis of bubble generation over the surface of the tape for several prospective currents in a liquid nitrogen bath at 68 K and 77 K.

These results encourage to further study the inhomogeneous quench of the tape. The **forth chapter** proposes to study the mechanism of the onset of quench occurring in these tapes. To do so, in the framework of a collaboration with TU Wien, the positions of bubble generation spots recorded with high-speed imaging are compared with the positions of defects in the REBCO layer recognized with Hall Scan Probe Microscopy. These defects are then modeled using a 3D Finite Element Method model of 2G HTS tape developed by partners from the Ecole Polytechnique de Montréal. The local thermo-electrical behavior occurring in the tape during the onset of quench is recreated in simulation and the results are compared with experimental data.

Having gain in confidence in the understanding of the operation of the tape itself as well as in the relevance of the conductor design approach, a zoom out is realized in the two last chapters to continue the work initiated in chapter 2. The use of 2G HTS tapes as a base to design conductors with high performances for R-SFCL applications is studied.

The **fifth chapter** is mainly presenting results obtained within Fastgrid in collaboration with several groups involved in this consortium. The conductors developed in the project are characterized and their performances are assessed in the scope of the development of a cost-effective conductor for R-SFCL. The experimental results obtained on the main conductor from the Fastgrid project are widely developed.

The **sixth chapter** questions the characterization of a conductor performed on samples with a small length in the scope of the development of a full R-SFCL. This study is developed using the 1D non-linear model of 2G HTS conductor, introduced in chapter 2, to detail the evolution of the temperature elevation in hot-spot regime as a function of the conductor length.

The main conclusions of this PhD thesis will be exposed at the end of this document as well as perspectives for future works.

**The tonne of oil equivalent (Toe) is a unit of energy, 1 Toe =* 11630 MWh.

CHAPTER 1

2G HTS tapes in R-SFCL for power grids protection purpose

This chapter first presents the large interest of fault current limitation to respond to tomorrow's increase of fault current levels. Among the existing technologies to achieve fault current limitation, the Resistive-type Fault Current Limiter (R-SFCL) shows many advantages. Moreover, the use of the 2^{nd} generation of High Temperature Superconductors (2G HTS) is particularly well adapted to this application. Nevertheless, R-SFCL with 2G HTS tape are not widely spread in power grids, a small number of devices is operating. The high conductor cost is identified as the main barrier to their development. The mitigation of the hot-spot phenomenon coming from the critical current inhomogeneity contributes to drive up the cost and the fear to damage the conductor leads not to fully use its performances.

1.1 Fault current limitation

1.1.1 Short-circuit current

The electrical grids are often introduced as World's largest man made systems. They include all the facilities from the power stations to the consumers.

In a single-phase grid, a short-circuit is a non desired connection between two positions of a circuit showing different electric potentials. It results a current, determined by the impedance of the connection and the voltage between the two positions of the circuit. A short-circuit can as well occur in three-phase power grids between two or three phases and between a phase and the ground or the neutral [8]. This fault current subjects the grid components to large stresses until the fault interruption and may degrade them (Laplace forces, arcing, excessive Joule losses,...). The fault currents represent threats to the integrity of the components of the electrical grids.

The fault current interruption is achieved by the circuit breaker. In AC grid, the time response between the fault detection and the fault interruption is at least the time necessary for the current to reach the natural zero-crossing but it generally takes much more time, around 100 ms for 100 kV system [3]. In DC grid, the interruption is more difficult and the systems become more complex. Indeed, the absence of a natural zero-crossing implies more energy to dissipate at the moment of the current interruption.

One key parameter for the utilities in order to select the electrical components ensuring the protection of their grids is the maximum prospective current. This parameter is defined as the highest short-circuit current which might flow in the grid without any fault current limitation device. For example, the current interruption devices, like breakers, have to present an interruption rating higher than the maximum prospective current. In the worst scenario, it can reach until 20 to 25 times the rated current I_n [8][9] but its value is generally not perfectly known by the grid operator. In addition, the maximum prospective current tends to increase with the recent development of distributed power generation and grid interconnections [10][11]. The utilities constraint the development of the power grid to limit the maximum prospective current. Indeed, upgrading the protection components to meet the increasing maximum prospective current could become very expensive [12]. Nevertheless, a grid with the possibility to have an infinite prospective current, through grid meshing, is ideal to ensure its stability.

It is important to keep in mind that a fault current is not always large: the fault may show an impedance, its amplitude depends on the fault type (three-phases, phase to ground ..) and on the grid (zero sequence impedance). The fault can take any values from the rated current I_n to the maximum prospective current.

For these reasons, the management of short-circuit currents is of primary interest [13]. A solution is the fault current limitation to limit their maximum values.

1.1.2 Principle of the Fault Current Limitation

Generally, a fault current limiter is a strategy or a technology which limits the fault current occurring in a power grid. Figure 1.1 schematically illustrates the action of a fault current limiter. When a fault occurs, at the time t_1, the current increases. The fault current limiter enables the limitation of the maximum current value. The technology is always associated with a circuit breaker to interrupt and isolate the fault, at the time t_2 in the example. This limitation of the fault current contributes to :

- Enable the possibility to have an "infinite" maximum prospective current
- Mitigate the damage sustained by the grid components
- Have an easier fault current interruption in DC transmission

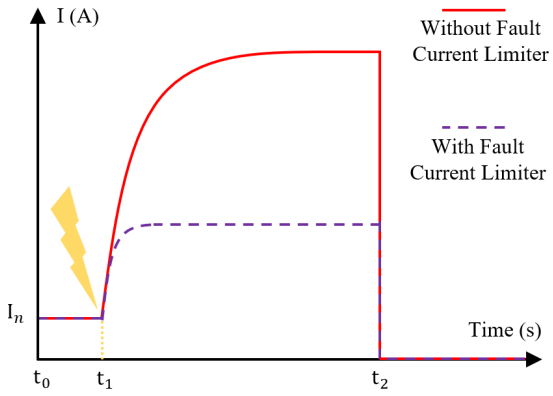

Figure 1.1: Schematic representation of the behavior of a fault current limiter in fault conditions occurring at t_1. The solid red line and the dotted violet line are the current without and with a fault current limiter respectively as a function of time.

Fault current limiters are either permanently or condition-based activated. Figure 1.2 adapted from [14] summarizes the existing methods or technologies of fault current limitation. Among the permanently activated fault current limiters, the split of the grid into sub-grids and the addition of impedances are some examples. Nevertheless, they imply topological grid constraints, voltage drops and permanent losses which are large drawbacks. The condition-based activated fault current limiters are more interesting because they show a higher impedance only when the fault occurs and remain almost transparent the rest of the time.

1.1.3 Condition-Based activated fault current limiters

The condition-based activated fault current limiters can be distinguished in two categories of technologies or methods: using or not using superconducting properties. Here, examples of non-superconducting fault current limiters are given below.

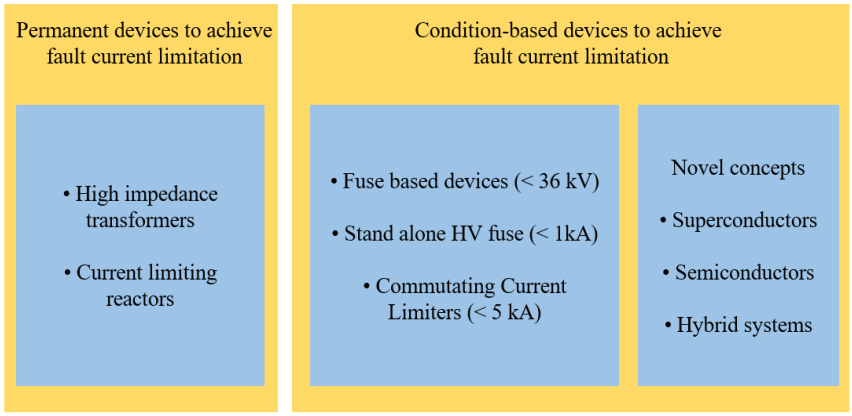

Figure 1.2: Overview of the fault current limitation methods adapted from [14]. Fault current limiters are permanently activated (left) or condition-based activated (right).

1.1.3.1 Non-Superconducting Fault Current Limiters

Fuse & IS-limiter A fuse consists of a material which melts when a current exceeding its rated current flows through it. There is no more contact which opens the circuit. The time-response of the fuse is a function of the current value. To increase the rated voltage of fuses, other solutions exist as the *IS-limiter* from ABB with a maximum rated voltage equals to 36 kV [15]. In normal operation, the current flows through a first conductor. When a fault occurs, an explosion destroys this conductor and the current circulates then through a fuse in parallel. Nevertheless, the traditional fuse and the IS-limiter are not reusable. A human intervention is required after a few uses.

FCL using semiconductors Many different FCL topologies use semiconductors to limit the current. Generally, these fast switches are used to redirect the current through an impedant element during the fault. A large drawback with the use of semiconductors is the on-state losses in normal operation [16]. Most of the applications are limited, at the maximum, to medium voltage levels due to the difficulty of the semiconductors to withstand high-voltage [12].

Metal Liquid FCL A liquid metal ensures the contact between two metallic conductors. In fault condition, a force applied on the liquid metal, the pinch effect, lifts up the liquid metal and degrades the contact between the two conductors. It results in an increase of the resistance of the contact [17]. This technology is dedicated to low voltage systems with mainly academic research.

Fault Current Limiter based on polymers Positive temperature coefficient of resistance materials show a highly increasing resistivity when their temperature increases. Used in fault current limitation, these materials significantly warm up during the fault which

strongly increases their resistance [18]. This technology has been demonstrated until 12 kV.

Some of these technologies have drawbacks: limitation in voltage, need for a human intervention, operation relying on sensors,... Most of the Superconducting Fault Current Limiters (SFCL) do not present these drawbacks.

1.1.3.2 Superconducting Fault Current Limiters

Below a certain temperature T_c, superconductors present no measurable resistance. This property is used to create almost free Ampere x turns. However, the resistance of a superconductor is highly non-linear with the current. If a current exceeding a certain current called critical current (I_c) flows through the superconductor, it becomes dissipative. This transition is called quench and the time necessary to come back to the superconducting state after a quench is the recovery time. The SFCL are distinguished in two categories:

- SFCL - Non-based on the quench
- SFCL - Based on the quench

Superconductivity basics will be described more in details in section 1.2.

The SFCL presented here use elements mainly coming from [16][19][20]. They are then compared in Table 1.1. The electrical circuits schemes are given in appendix A.

SFCL - Non-based on the quench

DC Biased iron core-type SFCL Developed in the eighties [21], the DC Biased iron core-type SFCL consists of the successive windings of a AC grid transmission around two different iron cores. One superconducting DC coil is wound between the two iron cores and loaded with a DC source to saturate the iron cores with almost no losses. In normal operation, the current in the grid transmission presents small enough variations which almost do not change the induction, the inductances of the two windings are small as well as the voltage drops over these two elements. Nevertheless, when a fault occurs, the grid current variations are larger and this desaturates alternatively one of the two iron cores in accordance to the current sign. The inductances significantly and alternatively increase during a half cycle. The sum of the voltage drops on the windings is large and it limits the current. This technology remains voluminous and heavy due to the presence of the iron cores. In 2012, a 220 kV-300 MVA DC biased iron core type SFCL was installed in China [22].

Bridge type SFCL A bridge type SFCL consists of a full bridge rectifier connected between a source and a load. A superconducting coil with a DC current source is inserted between the two branches of the rectifier. In normal operation, the current circulates only through the diodes and the voltage drop is limited. However, in fault conditions, the

current in the grid exceeds the current in the coil. At each half cycle, two diodes are in reverse position. The current constantly flows through the inductance which limits the current. This technology does not require any recovery time and the triggering current in the coil is easily controlled. Nevertheless, the forward state of the diodes implies constant losses [20]. A 10.5 kV bridge type SFCL was installed in 2011 and operates successfully in China [23].

Superconducting Fault Current Controller Limiter - SFCCL This structure from [24] consists of two superconducting coils each short-circuited through a thyristor and inserted between a source and a load. A constant DC current flows in the two superconducting coils. During fault conditions, the grid current exceeds the constant DC current, each semi-conductor will be alternatively close during a half cycle. A high inductance is then constantly appearing in the circuit.

SFCL - Based on the quench

Resistive-type SFCL A Resistive-type SFCL (R-SFCL) is a superconducting non-inductive coil inserted in series between the source and the load. It can be represented as a variable resistance: in normal operation, the superconducting conductor is almost invisible from an electrical point of view but in fault conditions, the current increases and exceeds the critical current which quenches the superconducting conductor and it becomes highly resistive. This technology works both in AC and DC grids and is compact compared with the other technologies using iron cores. Nevertheless, cryogenics losses exist due to the presence of current leads to connect the non-inductive superconducting coil to the rest of the circuit and the energy dissipation occurs in the system itself which implies a temperature elevation in the conductor during a fault. As a consequence, after a fault, a recovery time is required to cool down the device.

Shielded iron-core-type SFCL A shielded iron core SFCL is a transformer where the primary side is the grid transmission and the secondary side is a short-circuited superconducting conductor. In normal operation, the current induced in the secondary side is lower than the critical current but in fault conditions, the induced current increases and quenches the conductor. A large resistance appears in parallel with the magnetizing inductance, which limits the current. This technology presents no current lead which reduces cryogenics losses. Still, a recovery time is required to come back to the superconducting state after a fault and its weight and size is about four times higher than the R-SFCL [12]. No large scale shielded iron core type SFCL were installed in the recent years due to this reason. Some academic studies continue [16].

1.1.3.3 Comparison between the SFCL

The major requirements of a fault current limiter are [16]:

- Fast and effective current limitation

- Quick and automatic recovery
- Fail-safe and reliable operation
- Low permanent operation losses and voltage drop
- Compact and light

In this scope, the SFCL presented previously are compared in Table 1.1 using elements from [16][19][25][26].

SFCL Type	Recovery time	Footprint	Losses	Grid mode	Fail safe
DC biased iron core	Immediate	Large	Iron core losses AC losses primary coils	AC	Yes
Shielded iron core	tens of s	Large	AC losses primary coil AC losses superconducting coil	AC	Yes
Bridge	Immediate	Medium	On-state losses semiconductors Current leads losses	AC	Yes
Superconducting Fault Current Controller	Immediate	Medium	On-state semiconductors AC losses Current leads losses	AC	No
Resistive	tens of s	Small	AC losses Current leads losses	AC/DC	Yes

Table 1.1: Comparison between the different types of SFCL. The recovery time, footprint, losses in normal operation, the grid mode operation and the fail safe operation are elements of comparison.

All the technologies have a fast and effective current limitation. The R-SFCL is distinguished by its operation in both AC and DC grid, its relative small footprint, its small losses in normal operation and its fail-safe operation due to the absence of semiconductors. For these reasons, the R-SFCL is a very good candidate for fault current limitation in the future. Reference [27] shows that until 2018 more than the half of all the SFCL installed where R-SFCL (14 out of 26 devices). However, the technology is based on the quench which means that a recovery time is necessary after a fault to be operational. The R-SFCL is the framework of this PhD thesis.

It is rather difficult to properly explain the operation of the R-SFCL without introducing some basics elements of superconductivity. The next section aims to meet this objective and to introduce the 2nd generation of High Temperature Superconductors (2G HTS), particularly well adapted to this device. The operation of the R-SFCL will be developed in more details in subsection 1.3.1.

1.2 The 2nd generation of High Temperature Superconductors

1.2.1 Basics of Superconductivity

The R-SFCL operation relies on properties of superconducting materials. This explains the introduction of some basic elements of superconductivity, focused on describing the

trend of the E-J relationship. This was prepared using elements mainly coming from [28][29][30].

1.2.1.1 Definition of Superconductivity

Below a certain temperature called critical temperature T_c, a superconductor shows:

- Perfect electrical conductivity ($\rho = 0$ Ωm)
- Perfect diamagnetism ($\chi = 0$) (Meissner-Ochsenfeld effect) under a small enough external magnetic field

Figure 1.3 illustrates the absence of measurable resistivity below T_c on a superconducting conductor from SuperPower. The resistivity of the GdBaCuO suddenly drops when the temperature is below 92 K.

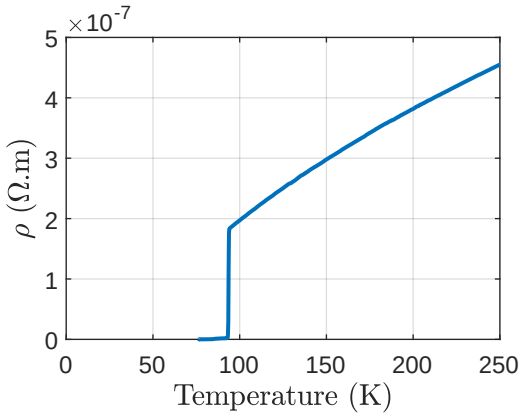

Figure 1.3: Electrical resistivity as a function of temperature of a GdBaCuO tape from SuperPower. The material presents a non measurable resistivity below 92 K.

Under an increasing external magnetic field H_{ext}, the superconducting properties of most common superconductors follow two main scenarii (illustrated in figure 1.4):

- Type-I superconductors - The perfect diamagnetism is lost when H_{ext} exceeds the critical magnetic field H_c. The material is then in the normal state. H_c is too small to enable practical use of type-I superconductors.
- Type-II superconductors - The behavior is identical below $H_{c,1}$ but when H_{ext} exceeds $H_{c,1}$, the magnetization is not equal to zero, there is a flux penetration in the material. Some regions of the material are superconducting and coexist with some other regions in the normal state. This is called the mixed state and it exists until H_{ext} reaches $H_{c,2}$. The magnetic flux penetrates the material in localized normal regions surrounded by supercurrents shielding the magnetic flux. These normal cores are called "vortices". $H_{c,2}$ can be very high, as an example $\mu_0 H_{c,2}$ =130 T at

0 K in [31] using a Klemm's High Field expansion. This is the reason why type-II superconductors are the only ones having practical applications.

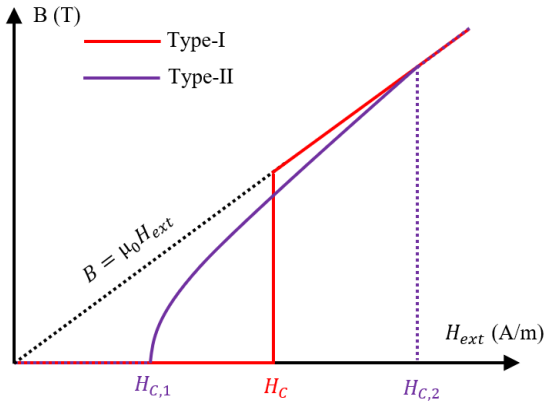

Figure 1.4: Magnetic induction B as a function of the external magnetic field H_{ext} in type-I and type-II superconductors. Type-I and type-II superconductors show an identical behavior below $H_{c,1}$ and above $H_{c,2}$ while the mixed state is specific to type-II superconductors.

1.2.1.2 E-J relationship in type-II superconductors

The superconductors studied in this thesis are Rare-Earth-BaCuO (REBCO) materials, YBCO or GdBaCuO for example, and they behave as type-II superconductors. In R-SFCL applications, there is generally no external magnetic field applied on the tape. The magnetic field of the Earth, around 47 µT, is as well not considered as $\mu_0 H_{c,1}$ is in the order of mT [32]. The circulation of current through a conductor creates a field called self-field. For type-II superconductors, the gradual penetration of that field can be described schematically using the Bean model [33]. It shows that the induction decreases from the edges of the superconducting layer in the direction of the center of the tape with a slope equals to $-\mu_0 J_c$ [28]. Vortices exist where the induction in the superconducting layer is different from zero in this model. The higher the current, the larger the zone where the vortices exist. Interacting with the transport current density $\overrightarrow{J}$, the vortices are submitted to Lorentz forces as it is shown in figure 1.5. With $\overrightarrow{\Phi_0}$ oriented perpendicularly to the vortex cross-section, the Lorentz force per vortex unit length is:

$$\overrightarrow{F_L} = \overrightarrow{J}\overrightarrow{\Phi_0} \tag{1.1}$$

If no pinning centers exist, as soon as a current is applied, the Lorentz force implies a motion of the vortices. However, the normal cores tend to be pinned on the imperfections of the material. The pinning centers act as an opposite force $\overrightarrow{F_p}$ to the Lorentz force. This absence of motion of the vortices is the flux pinning regime. When the current density increases, the Lorentz force increases until it reaches the pinning force. The current density giving (1.2) is the critical current density J_c.

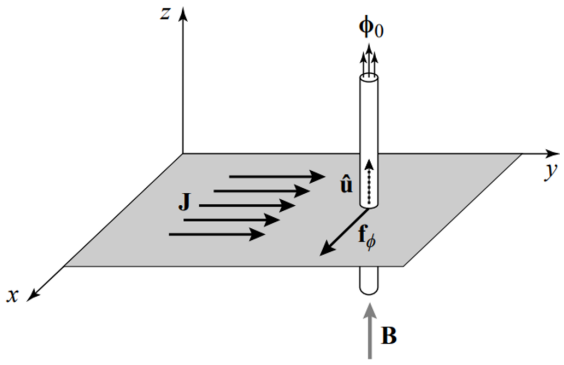

Figure 1.5: Force acting on a vortex in the presence of a uniform current density $\overrightarrow{J}$, from [28].

$$F_L = F_p \tag{1.2}$$

When the Lorentz force exceeds the pinning force (i.e. $F_L > F_P$), the cores are no longer pinned and they are set into motion. They are slowed down by a viscosity force $\overrightarrow{F_n}$ (1.3) existing in the opposite direction of $\overrightarrow{F_L}$ and proportional to the vortices speed $\overrightarrow{v_v}$ through a coefficient η. The application of the Newton's second law on a vortex subjected to $\overrightarrow{F_n}$, $\overrightarrow{F_L}$ and $\overrightarrow{F_p}$ gives the expression of the electric field E (1.4) coming from the dissipative motion of the vortices, with ρ_{ff} the resistivity of the flow of flux. This regime is called the flux flow regime.

$$\overrightarrow{F_n} = -\eta\overrightarrow{v_v} \tag{1.3}$$

$$E = \rho_{ff}(J - J_c) \tag{1.4}$$

A simple representation of the E-J relationship directly coming from (1.4) is presented in figure 1.6. Figure 1.7 gives an example of measurement of the E-J relationship performed on a GdBaCuO tape from THEVA. The transition between the flux pinning and the flux flow is not as sudden as what is schematically represented in figure 1.6. Indeed, vortices motions also occur when $F_L < F_p$. Flux lines can jump from a pinning center to another one due to thermal agitation [34]. This phenomenon is explained by two regimes : the flux creep and the Thermally Activated Flux Flow (TAFF).

This leads to define an international standard for the practical determination of J_c. The critical current density giving an electric field equals to the international standard E_c, with $E_c = 1$ µV/cm, is the critical current density J_c. The current giving E_c on a sample is the critical current I_c. In figure 1.7, J_c is $2.18 * 10^{10}$ A/m^2 and I_c is 835 A. The study of the imperfections to increase the pinning force is an active research field in order to increase the critical current of commercial tapes. In subsection 1.2.4, it will be shown that the I_c is not constant along the length of a superconductor.

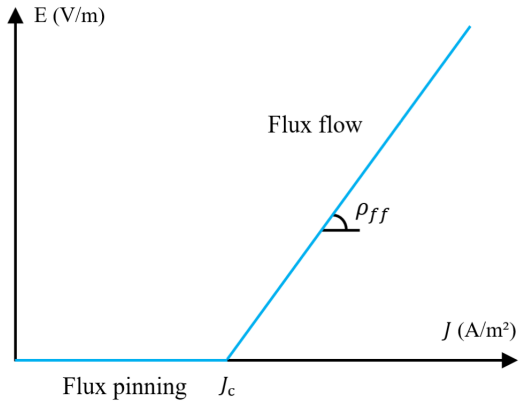

Figure 1.6: Schematic representation of the E-J relationship in a type-II superconductor with the flux pinning and flux flow regimes.

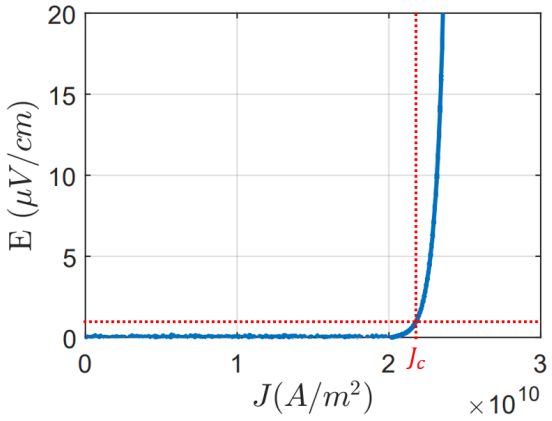

Figure 1.7: E-J measurement on a GdBaCuO tape from THEVA (plain blue line). Critical current density J_c is defined when the electric field reaches the standard E_c (dotted red lines).

Since the nineties [35], the non linear continuous relationship between the electric field and the current in a type-II superconductor can be modeled by the well-known power law given by (1.5) with J_{sc} the current density in the superconductor and the n-value defining the sharpness of the relationship E-J. The typical range for HTS is between 20 and 50 [36][37]. The n-value is temperature dependent as well as J_c (see subsection 1.2.4).

$$E = E_c(\frac{|J_{sc}|}{J_c(T)})^{n(T)} \tag{1.5}$$

The expression of the electric field given by (1.5) does not present a limit. One first solution is to give an upper bound of the electric field considering that the resistivity of a bulk superconductor is the resistivity given by the power law in parallel with the resistivity of the superconductor at the normal state, with an extrapolation below T_c [38]. Another solution considers that a superconducting material is generally arranged with other conductive materials to form a conductor. In such case, the equivalent resistance per unit length of the conductor $R_{l,cond}$ is given by (1.6) with $R_{l,nsc}$ the resistance per unit length of the conductive layers which is temperature-dependent and $R_{l,sc}$ the resistance per unit length of the superconductor. This is schematically represented in figure 1.8 and it is called the two resistances model. $R_{l,sc}$ is given by (1.7) with the power law below T_c and the normal resistance per unit length of the superconductor $R_{l,sc,normal}$ above T_c.

$$R_{l,cond}(J_{sc},T) = \frac{R_{l,sc}R_{l,nsc}}{R_{l,sc}+R_{l,nsc}} \tag{1.6}$$

$$R_{l,sc}(J_{sc},T) = \begin{cases} \frac{E_c}{I_c(T)}(\frac{|J_{sc}|}{J_c(T)})^{n(T)-1} & \text{with} \quad T < T_c \\ R_{l,sc,normal}(T) & \text{with} \quad T \geq T_c \end{cases} \tag{1.7}$$

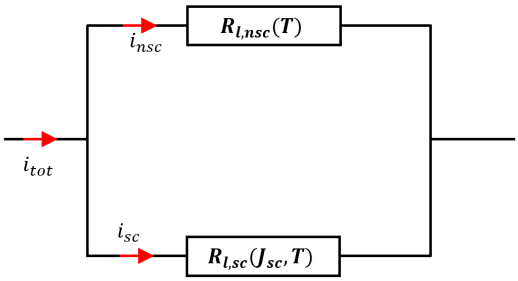

Figure 1.8: Electrical representation of a conductor with the superconductor showing a resistance per unit length $R_{l,sc}$ and the conductive layers showing a resistance per unit length $R_{l,nsc}$.

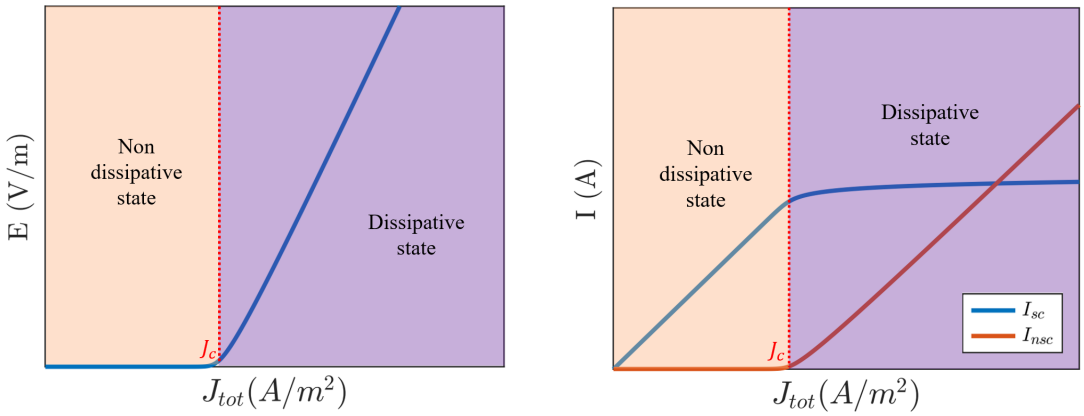

Figure 1.9: Schematic description of the evolution of the (a) electric field and (b) currents in a conductor with a type-II superconductor as a function of the current density (in the whole conductor) at a constant temperature.

A model detailed in chapter 2 enables the computation of the current sharing between both resistances. In such case, the E-J relationship on the conductor follows the shape given in figure 1.9a with J_{tot} the total current density in the conductor at a constant temperature. Below J_c, the conductor does not dissipate while above J_c, it dissipates. The electric field is also not infinite with this model. When the superconductor becomes dissipative, the current starts to circulate through the conductive materials (see figure 1.9b).

1.2.1.3 Critical surface

The introduction of $\mu_0 H_{c,2}$, T_c and I_c enables the presentation of the critical surface of some type-II superconductors in figure 1.10. It is a practical tool defining where the superconductor is in the lossless state.

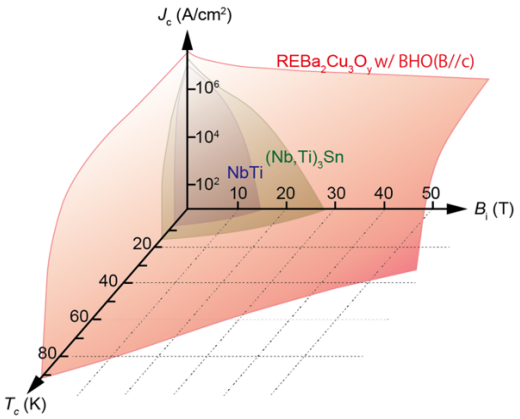

Figure 1.10: Critical surface of some materials behaving as type-II superconductors (Courtesy from S.Awaji).

1.2.1.4 Main applications

The absence of Joule losses and the possibility of very large current density ($> 100\ A/m^2$) are very interesting properties for applications. It enabled the creation of applications that are difficult to realize using conventional conductors such as high field magnets for Magnetic Resonance Imaging, Nuclear Magnetic Resonance, particle accelerators (CERN) or fusion confinement (ITER). Some other applications can show higher performances using superconductors: rotating machines, cables or transformers. To finish, new technologies appear using superconductors as magnetic bearing, Superconducting Fault Current Limiter (SFCL) and Superconducting Magnetic Energy Storage (SMES)[39].

1.2.2 Interests for R-SFCL applications

Until 1986, all the type-II superconductors were metal alloys. The discovery of superconductivity in BaLaCuO, a ceramic, in 1986 [40] with a critical temperature of 35 K and in YBaCuO compound in 1987 [41] with a critical temperature of 93 K led to distinguish low critical temperature superconductors (LTS), known at this time, and high temperature superconductors (HTS). Other materials showing superconducting properties are still discovered today. One of the last important families of materials for the applied superconductivity community are the iron-based superconductors [42]

LTS are widely used in most of the applied superconductivity applications (mainly $NbTi$ and Nb_3Sn). The use of HTS is developing with the 1st generation of HTS using a multifilamentary wires of Bi-2223 and the second generation of HTS (2G HTS), which are coated conductor available in tape. 2G HTS tapes generally refer to REBCO materials, exhibiting high-temperature superconductivity, with the crystallographic lattice shown in figure 1.11.

Their high critical temperature (93 K for YBCO for example) enables an operation in

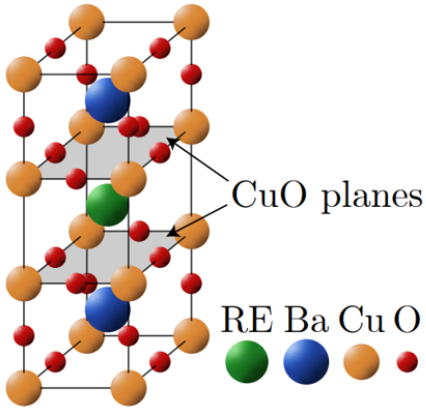

Figure 1.11: Crystal lattice of the REBCO superconducting compound from [43].

liquid nitrogen with small cryogenics cost. In addition, they present a high critical current density and a high critical magnetic field which contribute to their increasing use in large scale applications. Their availability under the shape of tape with a little quantity of high electrically conductive material makes them relatively resistive when compared to other conductors. This last additional property positions them as best candidates for R-SFCL applications [44]. Moreover, the development of the different manufacturing processes made it possible to now obtain long lengths of tape with good performances [44]. One indicator is the product length multiplied by $I_c(77K)$ which drastically increases in the last years [4]. The highest value is the just mentioned reference is 450 $A.km$ in 2011 by Fujikura. 2G HTS tapes are used in the framework of this thesis.

1.2.3 Architecture and Manufacturing Process

To obtain high J_c, it is important to have small-angled grain boundaries in the REBCO layer [45]. Indeed, the best superconducting properties are in the plan a-b in the copper oxides. To obtain this precise alignment of the REBCO grains, the layer is epitaxially grown on a bi-axially texture support [46]. A tape-based architecture of 2G HTS is the most adapted shape to obtain a biaxially texture [47].

Two main routes exist to create this texture. The first route consists of giving a biaxially texture to the buffer layers with a metallic substrate, generally made of Hastelloy® C276. This is achieved through Ion Beam Assisted Deposition (IBAD) where the appropriate template is generally obtained with Yttria-Stabilize-Zirconia (YSZ) using additional buffer layers to transfer the texture. The particular Incline Substrate Deposition (ISD) of MgO developed by THEVA [48] is another solution. With this first route, the metallic substrate, $50 - 100$ µm thick, is used to withstand the mechanical stresses of the structure [46]. The second route is to directly use a biaxially textured substrate in Ni-W alloys based on the Rolling-Assisted-Biaxially-Textured-Substrate (RABITS). With such method, the substrate shows the appropriate biaxially texture. The buffer layers only act as a chemical

barrier and they transfer the appropriate texture. The three manufacturers studied in this PhD work, Superpower, SuperOx and Theva, adopt the first route.

Once the suitable texture is obtained, the REBCO layer is deposited through epitaxial growth using either physical processes as pulsed laser depositions (PLD) (SuperOx [49]), metal evaporation (EV) (THEVA [48]) or chemical routes as Metal Organic Vapor Deposition (MOCVD) (Superpower [50]). The REBCO layer is $1-3$ µm thick. A stabilizer layer, generally silver, surrounds the structure to protect the superconducting layer from the environment and facilitate the current injection.

The general architecture of a 2G HTS tape is given in figure 1.12. Figure 1.13 shows an image from Scanning Electron Microscopy (SEM) of a cross-section of a REBCO coated conductor from THEVA where the different layers just described are presented. Table 1.2 gives the dimensions of the cross-sections of the tapes produced by the three manufacturers studied in this PhD work.

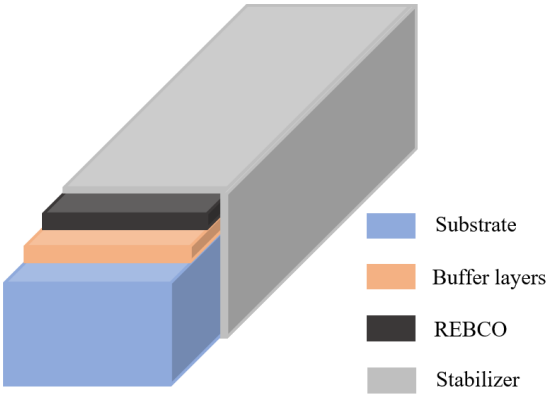

Figure 1.12: Simplified architecture of a 2G HTS tape.

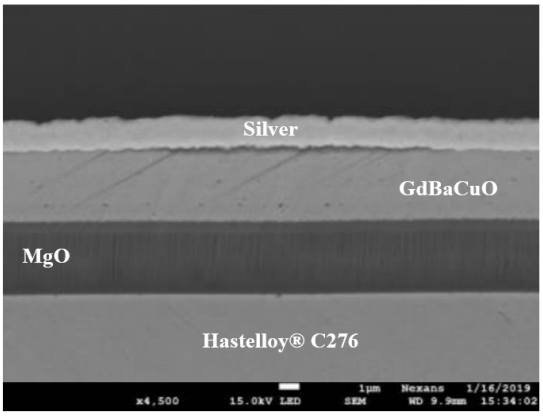

Figure 1.13: Cross-section of a REBCO coated conductor from THEVA (Scanning Electron Microscopy) (Courtesy of Nexans®).

Manufacturer	SuperOx	Superpower	THEVA
Width (m)	0.012	0.012	0.012
Substrate thickness (µm) (Hastelloy® C276)	100	100	100
Buffer layers thickness (µm)	0.4	0.2	3.3
ReBCO thickness (µm)	1.5	1	3
Top stabilizer thickness (µm) (Silver)	2	2	1.6
Bottom stabilizer thickness (µm) (Silver)	1	1.8	1.6
Lateral side stabilizer thickness (µm) (Silver)	1	1	1.6

Table 1.2: Dimensions of several 2G HTS tapes.

1.2.4 I_c dependencies

Figure 1.10 introduced the dependence of I_c on the temperature and magnetic induction. Considering 2G HTS tapes, the incidence angle of the external magnetic field θ is also affecting I_c. In addition, the production on long lengths of the tape does not make possible to obtain identical I_c over the position. At a microscopic scale, microcracks, twin planes, subgrain boundaries, stacking faults, dislocations, oxygen deficient regions or different growth sectors are known defects [51]. Extrinsic variations (width and thickness of the REBCO layer [52]) also exist. As a consequence, I_c depends on the position x along the length of the tape. These dependencies are summarized in (1.8).

$$I_c = f(x, T, B, \theta) \tag{1.8}$$

In the framework of the R-SFCL, there is no external magnetic field. The dependencies related to the position and the temperature are the only ones considered.

1.2.4.1 I_c temperature dependence

The temperature dependence of the critical current density is illustrated in figure 1.10 and precise measures are also shown in [53]. In this PhD work, the only cryogenics liquid used is nitrogen. It solidifies at 63 K and the critical temperature of 2G HTS tape is 92 K. In this range of temperature, the dependence on the temperature of the critical current is almost linear (see figure 1.14 from measurements from [54]) and the linear approximation given by (1.9) with T the temperature is used to model the temperature dependence of I_c on that range.

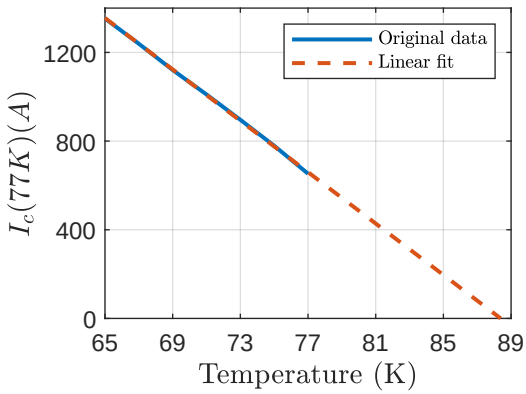

Figure 1.14: Measurement of the critical current of a conductor based on a 2G HTS tape from THEVA, measured from [54].

$$I_c(T) = I_c(77\text{ K})\frac{T_c - T}{T_c - 77} \tag{1.9}$$

The temperature dependence of I_c affects the E-J relationship of a superconductor in a conductor. Figure 1.15 illustrates that when the temperature increases, the dissipative state is reached with a lower critical current density.

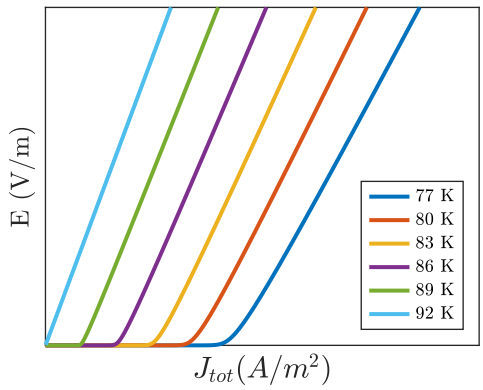

Figure 1.15: E-J relationship of a superconductor in a conductor at several constant temperatures of operation.

1.2.4.2 I_c position dependence

The dependence of the I_c as a function of the position is generally measured in self-field at 77 K with a characterization machine such as Tapestar [7]. One example is given in figure 1.16 with measures performed on a 1 m long 2G HTS tape from THEVA with a spatial resolution of 1.1 mm. This example highlights the inhomogeneity of the critical current as a function of the position. The I_c variations depend on the accuracy of the measure. Several previous works show that the I_c data follow statistical distribution as Gaussian distribution [52] or Weibull distribution [55][56]. The chapter 6 of this manuscript will particularly investigate the possible description of a I_c distribution by a Weibull distribution. The critical current density J_c depends not only on the position along the length x but also along the width y. This will be widely developed in chapter 4.

The presentation of the large interests of the R-SFCL in section 1.1 and the introduction of the high performances of the 2G HTS tapes presented in this section leads to question about the development of this technology in power grids.

1.3 Commercial development of the R-SFCL

1.3.1 Principle of the R-SFCL

The R-SFCL was introduced in subsection 1.1.3.2 and its principle is now more detailed thanks to the introduction of 2G HTS conductors.

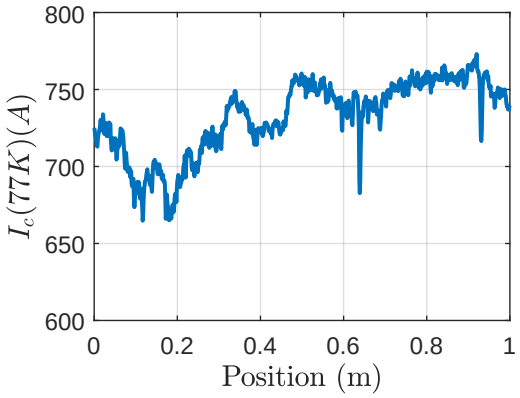

Figure 1.16: Critical current over position at 77 K in self-field of a 1 m long 2G HTS tape from THEVA (data from THEVA, spatial resolution: 1.1 mm).

A R-SFCL is composed of several modules. A module is non-inductive coils are arranged in series inserted in a cryostat to operate at low temperatures. A simple non-inductive coil consists of the winding of two 2G HTS conductors face to face, as it is shown in figure 1.17, keeping a sufficient distance to ensure insulation in fault event. The two conductors are connected in the center of the coil. More complex structures can be created like in figure 1.18 from [57]. This contributes to limit the losses in AC normal operation.

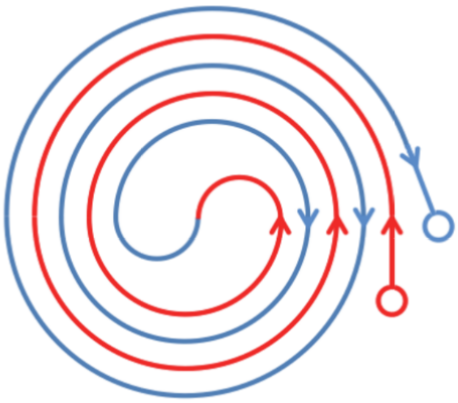

Figure 1.17: Scheme of a non-inductive coil for a R-SFCL from [58].

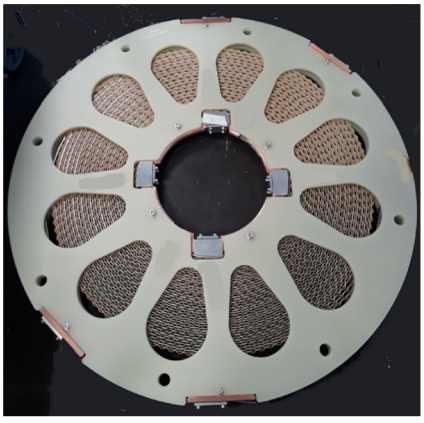

Figure 1.18: Example of a non-inductive coil, Fastgrid pancake (5 kV/1.5 kA) from [57]

The non-inductive coils realized with a conductor based on 2G HTS tapes can be electrically represented by the two resistances model introduced in subsection 1.2.1.2 and shown in figure 1.19. The power grid is modeled by a Thevenin equivalent circuit (V_{grid}, R_{grid} and L_{grid}) and the load by Z_{load}. R_{sc} is the superconducting layer of the conductor

and R_{nsc} represents the other conductive layers. S is the breaker associated to the R-SFCL.

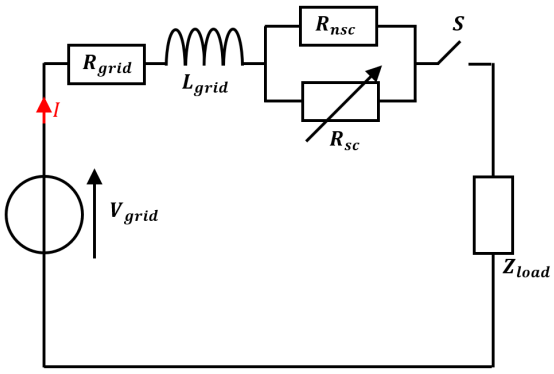

Figure 1.19: Scheme of an electrical circuit with a R-SFCL inserted in a power grid.

Figure 1.20 from [59] presents an experimental result of a R-SFCL operation. From 0 ms to 30 ms, the grid is in normal operation, the current is lower than the critical current and the R-SFCL is almost invisible from an electrical point of view (electric field mainly inductive). At 30 ms, a fault occurs, the current raises drastically and exceeds the critical current. The R-SFCL becomes dissipative and the electric field increases. The apparition of this sudden resistance limits the current. The electric field on the R-SFCL is in phase with the current. After 40 ms of operation in fault conditions, the breaker associated to the R-SFCL opens the circuit. It avoids the risk of damaging the conductor due to excessive heating during its operation. From 70 ms to 400 ms, the utility clears the fault and the R-SFCL conductor is cooled by the liquid nitrogen bath to come back to its superconducting state. At 400 ms, the breaker is closed, the normal operation starts again.

During the same test, the electric field on the R-SFCL as a function of the current from 30 ms to 70 ms is shown in figure 1.21. The E-J relationship is recognized at the beginning of the operation. Then, the evolution of the electric field is proportional to the current.

1.3.2 State-of-the-Art of the R-SFCL using 2G HTS tapes

To have a good picture of the development of the R-SFCL, this section summarizes the last R-SFCL developed and tested using 2G HTS tapes from 2010 to today.

In 2012, a single-phase 115 kV-900 A rated R-SFCL was designed, manufactured and tested by an association between AMSC, Siemens, Nexans and Southern California Edison [60]. The R-SFCL used a parallel shunt reactor. The European project ECCOFLOW

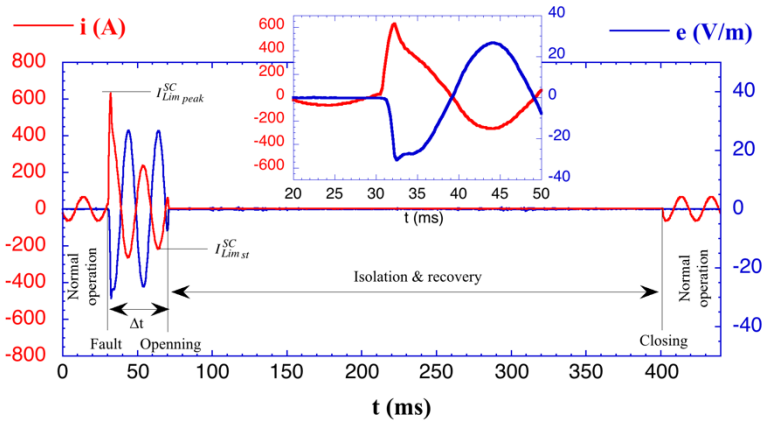

Figure 1.20: Current and electric field in a grid, in the presence of a R-SFCL, as a function of the time from [59].

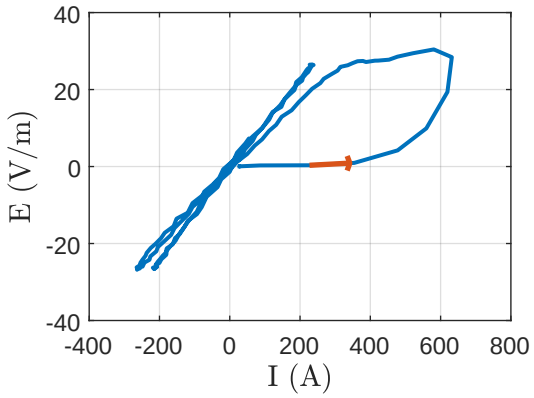

Figure 1.21: Electric field as a function of the current during the operation from 30 ms to 70 ms.

was completed the same year with the development of a 24 kV-1005 A module. It was successfully developed, tested in laboratory and installed but the commissioning was never performed [9]. An air core reactor is in parallel of the superconducting material. Another project that ended in 2012 is ENSYSTROB with German stakeholders and led by Nexans SuperConductors. It led to the installation in the German grid of a three-phase 12 kV-533 A rated R-SFCL for a one year's field test [61]. Nexans also developed, tested and installed a three-phase 12 kV-2310 A R-SFCL in Essen, Germany, in the framework of the AmpaCity project [5] (see figure 1.22). It successfully operates since 2014.

Figure 1.22: Picture of the R-SFCL from the Ampacity project installed in Essen, courtesy of Nexans®.

Figure 1.23: Picture of the 220 kV R-SFCL at the substation in Moscow, from [6].

R-SFCL were also under development in Asia. In 2014, a single-phase 154 kV-2000 A rated R-SFCL prototype was tested by KEPCO. The project still continues with the development of a new R-SFCL with equivalent characteristics but with a lower footprint. The prototype was developed, manufactured and tested in operation for one year [11]. In 2019, a collaboration between Jiangsu Zhongtian and Beijing Jiatong University led to the testing of a 220 kV-1.5 kA single phase R-SFCL. This is a large step forward with the development of a high-voltage R-SFCL. An even bigger achievement is the installation of a three-phase 220 kV-1200 A rated R-SFCL in a high-voltage substation at Moscow by SuperOx [6] (see figure 1.23) in 2019.

The research on R-SFCL also focuses on DC applications. Guangdong Grid Company of China Southern Power Grid, Co. is developing a 160 kV-1 kA DC R-SFCL. One prototype was already developed and tested [62]. Another DC 20 kV-400 A R-SFCL is under development for installation purpose in a substation [63].

This sum up of the last developments of the R-SFCL around the world shows that only a very small number of devices is today operating in power grids. The success of some projects as Ampacity [64] did not bring to reality a serial production of this technology.

Some beliefs explain the poor development of the R-SFCL. Indeed, the technology is quite a breakthrough technology and it does not present a long history of field experiences. This does not comfort the utilities to promote its development [65]. In addition to the reluctance of the utilities, techno-economic barriers exist and they are detailed in the following section.

1.3.3 Development barriers of the R-SFCL

1.3.3.1 High-cost of the REBCO tapes

In a recent survey about R-SFCL, reference [27] mentions that the high-cost of the R-SFCL is the biggest barrier to its development. Figure 1.24 from [66] shows that the cost of the tape represents two thirds of the total R-SFCL component's shares from the capital expenditure (CAPEX) at 77 K. This portion is reduced to half of the CAPEX at 65 K due to the increase of the current density at this temperature.

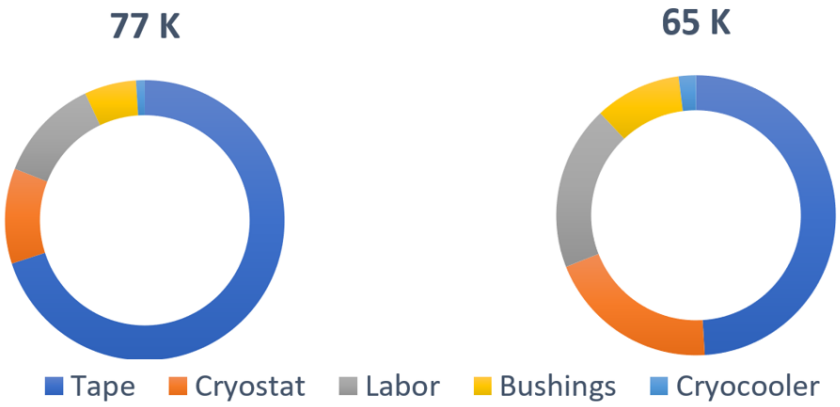

Figure 1.24: FCL component's shares from CAPEX at 77 K and 65 K from [66].

The expression of the conductor cost in a R-SFCL is given by (1.10) inspired from [67]. In this formula, C_{sc} is the cost of conductor per unit length. It is around 70 \$/m at 77 K in 2017 [67] and in the framework of this PhD work, the 12 mm wide tape bought was in the same price range. N is the number of conductors based on a 2G HTS tape in parallel. N is determined not to risk any quench during transient overstepping of the rated current I_a like it could happen during large motors starts. The coefficient k_a considers these transient overcurrents. N is at least equal to the normal transient over current divided by the critical current of a conductor I_c. The length L_{sc} is equal to the rated voltage of the R-SFCL V_{sfcl} divided by the electric field E_{sc} which is the voltage withstood by a meter of superconducting conductor.

$$Cost = C_{sc} N L_{sc} = C_{sc} \frac{k_a I_a}{I_c} \frac{V_{sfcl}}{E_{sc}} \tag{1.10}$$

The cost of the conductor is directly linked to the rated voltage of the R-SFCL, itself determined by the grid voltage. The voltage level to transport power tends to increase, especially with the development of DC transmissions. The development of the R-SFCL for high-voltage grids faces a prohibitive cost of tape [27]. The designer of a R-SFCL does not have possible actions on C_{sc}, $k_a I_a$ and V_{sfcl}. Nevertheless, it is possible to lower the cost through actions on the electric field E_{sc} withstood by the conductor or on the critical current.

1.3.3.2 Management of the critical current inhomogeneity

The inhomogeneity of the critical current along the tape length (see section 1.2) coupled with the low heat diffusion of 2G HTS tape implies the existence of hot-spot. This inhomogeneous quench of the tape leading to destructive temperature elevations is well known in the applications using superconducting magnets [68] and it also occurs with R-SFCL. The maximum temperature of the tape is dramatically increasing for prospective currents in the range of the I_c variations at the liquid nitrogen bath temperature. This temperature elevation threatens the tape integrity and can lead to its destruction. This requires to adapt the tape architecture to reduce this elevation of temperature. These adaptations bring additional costs over the cost of the tape itself. The chapter 2 of this manuscript will present in details the design challenge of the conductor.

1.3.3.3 Fear of I_c degradation

The R-SFCL has to show an outstanding reliability all over its lifespan as a protection device. A degradation of its performances is a large fear especially for the utilities. A non-desired quench due to a degradation of the conductor performances would have dramatic consequences.

To avoid any degradation, the designer of the conductor of the R-SFCL generally does not fully use the high performances of the 2G HTS tape. As an example, the theoretical maximum electric field which could be withstood by a bare commercial tape is 100 V/m for 50 ms (this will be widely developed with the expression (2.21)) which is practically never reached. Indeed, there is a fear of overheating the conductor which could lead to, at least, a degradation of its superconducting property (i.e. I_c degradation) or in the worst case to its total destruction. As an example, the electric field of the conductor of the Eccoflow project is 50 V/m for 50 ms [9]. These large margins result in a incomplete use of the full performances of the conductor which leads to increase the length of conductor to meet the specifications and it drives the cost up.

This concern is partially due to a lack of experience and understanding of the tape in long-term operation. An example will be given in subsection 5.1.4.1 in the figure 5.16. In this example, even if the conductor operation is thermally safe, there is a degradation of the performances after the successive quenches of the conductor without possibility to identify a clear cause after investigations. It would be exaggerated to claim that this technology

is perfectly known. Research is still under going to reach a better understanding of the operation of the 2G HTS tapes to increase the confidence level of the users and to gradually use the tapes closer to their full performances.

1.3.3.4 Cooling system

The cooling system is today well developed for R-SFCL applications. However, cryogenics may represent an additional fear for the utilities compared to other fault current limiters not using any cryogenics system. Nexans mentioned some issues in the cooling systems in the operation of two R-SFCL in UK [69].

1.3.4 The European Fastgrid Project

In this context, the improvements of the conductor performances to develop a cost-effective conductor is an important contribution. This is the main goal of the European project Fastgrid funded by the European Union through the Horizon 2020 program [57][70]. This project, coordinated by G2ELAB (France) gathers twelve teams dealing with applied superconductivity coming from academics (EPFL (Switzerland), EPM (Canada), G2ELAB (France), ICMAB (Spain), IEE (Slovakia), KIT (Germany), RSE (Italy), STUBA (Slovakia), TAU (Israël)) and industrial partners (Oxolutia (Spain), SuperGrid (France), THEVA (Germany)).

The consortium developed advanced conductor technologies. One of the main achievements of this project is the "Fastgrid conductor". Thanks to its high performances, a smaller length of conductor is required compared with the existing R-SFCL to meet the rated voltage and current of the R-SFCL which substantially decreases its cost. Few pancakes of a R-SFCL module were produced. The elements of design will be widely developed in chapter 5 but it can already been said that the two main routes to achieve this cost decrease were the increase of the electric field E_{sc} withstood by the conductor and the decrease of the number of conductors in parallel N thanks to an increase of the critical current. The conductor consists of a 2G HTS tape produced by THEVA and soldered to a thick resistive Hastelloy® C276 shunt operating in liquid nitrogen at 65 K. Two other conductors developed within Fastgrid will be developed (CFD and Sapphire-based tape) in the chapter 5.

1.4 Objectives of this PhD work

Fault Current Limitation is a response to the adaptation of the power grid to the increasing fault current levels. Among the several existing technologies to limit fault currents, the R-SFCL is particularly interesting due to its intrinsic and high limitation capability, compactness and operation both in AC and DC. The use of 2G HTS tapes is well adapted to this application with their high performances (high I_c, small cryogenics cost, high resistivity). These tapes are now available in long lengths with high critical currents.

R-SFCL came out of the laboratories with a few devices in operation in grids. To develop the attractiveness of this technology, it is necessary to reduce its cost and improve the confidence of all the actors, including the utilities, in this disruptive technology. The decrease of the cost of the conductor is one important objective of the applied superconductivity community. The European project Fastgrid highlights this trend with the gathering of many institutions to develop a cost-effective conductor.

In addition to the high-cost of the 2G HTS tapes, the cost is driven up by, on one hand, the mitigation of the negative impacts of the hot-spot implying dedicated architectures and, on the other hand, on the incomplete use of the performances of these tapes. In this PhD work, the work is dedicated more to the operation of the conductor in the R-SFCL than to the study of the R-SFCL as a component of the power grids. The main objectives are to contribute, on one hand, to a better understanding of the 2G HTS tape operation itself to develop confidence in their operation and facilitate the full use of their high performances and on the other hand, to develop cost-effective conductors.

The following chapter is common to both objectives just mentioned. It recalls the behavior of the conductor of a R-SFCL against a wide range of prospective fault currents leading to identify two meaningful extreme cases: the regime of hot-spot and the regime of limitation. The formalization of these two regimes, based on the I_c measured with characterization machines such as TapeStar ®, is a powerful tool to design conductors. This chapter positions this PhD work in the line with the research activities of the applied superconductivity group in Grenoble.

Questions arise when looking to the tape operation itself for many prospective currents: **what are the local mechanism occurring in the 2G HTS tapes in this range of operation ? Do they challenge the design approach introduced in chapter 2 ? Is the scale of the I_c measurement small enough to represent well the local behaviors ?** The chapters 3 and 4 are in this first axis of research. The chapter 3 tightens the focus on the experimental study of the hot-spot regime with the presentation of a dedicated set-up which enables optical observation and electrical measurements on the tape. The chapter 4 will further reduce the scope focusing on the onset of quench on 2G HTS tapes. Thanks to experimental and numerical simulation results, the quench mechanism occurring on a 2G HTS tape is described.

With the added comprehension of the local behavior of the 2G HTS tapes, it is chosen to come back to a larger scale initiated in chapter 2 with an adaptation of the design approach to develop high-performance conductors. In this perspective, one other question arises : **how can the performances of the 2G HTS tapes be fully used with a good long-term reliability ?** The chapters 5 and 6 are in this second axis of research. The chapter 5 studies advanced conductors showing high performances through characterizations or developments of innovative concepts. The chapter 6 deals with the reliability of the design of a conductor. A discussion about the influence of the conductor length on the hot-spot regime is initiated. It will question the representativeness of the characterization

performed on conductors with a small length when it is known that a R-SFCL consists of tens of meters of conductor.

CHAPTER 2

Operation of 2G HTS conductors on a wide range of prospective currents

This chapter presents the operation of the conductor of a R-SFCL on a wide range of prospective currents. The use of a 1D electro-thermal and lightweight model of a 2G HTS conductor considering the critical current inhomogeneity enables the computation of its maximum temperature over a wide range of operation. This study makes appear two extreme cases as relevant for the design of a conductor which are the limitation regime occurring when the prospective current is the highest and the hot-spot regime occurring when the prospective current is in the range of the I_c variations of the conductor. The formalization with analytic expressions of these regimes is a powerful tool to design a conductor. The chapter 3 will further continue this study by experimentally investigating the conductor operation.

The model described in details in this chapter will be used throughout the rest of this PhD work.

2.1 Experimental observation of inhomogeneous quench

The relationship between I_c inhomogeneity, introduced in 1.2, and inhomogeneous quenches was proposed in [26][71].

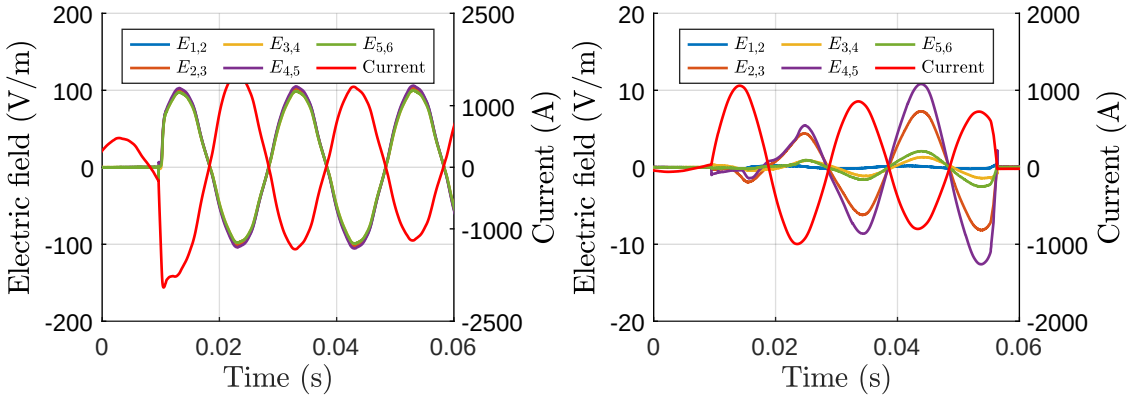

(a) $V_{source} = 30$ V (b) $V_{source} = 4$ V

Figure 2.1: Electric fields and current (inversed) as a function of time in a liquid nitrogen bath at 77 K with two different voltages in input.

Figure 2.1 was experimentally obtained with an AC voltage source V_{source} connected to a sample of 2G HTS tape from THEVA, where voltage taps are directly soldered on its surface. It shows that depending on the applied voltage, the quench is more or less homogeneous. With the highest voltage, the electric fields over the various tape segments are very similar while with the lowest voltage, electric fields are different. As an example, in the case where $V_{source} = 4$ V, the electric field measured between the voltage taps 1 and 2 remains mainly inductive while the electric field measured between the voltage taps 4 and 5 reaches a peak value of 12 V/m.

Following that observation, the applied superconductivity group in Grenoble developed a 1D electro-thermal model of 2G HTS conductor to design R-SFCL considering the I_c inhomogeneity along the conductor length. Modeling effort was continued in this work and the latest developments are presented.

2.2 Modeling of the 2G HTS conductor as R-SFCL

The model aims to emulate the behavior of a conductor based on a 2G HTS tape inserted in a power grid under a wide range of fault conditions. To do so, an electro-thermal model of the conductor is developed considering the I_c variations and inserted in an equivalent electrical circuit of a grid.

A 1D model is generally sufficient for a R-SFCL model thanks to its structure presenting no electrical or thermal connection between two successive turns to ensure dielectric

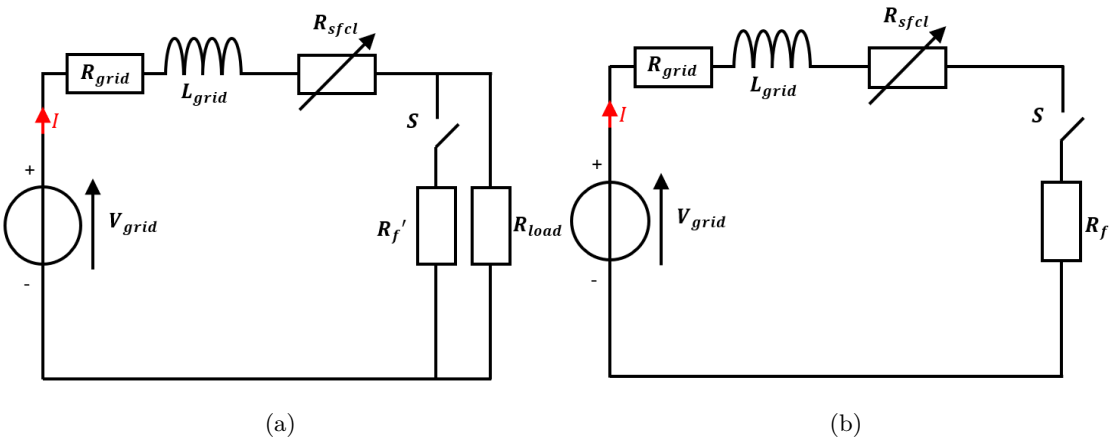

Figure 2.2: (a) Simplified representation of a power grid with a R-SFCL and (b) electrical circuit used to simulate the R-SFCL operation.

properties and efficient cooling. In addition, the I_c measurements, given by the manufacturers of tapes, are realized in the only longitudinal direction of the tape. A isothermal cross-section is assumed meaning that the model works when the diffusion time constant is smaller than the simulation duration. Its lightweight constitution explains the existence of similar models developed by other groups [72][73]. Nevertheless, when local behavior within the conductor cross-section needs to be evaluated, a 3D Finite Element Method (FEM) model of a 2G HTS tape is also used and will be introduced in section 4.3.

The beginnings of the development of this model appear in the work from N. T. Nguyen [20][74] where a R-SFCL is modeled by two elements of tape, each showing a different critical current. The heat diffusion between these elements were added in [75] by C. Gandioli. A. Badel in [76] and J. Vialle in [77] increased the number of elements to consider the variations of the critical current along the length of the tape. Some contributions were added during this thesis: the solving of the heat equation is now done with a backward Euler method instead of a forward Euler method to reinforce the stability of the model, especially for smaller discretizations and the resolution of the current sharing is done with a Newton-Raphson algorithm instead of an oscillation damping method. These changes are described in the appropriate context in this section.

2.2.1 Grid equivalent electrical circuit

The R-SFCL operates in power grids. A simple Thevenin equivalent circuit of a power grid is shown in figure 2.2a with a voltage source V_{grid}, a resistance R_{grid} and an inductance L_{grid} feeding a load R_{load}. The R-SFCL is modeled by R_{sfcl} and the fault resistance by R'_f occurring when the switch S is on. Assuming that the fault occurs at the beginning of the simulation (i.e always present during the simulation), the equivalent circuit is given in figure 2.2b with R_f modeling R'_f in parallel with R_{load}.

2.2.2 2G HTS conductor

In this manuscript, tape refers to the commercial "bare" tape sold by the manufacturers while conductor is what is wound to create the R-SFCL. The conductor can be simply the bare tape itself or in association with other materials.

2.2.2.1 Multiple elements

The 2G HTS conductor is divided in n elements along its length. This enables the consideration of the critical current variations giving to each element k (with $k \in [1, n]$) its own critical current value $I_{c,k}(77K)$. Each element k represents a unit length of 2G HTS tape. The number of elements depends on the length of the tape and the level of detail desired along the length, which is often limited by the accuracy of the critical current measurement described in section 1.2. As an example, with a space resolution Δl of 1.11 mm, 900 elements are required to model a 1 m long tape. The volume of each element is then the cross-section of the tape S multiplied by Δl.

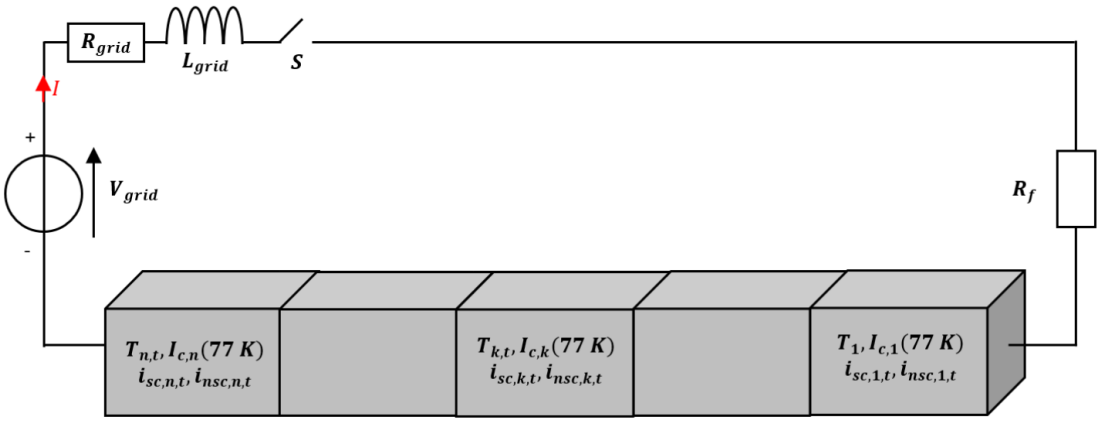

Figure 2.3: Division of the 2G HTS conductor in n elements.

The time discretization Δt is constant and equals to 0.0001 s. This value was determined by analyzing the evolution of the maximum temperature of the tape (the most important result of the simulation) at the end of a simulation as a function of the time step (see figure 2.4). The letter t, in subscript, refers to the time and t varies between 1 and t_{max}, with $t_{max}\Delta t$ the desired simulation duration. An overview of the model is given in figure 2.5 and is detailed in the following section.

2.2.2.2 Model of the conductor electrical behavior

Two resistances in parallel The representation of a conductor by the two resistances model introduced in section 1.2 is adopted in this model. The discretization of the tape length leads to a succession of elements in series (see figure 2.6). Resistance $R_{sc,k,t}$ represents the superconducting layer of the element and resistance $R_{nsc,k,t}$ the non-superconducting

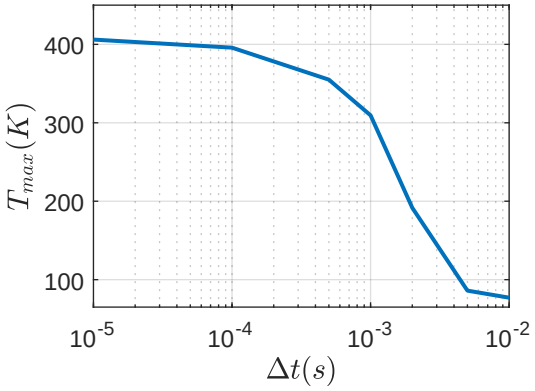

Figure 2.4: Maximum temperature of a conductor, at the end of the simulation, as a function of the time step.

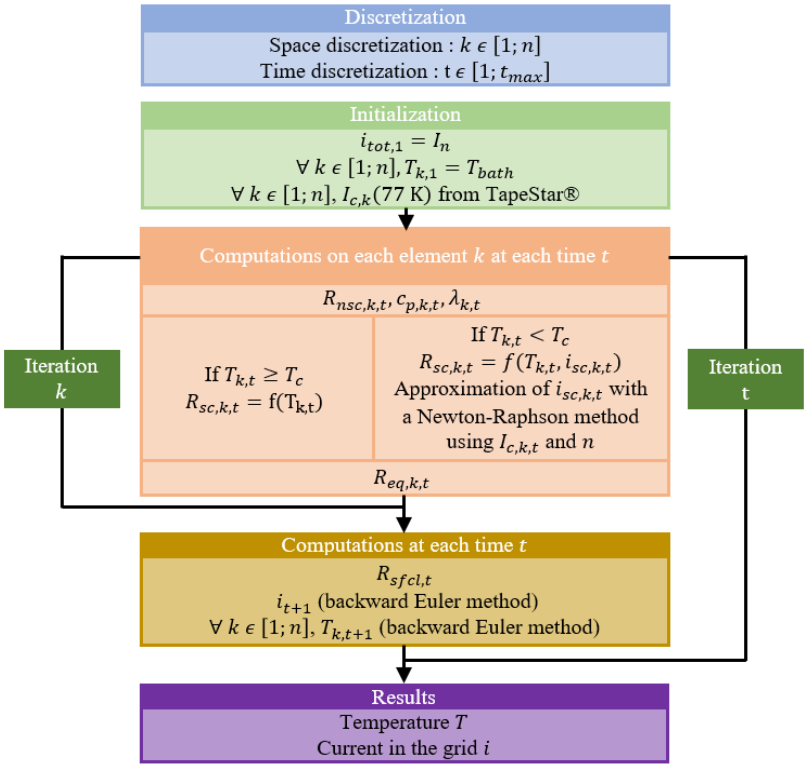

Figure 2.5: Overview of the model.

layers (substrate, buffer layers and stabilizer). The current in the circuit $i_{tot,t}$ is shared between the current in $R_{sc,k,t}$ which is $i_{sc,k,t}$ and the current in $R_{nsc,k,t}$ which is $i_{nsc,k,t}$.

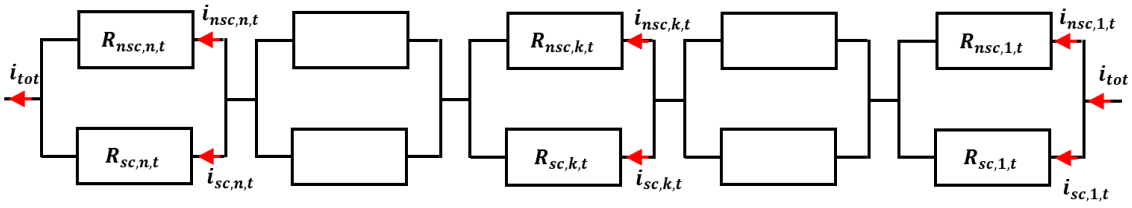

Figure 2.6: Electrical model of a 2G HTS conductor.

Description of $R_{sc,k,t}$ The non-linear continuous relationship between the electric field and the current in a type-II superconductor described by the power law was widely introduced in section 1.2. In this model, it becomes (2.1) with the standard E_c, the critical current $I_{c,k,t}$ of the element k at the time t and $i_{sc,k,t}$ the current in the superconducting layer. The n-value is considered constant and equals to 42 thanks to the measurements from [54] showing only slight variations from 65 K to 77 K.

$$E_{k,t} = E_c(\frac{\left|i_{sc,k,t}\right|}{i_{c,k,t}})^n \tag{2.1}$$

The temperature dependence of $I_{c,k,t}$ is modeled using the linear approximation given by (2.2) and introduced in subsection 1.2.4.

$$I_{c,k,t} = I_{c,k}(77\text{ K})\frac{T_c - T_{k,t}}{T_c - 77} \tag{2.2}$$

$R_{sc,k,t}$ is given by (2.3) with Δl the length of an element k. Above T_c, the resistance is only determined by the resistivity ρ_{sc} of the REBCO layer.

$$R_{sc,k,t} = \begin{cases} \frac{E_c}{I_{c,k,t}}(\frac{\left|i_{sc,k,t}\right|}{I_{c,k,t}})^{n-1}\Delta l & \text{with} \quad T_{k,t} < T_c \\ \rho_{sc}(T_{k,t}) & \text{with} \quad T_{k,t} > T_c \end{cases} \tag{2.3}$$

Description of $R_{nsc,k,t}$ The non superconducting layers are electrically in parallel. The equivalent resistance $R_{nsc,k,t}$ of these layers is given by (2.4) with e_x the thickness of the x layer, ρ_x its resistivity and w the width of the tape. x_{tot} is the total number of conductive layers.

$$R_{nsc,k,t} = \frac{\Delta l}{w * \sum_{x=1}^{x_{tot}} \frac{e_x}{\rho_x(T_{k,t})}} \tag{2.4}$$

Current sharing resolution The application of the Kirchhoff laws on the two resistances model gives (2.5). In this PhD work, the Newton-Raphson algorithm was prefered for its better efficiency compared to the damping method used in the previous versions of the model [76].

$$\begin{cases} f(i_{sc,k,t}) = i_{sc,k,t}^{n} + A i_{sc,k,t} - B = 0 \\ A = \dfrac{R_{nsc,k,t} I_{c,k,t}^{n}}{E_c} \\ B = \dfrac{i_{tot} R_{nsc,k,t} I_{c,k}^{n}}{E_c} \end{cases} \tag{2.5}$$

An approximation of the solution of this equation is obtained with (2.6) with a repetition of this process until a sufficiently precised value is reached (2.7).

$$i_{sc,k,t,n+1} = i_{sc,k,t,n} - \frac{f(i_{sc,k,t,n})}{f'(i_{sc,k,t,n})} \tag{2.6}$$

$$\left| i_{sc,k,t,n+1} - i_{sc,k,t,n} \right| < 10^{-10} \tag{2.7}$$

The initial guess is defined as follow in (2.8) with I_n the grid rated current:

$$\begin{cases} i_{sc,k,t,0} = I_n \; if \; t = 1 \\ i_{sc,k,t,0} = i_{sc,k,t-1} \; if \; t \neq 1 \end{cases} \tag{2.8}$$

Equivalent resistance Knowing $R_{sc,k,t}$ and $R_{nsc,k,t}$, the equivalent resistance $R_{eq,k,t}$ is (2.9).

$$R_{eq,k,t} = \frac{R_{sc,k,t} R_{nsc,k,t}}{R_{sc,k,t} + R_{nsc,k,t}} \tag{2.9}$$

Figure 2.7 represents R_{eq} as a function of i_{tot} and T using the resistivity data from [78][79]. The sum of these equivalent resistances gives the total resistance of the R-SFCL $R_{sfcl,t}$ at the time t in (2.10).

$$R_{sfcl,t} = \sum_{k=1}^{n} R_{eq,k,t} \tag{2.10}$$

Current computation The current at each time iteration t is computed using a Backward Euler method (2.11) and assuming $R_{sfcl,t+1} = R_{sfcl,t}$.

$$i_{t+1} = i_t + \frac{i_t + \dfrac{V_{grid} \Delta t}{L_{grid}}}{1 + \Delta t \dfrac{R_{sfcl,t} + R_{grid} + R_f}{L_{grid}}} \tag{2.11}$$

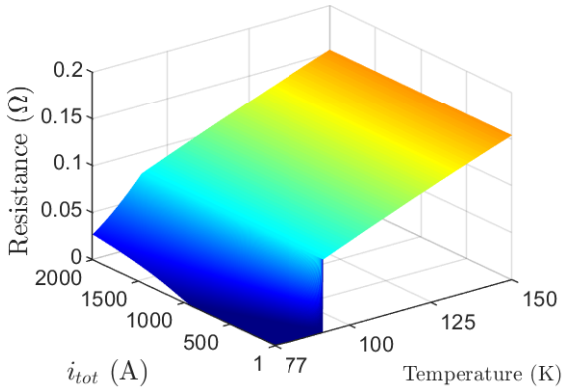

Figure 2.7: Resistance of a 1 m long 2G HTS tape as a function of the temperature and current ($I_c(77K) = 750A$).

2.2.2.3 Model of the conductor thermal behavior

The discretization of the thermal model is the same as the electrical model. For each element k, the electrical model gives a heating power $P_{k,t}$ (2.12) that is used in the thermal model to calculate the temperature variations (see figure 2.8). Heat transfer between elements is considered.

$$P_{k,t} = R_{eq,k,t} i_t^2 \tag{2.12}$$

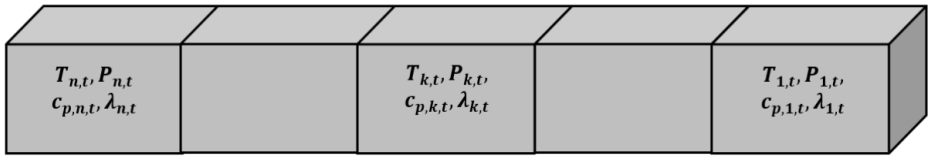

Figure 2.8: Thermal model of the 2G HTS conductor.

Homogenization of the thermal properties The specific heat capacity $c_{p,k,t}$, thermal conductivity $\lambda_{k,t}$ and density μ are homogenized over each element. The specific heat capacity $c_{p,k,t}$ and the thermal conductivity $\lambda_{k,t}$ at the temperature $T_{k,t}$ are respectively given by an average computation by the mass (2.13) and thickness (2.14) of each layer x , with a total number of layers x_{tot}. The computation of $\lambda_{k,t}$ is justified by the heat propagation occurring in the longitudinal axis of the tape. In this direction, the layers are thermally in parallel. The density μ is the sum of the mass of each layer divided by the total volume of the element V_{total} (2.15).

$$c_{p,k,t} = \frac{\sum_{x=1}^{x_{tot}} m_x c_{p,x}(T_{k,t})}{m_{total}} \tag{2.13}$$

$$\lambda_{k,t} = \frac{\sum_{x=1}^{x_{total}} e_x \lambda_x(T_{k,t})}{e_{total}} \tag{2.14}$$

$$\mu = \frac{\sum_{x=1}^{x_{tot}} m_x}{V_{total}} \tag{2.15}$$

Heat equation resolution The heat equation resolution (2.16) makes it possible to determine the temperature of each element k at each time t. One contribution of this thesis is to solve the equation using a backward Euler method (2.17) with some first order approximations (2.18). The backward Euler method solves the problem of instability when the spatial discretization becomes small. The temperature of the elements on the boundaries are set to the liquid nitrogen bath temperature (i.e. $\forall t \in [1, t_{max}],\ T_{1,t} = T_{n,t} = T_{bath}$).

$$\frac{\partial T_{k,t}}{\partial t} = \frac{\lambda_{k,t}}{\mu c_{p,k,t}} \nabla T_{k,t} + \frac{P_{k,t}}{m c_{p,k,t}} \tag{2.16}$$

$$(1 + 2\frac{\lambda_{k,t+1})\Delta t}{\mu c_{p,k,t+1})\Delta l^2})T_{k,t+1} = T_{k,t} + \frac{\lambda_{k,t+1}\Delta t}{\mu c_{p,k,t+1}\Delta l^2}(T_{k-1,t+1} + T_{k+1,t+1}) + \frac{P_{k,t+1}\Delta t}{m c_{p,k,t+1}} \tag{2.17}$$

$$\begin{cases} \lambda_{k,t+1} = \lambda_{k,t} \\ c_{p,k,t+1} = c_{p,k,t} \\ P_{k,t+1} = P_{k,t} \end{cases} \tag{2.18}$$

This model is now used to assess the influence of the critical current inhomogeneity on the tape operation in fault conditions.

2.3 Simulation of the 2G HTS conductor operation

2.3.1 Framework of the simulation

2.3.1.1 Number of elements

The I_c variations of a 1 m long 2G HTS tape shown in figure 1.16 and reminded in figure 2.9 are used ($I_c^{mean} = 733$ A, $I_c^{max} = 781$ A, $I_c^{min} = 665$ A, $\Delta I_c = 116$ A). The measure of the local I_c is done every 1.1 mm so 900 elements are needed to model the full length of the conductor.

2.3.1.2 Architecture

The thicknesses and the materials of the layers of the simulated architecture are given in Table 2.1. The thermal and electrical properties of the silver, MgO and YBCO come from [78] and the ones of Hastelloy® C276 from [79].

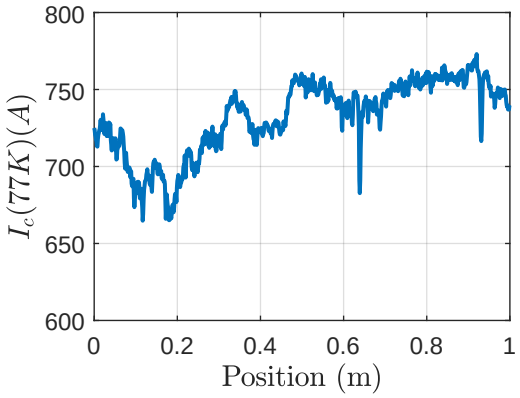

Figure 2.9: Critical current over position of a 1 m long 2G HTS tape from THEVA (data from THEVA, 77 K, self-field, Tapestar®).

Layers	Substrate	Buffer stack	Superconducting layer	Stabilizer
Materials	Hastelloy® C276	MgO	YBCO	Silver
Thicknesses (µm)	100	3	3	3.2

Table 2.1: Thicknesses and materials of the components of the conductor.

2.3.1.3 Range of prospective currents

A R-SFCL is designed to operate in a grid where the prospective current takes any value from the rated current I_n to the maximum prospective current which can typically reach $20I_n$ (see section 1.1). Nevertheless, higher maximum prospective current can be considered in the design of a R-SFCL. As an example, in the European project Eccoflow, the rated current of the R-SFCL was $I_n = 1005$ A [80] and the maximum prospective current was $25I_n$ [19].

In this simulation, the rated current is 350 A, the maximum prospective current is $20I_n$ and the parameters of the DC circuit are given in Table 2.2. The resistance R_f varies from 0 to 0.41 Ω. The simulation lasts for 15 ms and is run for the given range of R_f. The cooling is at 77 K.

Parameter	V_{grid} (V)	R_{grid} (Ω)	L_{grid}(µH)
Value	150	0.021	64

Table 2.2: Values of the circuit parameters.

2.3.2 Operation with various prospective currents

One result of the simulation is the maximum temperature of the conductor at the end of the simulation as a function of the prospective current (see figure 2.10). Contrary to what

could be expected in a homogeneous case, the temperature is not constantly increasing with the prospective current. A temperature excursion occurs when the prospective current is in the range of local I_c variations. This result is qualitatively similar for any I_c distributions.

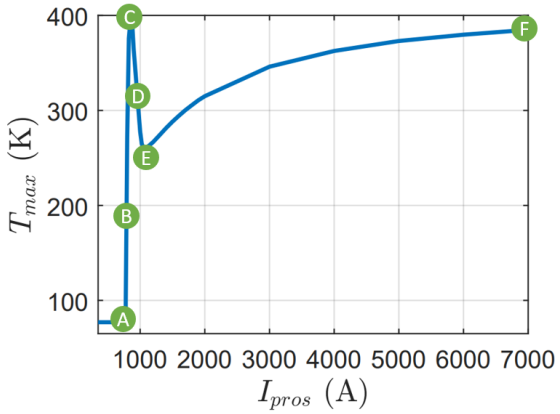

Figure 2.10: Maximum temperature of the conductor after 0.015 s of operation for a large range of prospective currents. A temperature elevation occurs in the range of I_c variations.

To better understand this result, the current in the grid during the simulation and the temperature of each element at the end of the simulation are given respectively in figure 2.11 and in figure 2.12 for several prospective currents.

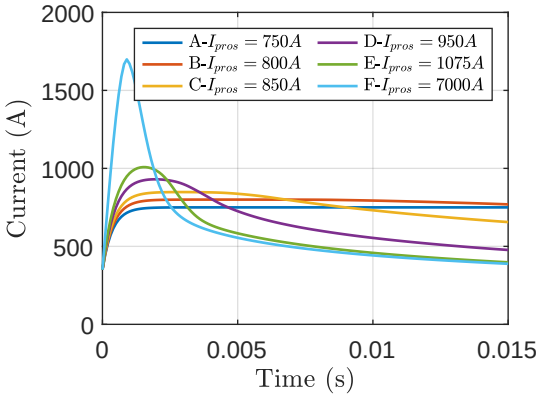

Figure 2.11: Current in the simulated grid as a function of the time at various prospective currents.

Case A - I_{pros} = 750 A: with low prospective current, the conductor remains superconducting at the liquid nitrogen bath temperature. The current in the grid is in steady-state and not high enough to initiate any thermal runaway.

Case B - I_{pros} = 800 A: when, the prospective current increases, the portions of

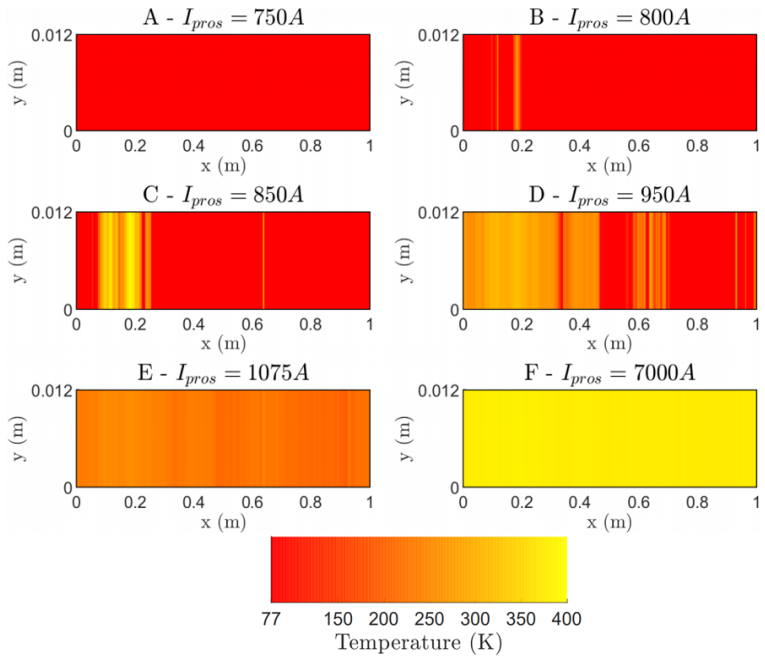

Figure 2.12: Temperature of the 2G HTS conductor for various prospective currents at 15 ms.

the conductor showing the lowest I_c become dissipative and start to heat. The current is slightly limited from 10 ms until the end of the simulation.

Case C - I_{pros} = 850 A: the highest maximum temperature is reached when the current in the grid is high enough to initiate a thermal runaway around the area where the critical current is lower but small enough not to quench the portions of the conductor having the highest critical currents and leading to a slight limitation. Moreover, the temperature elevation remains localized. The speed at which the resistive zone expands, called Normal Zone Velocity Propagation (NZPV), is low in 2G HTS tape. A precise value coming from the simulation is not given because the current should be constant for this estimation. In the literature [81] [82], an evaluation of 0.1 m/s is found.

From Case D - I_{pros} = 950 A **to Case E -** I_{pros} = 1075 A: the prospective current is high enough to quench a larger part of the conductor , the current limitation is more efficient and the maximum temperature decreases. This maximum temperature continues to decrease with an increasing prospective current until the quench is homogeneous over the whole conductor (E - I_{pros} = 1075 A).

From Case E - I_{pros} = 1075 A **to Case F -** I_{pros} = 7000 A: the quench is homogeneous over the whole conductor and the maximum temperature increases with the prospective current. Indeed, when the prospective current increases, the resistance R_f decreases while V_{grid} is constant. The electric field withstood by the conductor increases

with the prospective current. Figure 2.13 shows that the rms current, given by (2.19) where Δt is the simulation duration, increases with the prospective current from (E - $I_{pros} = 1075$ A) to (F - $I_{pros} = 7000$ A).

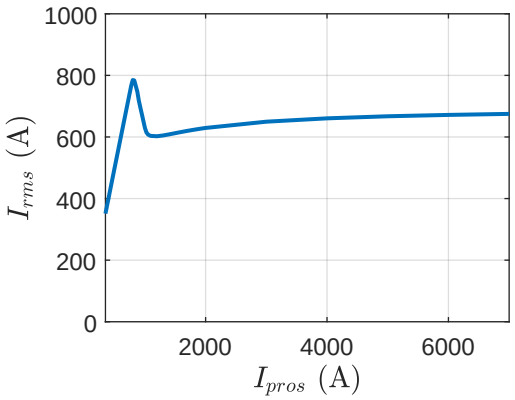

Figure 2.13: RMS value of the current in the circuit as a function of the prospective current.

$$I_{rms} = \sqrt{\frac{1}{\Delta t}\int_{t_0}^{t_0+\Delta t} i(t)^2 dt} \tag{2.19}$$

This evolution of the maximum temperature of the conductor as a function of the prospective current was obtained in [19][74][77] and also by another group in [72]. It predicts an elevation of the temperature when the prospective current is in the range of I_c variations and naturally when I_{pros} becomes very large. This leads to define two main operation regimes of the 2G HTS tape in the framework of the R-SFCL, which are important to consider in the design of the conductor of a R-SFCL: the limitation regime and the hot-spot regime.

2.4 Two regimes of operation

2.4.1 Definitions

The evolution of the maximum temperature of the conductor as a function of the prospective current is once again given in figure 2.14. As just mentioned, two ranges of prospective current are of particular interest the hot-spot regime and the limitation regime. As shown in [67], the study of these two domains makes it possible to derive design constraints for the R-SFCL conductor from analytic calculations.

Limitation regime : it occurs with the highest prospective current, in the event of a zero-impedance short-circuit. In such case, the current in the grid is high enough to quench the whole conductor. Considering the circuit parameters given in Table 2.2, the

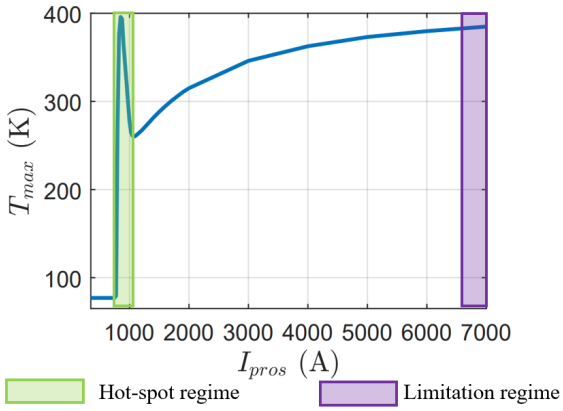

Figure 2.14: Maximum temperature of the 2G HTS conductor as a function of the prospective current with the hot-spot regime and limitation regime.

resistance of the R-SFCL R_{sfcl} is high enough (see figure 2.15a) to consider that the grid voltage V_{sfcl} is almost entirely applied on the R-SFCL (see figure 2.15b). From an energy balance in adiabatic conditions applied on the conductor with a length L_{sc} inserted in the circuit in figure 2.15b, the temperature elevation ΔT is analytically expressed by (2.20) where Δt is the clearing fault time given by the grid operator, ρ the electrical resistivity of the conductor and $c_{p,v}$ its heat capacity per volume unit. Temperature dependence of ρ and $c_{p,v}$ are not mentioned here to make the expression clearer. With the introduction of the electric field E_{sc} withstood by the conductor, (2.20) becomes (2.21).

$$\Delta T = (\frac{V_{sfcl}}{L_{sc}})^2 \frac{\Delta t}{c_{p,v}\rho} \tag{2.20}$$

$$\Delta T = \frac{E_{sc}^2 \Delta t}{c_{p,v}\rho} \tag{2.21}$$

Hot-spot regime : it is obtained when the prospective current is in the range of I_c variations of the conductor. In such case, only the portions of the conductor showing the weakest I_c quench, R_{sfcl} is small compared to R_{grid} in series with R_f (see figure 2.16a). The current is almost not limited and mainly determined by the grid and fault impedances. The grid can be modeled as a current source delivering the critical current (see figure 2.16b). From an energy balance in adiabatic conditions applied on the section of the conductor where the quench occurs, the temperature elevation is given by (2.22) with e_{cond} the conductor thickness, I_c the critical current and w the width of the conductor. Introducing $I_{c,w}$ the critical current per unit width, (2.22) becomes (2.23).

$$\Delta T = \frac{\rho \Delta t}{c_{p,v}} (\frac{I_c}{e_{cond} w})^2 \tag{2.22}$$

$$\Delta T = \frac{\rho \Delta t}{c_{p,v}} (\frac{I_{c,w}}{e_{cond}})^2 \tag{2.23}$$

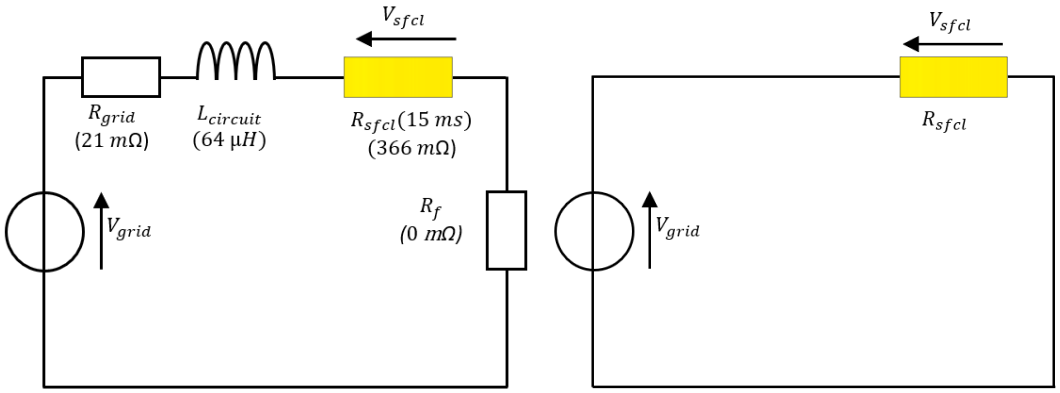

(a) (b)

Figure 2.15: (a) Electrical circuit giving the maximum temperature of the conductor in limitation regime and (b) simplified circuit giving an analytic expression of the temperature elevation for this regime.

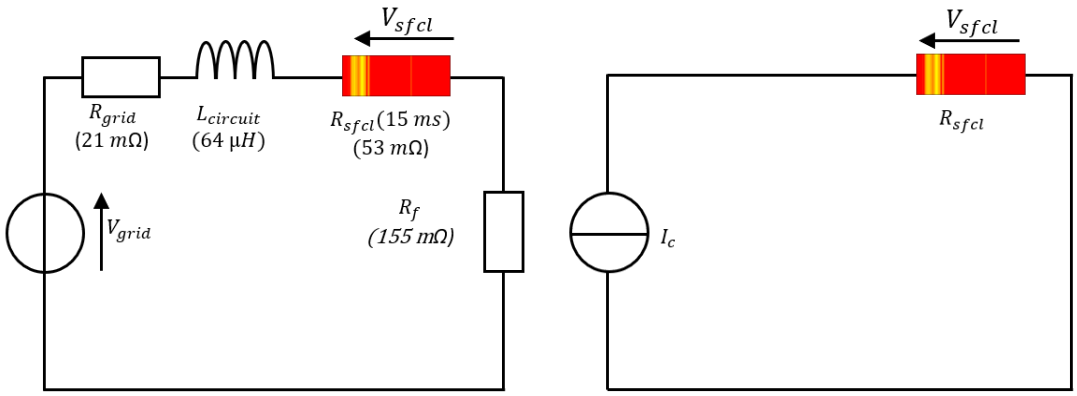

(a) (b)

Figure 2.16: (a) Electrical circuit giving the maximum temperature of the conductor in hot-spot regime and (b) simplified circuit giving an analytic expression of the temperature elevation for this regime.

The formalization of these two regimes is a powerful tool to design the conductor of R-SFCL.

2.4.2 Design of a conductor

Reference [67] shows that the length of the conductor L_{sc} and the thickness of the conductor e_{cond} can be given from the expressions (2.21) and (2.23) just introduced.

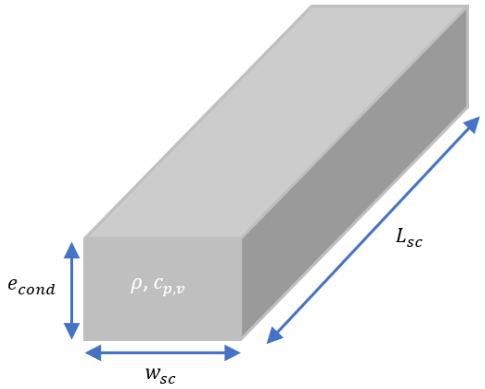

Figure 2.17: Dimensions of a conductor showing homogeneous resistivity and heat capacity per unit volume.

The designer gives the maximum temperature elevation ΔT_{max} allowed not to risk any damage of the conductor. Generally, it is around 350 K. The utility gives Δt and V_{sfcl}. As a consequence, the length of the conductor is given by the operation in limitation regime with (2.24) and its thickness by its operation in hot-spot regime with (2.25).

$$L_{sc} = V_{sfcl}\sqrt{\frac{\Delta t}{\Delta T_{max} c_{p,v} \rho}} \tag{2.24}$$

$$e_{cond} = I_{c,w}\sqrt{\frac{\rho \Delta t}{\Delta T_{max} c_{p,v}}} \tag{2.25}$$

The width of the conductor is given by the operation in normal operation. Most of the design was introduced in subsection 1.3.3.1. The total width of the conductors in parallel w_{sc} has to present a critical current I_c at least equals to the normal transient overcurrent in a grid represented by $k_a I_a$. This gives the total width of the conductors in (2.26). Commercial 2G HTS tapes can be 12 mm wide. In such case, the number of conductors based on 2G HTS tapes is given by (2.27).

$$w_{sc} = \frac{k_a I_a}{I_{c,w}} \tag{2.26}$$

$$N \geq \frac{w_{sc}}{0.012} \tag{2.27}$$

2.4.3 Mitigation of the temperature elevation in hot-spot regime

2.4.3.1 Considerations from the temperature elevation in hot-spot

The study of the expression of the temperature elevation in hot-spot regime given in (2.22) makes it possible to propose solutions to decrease the temperature in this regime. Indeed, it was introduced in subsection 1.3.3.2 as an operation range where the current could highly threatens the integrity of the conductor. The impact of the solutions, which are presented here, on the cost of the conductor is also mentioned using the cost expression given by (2.28) and introduced in subsection 1.3.3.1.

$$Cost = C_{sc} N L_{sc} = C_{sc} \frac{k_a I_a}{I_c} \frac{V_{sc}}{E_{sc}} \tag{2.28}$$

Influence of the resistivity The conductor equivalent resistivity can be modified by changing the thickness of the layers. The variation of the highly conductive silver layer thickness largely changes the equivalent conductor resistivity. Figure 2.18a shows that a decrease of the resistivity due to a thicker silver layer decreases the maximum temperature in hot-spot regime as it is predicted by (2.23). This solution was adopted in the European Project Eccoflow [9]. With a critical current per cm-width around 300 A, the solution to limit the temperature elevation in hot-spot regime was to increase the thickness of the stabilizer layer to at least 3 µm.

This approach has a drawback on the cost of the conductor. Expression (2.21) shows that a smaller resistivity implies a higher temperature elevation in limitation regime, the electric field E_{sc} must be reduced to maintain an acceptable temperature elevation which drives the cost of the conductor up (see (2.28)). In the opposite way, the increase of the resistivity leads to a higher temperature in hot-spot regime but a lower temperature in limitation regime which could result in a possible increase of the electric field E_{sc}.

Influence of the temperature of the bath As it has been introduced in subsection 1.2.4, the critical current of a superconducting material decreases when the temperature increases. The operation in a liquid nitrogen bath at a higher temperature would contribute to decrease the coefficient $I_{c,w}$ in (2.23). Figure 2.18b shows that the temperature elevation in hot-spot regime is lower at 80 K than at 77 K.

However, this method is of small interest as it increases the total width of the conductors associated in parallel in a R-SFCL (2.26), as a consequence the number of conductors

N (see 2.27) and the cost (2.28). In the opposite way, a diminution of the bath temperature would allow a reduction of the number of conductors required to transport the rated current, but at the cost of a more severe hot-spot regime (see 2.18b).

Influence of the conductor thickness Figure 2.18c shows that an increase of the conductor thickness e_{cond} by an increase of the thickness of the substrate has a small impact on the conductor equivalent resistivity of the conductor but it significantly enables a decrease of the temperature elevation in hot-spot regime.

This solution is very attractive. It would make it possible to increase the resistivity of the conductor to reach higher electric field in limitation regime and increase $I_{c,w}$ without threatening the operation in hot-spot regime. These two actions decrease the total cost of the conductor (see (2.28)) by decreasing its length L_{sc} and the number of conductors in parallel N respectively. This solution is adopted in the Fastgrid project, the design of the conductor is widely explained in section 5.1.

2.4.3.2 Enhancement of the heat dissipation homogeneity

One other approach is the enhancement of the heat dissipation to faster reach a homogeneous dissipation. The hot-spot would more rapidly propagate which limits the current and as a consequence, the temperature elevation.

Enhancement of the heat diffusion with a Sapphire-Based substrate A first route is the improvement of the thermal conductivity of the conductor. This is simply evaluated in [57] where the curve $T_{max} = f(I_{pros})$ is compared with the heat conductivity of the conductor multiplied by a factor of 100 and without the multiplication. The result is displayed in figure 2.19. The increase of the heat conductivity leads to a drastic decrease of the peak temperature in hot-spot regime.

The use of sapphire wafer as substrate to develop SFCL conductor is well known in the literature [71] [83] [84]. It also exists in the shape of tape in [85]. The high diffusivity of the sapphire contributes to propagate the heat in the event of a hot-spot and to limit the current. Unfortunately, the cost of this technology is very high. Some improvements exist and will be detailed in chapter 5.3 with one advanced conductor developed by Tel-Aviv University in the framework of the Fastgrid project showing an outstanding electric field but with a low critical current up to now.

Enhancement of the NZPV with the concept of Current Flow Diverter One other way to homogenize the heat dissipation in a 2G HTS conductor is to increase the Normal Zone Propagation Velocity (NZPV). C. Lacroix and F. Sirois in [82] present the concept of Current Flow Diverter (CFD). The idea is to increase the current transfer length from the superconducting layer to the stabilizer layer to increase the NZPV. This is realized with the addition of a highly resistive interface between these two layers. The interface is not uniform, only the center portion of the width is highly resistive (see figure 2.20).

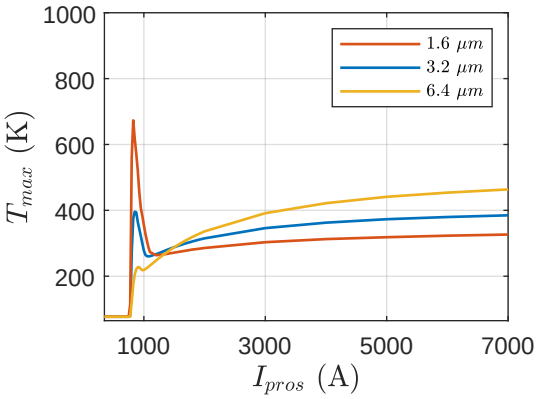

(a) Thickness of the silver layer

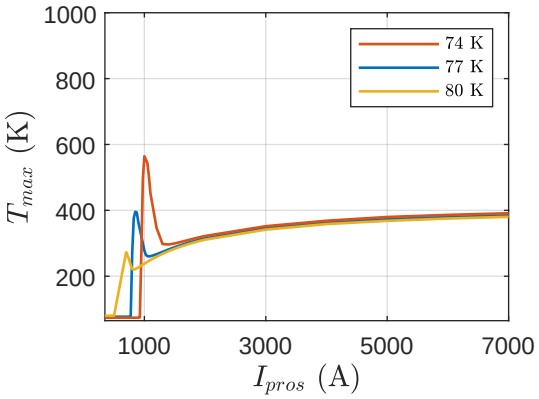

(b) Liquid nitrogen bath temperature

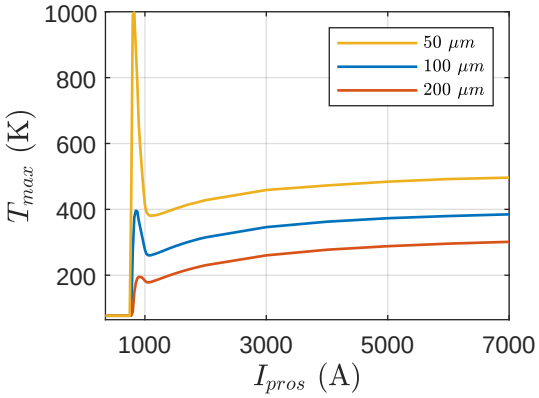

(c) Thickness of the substrate layer

Figure 2.18: Maximum temperature of the 2G HTS conductor as a function of the prospective current considering the influence of several parameters.

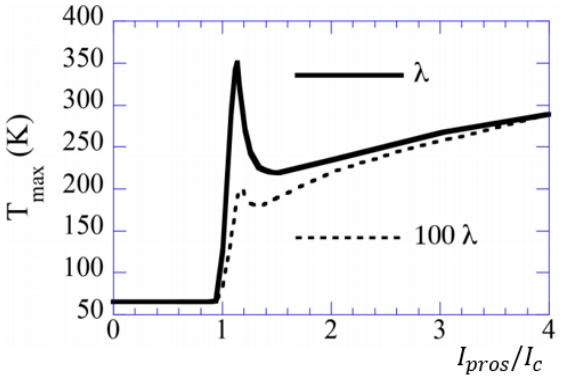

Figure 2.19: Maximum temperature as a function of the prospective current divided by the critical current of the conductor with the conductivity of the conductor as a parameter, from [57].

A uniform highly resistive interface on the width would result in a large amount of heat on the current leads. In simulation, this architecture increases the NZPV to 20 m/s [82] while it is generally in the order of 0.1 m/s.

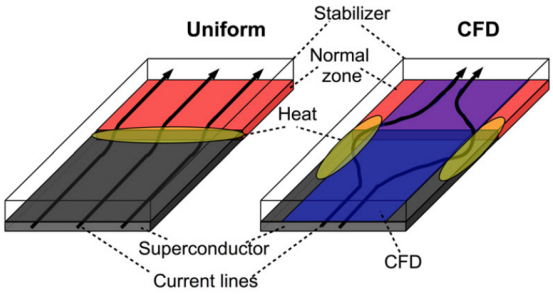

Figure 2.20: Schematic drawing of the current path flows in a uniform (left) and CFD tape (right) from [82].

There is no easy way to produce long lengths of tape with this architecture, mainly due to the difficulty to realize the interface. In the Fastgrid project, ICMAB and Oxolutia strongly collaborated with EPM to develop a way to industrialize the manufacturing process of the CFD. This is one important aspect of the PhD activities of P. Barusco. One sample from his work is characterized in 5.2 as well as one sample of the sapphire-based substrate tape developed by TAU.

2.5 Conclusion

This chapter described the behavior of the R-SFCL for a wide range of prospective currents when considering the I_c variations along the conductor length based on a modeling approach. That approach started with the presentation of improvements of a 1D electro-thermal model of 2G HTS tape-based conductor in operation in a circuit emulating fault conditions. The further developments on this model made it possible to have a thinner spatial discretization and a simpler solving of the current sharing with the use of a Newton-Raphson method.

One important result of the simulations carried out with this model is the maximum temperature as a function of the prospective current. Two particular regimes of operation leading to the highest temperatures of the conductor are observed. The first is the limitation regime occurring with the highest prospective current and the second is the hot-spot regime occurring with prospective currents in the range of the I_c variations of the tape.

The formalization of these two regimes of operation with analytic expressions makes it possible to assess the influence of parameters on the temperature elevations occurring during these regimes. It is a powerful tool to design the conductor of a R-SFCL. The 1D model developed here can also be used to assess the impact of the conductor length on

the hot-spot regime (see chapter 6). However, to observe local behaviors occurring in a 2G HTS conductor, a 3D model is more adapted and will be used in chapter 4.

There is only a few experimental observations of these regimes of the conductor over the whole prospective current range. The next chapter presents a dedicated experimental set-up to observe them.

CHAPTER 3

Experimental study of the hot-spot regime

After the introduction of the conductor operation on a wide range of prospective currents, this chapter focuses on the hot-spot regime, using an experimental approach. A dedicated set-up is developed to observe the fault current operation of a sample of 2G HTS conductor. It consists of an electrical circuit emulating the grid associated with a cryogenics environment where the temperature of the bath can be changed. Electrical measurements (current and electric fields) are realized and a high-speed imaging system is used to observe bubbles generated on the surface of the sample. The computation of the maximum temperature, using electrical measurements, is recalled and its use on a wide range of operation points enables the experimental observation of the hot-spot regime. Moreover, the evolution of the dissipation homogeneity as a function of the prospective current is discussed.

The experimental set-up described exhaustively in this chapter will be used throughout the rest of this PhD work.

3.1 Emulation of the R-SFCL environment

3.1.1 Fault current set-up

The role of this set-up is to place the studied sample in the R-SFCL operation conditions, with the ability to adjust the prospective fault current. Both an AC and a DC electrical circuits are proposed.

3.1.1.1 Simulation with a variable V_{grid} or R_f

Simulations are first realized to highlight the importance of key parameters having consequences on the hot-spot regime.

As it is mentioned in subsection 2.2.1, the grid can be represented by the scheme in figure 3.1. The prospective current in this DC circuit is (3.1). In a lab set-up, it is possible to vary the prospective current either by modulating V_{grid} or R_f. R_{grid} is the sum of the resistances of the wires, contacts, etc.

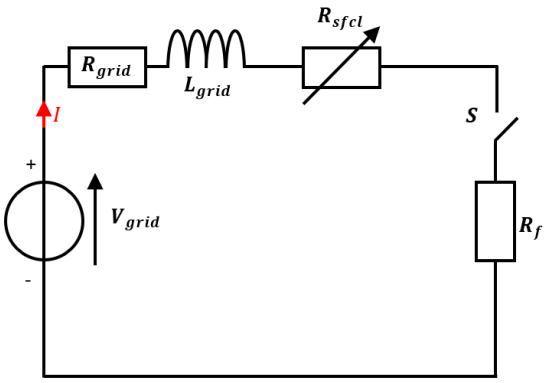

Figure 3.1: Equivalent circuit of a power grid with a R-SFCL.

$$I_{pros} = \frac{V_{grid}}{R_{grid} + R_f} \tag{3.1}$$

Although, in lab conditions, it appears easier to vary V_{grid} but in actual power grids, it is the voltage that is constant and the impedance of faults varies. A simulation is thus performed in order to check if the two methods give similar results in terms of R-SFCL behavior. The maximum temperature is computed with the prospective current varying from 350 A to 7000 A. R_{grid} is 21 mΩ and L_{grid} is 64 µH. In the case where the voltage is constant, called $R - var$, V_{source} is 150 V and R_f varies from 0 to 0.41 Ω. In the case where the fault resistance is constant, called $V - var$, R_f is zero and V_{source} varies from 7.5 V to 150 V.

Figure 3.2 shows identical temperatures with the highest prospective current but they are different in hot-spot regime. The currents leading to the maximum temperature at $I_{pros} = 850$ A are displayed in figure 3.3a. In the $V - var$ case, the prospective current current is reached less quickly than in the $R - var$ case. As a consequence, the heat dissipation in the region of the tape showing the weakest critical current lasts less time, therefore leading to a smaller temperature elevation.

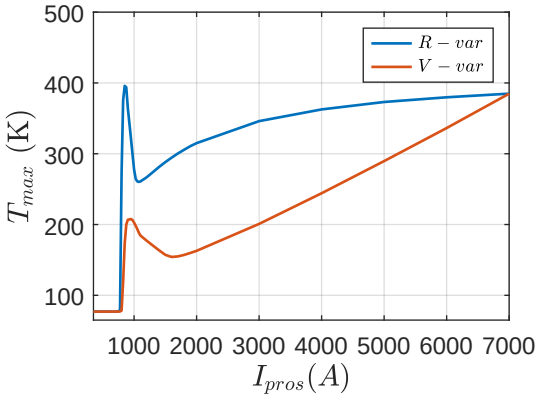

Figure 3.2: Maximum temperature over the tape as a function of the prospective current in the $R - var$ case (solid blue line) and in the $V - var$ case (solid red line).

This difference of current dynamics comes from the non instantaneous current increase in the circuit. The time constant τ is (3.2) in the $V - var$ case, remaining constant whatever the voltage (see figure 3.3) while τ is (3.3) in the $R - var$ case, changing for all prospective currents.

$$\tau = \frac{L_{grid}}{R_{grid}} \tag{3.2}$$

$$\tau = \frac{L_{grid}}{R_{grid} + R_f} \tag{3.3}$$

Although the behavior is qualitatively similar in both configurations, in this thesis, it is chosen to develop circuits in $R - var$ configuration to be in grid configuration.

3.1.1.2 Simulation with an AC and DC grid

One other concern arising when going from simulation to experiments, is the similarity between simulations performed in DC and measurements in AC. Indeed, the measurements in AC are easier with the possibility to use the power grid as a source. With the model detailed in section 2.2 and the simulation framework developed in section 2.3, the equivalence of DC and AC measurements is studied. In DC, the source is a constant voltage $V = 150$ V and in AC, the voltage is defined by (3.4) with f the grid frequency

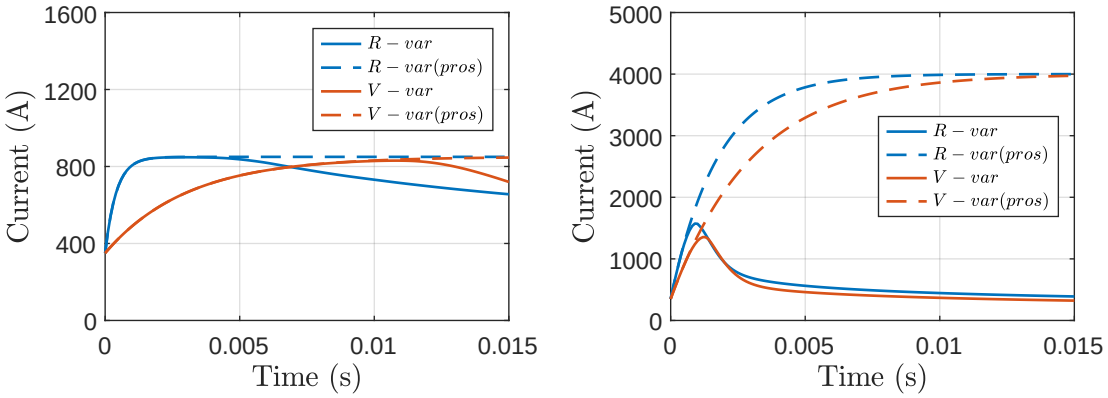

(a) $I_{pros} = 850$ A (b) $I_{pros} = 4000$ A

Figure 3.3: Current in the circuit as a function of the time with a prospective current of (a) 850 A and (b) 4000 A in $V - Var$ and $R - var$ configurations.

(50 Hz). The results in figure 3.4 shows that the hot-spot regime are particularly different. Indeed, in a superconductor, the resistance depends on the temperature but also on the instantaneous value of the current below T_c (see (2.3)).

$$V(t) = \sqrt{(2)}Vcos(2\pi ft) \tag{3.4}$$

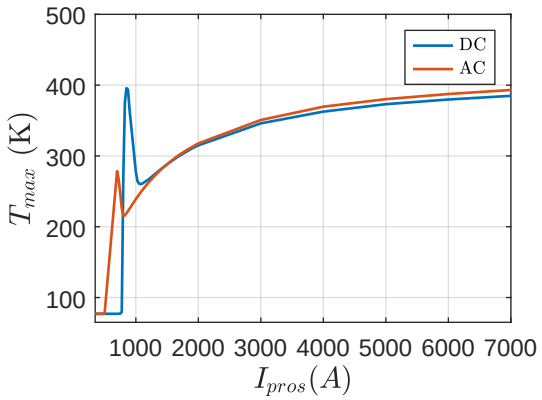

Figure 3.4: Maximum temperature over the tape as a function of the prospective current with a DC source (solid blue line) and an AC source (solid red line).

A DC and an AC fault current set-up are developed. The development of a DC fault current set-up is a big achievement due to the difficulty to have a source with a high dynamic and the realization of the current interruption. However, it can already been said that further developments have to be realized to control the prospective current in this circuit.

3.1.1.3 AC circuit

Th AC circuit was already present in the applied superconductivity group in Grenoble. One contribution of this PhD work is to arrange it in $R-var$ configuration. It consists of a $0-400$ V auto-transformer, with a variable ratio, powering the R-SFCL conductor R_{sfcl} through a transformer with a ratio m smaller than 1 to increase the current through the sample (see figure 3.5). To vary the prospective current, a variable resistance R_{var} is inserted between the auto-transformer and the transformer. The resistance consists of several 4.9 Ω power resistances stacked in parallel or in series. A switch S_2 controlled by the user connects the sample to the voltage source for the desired duration. An additional 3000 A switch S_3 opens the circuit in the event of a non-opening of S_2.

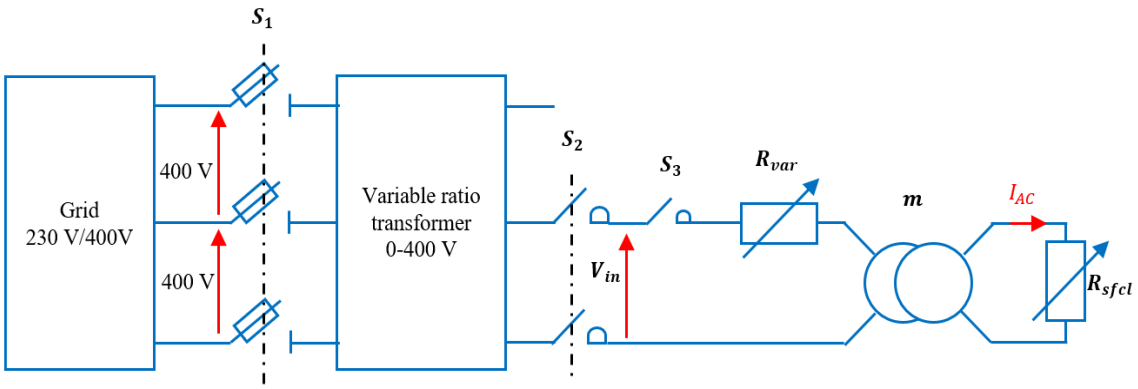

Figure 3.5: Scheme of the AC electrical circuit used to characterize 2G HTS conductor samples.

Figure 3.6 gives a practical representation of this circuit. The parameters are listed in Table 3.1. The user sets the voltage V_{source} (through V_{in}) at the desired value while R_{fault} (through R_{var}) is changed at each test. The switch S_2 is still controlled an represented by S in figure 3.6. R_{fault} varies from 0 Ω to 0.085 Ω. The prospective current in the grid is given by (3.5). As an example, with $V_{source} = 30$ V, I_{pros} varies from 350 A to 7000 A. The current is measured with a 5000 A rated sensor.

Parameters	m	$R_{circuit}$ (Ω)	$X_{circuit}$ (Ω)
Values	30/380	0.0038	0.002

Table 3.1: Values of the circuit parameters.

$$I_{pros} = \frac{V_{source}}{\sqrt{(R_{circuit} + R_{fault})^2 + (X_{circuit})^2}} \tag{3.5}$$

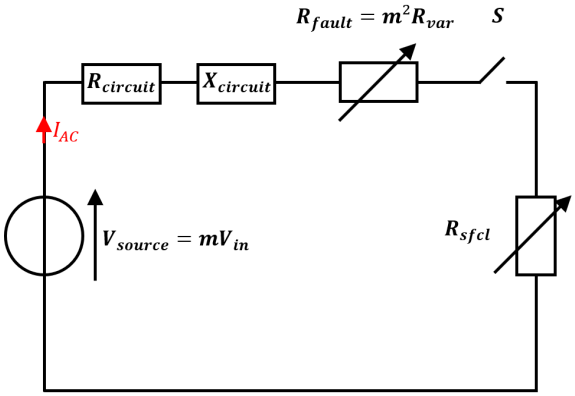

Figure 3.6: Simplified representation of the AC electrical circuit.

3.1.1.4 DC circuit

A. Derbey and B. Sarrazin, from the power electronics group of the G2ELab, fully developed the DC switch.

The DC circuit was entirely developed (see figure 3.7). It consists of a source which is a Maxwell supercapacitor (165 F-48 V), whose capacity is big enough to ensure negligible voltage drop. It is reloaded between experiments by a low current DC source. $R_{circuit}$ is 23 mΩ and $L_{circuit}$ is 3.6 µH. Interrupting DC current is difficult as energy must be dissipated in the switch. The switch S uses five half-bridge MOSFET in parallel, allowing a very fast interruption of the current. R_{fault} is a variable power resistance varying from 0 to 0.1 Ω. The development of the circuit during this PhD work is a first step. Indeed, R_{fault} is to small compared with the values of the contact resistances of the circuit to control the prospective current.

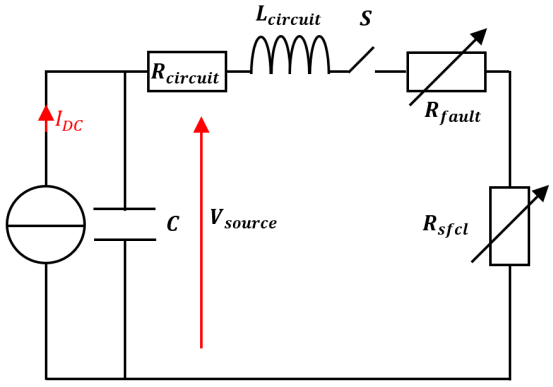

Figure 3.7: Scheme of the DC electrical circuit used to characterize 2G HTS conductor samples.

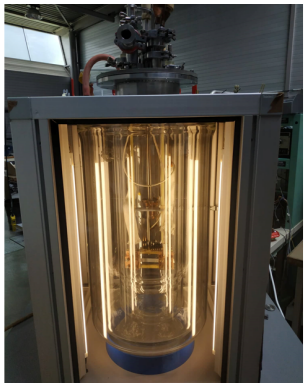

(a) Transparent cryostat

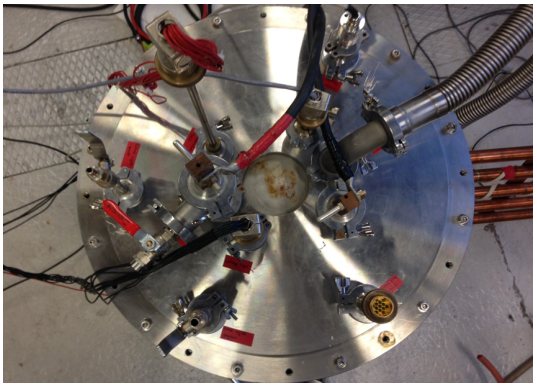

(b) Fastgrid cryostat

Figure 3.8: Cryostats used during this PhD work with (a) the transparent cryostat and (b) the cryostat used to characterize the FASTGRID conductor.

3.1.2 Cryogenics environment

3.1.2.1 Cryostats

Two cryostats were used throughout this PhD work (see figure 3.8). The first one is a transparent cryostat with an inner diameter of 16 cm and the second one is a stainless steel cryostat with an inner diameter of 40 cm. The latter cryostat is mainly used to characterize the Fastgrid conductor in subsection 5.1.3.

3.1.2.2 Temperature of the nitrogen bath

In all cases, the cooling is done by a liquid nitrogen bath. The temperature of the bath impacts the hot-spot regime as it was introduced in subsection 2.4.3.1. The temperature variation is achieved by varying the pressure.

Operation below 77 K The phase diagram of Nitrogen is shown in figure 3.9 (data from [86]). The Nitrogen solidifies at 63 K. As a consequence, the temperature of the bath can not be practically lower than 65 K. In a closed cryostat, the temperature of the liquid is modified by controlling the pressure. As an example, to reach 68 K, the pressure is decreased down to 290 hPa (figure 3.9, B). This decrease of pressure is performed in this set-up using two pumps in parallel connected to the cryostat through a heat exchanger (see figure 3.10). The role of the heat exchanger is to warm up the pumped gaseous nitrogen to avoid damaging the pumps. Nevertheless, the dielectric properties of gas at low pressures are not good (Paschen's law). In order to improve it, the pressure is then increased to the ambient pressure (figure 3.9, C). The bath is therefore not at equilibrium during the experiment but the rate of temperature increase is negligible compared with the duration of the tests.

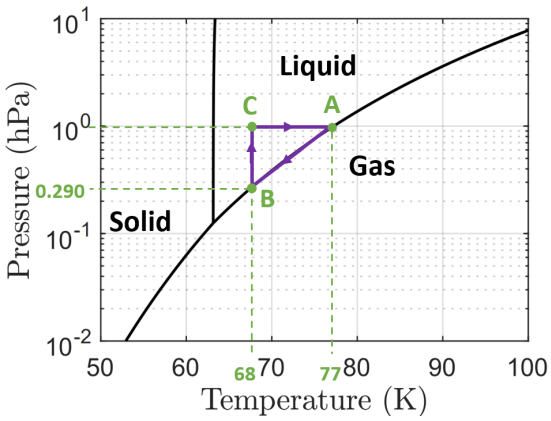

Figure 3.9: Phase diagram of Nitrogen. The data come from the website of Air Liquid [86].

Figure 3.10: Picture of the experimental set-up used to decrease the pressure over the cryogenics bath: two pumps are associated in parallel (background) and connected to a heater (foreground).

Operation above 77 K To operate at higher temperatures than 77 K, cryostat shown in figure 3.8b is used. Inside the bottom part of the cryostat, power resistances thermally connected through Apiezon N grease to a disk in copper to obtain a large surface of heat transfer are installed. The pressure in the cryostat is controlled using a valve and set to 1500 hPa. In such conditions, the temperature of the saturated nitrogen stabilizes at 81 K. If the heating power stops, the nitrogen comes back rapidly to 77 K.

3.2 Measures on the 2G HTS conductors

3.2.1 Electrical measurements

To observe the inhomogeneities of the dissipation on a 2G HTS conductor, a first method, as presented in chapter 2 in figure 2.1, consists of the measurements of voltages along the sample. Voltage taps are positioned on its surface (see figure 3.11). They are soldered with low melting temperature solder not to damage the conductor. Indium-Tin was selected and warmed up to 410 K. The current in the circuit is also measured.

3.2.2 High-speed imaging set-up

This high-speed imaging set-up was developed with the kind help of M.Gibert and J.Vessaire from Institut Néel.

In addition to voltage measurements, the localization of disipation can be observed optically through the generation of bubbles. Investigations on the conductor operation through optical observation were initiated by N.T. Tung and C. Barnier in [87]. Here, a new high-speed imaging set-up using a camera with higher performances is proposed.

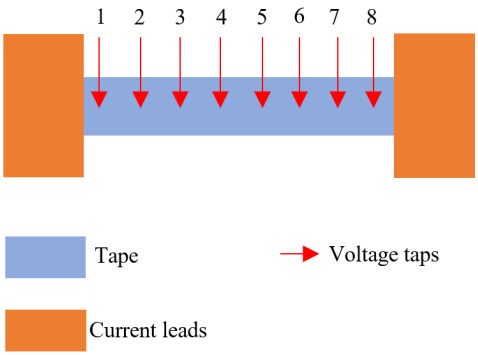

Figure 3.11: Illustration of voltage taps soldered on the surface of a 2G HTS conductor.

Other investigations using camera can be found in the literature either with a similar set-up [83] or with the use of fluorescent thermal imaging to measure quench propagation in HTS tapes [88].

3.2.2.1 Sample-holder and cryostat

The transparent cryostat (figure 3.8a) is used with a sample from a 2G HTS tape inserted in. The sample is either connected to the AC electrical circuit or DC electrical circuit by using the sample holder shown in figure 3.12. To inject the current, each extremity of the sample is pressed between two copper pieces. The screws are tightened until a torque equals to 5 Nm is reached. The copper elements are 4 cm wide and the length of the sample not covered by the copper pieces is 6 cm long. The structure is mechanically supported by a FRP piece to ensure that no current flows between the two ends of the sample, except through the sample itself.

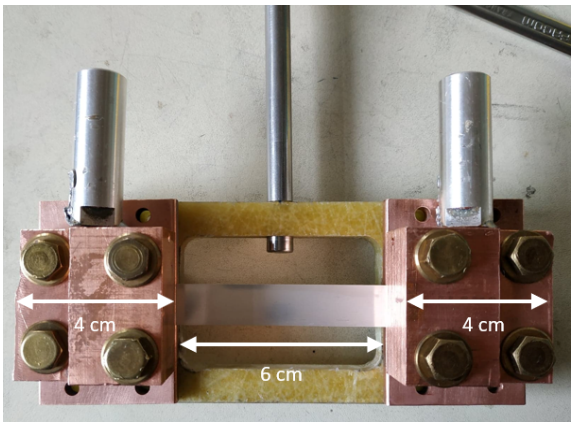

Figure 3.12: Sample holder used to characterize by optical observation 2G HTS tapes.

3.2.2.2 Camera

A high-speed camera records the bubble generation on the surface of the sample. It is a Phantom V311 with a frame rate set to 50000 fps, which means that an image is recorded each 20 µs to observe phenomena with high dynamics. Exposure time is 3 µs and the resolution is $560x96$ pixels. A powerful light source is necessary to perform high-speed imaging. The camera is triggered by a pulse signal sent by the user that can be synchronized precisely with the electrical measurements system.

3.2.2.3 Boiling heat transfer in liquid nitrogen

The Nukiyama curve [89] describing the boiling heat transfer is detailed in appendix C. During this PhD work, the measure of the heat transfer as a function of the temperature difference between a copper tape and the liquid nitrogen bath was experimentally tried. It did not give relevant results. The Nukiyama curve is obtained with a power-controlled heating or a temperature-controlled heating. While during a quench, none of both cases exist, the power received by the sample is transient. The different heat transfer regimes are transient too during such a small time (few tens of milliseconds).

Even if assuming that the 2G HTS tape is in steady state regime during a quench, no universal value would be obtained for the heat transfer. It depends practically on other parameters like the shape and the orientation of the sample in the bath, the surface of the sample (wettability, rugosity,..) or the operation in saturated or subcooled nitrogen.

As a consequence, the important element to remember from the Nukiyama curve is that the temperature of the Onset of Boiling is higher than the saturated temperature. This means that the tape will present a temperature higher than the liquid nitrogen bath temperature when the first bubbles will appear.

3.2.3 Maximum and Mean Temperatures

3.2.3.1 Concepts of these temperatures

The inhomogeneous quench occurring on the 2G HTS tape leads to an inhomogeneous temperature along its length. Accurate direct temperature measurement is very difficult in a system with such a fast dynamic and immersed in a cryogenics liquid. Instead, *Tixador et al.* in [90] formalize methods to compute the mean temperature T_{mean} and the maximum temperature T_{max} of the tape from electrical measurements. The comparison of these two temperatures makes it possible to assess the homogeneity of the quench.

The approach consists in establishing an energy balance of the tape at two different scales :

- on the volume $V_{i,j}$ between two voltage taps i and j for $T_{mean,i,j}$ (see figure 3.13a)
- on the section S for T_{max} (see figure 3.13b)

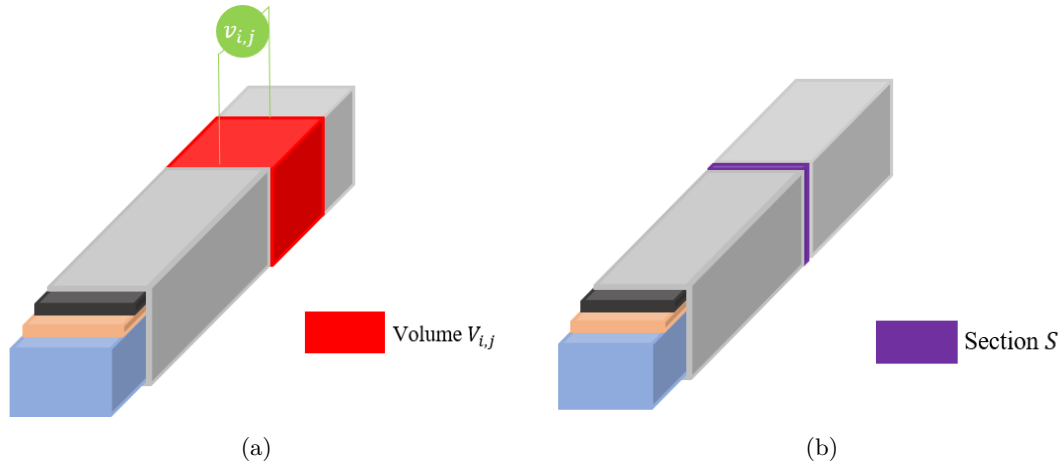

(a) (b)

Figure 3.13: Schematic representation of a tape with (a) the volume $V_{i,j}$ between the voltage taps i and j and with (b) the cross-section S of the tape.

The expressions rely on the assumptions that both temperatures are homogeneous at the scale of their computations and the hypothesis of adiabatic conditions. It should result in a certain over estimation of the actual temperature. This effect is supposed to remain limited: *Tixador et al.* in [90] compared the temperatures computed with this theoretical approach and experimental measures on a sample with a sensor directly deposited on its surface and obtained a difference about 10 %.

3.2.3.2 Mean temperature

The energy balance in the volume $V_{i,j}$ gives (3.6) with $c_{p,v}$ the heat capacity per volume unit, $v_{i,j}$ the voltage between the two voltage taps i and j and $i(t)$ the current across the tape. The temperature in this expression is the mean temperature $T_{mean,i,j}$ over the volume $V_{i,j}$.

$$v_{i,j}(t)i(t)dt = V_{i,j}c_{p,v}(T)dT \tag{3.6}$$

The voltage $v_{i,j}$ and the current i are measured every δt by an oscilloscope. The mean temperature in a volume $V_{i,j}$ is computed using a forward Euler method given in (3.7).

$$T_{mean,i,j,t+1} = T_{mean,i,j,t} + \frac{v_{i,j,t}i_t\delta t}{V_{i,j}c_{p,v}(T_{mean,i,j,t})} \tag{3.7}$$

3.2.3.3 Maximum temperature

The local energy balance over the cross-section S gives (3.8) with the resistance per unit length R_l depending on the current i and the local temperature in the section below T_c and only on the temperature above T_c. The temperature in these expressions is the maximum temperature T_{max} of the tape.

$$\begin{cases} R_l(i(t),T)i(t)^2dt = Sc_{p,v}(T)dT \; with \; T < T_c \\ R_l(T)i(t)^2dt = Sc_{p,v}(T)dT \; with \; T > T_c \end{cases} \tag{3.8}$$

In hot-spot regime, the mean temperature does not represent well how close the tape is from its operation limit. Obtaining T_{max} is critical. The computation of the maximum temperature is more complicated than the mean one. The computation starts when a quench is detected, i.e when one of the measured voltages is higher than 0.1 V in the system. The recognition of a dissipation spot is practically limited by the acquisition system. The temperature in the dissipation zone giving this voltage is not known. However, a value is needed to initiate the computation.

A first assumption consists of initiating the computation at the liquid nitrogen bath temperature at the moment of the recognition of the dissipation. This leads to **underestimate the temperature** in the dissipation zone but there is no easy way to estimate the temperature at the origin. A second assumption is the non consideration of the current dependence of R_l below T_c. The extrapolation of the temperature dependence of R_l below T_c is shown in figure B.1a in appendix B and is used to compute the temperature. This leads to an **over estimation of the temperature** through an over estimation of the actual resistance of the dissipation zone. The maximum temperature on the cross-section S where the dissipation first occurred is computed using a forward Euler method given in (3.9).

$$T_{max,t+1} = T_{max,t} + \frac{R_l(T_{max,t})i_t^2\delta t}{Sc_{p,v}(T_{max,t})} \tag{3.9}$$

3.2.3.4 Tape characteristics

The resistance per unit length and the heat capacity per volume unit of the tape as a function of the temperature are required to compute T_{mean} and T_{max}. The temperature dependence of the tape resistance per unit length is measured from 77 K to the ambient temperature. Examples of these measurements are shown in Appendix B. A curve extrapolation is generally proposed to obtain a larger range of values above the ambient temperature and below T_c to compute T_{max}. The Hastelloy® C276 thickness represents 90 % of the total thickness of a tape (see section 1.2). It is assumed for the computations of T_{mean} and T_{max} that the heat capacity per volume unit of this material is the heat capacity per volume unit of the whole tape with the data from [79] given in appendix B. A curve extrapolation is also proposed.

3.3 Observation of the 2G HTS conductor operation

To introduce the experimental approach, a "bare" 2G HTS tape from Superpower® [91] is studied under different prospective currents varying from 500 A to 1500 A in a liquid nitrogen bath at 77 K and 68 K.

3.3.1 Experimental details

3.3.1.1 Sample

The dimensions of the cross-section of the sample are introduced in Table 1.2. Its critical current is around 650 A. Additional information about its manufacturing process are given in subsection 1.2.3. Several voltage taps are positioned on the superconducting side of the sample in order to measure the electric fields. The space between two voltage taps is 1 cm (see figure 3.14).

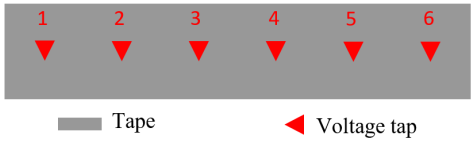

Figure 3.14: Positions of the voltage taps soldered on the superconducting side of the sample.

3.3.1.2 Test bench and measures

The sample is inserted in the AC fault current set-up (see figure 3.6) where the prospective current varies adjusting R_f. The voltage source V_{source} is 16 V. The sample is studied at 77 K and then 68 K following the procedure detailed in subsection 3.1.2. The user sets the duration Δt of a pulse by controlling the closure of the switch S.

At 77 K, the fault resistance R_{fault} varies from 12.5 mΩ until 29.8 mΩ to obtain prospective currents varying from 475 A to 975 A (in terms of mean I_c, from $0.7I_c$ to $1.5I_c$). The limitation phase lasts for 30 ms. At 68 K, R_{fault} varies from 6.7 mΩ until 12.5 mΩ to obtain prospective currents varying from 975 A to 1500 A (from $1.5I_c$ to $2.3I_c$). The limitation phase lasts for 15 ms which is smaller than at 77 K due to higher Joule losses at this temperature.

The high-speed imaging system, detailed in subsection 3.2.2, is used. The camera operates at 50000 fps. Electrical measurements, similar to subsection 3.2.1, are realized with a sampling frequency of 100 kHz. Thanks to these electrical measurements and the resistance per unit length of the sample (see figure B.1a) as well as the heat capacity per unit volume of the Hastelloy® C276, T_{mean} and T_{max} are computed.

The pulse generator controlling the switch S also triggers the camera and the data acquisition of the electrical measurements. A schematic representation is given in figure 3.15. Figure 3.16 presents the set-up with the transparent cryostat and the Phantom camera with the light source on the foreground. In this figure, the electrical circuit is the DC circuit but in this experiment, the AC circuit is used.

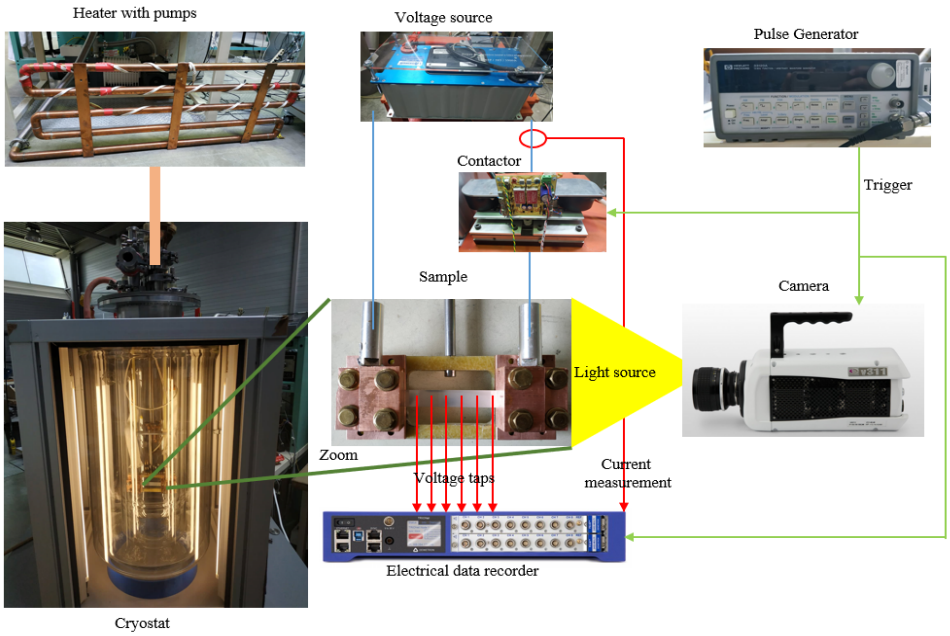

Figure 3.15: Scheme of user-controlled elements of the set-up.

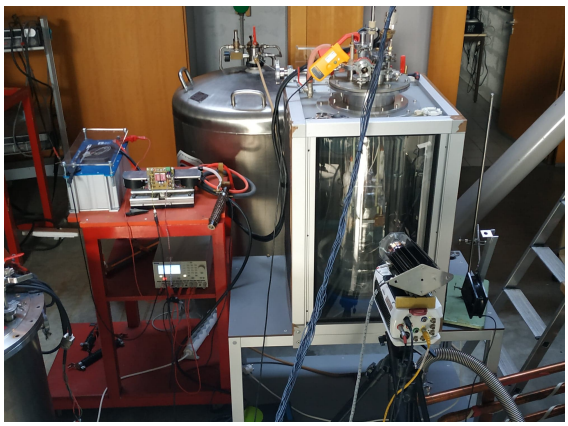

Figure 3.16: Picture of the set-up with the DC electrical source (left) connected to the sample. The high-speed camera with the light source is at the right on the foreground.

3.3.2 Experimental results

3.3.2.1 Operation at 77 K

Table 3.2 summarizes the five cases realized at 77 K.

Case	Figure	I_{pros} (A)
A_{77}	3.17	540
B_{77}	3.18	589
C_{77}	3.19	662
D_{77}	3.20	684
E_{77}	3.21	918

Table 3.2: Summary of the tests detailed at 77 K.

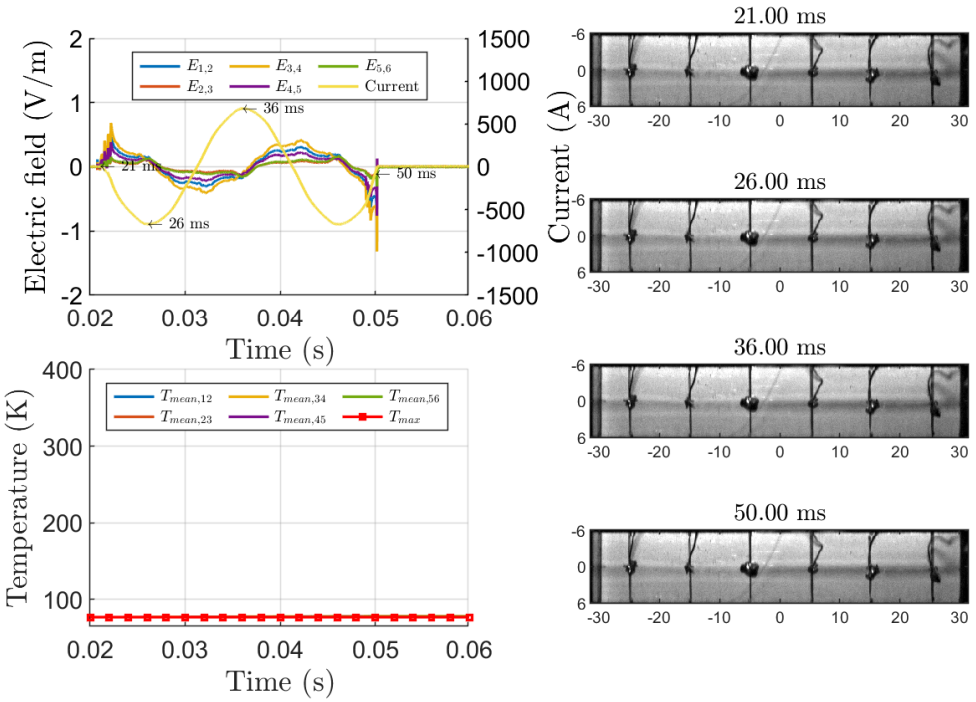

Figure 3.17: Case A_{77} - Electric fields and current as a function of time, temperatures as a function of time and images of the tape at several times with I_{pros}=540 A at 77 K.

Case A_{77} presents the lowest prospective current, the electric fields remain mainly inductive and the pictures do not show any bubble generation. The current is not high enough to initiate a thermal runaway.

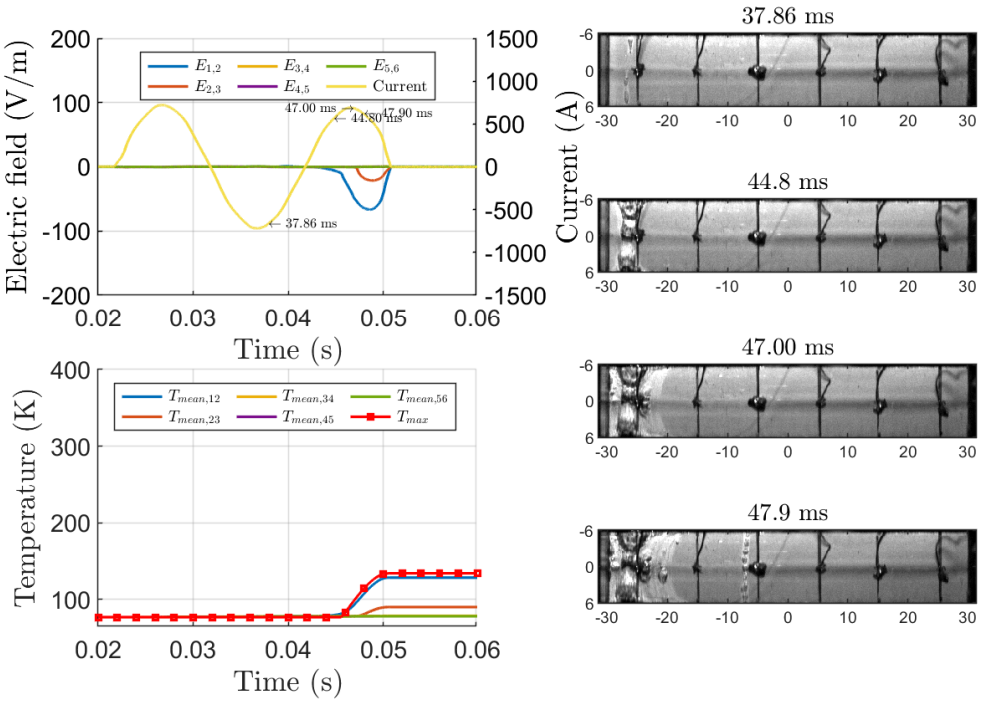

Figure 3.18: Case B_{77} - Electric fields and current as a function of time, temperatures as a function of time and images of the tape at several times with I_{pros}=589 A at 77 K.

In case B_{77}, the current initiates a dissipation leading to bubble generation at 37.86 ms between the left extremity of the sample and voltage tap 1. The closest portion of the tape where the electric field is measured, $E_{1,2}$, shows a resistive component from the time 39.7 ms. The electric field $E_{2,3}$ becomes resistive from 47.0 ms while the bubble generation is observed in portion 2-3 at 47.9 ms. As only a small portion of the sample quenches, the current is only slightly limited. However, this dissipation occurs late in the limitation test, almost at the end, which does not lead to a large temperature increase (T_{max} = 135 K).

The second peak of current is 675 A in case A_{77} while it is 715 A in case B_{77}. The increase of the prospective current leads to an increase of the instantaneous current which becomes high enough to initiate localized thermal runaways.

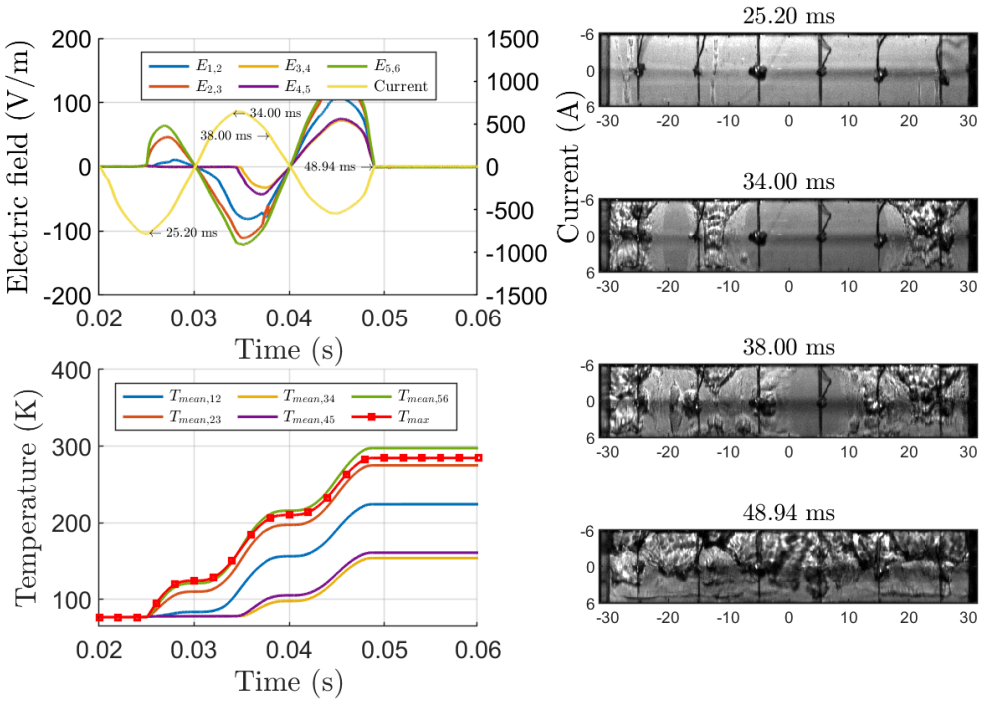

Figure 3.19: Case C_{77} - Electric fields and current as a function of time, temperatures as a function of time and images of the tape at several times with I_{pros}=662 A at 77 K.

In case C_{77}, at 25.20 ms, three dissipation zones are recognized on the first picture. These zones of bubble generation propagate until the whole sample is covered with bubbles at 48.94 ms. The propagation speed is related to the instantaneous current value: the propagation remains slow until 34 ms and then becomes significantly faster between 34 ms and 38 ms. There is no dissipation zone directly initiated by the current in the portions 3-4 and 4-5, the electric fields show a resistive component when the dissipation propagates in these segments.

In case B_{77}, the first peak of current reaches 720 A while it reaches 783 A in case C_{77}. The increase of the instantaneous current results in the initiation of multiple localized thermal runaways. The maximum temperature at the end of the test is also higher in case C_{77} than in B_{77} (285 K versus 135 K) due to a longer dissipation period (23 ms versus 3 ms, in the zone where the measures are realized). The longer the dissipation, the higher the temperature in the tape.

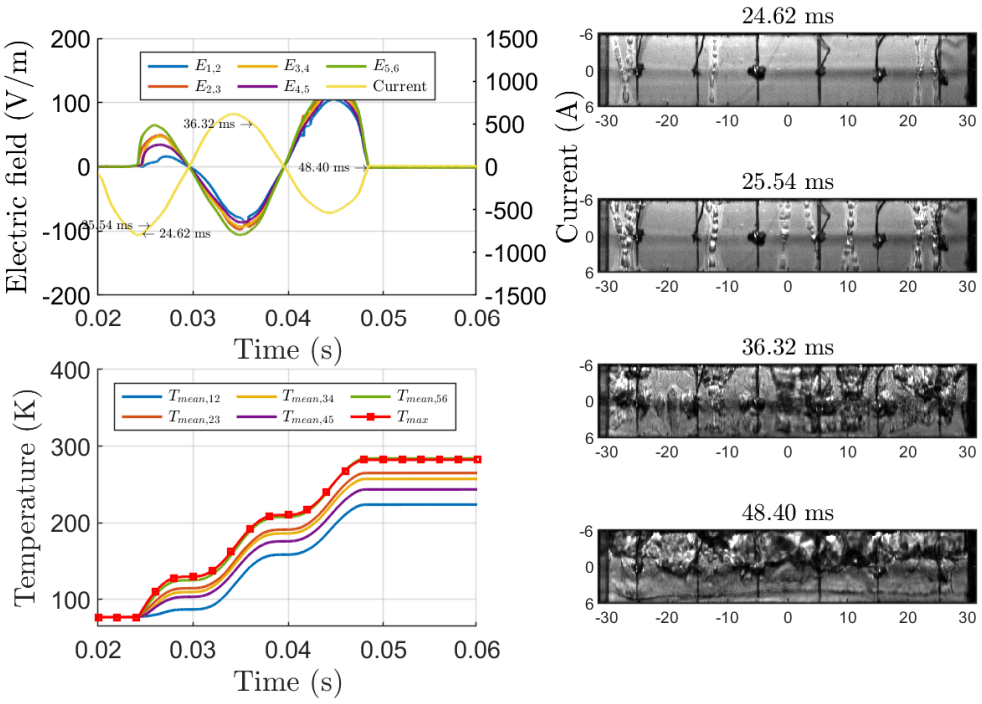

Figure 3.20: Case D_{77} - Electric fields and current as a function of time, temperatures as a function of time and images of the tape at several times with I_{pros}=684 A at 77 K.

In the first image of case D_{77}, the dissipation zones already appearing in case C_{77} are present. In the second image, additional dissipation zones can be observed. The quench ultimately propagates on the whole sample at 36.32 ms.

The increase of the prospective current between case C_{77} and case D_{77} multiplies the number of dissipation zones. The time between the apparition of the first bubble and the time when bubbles covered the whole sample is about 24 ms in case C_{77} while it is about 12 ms in case D_{77}. The complete quench of the sample is faster in case D_{77} due to a larger number of dissipation zones initiated by the current.

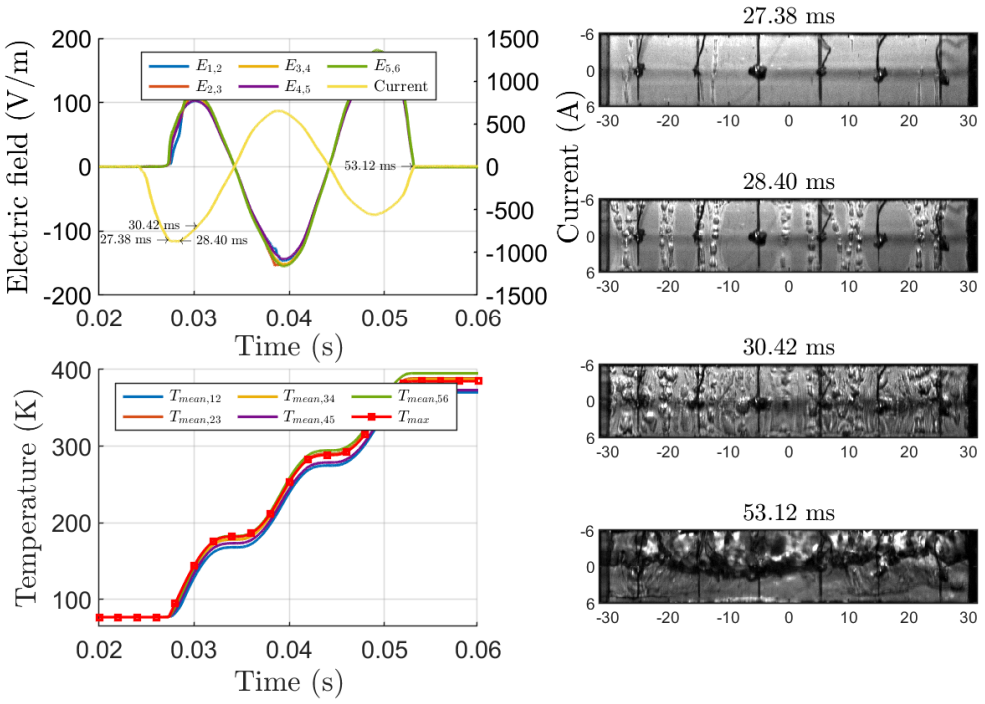

Figure 3.21: Case E_{77} - Electric fields and current as a function of time, temperatures as a function of time and images of the tape at several times with I_{pros}=918 A at 77 K.

To finish the description at 77 K, in case E_{77}, the quench is the most homogeneous. The electric fields measured along the length are similar. The peak current, reaching 870 A, leads to 13 bubble generation zones which rapidly propagate until the complete quench occurs after 3 ms.

At the end of the limitation test, in case D_{77}, the maximum temperature was 282 K while in case E_{77}, it reaches 384 K. This latter case is the one where the current is the most effectively limited thanks to the fastest quench completion (3 ms in case E_{77} versus 12 ms in case D_{77}). However, R_{fault} is smaller leading to a higher current in the circuit and so higher energy dissipation in the tape.

3.3.2.2 Operation at 68 K

Table 3.3 summarizes the five cases realized at 68 K.

Case	Figure	I_{pros} (A)
A_{68}	3.22	1033
B_{68}	3.23	1124
C_{68}	3.24	1171
D_{68}	3.25	1192
E_{68}	3.26	1473

Table 3.3: Summary of the tests detailed at 68 K.

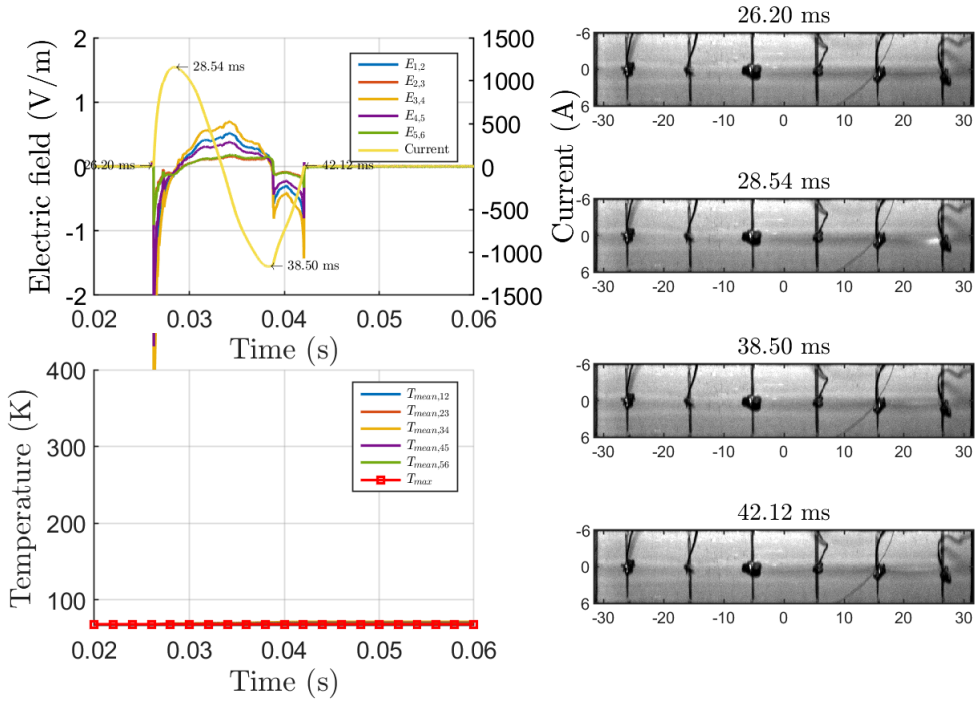

Figure 3.22: Case A_{68} - Electric fields and current as a function of time, temperatures as a function of time and images of the tape at several times with I_{pros}=1033 A at 68 K

Case A_{68} is realized with the lowest prospective current. The electric fields are mainly inductive and no bubble generation occurs. The current is not high enough to initiate thermal runaway.

The prospective current is much higher than in case A_{77} at 77 K but the critical current is also higher at 68 K, which explains why there is no dissipation.

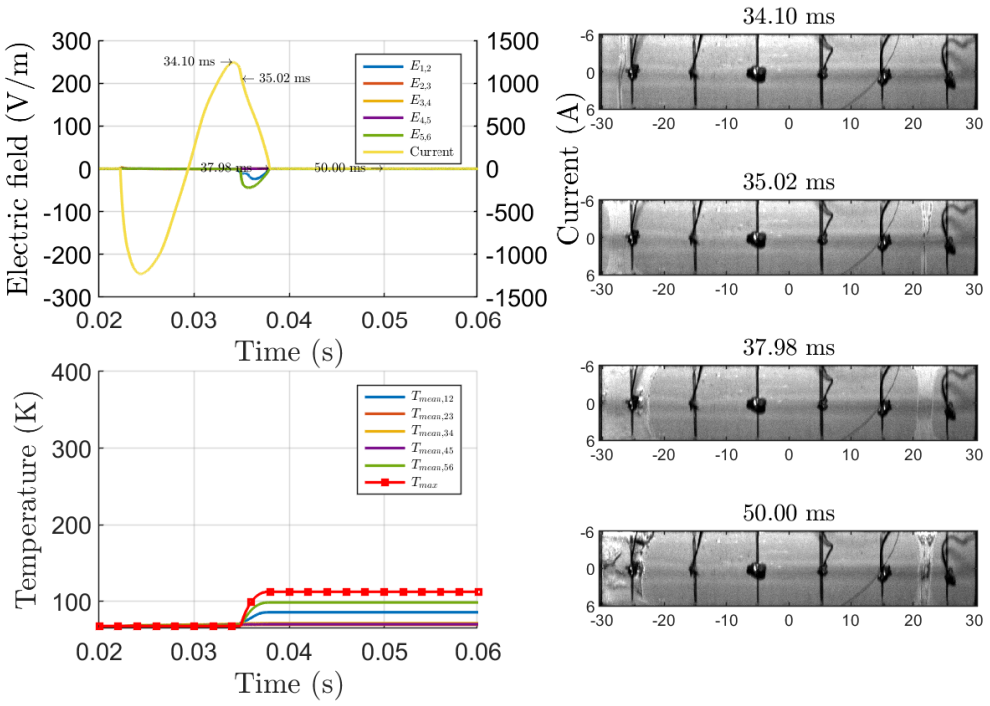

Figure 3.23: Case B_{68} - Electric fields and current as a function of time, temperatures as a function of time and images of the tape at several times with I_{pros}=1124 A at 68 K

Two bubble generation zones are initiated, in case B_{68}, between the left current lead and the voltage 1 and in the segment 5-6.

The dissipation also first appeared on these zones in case C_{77} at 77 K, with an additional zone in segment 2-3 which is however not observed in case B_{68} at 68 K.

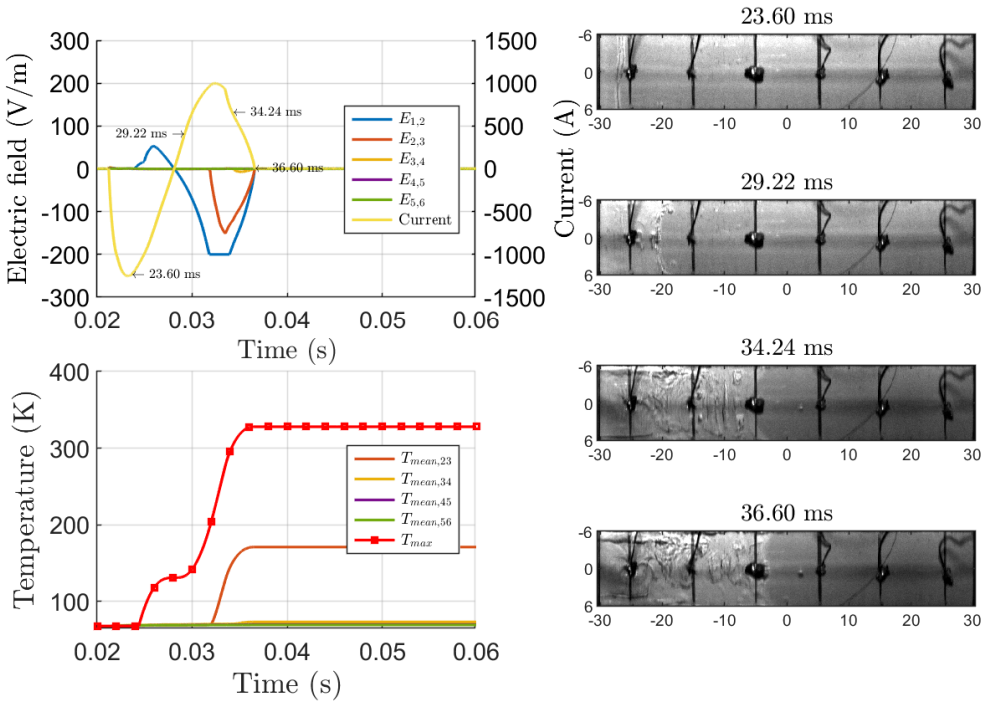

Figure 3.24: Case C_{68} - Electric fields and current as a function of time, temperatures as a function of time and images of the tape at several times with I_{pros}=1171 A at 68 K

In this case, a single dissipation zone is initiated at 23.6 ms between the left current lead and voltage tap 1. This zone propagates until the end of the limitation test. It makes successively appear a resistive component in the electric field of the segments 1-2, 2-3 and 3-4. The measure of the electric field of the portion 1-2 is out of range of the scope between 30 ms and 40 ms. The dissipation lasts almost 13 ms on a small portion of the sample. The current is slightly limited. The maximum temperature in this zone is estimated to 330 K at the end of the limitation test.

The initiation of a thermal runaway relies on the superconducting properties of the zone, the current as well as the time. In case B_{68}, the peaks of current reach 1220 A while in case C_{68}, the first peak of current is 1250 A and the next ones are smaller. The configuration of the limitation test in case C_{68} leads to a single dissipation zone.

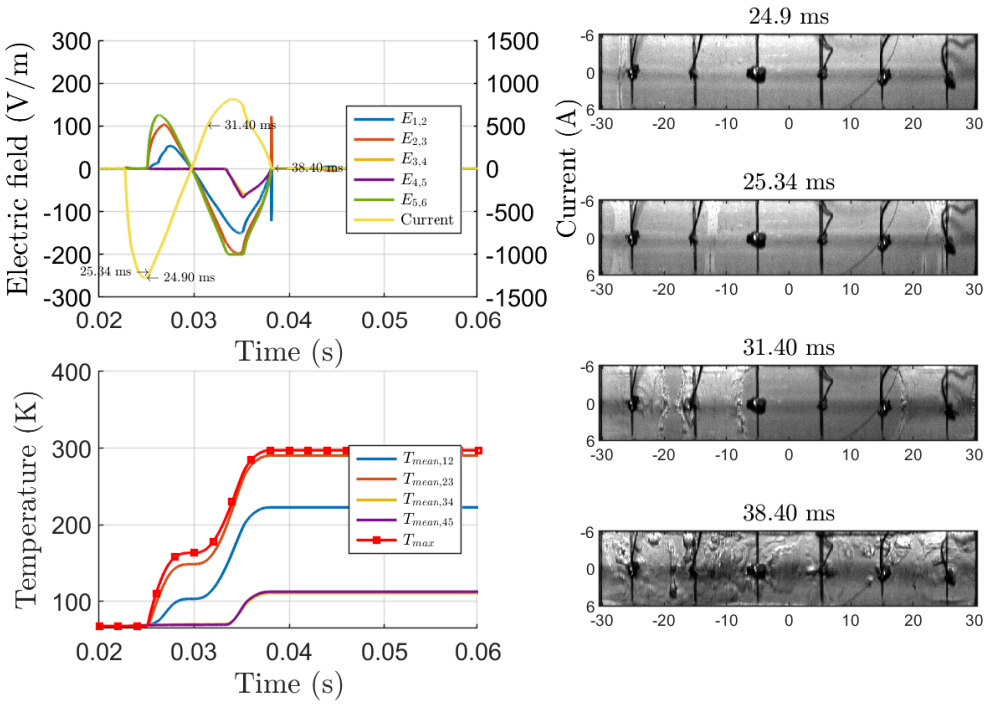

Figure 3.25: Case D_{68} - Electric fields and current as a function of time, temperatures as a function of time and images of the tape at several times with I_{pros}=1192 A at 68 K

In case D_{68}, the current initiates three dissipation zones which propagate until that the whole sample generates bubbles at 38.4 ms.

The increase of the first peak of current between the limitation tests C_{68} and D_{68} (through the prospective current) leads to initiate more dissipation zones, hence contributing to achieving a faster quench of the whole sample. The current is limited more efficiently than in previous cases and the maximum temperature remains smaller (297 K in case D_{68} versus 350 K in case C_{68}).

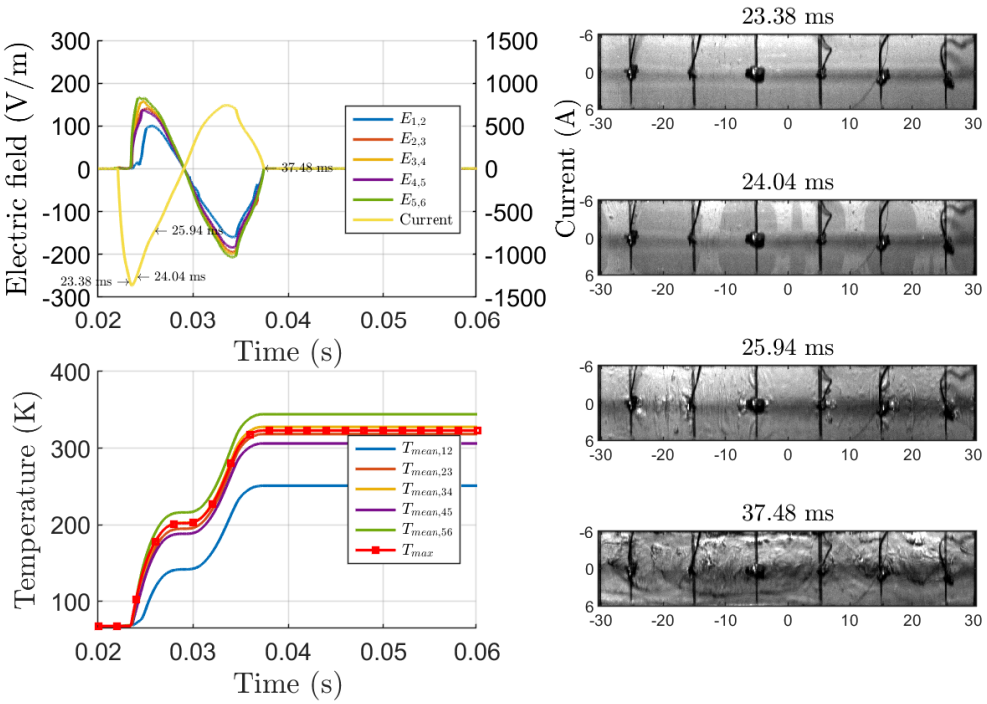

Figure 3.26: Case E_{68} - Electric fields and current as a function of time, temperatures as a function of time and images of the tape at several times with I_{pros}=1473 A at 68 K

In case E_{68}, six dissipation zones are initiated and they rapidly propagate (complete quench is obtained in 2.5 ms).

The maximum temperature at the end of this limitation test reaches 325 K compared to 297 K in case D_{68}. Even if the resistance R_{sfcl} appears faster, the current in the circuit is higher due to a smaller value of R_{fault}, set to reach the highest prospective current.

3.3.3 Discussion

First of all, the phenomena described in section 2.1 are recognized during these tests. When the prospective current is in the range of I_c variations, the electric fields are not homogeneous. Also, as mentioned in subsection 3.2.2.3, the dissipation is first recognized by electrical measurements and then by optical measurements. The apparition of bubbles requires a difference of temperatures between the sample and the liquid nitrogen bath temperature.

Based on the afore mentioned cases as well as additional tests performed at 77 K and 68 K, the maximum temperature was computed and the results are provided in figure 3.27. The hot-spot regime is barely visible at 77 K while it appears clearly at 68 K. The qualitative analysis of the maximum temperature evolution over prospective current, derived from modeling effort in section 2.3, is confirmed experimentally with a higher temperature in hot-spot regime at the lowest temperature due to higher Joule losses. The peak of maximum temperature in hot-spot regime is reached when the current is high enough to initiate thermal runaways but small enough not to be limited due to numerous dissipation zones. This regime is difficult to observe experimentally. References [92][93] provide well-developed similar experimental results.

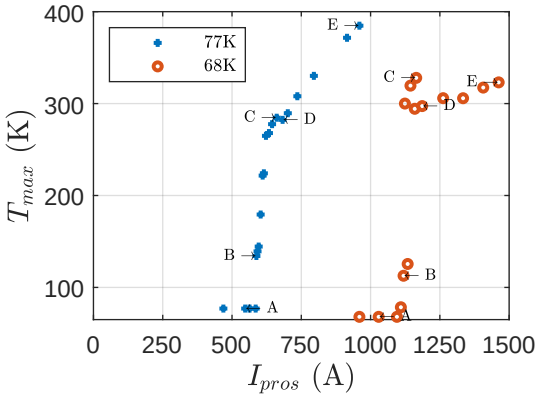

Figure 3.27: The maximum temperature of the sample is computed thanks to electrical measurements on a large range of prospective currents in a liquid nitrogen bath temperature at 77 K (blue markers) and at 68 K (red markers).

When the prospective current is high enough to initiate thermal runaway, the dissipation starts in very localized zones whose sizes are way smaller than the voltage taps inter distance. From these precise spots, the heat first propagates in the width of the sample very rapidly to form dissipation column and then spreads in the longitudinal direction of the sample, with the distinctive shape of hourglass. When the prospective current increases, the peak of current increases as well. The number of bubble generation zones increases with the maximum current in the circuit. The more numerous these zones are, the faster the homogeneous quench of the tape is reached.

An important result obtained from optical measurements is that homogeneous quenches are always preceded by inhomogeneous dissipation, even in the case of a high prospective current. The hot-spot regime was introduced in subsection 2.4.1 as the regime of operation where the tape is quenching inhomogeneously, in opposition to the limitation regime. The study demonstrates that inhomogeneous and homogeneous quenches are successive operation states. Of course, if the limitation test is sufficiently short, the dissipation may remain inhomogeneous.

3.4 Conclusion

The aim of this chapter was to observe experimentally the hot-spot regime introduced in chapter 2 from the consideration of the I_c variations given by measurements such as Tapestar®. A dedicated experimental set-up emulating the environment of a R-SFCL with an electrical circuit and cryogenics conditions was developed. The AC circuit that was used was derived from an existing circuit, while the DC circuit was fully developed. In AC mode, the prospective current can be varied manually. The cryogenics environment makes it possible to observe the conductor operation from 65 K to T_c.

A sample of 2G HTS tape operating in the afore mentioned conditions was characterized by carrying out electrical measurements. These measurements were used to compute estimations of the sample temperature. The computation of the maximum temperature as a function of the prospective current leads to the observation of the hot-spot regime at 68 K while it is barely visible at 77 K. These results can be explained by higher Joule losses at lower bath temperature due to a higher critical current. This result also confirms the validity of the design approach developed in chapter 2 with the observation of the hot-spot regime occurring when prospective currents are in the range of I_c variations of the sample.

The recording of the bubble generation on the surface of this sample with a high-speed imaging system showed that whatever the prospective current, bubble generation first starts on very localized areas of the tape. These areas are at a way smaller scale than the voltage taps inter distance. When the bubble generation is fully developed in the width of the sample, the dissipation then propagates along its length until its total quench. The number of dissipation zones increases with the prospective current and tends to facilitate the total quench of the sample. Nevertheless, even when the prospective current significantly exceeds the critical current, the onset of the quench goes through an inhomogeneous phase. An important take-away of the study is that whatever the prospective current, inhomogeneous and homogeneous dissipation are occurring successively. When describing the local behavior of the tape, talking about "hot-spot regime" in opposition to "limitation regime" is therefore not completely appropriate.

The local behavior of the tape that was observed using optical measurements raises many questions. Why do bubbles first appear in very localized positions ? Are they

matching the positions of lowest critical currents as it is assumed in the design approach developed in chapter 2 ? These questions are investigated in the following chapter.

CHAPTER 4

Mechanism of quench onset in a 2G HTS tape

In this chapter, the dissipation behavior at the very beginning of a quench occurring in a 2G HTS tape is studied using high-speed imaging system, electrical measurements and Scanning Hall Probe Microscopy. The bubble generation appears not only to be inhomogeneous along the length of the tapes but also along the width. Local analysis of the REBCO layer is performed by means of scanning Hall probe microscopy on the same samples in the framework of a collaboration with a group in TU Wien. Analysis of the local current density distribution demonstrates that the bubble generation occurs at positions of local inhomogeneities in the REBCO layer.
In a second part, a 3D FEM model of 2G HTS tape developed by a group from Ecole Polytechnique de Montréal is used to simulate the local thermo-electrical behavior not only along the length (as in chapter 2) but also along the cross-section. The simulation gives access to the current distribution in the tape volume and the results are coupled with experimental measurements highlighting the non-equipotential cross-section of 2G HTS tape. The impact of possible lack of silver on a lateral side of the tape is investigated.

4.1 Influence of inhomogeneities in the REBCO layer of 2G HTS tapes

This work was conducted in collaboration with Sigrid Holleis (PhD Student) & Dr. Michael Eisterer (Senior Scientist) from TU Wien-Atominstitut. The collaboration resulted in the submission of an article entitled "Influence of local inhomogeneities in the REBCO layer on the quench mechanism of 2G HTS tapes" [94].

The results presented in section 3.3 highlight the occurrence of an inhomogeneous bubble generation in the first milliseconds of a quench for any prospective current. This motivates the study of the onset of a quench to determine the causes and the evolution of this localized dissipation. Samples from Superpower and SuperOx are studied using the set-up introduced in chapter 3. These samples were then sent to TU Wien where magnetic analysis was performed by means of Scanning Hall Probe Microscopy (SHPM). SHPM has proven to be a powerful tool for investigations of the local current distribution in superconductors [95].

In this chapter, "spot" refers to a dissipation partially developed in the width and "column" refers to a dissipation covering the entire width.

4.1.1 Observation of bubble generation

4.1.1.1 High-speed imaging

The high-speed imaging set-up summarized in figure 3.15 is used to record the bubble generation on the surface of 2G HTS tapes. It is the DC set-up (described in subsection 3.1.1.4) that is used to initiate thermal runaways with V_{source} =18 V. The tests are carried out at 77 K for $\Delta t = 15$ ms.

4.1.1.2 Samples

One sample from SuperOx and one sample from Superpower are studied. These two companies use different manufacturing processes to produce their tapes. As an example, the HTS layer growth is done by a chemical route with Superpower while it is a physical route for SuperOx (see subsection 1.2.3). The samples are inserted in the sample-holder presented in figure 3.12 where the length of the sample between the current leads is adjustable. This length is 65 mm for the SuperOx sample and 68 mm for the Superpower sample. The voltage over the sample is measured by voltage taps connected to each current lead. A 1000 A rated sensor is used to measure the current through the sample.

4.1.1.3 Bubble generation

Figure 4.1 shows the current in the circuit and the electric field (voltage divided by the sample length) across the Superpower sample and the SuperOx sample. The current in

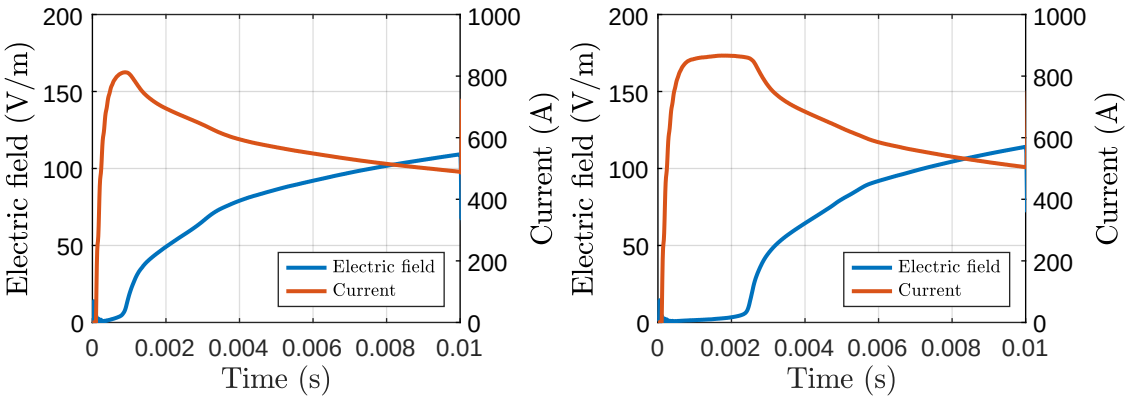

(a) Superpower (b) SuperOx

Figure 4.1: Electric field (solid blue line) and current (solid red line) as a function of time measured on the (a) Superpower sample and (b) SuperOx sample.

the circuit is almost constant until 1.00 ms with the Superpower sample and 2.50 ms with the SuperOx sample.

The images of the Superpower sample recorded during the test are displayed in figure 4.2a. The first bubble generation spot appears in image A. Additional spots appear in images B and C. The bubble generation generally starts on the edges of the sample. The bubbles extend to the whole width of the tape forming bubble columns at all the positions where dissipation originally appeared (at 2.80 ms). The dissipation then propagates in the longitudinal direction of the sample until the whole sample is covered by bubbles at 5.20 ms.

Figure 4.2b shows the images at several times of the SuperOx sample. The two first bubble generation spots appear at 2.46 ms. Additional dissipation spots appear at 2.54 ms and 2.66 ms. Image B and C highlight that bubbles generally appear at the center of the width of the sample. Similarly to Superpower, dissipation spots first propagate along the width. At 3.30 ms, all the columns have appeared and the dissipation propagates in the longitudinal direction of the sample until bubbles cover the entire sample at 6.36 ms.

Letters A and B in figure 4.2a describes two behaviors to form a dissipation column. To form column A, the dissipation starts at a point in the middle of the width, then it propagates in the direction of the two lateral sides. To form column B, the dissipation starts at two distinct points and each point propagates in the direction of the other point. The formation of bubble columns from localized spots is very fast, in the order of ten microsecond. A first explanation for the bubble generation appearing on distinct positions at the onset of the quench would be a lower critical current at these positions and a higher critical current elsewhere. In order to confirm this hypothesis, the HTS layer is analyzed using SHPM.

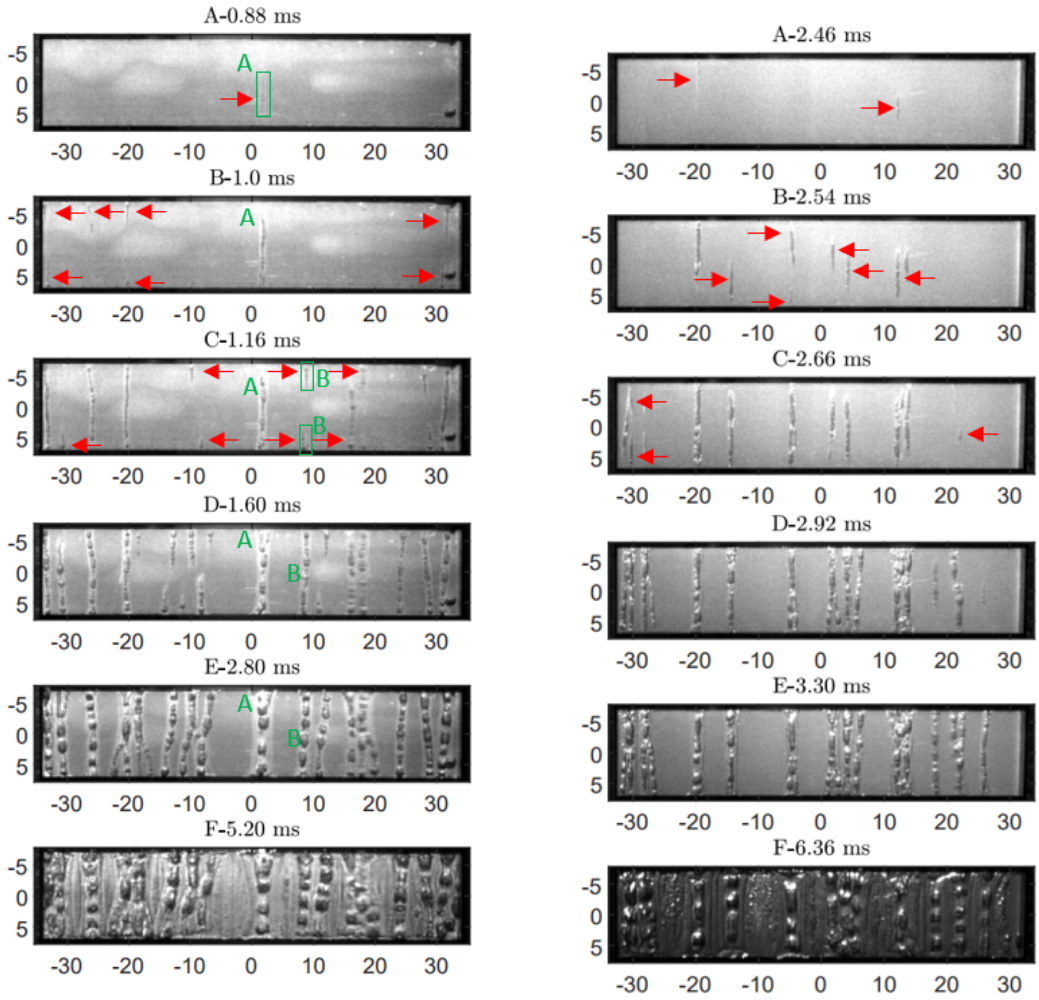

(a) Superpower

(b) SuperOx

Figure 4.2: Images of the (a) Superpower sample and (b) SuperOx sample at several times during the tests. Starting points of bubbles are indicated by red arrows

4.1.2 Recognition of local inhomogeneities

4.1.2.1 Scanning Hall probe microscopy

The description of the SHPM set-up used to characterize the samples by S. Holleis can be found in [94].

In a SHPM, an external magnetic field is applied on a 2G HTS tape cooled below T_c, generally with liquid nitrogen. This creates sheet currents shielding the external magnetic field and remaining when the external magnetic field is not anymore applied. The magnetic field induced by these sheet currents is called remnant field and is measured with a Hall probe. The resolution of the inverse magnetic problem gives a 2D map of J_c over the surface of the sample. A description of this procedure is given in [96].

There are two main ways to measure the remnant field in a 2G HTS tape. On one hand, when the length of the tape is long, a Reel-to-Reel system is used to move the tape under a fix permanent magnet [7]. A Hall probe is moved across the width, on the y-direction, to measure the remnant field at several positions. The tape is moved on the x-direction and the remnant field is again measured until the measurement of the whole length is realized. On the other hand, when the sample is short, about tens of centimeters, it is positioned into a liquid nitrogen tank where a permanent magnet is dragged over its length. After the magnetization, the Hall probe moves on the x-direction and y-direction to measure the remnant magnetic field.

This second option is used by TU Wien. The main interest of their set-up is to furnish an accurate measurement of the remnant field. For that, a Hall probe with an active area of 50 x 50 μm^2 is mounted at the end of a cantilever. Contact to the sample surface is monitored by strain gauges. The distance from the Hall probe to the sample surface is set to 30 µm to achieve high resolution scans. The spatial step is Δx over the sample length and Δy over the sample width. A more detailed description of the setup can be found in [95]. In order to obtain a mapping of the J_c on the entire surface of the sample, the inversion of Biot-Savart's law is performed. S. Holleis followed the procedure described in [97]. The inversion of the magnetic problem gives the local distributions of the critical current density J_c as well as the longitudinal (J_x) and transverse (J_y) current densities. The critical current I_c along the length of the sample is obtained by integrating J_x over the cross-section of the superconducting layer at each position where the measurement is made along the length (see (4.1), where d denotes the thickness of the superconducting layer and N the number of measures over the width). The indicator I_y, obtained with (4.2), is useful to highlight the positions where the current has to meander around non-superconducting areas in the remnant state. This reveals the positions of local defects in the REBCO layer.

$$I_c(x) = \sum_{k=1}^{N} J_{x,k} d \Delta y \tag{4.1}$$

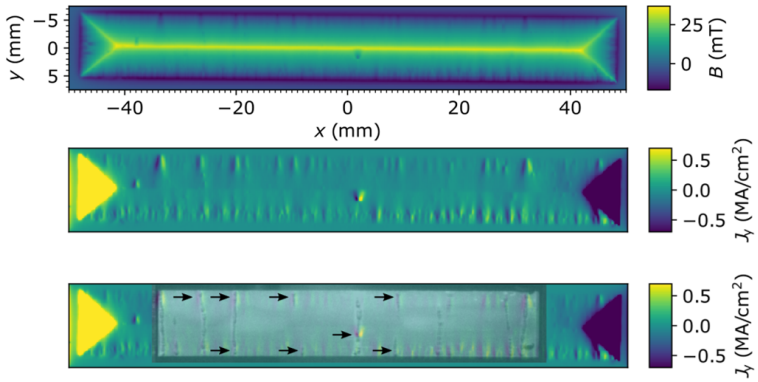

Figure 4.3: The upper panel shows the remnant field profile measured with a spatial resolution of 150 µm. The middle panel shows the calculated J_y. The lower panel is the image in the middle panel overlaid by image C in figure 4.2a. At points where bubbles start to emerge (indicted by black arrows) J_y shows high values in the upward and downward direction. Figure and measurements from S. Holleis in [94] on the Superpower sample.

$$I_y = \frac{1}{N} \sum_{k=1}^{N} J_{y,k} d\Delta x \tag{4.2}$$

4.1.2.2 Results of SHPM

S. Holleis measured the remnant field over the surface of the two samples from Superpower (see figure 4.3) and Superox (see figure 4.4). The first panel in figure 4.3 shows the measured trapped field of the Superpower tape at 77 K with a spatial resolution of 150 µm. The transverse current density J_y further emphasizes the positions of the defects in the tape as it can be seen in the middle panel. Such areas are very prominent at the upper and lower edges of the Superpower tape. When overlaying the image C in figure 4.2a with the map of J_y, it is evident that the bubbles first originate in areas with high J_y values, indicated by the black arrows. The investigations on the SuperOx tape shows that the positions of the dissipation columns match the locations where J_y is the highest too (see figure 4.4).

S. Holleis also computed I_c and I_y for the Superpower tape. Overlaying these data to image E in figure 4.2a, it appears that the I_c shows well the presence of the defect in the central part of the tape with a clear drop but it does not provide significant information about the other dissipation columns while I_y shows clear increases at the positions of dissipation columns (see figure 4.5). The transverse current density proves to be more suitable than the critical current to describe the onset of a quench in a 2G HTS tape. Local I_c based on magnetization does not describe all the dissipation phenomena.

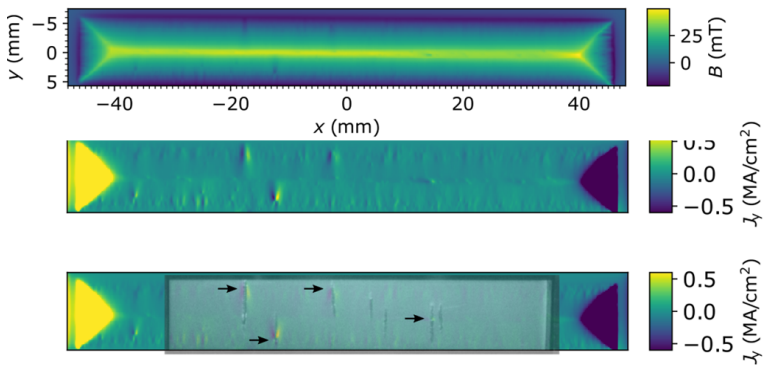

Figure 4.4: The upper panel shows the remnant field profile measured with a spatial resolution of 150 µm. The middle panel shows the calculated J_y. The lower panel is the image in the middle panel overlaid by image C in figure 4.2b. At points where bubbles start to emerge (indicted by black arrows) J_y shows high values in the upward and downward direction. Figure and measurements from S. Holleis in [94] on the Superox sample.

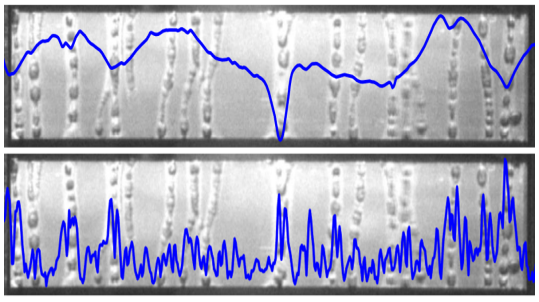

Figure 4.5: Average I_c (blue line)(top) and I_y (blue line)(bottom) of the Superpower tape calculated from the measured remnant field overlaying image E in figure 4.2a.

4.1.2.3 Defects in the REBCO layer

The contributions of the author in the following paragraphs is not significant. As a consequence, it is chosen to show them as they were originally written by S.Holleis and M.Eisterer in [94].

In order to investigate the origin of the bubbles further, the silver coating of both tapes was removed by chemically etching with hydrogen peroxide, ammonium hydroxide and distilled water in a ratio 1:1:1. A small piece from the center of the Superpower tape was cut out in order to obtain a sample where one line of bubbles starts in the middle and one at the edge of the tape. The right panel in figure 4.6 shows the trapped field profile of this center piece at 77 K with a spatial resolution of 50 µm. By comparison with the trapped field scan of the entire tape, areas a and b were identified as starting points of bubbles. The left panel in figure 4.6 shows the high-speed imaging photos where the bubbles in area a and b start at 0.56 ms in the center and at 0.7 ms at the edge, respectively.

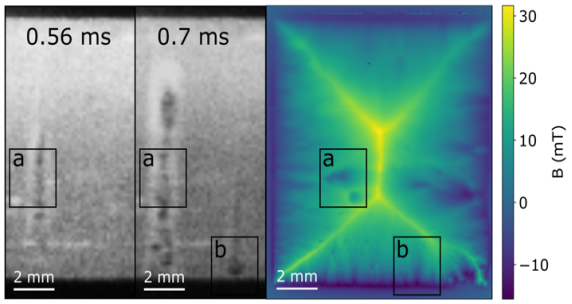

Figure 4.6: Remnant field scan of the middle section of the Superpower tape with a spatial resolution of 50 µm (left panel) and corresponding images of the bubble formation (right panel). Areas a and b indicate the starting points of bubbles at 0.56 ms and 0.7 ms, respectively.

Scanning Electron Microscopy (SEM) images were obtained with a FEI Quanta 250 FEGSEM with an accelerating voltage of 20 kV. Figure 4.7a shows an SEM image of area a from figure 4.6. While the surrounding area shows the typical smooth surface morphology of a YBCO film with some misoriented grains, in the center of the image a large area of randomly oriented grains that appear brighter in the secondary electron detector can be observed. It can be assumed that a scratch in the substrate or buffer layers hindered the epitaxial growth of the superconducting layer in this area. A similar defect was found in area b of the Superpower tape (see figure 4.7b).

EDX analysis (not shown here) showed no difference in the spectrum of the smooth and granular film surface, therefore secondary phase precipitates can be excluded as the cause of the bubble origin. Along the edges of the Superpower tape many such areas were found, and also in places where bubbles start in the SuperOx tape. From these comparisons it is evident, that an area of just a few microns of non-epitaxial film growth can be the origin

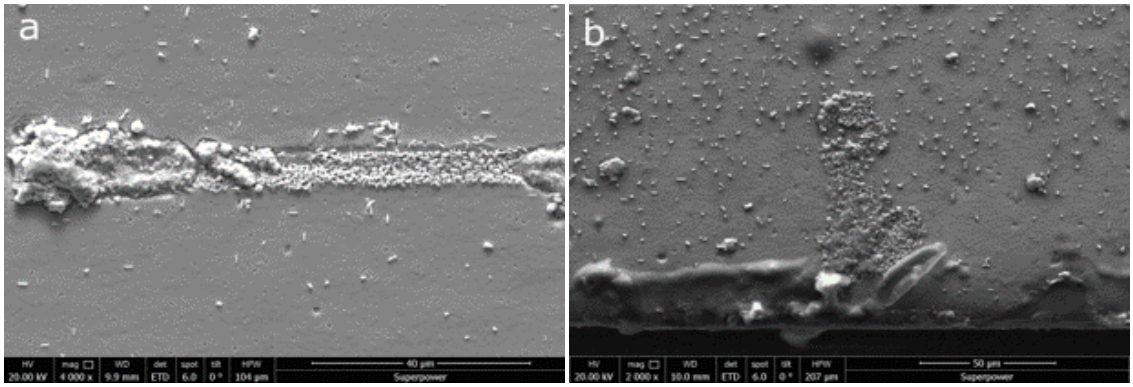

(a) Superpower (b) SuperOx

Figure 4.7: SEM images of areas a and b in figure 4.6. The images show defects in the REBCO layer. The granular nature of these defects indicates a non-epitaxial growth of the superconducting film.

of inhomogeneous quench behavior. These rather small areas of tiny misoriented grains are the reason for thermal instabilities of the tape despite their rather small influence on the critical current itself.

4.2 Experimental measurements around a dissipation column

The tape is studied when bubble generation occurs in the entire width. Electrical measurements and high-speed imaging are used to study the current distribution and the heat propagation, respectively.

4.2.1 Experimental details

Electrical measurements are performed on a 60 mm long 2G HTS tape from SuperOx ($I_c(77K)$ about 700 A), whose cross-section is detailed is detailed in Table 1.2. It is equipped with six voltage taps soldered with Indium-Tin every 1 cm on the top and bottom stabilizer sides symmetrically on the longitudinal axis of the sample (see figure 4.8). A permanent magnet was positioned in the middle of the sample to locally decrease the critical current. The sample is connected thanks to pressed contacts to the electrical circuit already presented in figure 3.7 with the parameters given in Table 4.1. The prospective current is 665 A and the actual current in the circuit is measured with a 1000 A rated current sensor.

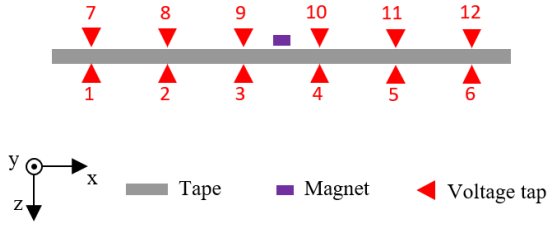

Figure 4.8: Positions of the voltage taps on the sample and position of the magnet.

$V_{circuit}$ (V)	$R_{circuit}$ $(m\Omega)$	$L_{circuit}$ (mH)
18	27	0.0038

Table 4.1: Parameters of the circuit used to observe the current distribution around a hot-spot.

The same high-speed imaging set-up is again used. The limitation test duration, controlled with the switch S is set to 15 ms. The electrical measurements (voltages and current) as well as pictures of the sample are recorded during this time.

4.2.2 Results of optical measurements

The size of the dissipation column is recognized thanks to image processing. In section 4.3, the evolution of the size of the column will be compared with results from numerical simulation.

The size of the bubble generation column on the median longitudinal line of the tape is recognized with the following procedure. First, the image recorded just before the apparition of the first bubble (image at 3.80 ms in figure 4.9a) is subtracted to all the other pictures of the dissipation spot and it gives figure 4.9b. To recognize the variations as a function of time on this zone, the gradient in the x-direction is computed and displayed in figure 4.9c.

The method is applied only on the center line of pixels in the median longitudinal direction of the tape ($y = 0$ mm) from $x = -10$ mm to $x = +10$ mm. The evolution of the

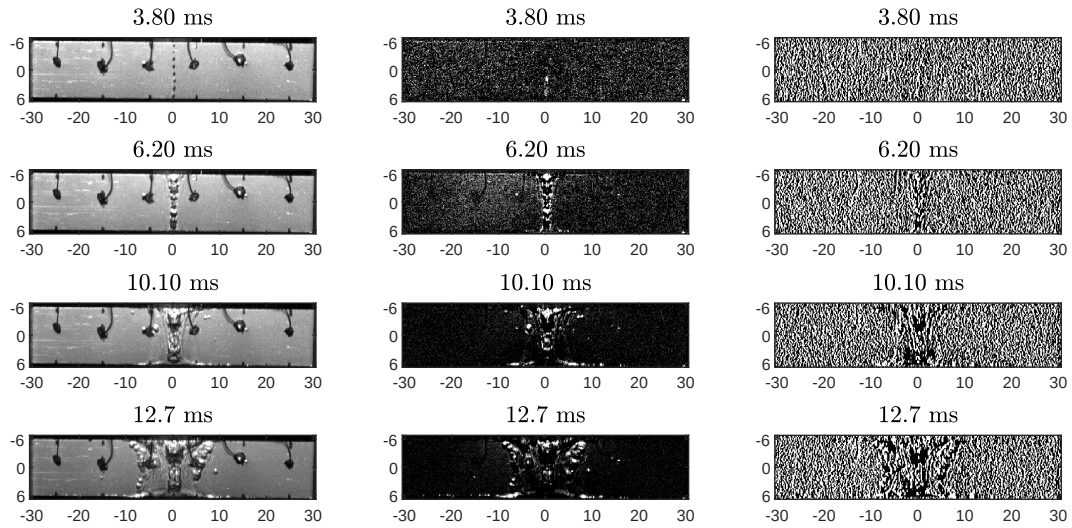

Figure 4.9: Images (a) present the bubble generation on the surface of the tape, Images (b) are the images (a) without the first image at 3.80 ms and Images (c) are the gradient in the x-direction computed with images (b).

gradient along that line of pixels as a function of time is displayed in figure 4.10a. The evolution is hardly recognizable. To suppress the noise, the value of each pixel is binarized and then filtered using the function *med2filt* from Matlab. That function realizes a median filtering on the image along the two directions. Each output pixel contains the median value in a 3-by-3 neighborhood around the corresponding pixel in the input image. The result is shown in figure 4.10b. The minimum and maximum positions of the dissipation column is displayed in figure 4.10c. The difference between the data in figure 4.10c gives the evolution of the size of the dissipation column at $y = 0$ mm (see figure 4.11). Naturally, it is observed that the propagation stops when the current stops.

Identical limitation test was also carried out looking to the surface on the substrate side of the sample. The size of the bubble generation column appears very similar on both faces of the sample.

4.2.3 Results of electrical measurements

Figure 4.12 shows the voltages measured on the sample and the current in the circuit when the applied current is higher than the critical current at the magnet location but lower than the critical current of the tape away from the magnet. Firstly, all the voltages measured on the bottom side of the stabilizer (substrate side) appear simultaneously at 4 ms. The magnitude of the voltage is smaller on the portions of the sample far from the

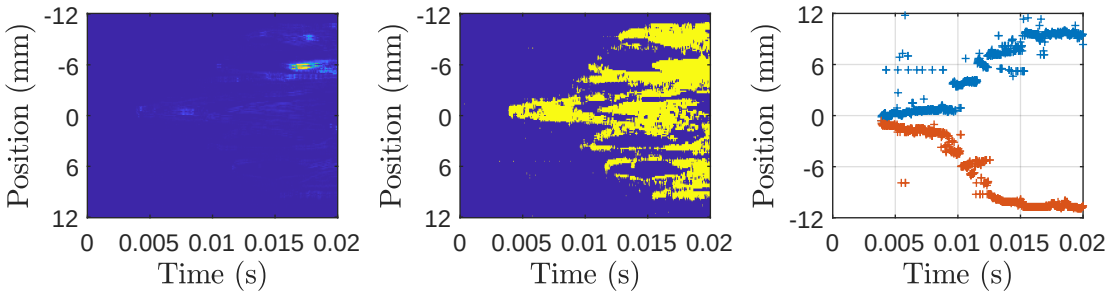

Figure 4.10: (a) presents the gradient in the x-direction on the center line of pixels of the images recorded, (b) is the same data after binarization and filtering and (c) shows the minimum and maximum positions of the dissipation column.

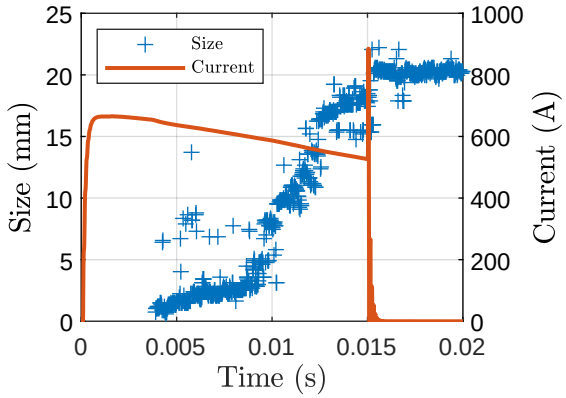

Figure 4.11: Evolution of the size of the dissipation column at $y = 0$ mm and current in the circuit as a function of time.

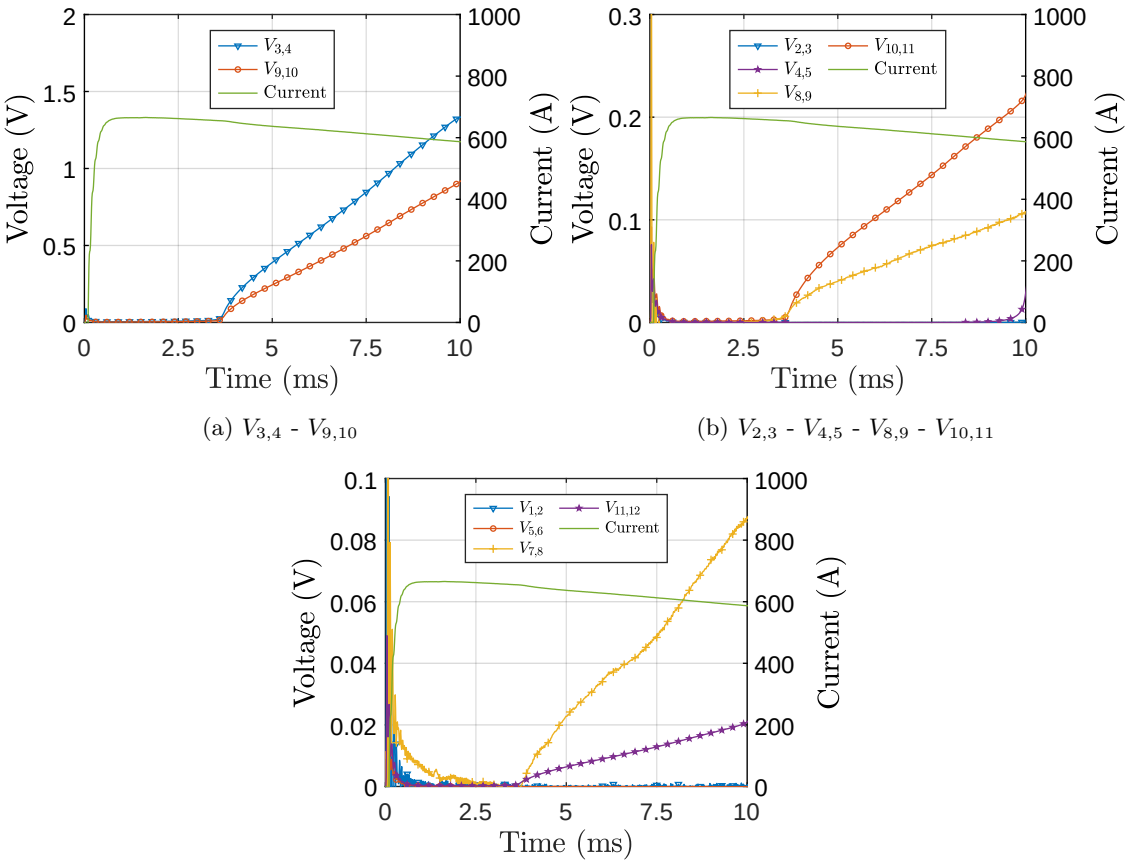

(a) $V_{3,4}$ - $V_{9,10}$

(b) $V_{2,3}$ - $V_{4,5}$ - $V_{8,9}$ - $V_{10,11}$

(c) $V_{1,2}$ - $V_{5,6}$ - $V_{7,8}$ - $V_{11,12}$

Figure 4.12: Voltages measured on the SuperOx sample as a function of time and the current in the circuit as a function of time (green plain line).

defect location, where the thermal runaway is initiated. On the top side of the stabilizer (HTS side), only the voltage measured between voltage taps 3 and 4 is different from zero. It can be noted in figure 4.12 that the voltages are not identical with respect of the center of the tape. As an example, the magnitude of $V_{3,4}$ and $V_{9,10}$ are not identical. This may come from the fact that the voltage taps are not perfectly soldered with a regular spatial step. Similar results, not presented in this paper, were experimentally obtained on a sample coming from a 2G HTS tape from another manufacturer (Superpower).

4.2.4 Discussion of the electrical measurements

Two papers report experimental results that highlight the non-equipotential cross-section of two older generation non-commercial 2G HTS tapes, during inhomogeneous quenches. First, in [98], on a structure consisting of a Nickel substrate covered by a buffer layers stack, a YBCO layer, and a silver layer on the top where a 2 mm wide section of YBCO

layer is removed along the length of the sample (i.e. there is a connection between the silver and the substrate). During a critical current measurement, the authors measured differences in the voltages measured on the substrate side and on the stabilizer side while the positions of these voltage taps were identical on the longitudinal axis of the sample. On a similar structure, from AMSC [99], without removing a portion of the width of the YBCO but with an additional copper layer on the top of the structure, where a transition is initiated in the center of the sample with a heater, the voltages measured on the Nickel substrate side are different from zero while no voltage is measured on the copper side [100]. The authors mention the non-equipotential cross-section of this structure during inhomogeneous transition.

The results, obtained during the experiment presented in subsection 4.2.3, confirm a difference of current transfer lengths between the top stabilizer layer and the HTS layer on one side and the bottom stabilizer layer and the HTS layer on the other side. Indeed, the current circulates in a wider zone in the silver layer located on the bottom of the tape. Furthermore, from the amplitude of the measured voltages, it is deduced that the current density in the bottom stabilizer layer gradually increases as we approach the defect and reaches its maximum at the defect location.

4.3 Simulation of a dissipation phenomenon

The simulations presented here are realized with a 3D Finite Element Method (FEM) model of 2G HTS tape developed on COMSOL by C. Lacroix and F. Sirois from Ecole Polytechnique de Montréal. In addition, they carried out a precise review of this part of the manuscript.

The results of section 4.1 highlighting the correlation between the positions of the inhomogeneities in the 2G HTS tape and the dissipation zones as well as the experimental observations of section 4.2 studying the dissipation column motivate the simulation of a dissipation phenomenon to reproduce local behavior along the tape cross-section and length.

4.3.1 Model of 2G HTS tape

Details of the electro-thermal model can be found in [82]. Here, the main points of the model are given to understand how the simulation results are obtained.

4.3.1.1 Geometry and materials

A 6-cm long tape is modeled with dimensions corresponding to SuperOx tape (see Table 1.2). Note that the stack of buffer layers is not modeled as a volume element but rather as an insulated interface (2D element). The heat capacity per volume unit, the resistivity and the heat conductivity are taken from [78][79].

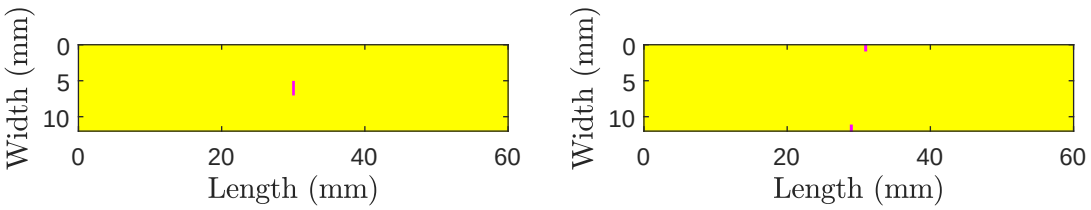

(a) Defect in the center

(b) Defects on the edges

Figure 4.13: Two critical current density distributions in input of the simulation, $J_c = 3.35 * 10^{10}$ (A/m^2) in yellow and $J_c = 0.335 * 10^{10}$ (A/m^2) in purple.

Two different critical current density distributions are considered (see figure 4.13). Each current density distribution was implemented to reproduce the initial dissipation areas located either in the middle of the width or at two positions close to the lateral sides (see columns A and B in figure 4.2). In the distribution of figure 4.13a, the tape has an uniform critical current density with one 400 µm long and 2 mm wide single defect. In the second distribution in figure 4.13b, two 400 µm long and 1 mm wide defects at a slightly different positions along the sample length was included. The areas of low superconducting properties model defects in the REBCO coated conductor following the analysis detailed in section 4.1. The critical current density of the tape away from the defects (in the yellow parts) was adjusted to obtain an initiation of the thermal runaway at the same time as it occurred experimentally in section 4.2.

4.3.1.2 Comsol Multiphysics modules

Electric currents and electrical circuit The tape is inserted on a circuit similar to the circuit described in figure 4.14 using the same parameters values of Table 4.1 but with a proper constant DC voltage source. The surface of the HTS layer on the cross-section at each extremity of the tape is connected to the electrical circuit. The current can flow in all layers except through the buffer layers between the HTS layer and the Hastelloy® C276 substrate since it is represented as a 2D element (however, it is noted that because of the high resistivity of the buffer layers the current would be negligible).

Heat Transfer in Solids The temperature at the two extremities, at the positions 0 mm and 60 mm along the length, remains equal to 77 K, the temperature of the liquid nitrogen bath, during the simulation. The heat transfer of the tape with the liquid nitrogen bath is not considered in the simulations.

4.3.1.3 Voltages probes

Local evaluations of the voltage are sampled with probes inserted in the model to follow the evolution of the voltage on the top and bottom stabilizer layers of the tape in specific locations. The voltage probes are positioned in the same way as described in the

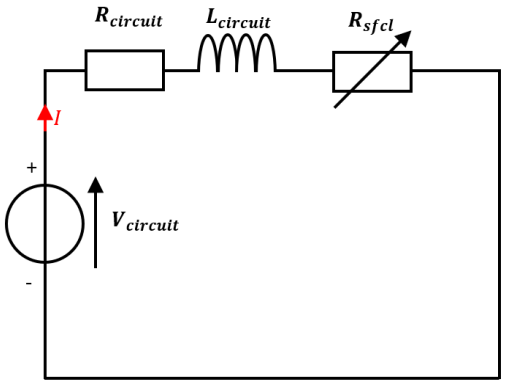

Figure 4.14: Electrical circuit modeled to simulate the behavior of the 2G HTS tape.

experiments (see figure 4.8).

4.3.2 Inhomogeneous dissipation in the width

The main objective is to simulate the dissipation behaviors of columns A and B described in figure 4.2a.

One single centered defect The temperature in figure 4.15 observed on the top of the tape shows an evolution similar to what is observed experimentally (column A). The heat propagates at first along the width starting from the defect until it reaches the lateral sides of the tape.

Figure 4.16a shows that the current density is higher in the direct surrounding of the defect ($x = 30$ mm). Indeed, the very low superconducting property of the defect forces the current to meander around it. This higher current density in this area compared to the rest of the tape initiates dissipation starting at the border of the defect and gradually decay until the dissipating area reaches the lateral sides of the tape. Once the tape has quenched across the entire width, the current does not circulate anymore through the superconducting layer (see figure 4.16d).

Two distinct defects on edges The temperature evolution for a critical current density distribution with two defects is presented in figure 4.17. It increases in the immediate vicinity of the defects (where the current density is highest, but not directly on it). The heat then propagates in a straight line between the two defects. This case reproduces very well what was observed in figure 4.2a in the case where the dissipation column B is not perfectly parallel with the direction of the width.

At the very beginning of the simulation, the current density increases between both defects and is the highest in the direct vicinity of the defects (see figure 4.18a). This initiates

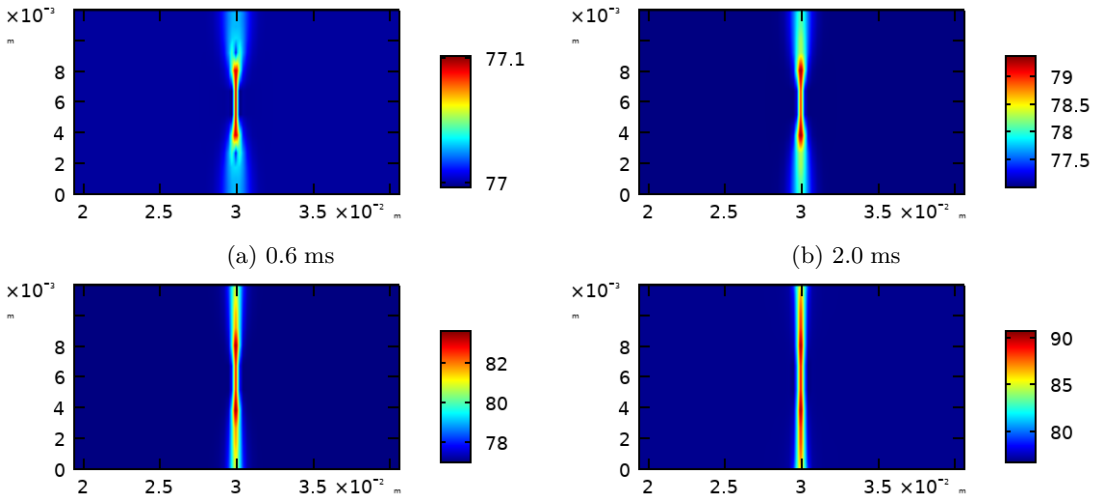

(a) 0.6 ms (b) 2.0 ms

(c) 2.7 ms (d) 3.0 ms

Figure 4.15: Temperature on the top stabilizer layer of the tape at several times with a single defect (zoom between $x = 2$ cm and $x = 4$ cm).

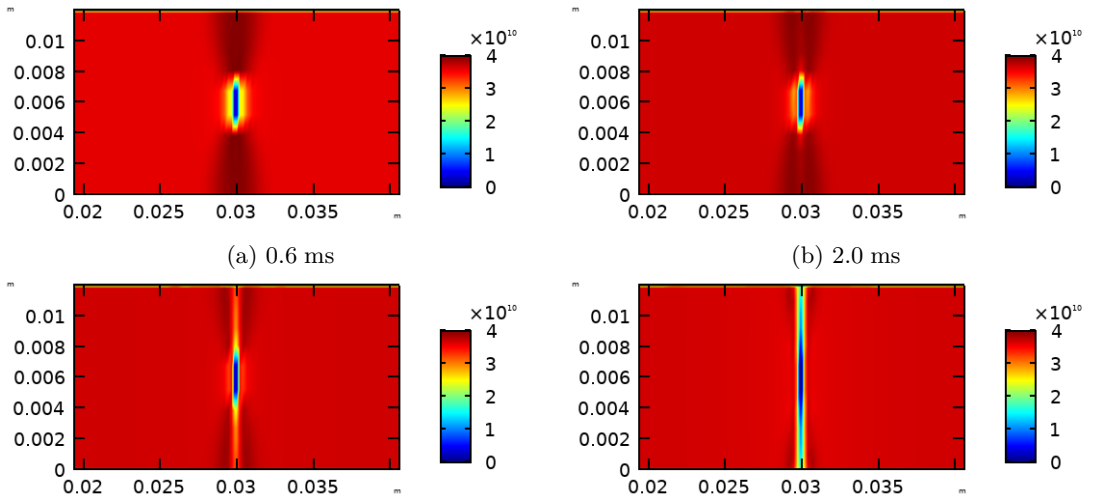

(a) 0.6 ms (b) 2.0 ms

(c) 2.7 ms (d) 3.0 ms

Figure 4.16: Current density in the superconducting layer (in the center of the thickness on the z-direction) with a single defect (zoom between $x = 2$ cm and $x = 4$ cm).

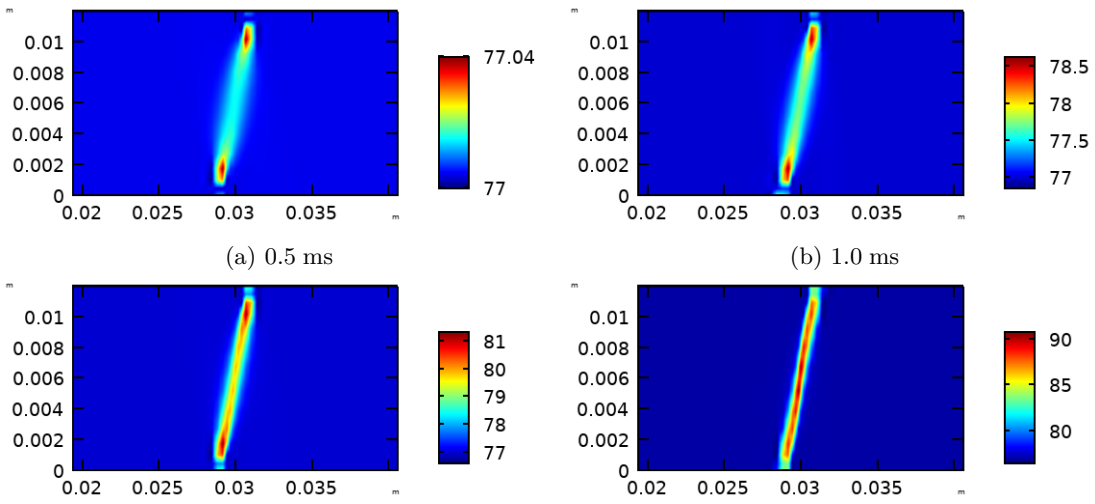

(a) 0.5 ms

(b) 1.0 ms

(c) 1.5 ms

(d) 2.0 ms

Figure 4.17: Temperature on the top stabilizer layer of the tape at several times with two distinct defects (zoom between $x = 2$ cm and $x = 4$ cm).

a heat dissipation and it contributes to reduce the effective cross-section of superconductor available between the two defects. This mechanism continues until the cross-section between the two defects is sufficiently hot to force current sharing with the other layers (see figure 4.18d).

The evolution of the temperature obtained with numerical simulations and the evolution of the bubble generation are qualitatively similar. However, it is important to mention that the evolution of the temperature and the evolution of the bubble generation are not the same phenomena since the dynamics are different. The time to obtain an elevation of temperature fully developed in the width observed with numerical simulations and the time to obtain a dissipation column fully developed in the width observed in the experimental results in section 4.1 are different. Indeed, a difference of temperature is required between the tape surface and the liquid nitrogen bath to initiate bubble generation [101].

4.3.3 Inhomogeneous dissipation along the length

The dissipation is now developed in the width forming a column of dissipation. The current distribution in the vicinity of this column is studied. The numerical results are compared with the experimental results presented in section 4.2. All numerical simulations are done for 15 ms at 77 K considering the case of a single defect in the center of the tape.

4.3.3.1 Current distribution in the vicinity of a dissipation column

Figure 4.19 presents the current density on the surfaces of the top and bottom stabilizer layers. The current circulates on a larger zone in the bottom stabilizer layer than on the

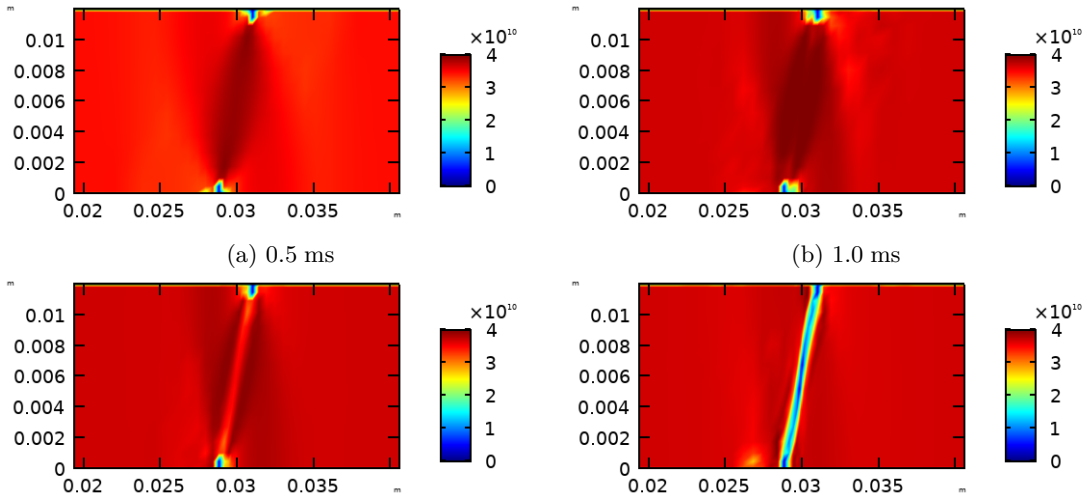

(a) 0.5 ms (b) 1.0 ms

(c) 1.5 ms (d) 2.0 ms

Figure 4.18: Current density in the superconducting layer (in the center of the thickness on the z-direction) with two distinct defects (zoom between $x = 2$ cm and $x = 4$ cm).

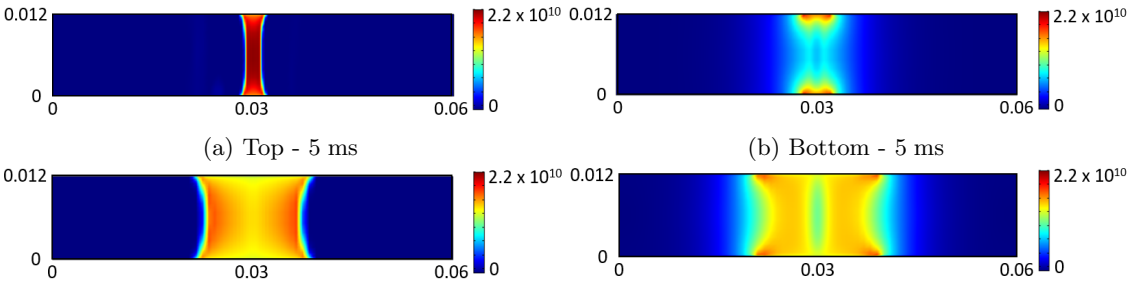

(a) Top - 5 ms (b) Bottom - 5 ms

(c) Top - 10 ms (d) Bottom - 10 ms

Figure 4.19: Current density on the top and bottom stabilizer layers at 5 ms and 10 ms.

top stabilizer layer. In [102], the difference of current distribution between the substrate and the top stabilizer layer is explained by a higher interface resistance between the HTS layer and the bottom silver layer (and substrate) than between the HTS layer and the top silver layer. Indeed, it is easier for the current to transfer to the top silver layer, directly in contact, than to transfer to the bottom silver layer, only accessible by passing through the silver on the lateral sides. This result is now also found on a 3D FEM model of a commercial tape.

It is also interesting to observe the components of the current density on the y-axis (width) and z-axis (thickness) to highlight the path of the current in the vicinity of a dissipation column. When the tape is entirely superconducting, the current flows almost entirely in the superconducting layer. When a dissipative zone is encountered, the current leaves the superconducting layer and is shared between the top silver layer, the bottom

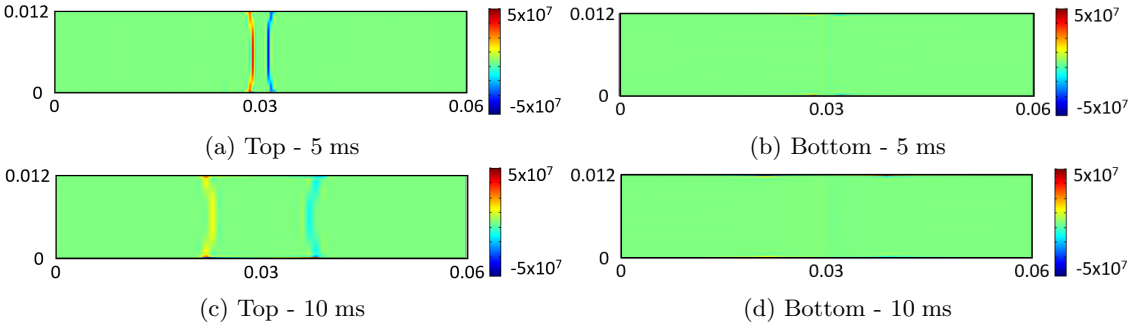

(a) Top - 5 ms (b) Bottom - 5 ms

(c) Top - 10 ms (d) Bottom - 10 ms

Figure 4.20: Component of the current density on the z-direction (thickness) on the top and bottom stabilizer layers at 5 ms and 10 ms.

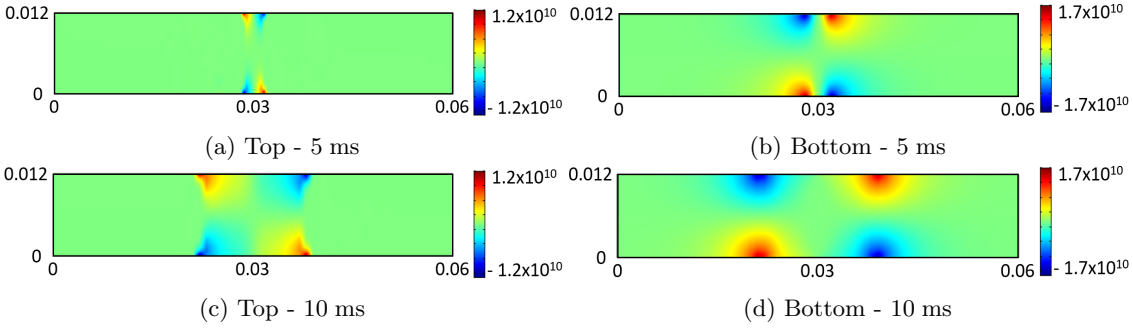

(a) Top - 5 ms (b) Bottom - 5 ms

(c) Top - 10 ms (d) Bottom - 10 ms

Figure 4.21: Component of the current density on the y-direction (width) on the top and bottom stabilizer layers at 5 ms and 10 ms.

silver layer and the substrate. Figures 4.20a and 4.20c show that the current penetrates the top silver layer and comes back to the superconducting layer after the dissipative zone with the existence of the component of the current density on the z-axis. To reach the bottom stabilizer layer, the current leaves the top silver layer and circulates through the lateral sides and then penetrates in the bottom silver layer. This is shown through the existence of the component of the current density on the y-axis on the top stabilizer layer (see figure 4.21a and 4.21c) and on the bottom stabilizer layer (see figure 4.21b and 4.21d).

4.3.3.2 Temperature in the vicinity of a dissipation spot

The temperature on the top and bottom surfaces of the tape are shown in figure 4.22. The heat propagation fronts are almost identical on the top and bottom stabilizer layers even if the current distributions are not. This is not surprising due to the low thickness of the tape (100 µm). However, the temperature distribution is not identical along the width. As explained in [103], this is due to the current that flows through the lateral sides of the tape to reach the bottom stabilizer layer. The current density in the lateral side becomes higher than in the rest of the tape which leads to a higher temperature. A similar pattern was experimentally observed on 2G HTS tape during an inhomogeneous quench in section in section 3.3. It was observed that the bubbles created from the heat dissipation had the

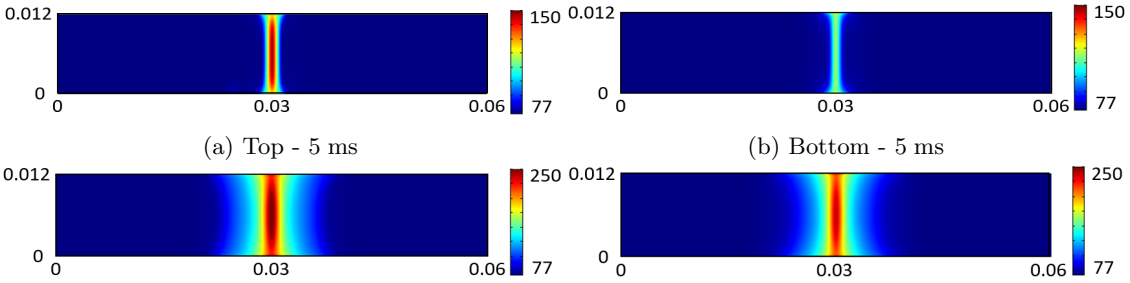

(a) Top - 5 ms

(b) Bottom - 5 ms

(c) Top - 10 ms

(d) Bottom - 10 ms

Figure 4.22: Temperature on the top stabilizer layer and bottom stabilizer layer at 5 ms and 10 ms.

shape of a hourglass.

4.3.3.3 Comparison of electrical measurements

Since the results are symmetrical between the center of the sample and each side of the model, only the results on one side of the tape are displayed to make the figure clearer (from x=0 mm to x=30 mm). Figure 4.23 shows that the simulation results are similar to the experimental results. The voltages on the portions 7-8, 8-9, 9-10, on the bottom surface of the stabilizer appear simultaneously at 4 ms while only the voltage on the portion 3-4 on the top surface of the stabilizer appears. Also, similar to the experiments, the voltage on the bottom surface is also decreasing when the distance between the probe and the center of the tape is increasing. However, even if simulations and experiments qualitatively agree, the heat propagation appears to be faster on the simulation because $V_{2,3}$ remains equal to zero in the experiment while $V_{2,3,simu}$ increases at 8 ms in the simulation. This could be due to the adiabatic hypothesis in the model.

4.3.3.4 Comparison of the size of the dissipation column

The evolution of temperature along a longitudinal line in the middle of the width of the tape as a function of time is extracted from the numerical results. To compare it with the experimental results, a temperature for which one the sample generates bubbles has to be chosen. Indeed, the onset of boiling occurs only when a difference in the temperature between the tape and the bath exists. Reference [101] presents a value around 90 K. This value is adopted but it is quite arbitrary because, as it has already been introduced, the onset of boiling depends on many parameters (see subsection 3.2.2.3). Figure 4.24 presents the evolution of the size of the dissipative column obtained with the numerical results and compared with the experimental results. The evolutions are qualitatively similar in both cases with a slow increase and then a fast increase of the size. The propagation develops faster in the simulation than in experiment. This probably comes from the hypothesis of adiabatic conditions in simulation.

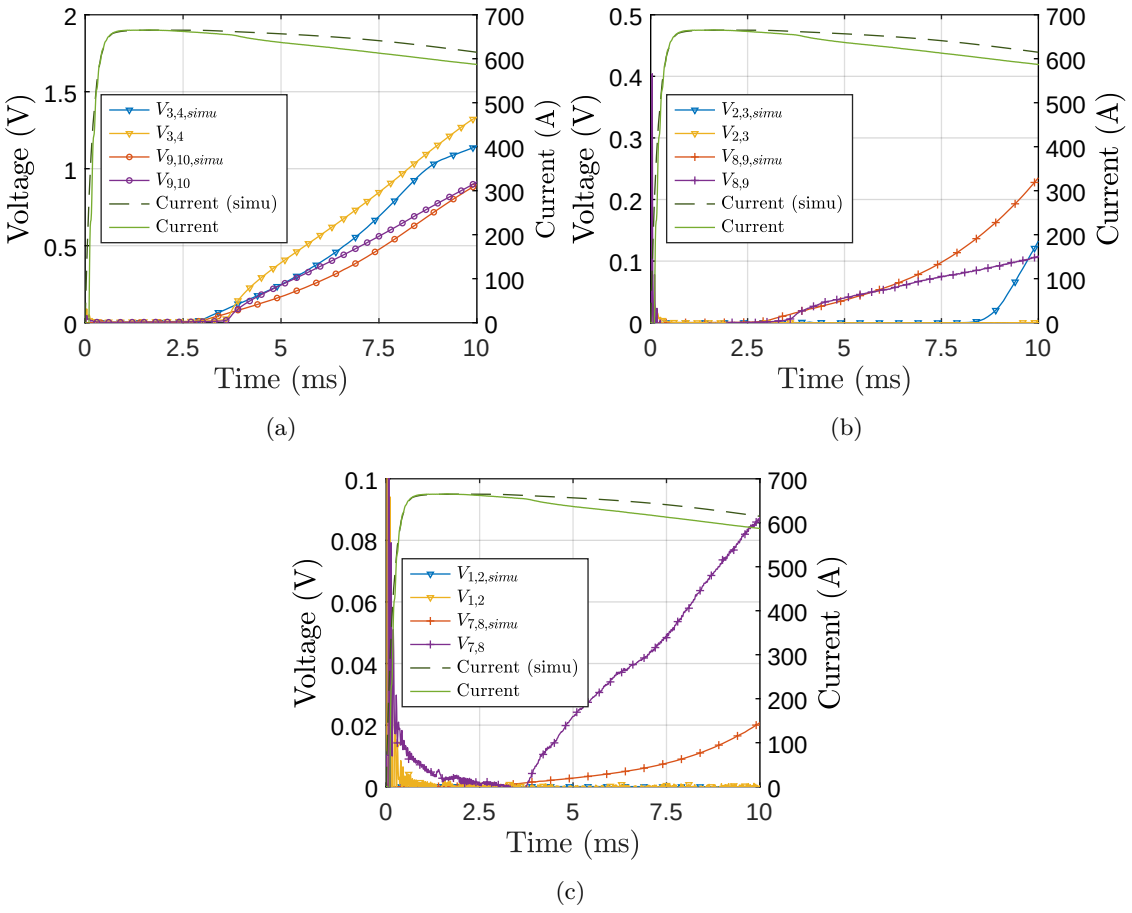

Figure 4.23: Voltages as a function of the time on several portions of the tape from measurements and simulation on the top and bottom stabilizer layers.

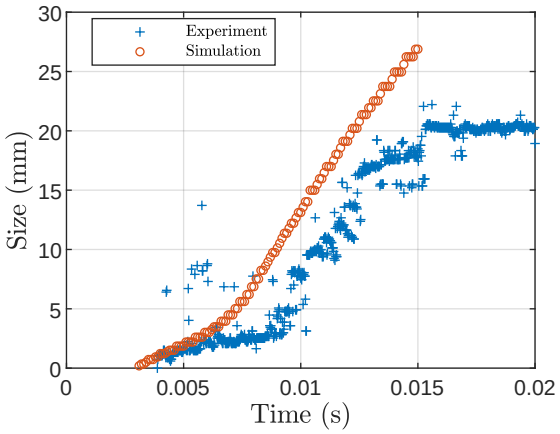

Figure 4.24: Comparison of the size of the dissipative column between experimental and simulation behavior.

4.4 Influence of the lack of silver on the lateral sides

The simulations presented here are realized with a 3D Finite Element Method (FEM) model of 2G HTS tape developed on COMSOL by C. Lacroix and F. Sirois from Ecole Polytechnique de Montréal. In addition, they carried out a precise review of this part of the manuscript.

A better understanding of the quench mechanism is useful also to evaluate the impact of issues that may occur on commercial 2G HTS tapes. The two previous sections highlighted the importance of the stabilizer on the lateral sides to enable the circulation of the current from the HTS layer to the bottom stabilizer layer. The corresponding current transfer length is much larger than the current transfer length between the HTS layer and the top stabilizer layer. It is known that partial lacks of silver may occur on the lateral sides of the tape. This may impact the safe operation of the tape due to the circulation of the current through the lateral sides. This section aims to investigate this possible issue.

4.4.1 Description of the model

The same model as described in subsection 4.3.1 is used with the difference that silver is locally removed over a length of 1 cm or entirely removed on one lateral side of the tape (see figure 4.25).

4.4.2 Simulation results

Figure 4.26 shows the temperature of a tape in the case of a complete coverage of silver (no lack) and compared with the cases of a 1 cm lack and a total lack of silver. In all cases, the temperature over the top stabilizer layer is very similar at 5 ms. The maximum temperature on the whole volume of the model, at the end of the simulation, reaches 272 K

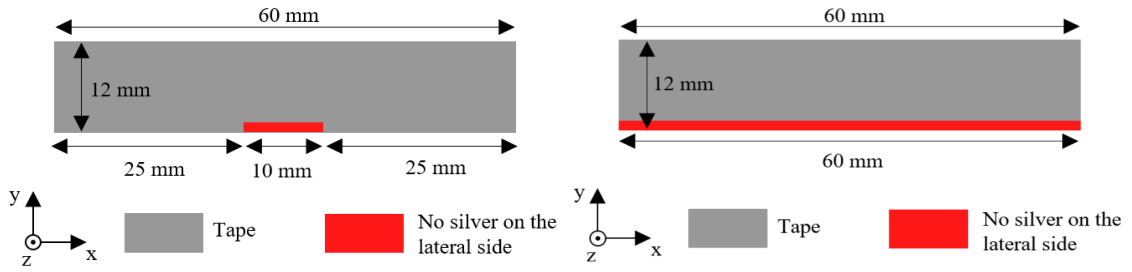

(a) 1 cm (b) 6 cm

Figure 4.25: Illustration of the lack of silver on the lateral side of the tape with a view on the top stabilizer surface.

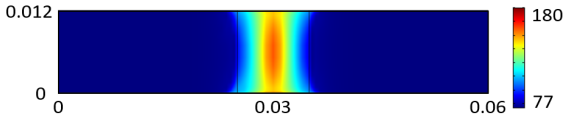

(a) No lack

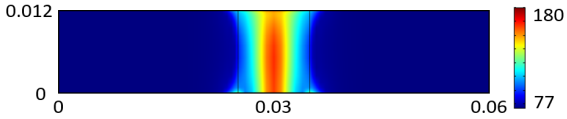

(b) 1 cm

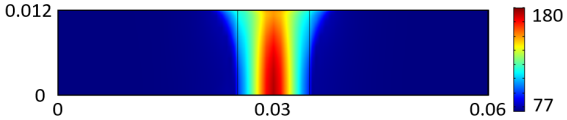

(c) 6 cm

Figure 4.26: Temperature on the top stabilizer layer at 5 ms with several cases of lack of silver.

with the 6 cm long lack of silver, 257 K with the 1 cm lack and 251 K without the lack of silver. It is concluded that the lack of silver does not induce a huge difference in the temperature of the tape.

The current density on the top silver layer is highest in the configuration with no silver on one lateral side (see figure 4.27). It is supposed that the higher current density on the top stabilizer layer comes from an interface resistance between the HTS layer and the bottom stabilizer layer twice higher than the case with a full coverage of both lateral sides. Figure 4.28 shows that the component of the current density along the width on the bottom stabilizer side is the more important when the silver is totally removed from one lateral side. The lack of silver increases the transfer length but does not change significantly the current density which justifies the almost no change in the temperature elevation. There is more current on a larger tape portion but with a similar current density. It is concluded that a lack of silver does not comprise the good operation of a commercial tape.

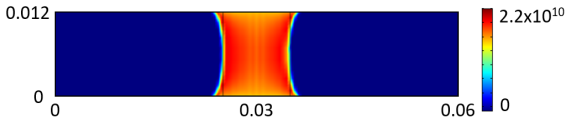

(a) No lack

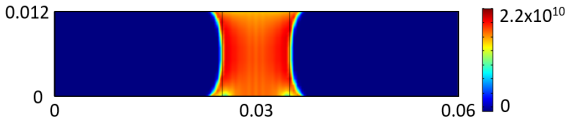

(b) 1 cm

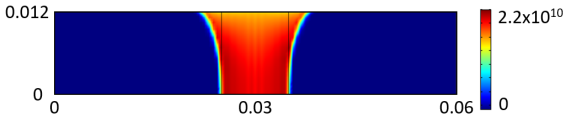

(c) 6 cm

Figure 4.27: Current density on the top stabilizer layer at 5 ms with several cases of lack of silver.

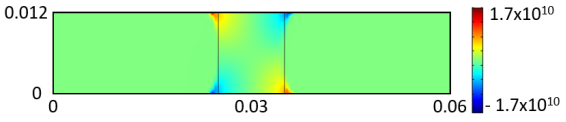

(a) Top - No lack

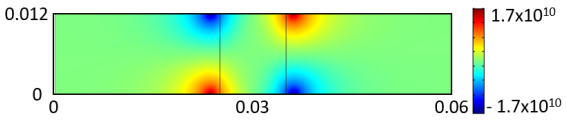

(b) Bottom - No lack

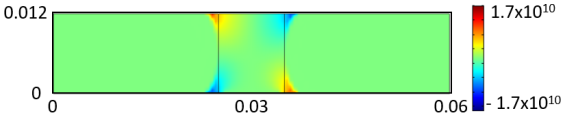

(c) Top - 1 cm

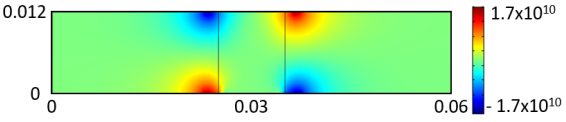

(d) Bottom - 1 cm

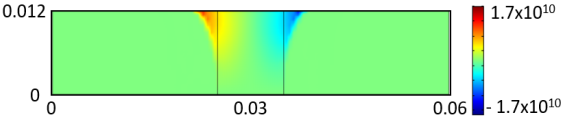

(e) Top - 6 cm

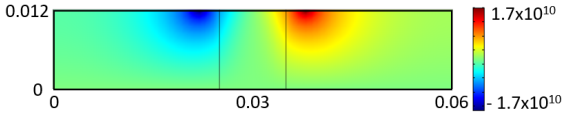

(f) Bottom - 6 cm

Figure 4.28: Component of the current density in the y-direction (width) on the top and bottom surfaces of the tape at 5 ms with several cases of lack of silver.

4.5 Conclusion

This chapter proposes to study the mechanism of the onset of quench in 2G HTS tapes when the dissipation is not only inhomogeneous along the length but also along the width.

In a framework of a collaboration with TU Wien, local analysis of the REBCO layer is performed by means of scanning Hall probe microscopy and compared to optical observation of the bubbles generated during the onset of quench. It demonstrates that the bubble generation occurs at positions of local inhomogeneities in the REBCO layer.

At the positions of these inhomogeneities along the length, the dissipation first propagates in the width of the tape. When the dissipation is fully developed in the width, the propagation develops along the length. Experimental measurements show that the current distribution in the vicinity of the dissipation column is not identical on the top and bottom surfaces of the tape, highlighting that the cross-section of the tape cannot be considered as equipotential during an inhomogeneous quench.

These experimental observations motivated the use of a 3D FEM model to simulate the quench mechanism. The presence of inhomogeneities in the tape is modeled by areas of very low J_c. These areas force the current to meander and this locally increases the current density in the direct vicinity of these defects, initiating the dissipation and thus, reducing the effective cross-section. The dissipation propagates to cover the entire width. Then, the current sharing occurs with the top and bottom silver layers. The current transfer length from the superconducting layer to the bottom silver layer is higher than the current transfer length from the superconducting layer to the top silver layer. As a consequence, current circulates in a larger portion on the bottom stabilizer layer of the tape in the vicinity of a dissipation column compared with what is observed on the top stabilizer layer, during an inhomogeneous quench.

These results highlight the role of the silver covering the lateral sides of the tape during an inhomogeneous quench to transfer the current. The influence of a lack of silver on one lateral side is assessed. It appears that a partial lack does not significantly change the operation of the tape.

This chapter concludes the study initiated in chapter 3 about the operation of the tape during an inhomogeneous quench. It determined that the dissipation is well predicted by the positions of the inhomogeneities in the REBCO layer. The critical current as a function of the position does not appear as the appropriate indicator to predict the dissipation. In section 2.3, $I_c(z)$ is used as the input of the model. The following chapter will move back to the system scale with the development of conductors based on 2G HTS tapes with a design approach adapted to the conclusions of this chapter.

CHAPTER 5

Advanced R-SFCL conductors with high performances based on 2G HTS tapes

The chapters 3 and 4 contributed to a better understanding of the local electro-thermal behavior of the 2G HTS tapes. The observations realized in these chapters do not comprise the conductor design approach developed in chapter 2, based on the formalization of two regimes of operation of the conductor. For example, the hot-spot regime as a macroscopic phenomenon was experimentally observed. The existence of this regime was predicted using the critical current as a function of the position. It appeared not to be a good indicator to describe the dissipation phenomena. This input in the design approach, to reflect the existence of the I_c inhomogeneities, will be adapted in this chapter. One objective of this PhD work is the increase of the cost-effectiveness of the conductors of R-SFCL. The architectures developed in this chapter show high performances in order to decrease the conductor quantity and as a consequence, the price of a R-SFCL. Simulations and characterizations are used to assess the cost-effectiveness of these innovative conductors. Five structures are introduced at different stages of development: from early stage concepts to conductors close to industrialization. This activity was conducted in the framework of Fastgrid and represents the bulk of the contribution of Grenoble in this project. Three out of five of these concepts were developed for Fastgrid, the last two were considered in parallel.

5.1 Development of the Fastgrid conductor

Fastgrid was a project focusing on the conductors of R-SFCL with a strong component of material science. The main contribution of Grenoble in this project was the design and the characterization of the "Fastgrid conductor", the architecture with the highest Technology Readiness Level (TRL). This PhD work positions in this contribution through the characterization of the Fastgrid conductor.

This project was much more than the development of an unique conductor. Several partners coming from material science developed innovative architectures of advanced conductors. These structures present a lower TRL but are promising for the future. On this second axis, this PhD work is positioned on the characterization of these innovative structures in section 5.2.

5.1.1 Conceptual design

5.1.1.1 Two main actions on the cost

The main objective of the Fastgrid conductor is to present high performances. The cost of the conductor of a R-SFCL was introduced in subsection 1.3.3.1 and reproduced in expression (5.1). It was mentioned that the designer can only have an action on the cost through the electric field withstood by the conductor E_{sc} and its critical current I_c. The specifications of the conductor based on a 2G HTS tape produced by THEVA [48] can be simply summarized:

- Maximization of the electric field E_{sc}
- Operation with the maximum critical current I_c
- Limitation of the conductor maximum temperature on its whole operation range to 400 K
- Operation for $\Delta t = 50$ ms in fault conditions (requirement from Supergrid Institute)
- Safe operation from $I_n = 700$ A to $20I_n$

The last specification was defined by the author to complete the frame of design. To meet the specifications, the Fastgrid conductor is based on the work presented in [67].

$$Cost = C_{sc} N L_{sc} = C_{sc} \frac{k_a I_a}{I_c} \frac{V_{sc}}{E_{sc}} \tag{5.1}$$

Maximization of the electric field The temperature elevation in limitation regime is given by (2.21). To fulfill the specification in terms of temperature elevation but with an increase of E_{sc}, a solution is to increase ρ the conductor resistivity. Indeed, $c_{p,v}$ does not change significantly from a metal to another one and Δt is a specification. The increase of ρ is completed through the soldering of a highly resistive material to the 2G HTS tape. This

will reduce the resistance per unit length of the tape itself but it will increase its resistivity. Hastelloy® C276 presents a high resistivity (1.26 μΩcm at room temperature [79]) but its cost is high. Stainless steel would have been a better option from that point of view, yet it would have led to a lower electric field due to a lower resistivity than Hastelloy® C276. Moreover, trials using Stainless Steel were not successful due to differential contractions while this is not a problem with Hastelloy® C276 as the tape substrate is made with this material. Inconel [104] could also be an option (1.44 μΩcm) though, this was not tried. Another option would have been to directly act on the silver layer to increase the tape resistivity by decreasing its thickness or using a silver alloy instead of pure silver but it means that the tape becomes non-standard.

Operation with the maximum critical current Figure 1.14 highlighted that a decrease of the temperature of a tape increases its critical current. The liquid nitrogen solidifies at 63 K. As a consequence, an operation at 65 K is chosen to increase I_c, almost twice higher at 65 K than at 77 K.

5.1.1.2 Adaptation of the conductor thickness

These two actions modify the operation in hot-spot regime. The temperature elevation in this regime was given by (2.23). The increases of the conductor resistivity as well as the critical current lead to a high temperature elevation in hot-spot regime. The solution to keep the maximum temperature below 400 K is the conductor thickness adaptation as introduced in subsection 2.4.3.1.

To determine the thickness of the Hastelloy® C276 to solder to the 2G HTS tape, the model described in section 2.2 is used [105]. However, due to the observations realized in chapter 4, the I_c measurement used as an input to predict the maximum temperature in hot-spot regime should be changed. As $I_c(z)$ does not describe in an appropriate way the local dissipation phenomena and as a very precise SHPM is not feasible on long samples length, the proposition is to use a non realistic I_c distribution shown in figure 5.1. The idea is to consider the worst possible case where there is a single dissipation spot with almost no current limitation. A length of 1 m and a defect of 580 A is chosen and this will be justified in chapter 6.

The conductor behavior is simulated for 50 ms in operation at 65 K on the range of prospective currents mentioned in the specifications of the conductor. One result of the simulation is the maximum temperature of the conductor as a function of the prospective current normalized by the rated current. This simulation is run several times with different Hastelloy® C276 shunt thicknesses and electric fields. The objective is to obtain a similar temperature in hot-spot regime and limitation regime. Figure 5.2 presents the results obtained with an electric field of 130 V/m and several shunt thicknesses as introduced in [76]. A shunt thickness of 500 μm gives a temperature of 400 K in hot-spot and limitation regimes which is sufficiently thin to enable the winding of the conductor for R-SFCL applications.

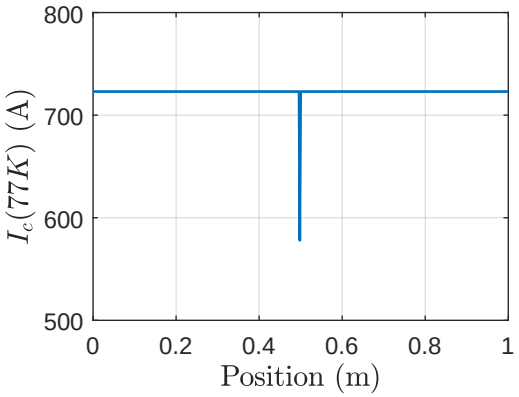

Figure 5.1: Critical current over position used as an input to determine the Hastelloy® C276 shunt thickness.

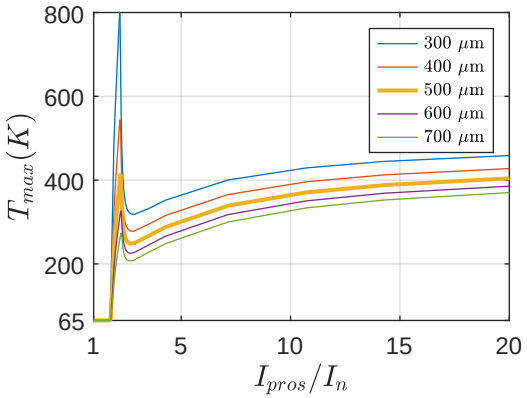

Figure 5.2: Maximum temperature as a function of the prospective current normalized by the rated current of the circuit at several Hastelloy® C276 shunt thicknesses.

5.1.2 Implementation of the design

5.1.2.1 Manufacturing processes

The bonding of the Hastelloy® C276 shunt to the "bare" THEVA tape is quite challenging. The shunt is tin but it requires to first deposit a thin Nickel layer on the shunt. Then, the shunt and the tape are heated together to enable the bonding. In the framework of the project, THEVA was in charge of the bonding of the Hastelloy® C276 shunt to the bare tape produced by the company. The structure of the Fastgrid conductor is shown in figure 5.3.

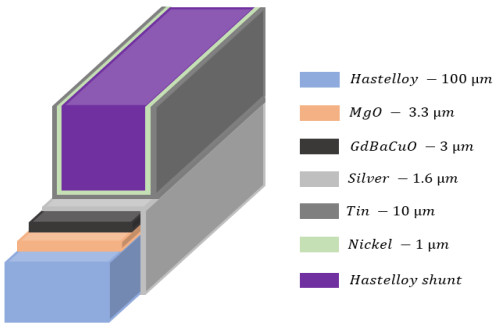

Figure 5.3: Structure of the Fastgrid conductor. A thick Hastelloy® C276 shunt is soldered to a bare THEVA tape using a tin solder.

The company started the bonding process with a first manufacturing process named

as "lab process" in this PhD work. Figure 5.4 shows the machine used to produce small lengths of conductor. Tape and shunt are positioned on a heating bar. Then, a heated roll (inside the carriage on the right side of the figure) is pulled over the tape to apply pressure and solder the two elements. To produce long lengths of conductor, a second manufacturing process named as "industrial process" was developed by THEVA based on a Reel-to-Reel system where one of the roll is heating to achieve the bonding.

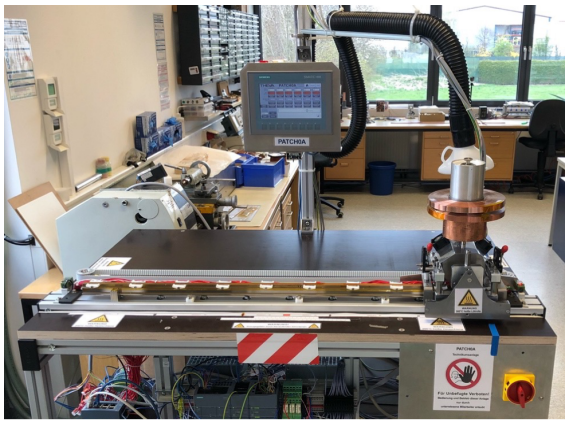

Figure 5.4: Machine used to solder the bare tape and shunt together on small lengths. Courtesy of THEVA.

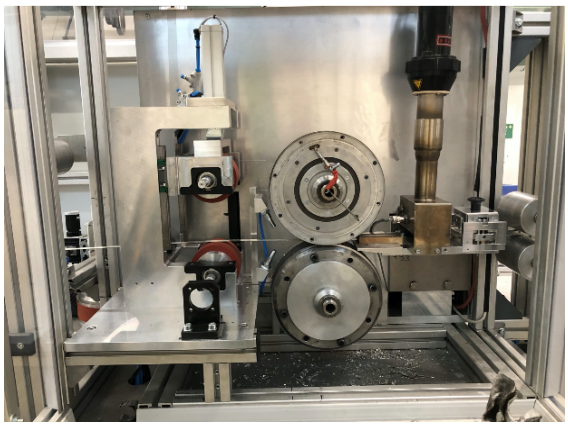

Figure 5.5: Machine used to solder bare tape and shunt together on long lengths. Courtesy of THEVA.

5.1.2.2 Analysis of the manufactured conductor

The resistivities of the bare THEVA tape and Fastgrid conductor, shown in figure 5.6, are measured and compared in figure 5.7. The soldering of the resistive shunt enables an increase about 50 % of the resistivity compared with the bare tape. Nevertheless, it is still far from the resistivity of pure Hastelloy® C276 due to, in particular, the presence of the protective silver layer.

The 1D model of the 2G HTS conductor is once again used. Instead of using an analytic expression (2.4) to compute the resistance per unit length of the conductor, the measurement is used. With the same framework used to obtain figure 5.2, the maximum temperature as a function of the prospective current is given in figure 5.8. With an initial objective of 130 V/m, the maximum temperature in limitation regime exceeds 400 K because the resistivity of the conductor is a bit smaller than the resistivity predicted by the simulation. It would be safer not to exceed an electric field of 125 V/m not to risk any damage of the tape. Unlike the limitation regime, in hot-spot regime, this smaller resistivity contributes to decrease the temperature, as it was predicted in subsection 2.4.3.1. The conductors manufactured with the two processes are characterized.

Figure 5.6: Picture of the bare tape from THEVA (top) and Fastgrid conductor (bottom).

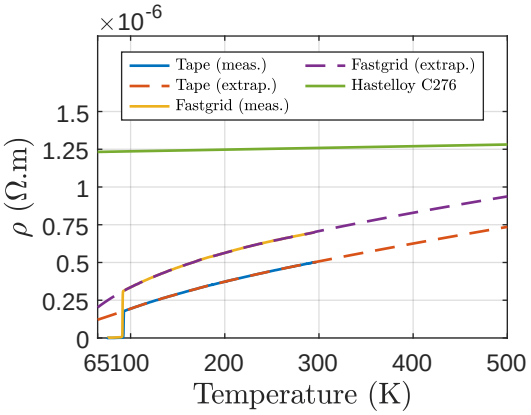

Figure 5.7: Resistivities as a function of temperature of the bare THEVA tape and Fastgrid conductor.

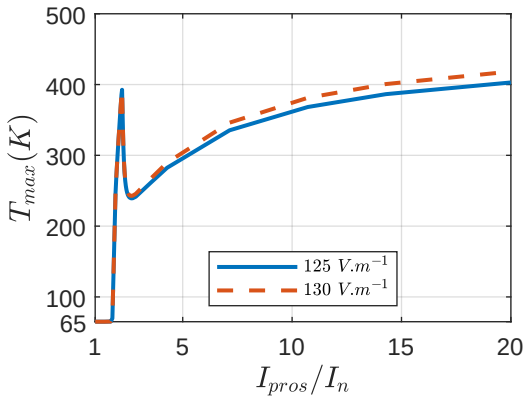

Figure 5.8: Maximum temperature as a function of the prospective current normalized by the rated current of the circuit using the actual resistance per unit length of the conductor at two electric fields.

5.1.3 Characterization on a small length of the conductor made with the "lab process"

5.1.3.1 Experimental details

The sample-holder showed in figure 5.9 was developed during this PhD work. The current leads are long (7 cm) to maximize the surface of contact between copper and the conductor to avoid damaging heating. One of the current leads is not fixed to make the translation in the longitudinal axis of the sample possible. The length of the sample between the current leads is 20 cm. This is the maximum length that can be tested with the available power source. Six voltage taps are soldered with indium-tin on the tape side of the sample to measure the electric fields and compute T_{mean} and T_{max}. The sample-holder is inserted in the cryostat shown in figure 3.8b where tests are first carried out at 77 K before a decrease of the temperature to 65 K following the procedure detailed in subsection 3.1.2.

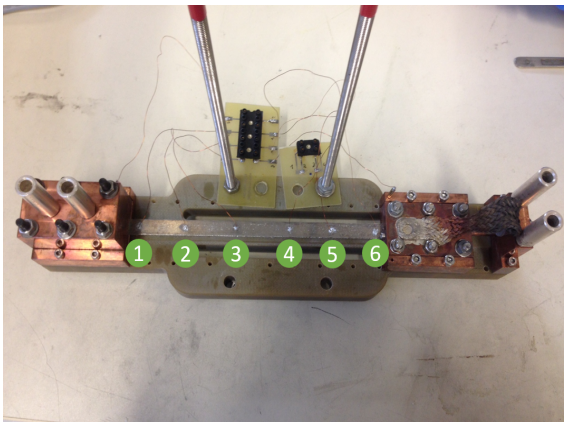

Figure 5.9: Sample-holder used to characterize the Fastgrid conductor. Six voltage taps are soldered with Indium-Tin soldering on the tape side of the conductor.

The current leads are connected to the AC circuit introduced in subsection 3.1.1.3 and presented in figure 3.6. The voltage V_{source} is set to 30 V and the switch S is on for 50 ms. Twenty tests are carried out at 77 K with R_{fault} varying between 0 mΩ and 42 mΩ (i.e. a prospective current varying between 650 A and 7000 A). Eighteen tests are carried out at 65 K with R_{fault} varying between 0 mΩ and 30 mΩ (i.e. a prospective current varying between 900 A and 7000 A). Two tests realized at 65 K are presented, one in hot-spot regime and the other one in limitation regime.

The reader may have noted that with $V_{source} = 30$ V and a conductor length equals to 20 cm, the electric field withstood by the sample should be 150 V/m which would lead to a higher temperature than 400 K in limitation regime. The design of the Fastgrid conductor was realized with a maximum prospective current equals $20I_n$, with the grid rated current $I_n = 700$ A. While with the experimental set-up, the maximum prospective

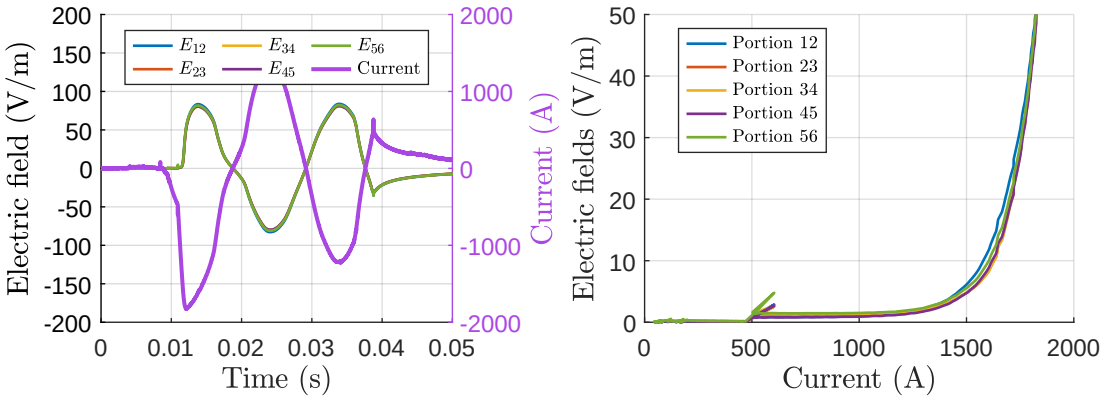

(a) (b)

Figure 5.10: Results obtained before the series of forty tests at 77 K for 30 ms with $V_{source} = 16$ V (a) electric fields as a function of time and (b) electric fields as a function of the first current increase.

current possible to reach is 7000 A, as a consequence, it is possible to operate with a higher theoretical electric field because it will never operate with a prospective current of $20I_n$.

5.1.3.2 Criterion to asses the robustness against repetitive faults

A criterion is proposed to assess if the repetitive tests (here, forty) did not damage the conductor. The method is similar to the determination of a critical current by pulse measurement. Not to damage the sample by changing the set-up, the same set-up is used. The idea is to carry out the measure before and after the series of tests. It consists of determining the current giving an electric field of 10 V/m. For this measure, the parameters of the set-up are given in Table 5.1. A criterion of 10 V/m was chosen instead of E_c equals to 1 µV/cm due to the inductive component of the electric fields.

V_{source} (V)	Δt (ms)	R_{fault} Ω	T_{bath} (K)
16	40	0	77

Table 5.1: Parameters of the set-up to determine the current giving an electric field of 10 V/m.

The results of the measurements performed before the sample characterization are given in figure 5.10a and after in figure 5.11a. These data are used to plot the electric fields against the first increase of current (see figures 5.10b and 5.10b). The current giving an electric field of 10 V/m over each portion is given in Table 5.2. The currents are very similar before and after the characterization. A very slight decrease is observed but it is not significant considering the precision of the current measurement (2 %) and the fact that the two measurements were not carried out on the same day. The ambient pressure may not have the same effect on the liquid nitrogen bath temperature.

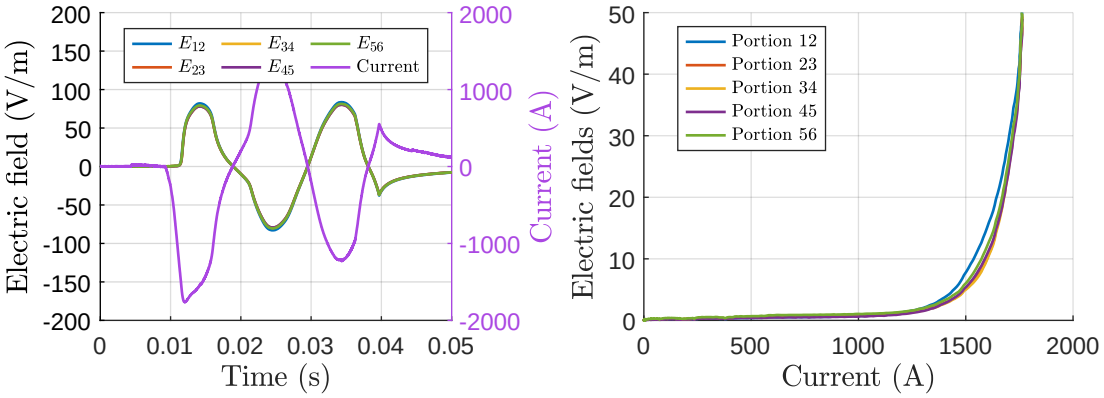

(a) (b)

Figure 5.11: Results obtained after the series of forty tests at 77 K for 30 ms with $V_{source} = 16$ V (a) electric fields as a function of time and (b) electric fields as a function of the first current increase.

Measurements	Portion 1-2	Portion 2-3	Portion 3-4	Portion 4-5	Portion 5-6
Before	1640 (A)	1680 (A)	1680 (A)	1670 (A)	1660 (A)
After	1600 (A)	1640 (A)	1670 (A)	1630 (A)	1630 (A)

Table 5.2: Currents giving an electric field equals to 10 V/m before and after the sample characterization.

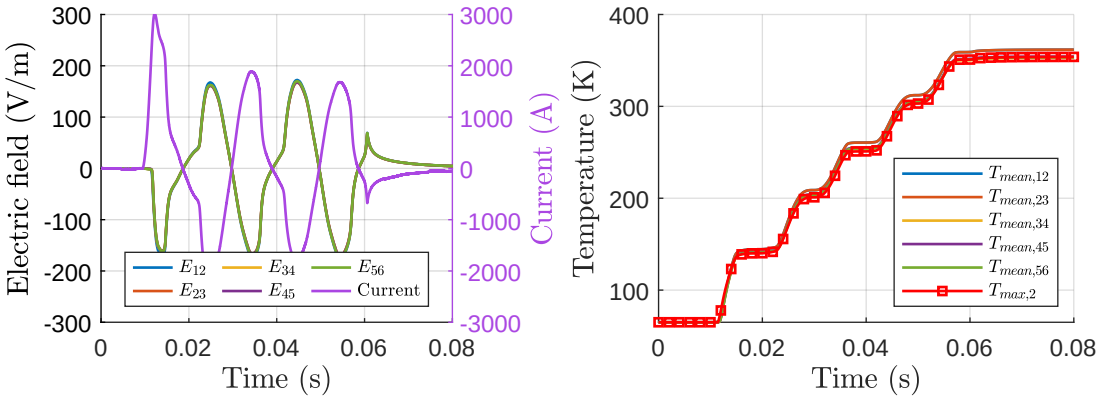

(a) (b)

Figure 5.12: (a) Electric fields as a function of time and (b) temperatures as a function of time. Results for I_{pros}=7000 A obtained on the Fastgrid conductor in operation at 65 K for 50 ms.

This criterion assessing the robustness of the sample against repetitive faults is not perfect. A real critical current measurement would be more appropriate but if a degradation occurs, this is noted.

5.1.3.3 Results

Limitation regime (I_{pros}=7000 A at 65 K) The resistance R_{fault} is set to 0 Ω and the prospective current is 7000 A. Figure 5.12a shows that the electric fields are highly similar on the overall sample, which is typical in limitation regime. They reach a rms value around 120 V/m. The temperature at the end of the test is around 350 K (see figure 5.12b). However, for this electric field the temperature should be very close to 400 K. A current distortion occurs for high prospective currents due to the inrush current of the transformer used in this set-up. This reduces the energy dissipated in the sample and as a consequence its temperature.

The electric field withstood by the sample is close to the value used for the design (130 V/m) and it did not degrade the sample. This test validates the design of the Fastgrid conductor for an operation with an electric field of 120 V/m for 50 ms in limitation regime.

Hot-spot regime (I_{pros}=1450 A at 65 K) The resistance R_{fault} is set to 17 mΩ and the prospective current is 1450 A, in the range of the critical current variations at 65 K. The electric fields over the sample shown in figure 5.13a are very inhomogeneous. For example, the electric field of the portion 1-2 reaches an instantaneous value of 100 V/m while the electric field of portion 3-4 remains mainly inductive. This behavior is typical of what is observed in hot-spot regime (see chapter 2). The maximum temperature reaches 300 K (see figure 5.13b). In the design, the maximum temperature can reach until 400 K (see figure 5.8). This small temperature may be related to the sample length as it will be

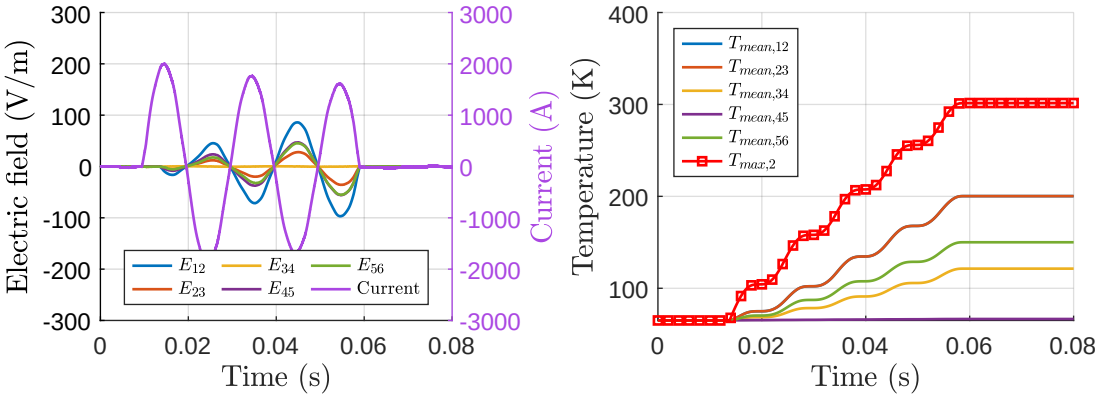

(a) (b)

Figure 5.13: (a) Electric fields as a function of time and (b) temperatures as a function of time. Results for I_{pros}=1450 A obtained on the Fastgrid conductor in operation at 65 K for 50 ms.

introduced in chapter 6 and to the non-consideration of the heat transfer with the bath. This test confirms the operation of the Fastgrid conductor in hot-spot regime at 65 K.

Maximum temperature as a function of the prospective current The maximum temperature is computed for all the tests carried out at 77 K and 65 K. Figure 5.14 shows that the maximum temperature follows the evolution predicted by the simulation with a temperature elevation occurring in hot-spot regime. The hot-spot regime is clearly observed at 65 K and barely observed at 77 K. The impact of the bath temperature was introduced in subsection 2.4.3.1 and the analytic expression of the temperature elevation in hot-spot regime, given by 2.23, shows that the temperature elevation is four times higher at 65 K than at 77 K due to the doubling of the critical current. The observation of the hot-spot regime is better observed on this sample than on the sample characterized in chapter 3. The temperature decreases for high prospective currents while in simulation, the opposite behavior is occurring. This comes from current distortions occurring for high-prospective currents in the set-up due to the inrush current of the transformer.

In the range where the Fastgrid conductor was tested, the temperature did not exceed 400 K. The design is then validated on a small length sample. The Fastgrid conductor respects the specifications with a safe operation at 65 K (with a critical current doubled) and with an electric field of 120 V/m for 50 ms.

5.1.4 Towards an industrial manufacturing process

CNRS collaborated closely with THEVA when the company shifted from the lab process to the industrial process to realize the bonding of the tape with the Hastelloy® C276 shunt.

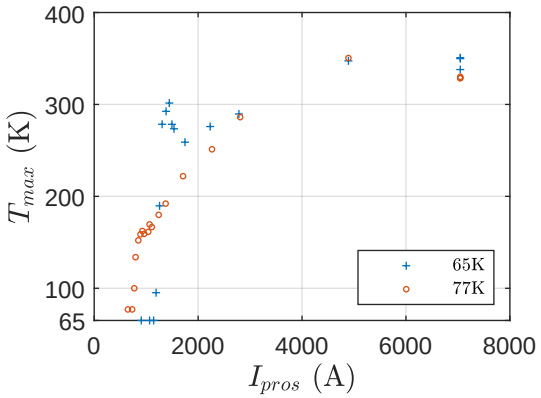

Figure 5.14: Maximum temperature as a function of the prospective current obtained at 77 K (round red circles) and at 65 K (blue crosses).

5.1.4.1 Continuous degradation of the conductor performances

Several samples made with the industrial manufacturing process of THEVA were tested coming from batches produced during different times of the project and they all showed a similar continuous degradation mechanism.

Experimental details One example is detailed using the same set-up described in subsection 5.1.3 with the parameters given in Table 5.3. The sample is five times successively connected to the AC source. The criterion of safe operation of the sample described in subsection 5.1.3.2 (i.e. current giving an electric field of 10 V/m) is computed for each test.

V_{source} (V)	Δt (ms)	R_{fault} Ω	T_{bath} (K)
25	50	0	69

Table 5.3: Parameters of the set-up used to characterize the Fastgrid conductor made with the industrial manufacturing process.

Experimental results Figure 5.15 shows that the electric fields are inhomogeneous along the length of the sample while the prospective current is 5800 A which should ensure a homogeneous quench. The temperature of the sample is around 300 K. Figure 5.16 shows that the current giving an electric field of 10 V/m is decreasing as a function of the test number, except in portion 1-2 where it remains constant. This reveals that the tests are damaging the sample. Some investigations are carried out to determine the origin of this degradation of the performances. The sample does not seem having been overheated and the computed temperature is way below 400 K.

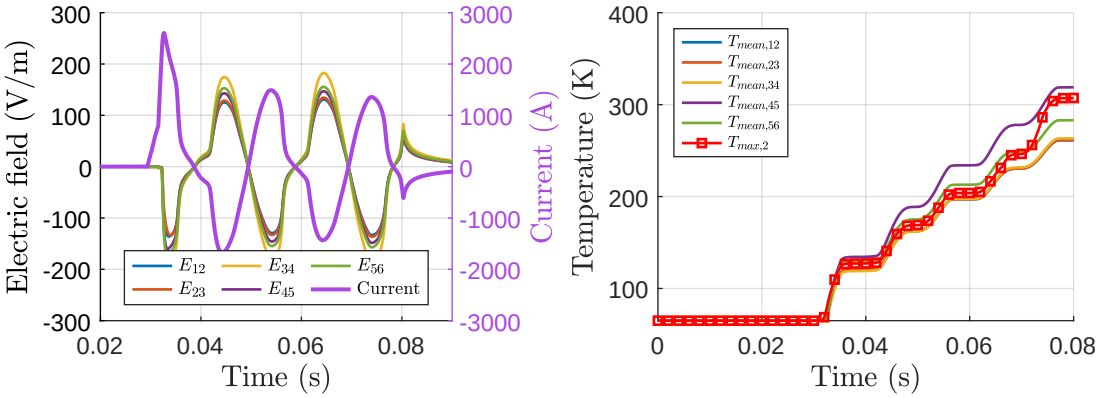

(a) (b)

Figure 5.15: (a) Electric fields as a function of time and (b) temperatures as a function of time. Results obtained during the first test of the series of five test.

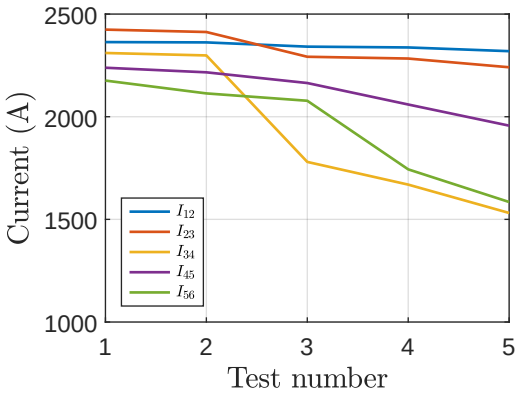

Figure 5.16: Evolution of the current giving an electric field of 10 V/m on the five portions of the sample of the conductor produced with the industrial manufacturing process of THEVA as a function of the test number.

5.1.4.2 Investigations on the conductor degradation

Analysis of the solder A sample from the industrial process is delaminated in purpose (see figure 5.17). The same process is done on a sample produced with the lab process. The surface of each piece is analyzed thanks to Scanning Electron Microscopy (SEM) to determine where the delamination occurred (see figure 5.18). An uniform color is observed on each surface of the sample made with the lab process (1 & 2). The compound on surface 1 is Hastelloy® C276 and it is MgO on surface 2. The bonding is strong because the delamination did not occur between silver and tin. However, two colors are distinguished on each surface of the sample from the industrial process (3 & 4). The compounds on surface 4 are tin (light color) and MgO (dark color) and they are silver (light color) and Hastelloy® C276 (bright color) on surface 3. The bonding made with the industrial process is weak and tin does not cover the whole interface between the tape and the shunt.

Figure 5.17: Fastgrid conductor manufactured with the industrial process. The sample was delaminated in purpose.

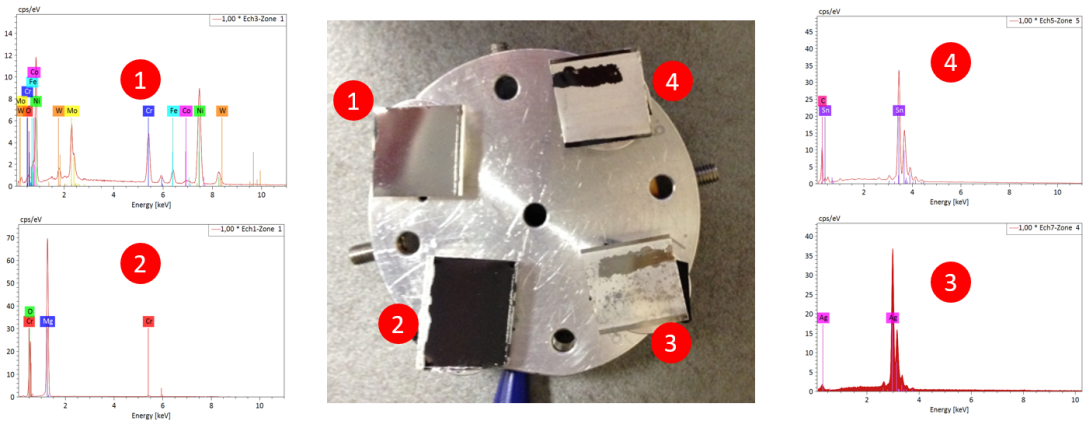

Figure 5.18: EDX analysis using a SEM imaging.

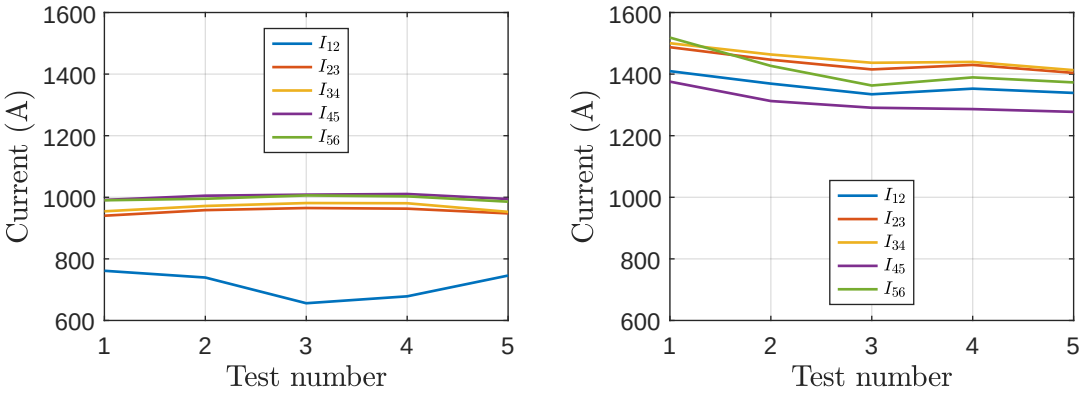

(a) 81 K

(b) 77 K

Figure 5.19: Evolution of the currents giving an electric field of 10 V/m on the five portions of the sample of the bare THEVA tape at (a) 81 K and (b) 77 K.

Analysis of the 2G HTS tape operation The bare tape from THEVA is characterized to observe if the degradation comes from the manufacturing process or from the tape itself. The same set-up described in subsection 5.1.3 is used with the parameters given in Table 5.4. Five fault tests are successively applied on one sample at 81 K and on another sample at 77 K. Both samples are from the same batch.

V_{source} (V)	Δt (ms)	R_{fault} (Ω)
20	30	0

Table 5.4: Parameters of the set-up used to characterize the bare THEVA tape.

The criterion success, introduced in subsection 5.1.3.2, shows that a similar degradation of the performances is observed at 77 K while it did not occur at 81 K (see figure 5.19). The only difference between the operation at 81 K and 77 K is the peak value of the current. Indeed, figure 5.20 shows that the peak of current is 1010 A at 81 K while it is 1520 A at 77 K. This highlights the importance of the peak of current in this mechanism of degradation.

Lack of silver on the lateral sides When the peak of current in a limitation test is reached, current sharing occurs and the current flows through the lateral sides of the tape. This is the reason why the influence of a possible lack of silver on the lateral sides was investigated in section 4.4 but it showed that it does not significantly impact the safe operation of the tape.

Despite the efforts to understand how the degradation mechanism is working, no clear answer was obtained. However, it is possible to say that the degradation mechanism comes from the tape itself and not from the act of soldering the tape with the shunt. In the case

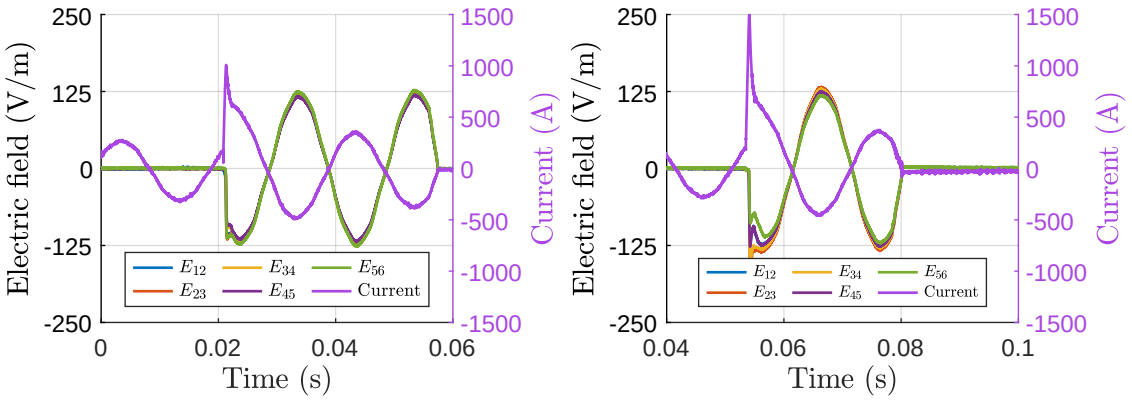

(a) 81 K (b) 77 K

Figure 5.20: Electric fields as a function of the time obtained for the first test of the series of five tests realized at (a) 81 K and (b) 77 K.

of the conductor, when the bonding is well realized, the addition of a conductive layer on the top of the tape enables the safe operation but if the bonding is weak, the degradation mechanism still occurs. Moreover, the influence of the peak of current was highlighted with the absence of degradation at 81 K. The partners from IEE and STUBA in Bratislava are also investigating this phenomenon [106].

5.1.5 Assessment of the cost-effectiveness

The cost improvement is assessed compared to the results obtained in the previous European Project before Fastgrid, the Eccoflow project [80]. The conductor developed in this project withstood 50 V/m for 50 ms with a coefficient C_{sc} having a value similar to its current value. The Fastgrid conductor tested in subsection 5.1.3.3 shows:

- an electric field higher by a factor 2.4
- a safe operation with a critical current 4 times higher (operation at 65 K and the doubling of the rated I_c at 77 K of commercial THEVA tapes)

The sum of these contributions leads to a cost division of the conductor by a factor of 10 compared with the Eccoflow project. However, the expression (5.1) does not consider neither the cost of the Hastelloy® C276 shunt nor the bonding of the shunt with the tape. It is reasonable to estimate that the cost reduction remains significant even including the cost of the shunt.

Even if the architecture of the conductor appears simple, the bonding of a Hastelloy® C276 shunt to a commercial tape from THEVA is challenging due to the high thermal constraints when dealing with superconducting tapes. With an efficient manufacturing process, the Fastgrid conductor will answer well to the challenge highlighted in chapter

1 of the PhD work: the development of a cost-effective conductor. There are still ways to further improve the Fastgrid conductor to reach a higher electric field through the increase of the tape resistivity itself (thinner stabilizer layer, degradation of the electrical conductivity of the stabilizer, ...) or the use of a more resistive shunt as Inconel.

5.2 Characterization of two alternative architectures developed in Fastgrid

The Fastgrid project is not only the development of the "Fastgrid conductor". Alternative architectures of future conductors, at a lower level of industrial maturation, were developed. Among them, two architectures were studied during this PhD work.

5.2.1 2G HTS tape with a Current Flow Diverter

This work was entirely carried out in a collaboration with Pedro Barusco from ICMAB in Barcelona in the framework of the Fastgrid project.

In subsection 2.4.3.2, it was introduced that one way to mitigate the hot-spot regime is the acceleration of the NZPV and this can be realized with the Current Flow Diverter. However, the manufacturing of long lengths of tapes showing a CFD is not trivial. During Fastgrid, ICMAB, OXOLUTIA and EPM worked closely on this topic. P. Barusco, from ICMAB, mainly focused his PhD work on the industrialization of the realization of the highly resistive interface. Grenoble contributed to the development of the CFD with the characterization of one structure.

5.2.1.1 Experimental details

Sample To prepare the sample with a CFD, P. Barusco follows the procedure developed by EPM. On the top stabilizer layer, the edges of the commercial tape are masked with Kapton® and the silver on the remaining part of the width is etched with a Hydrogen peroxide solution. The Kapton® is removed and the sample is exposed to ambient air for some hours. P. Barusco chose to re-sputter a 1 µm thick copper layer instead of silver on the top of the tape. The sample is inserted in a sample-holder similar to the one shown in figure 3.12 where the distance between the current leads is 65 mm (see figure 5.21). One voltage tap is present on each current lead to measure the voltage. A magnet is positioned on the middle of the sample to locally decrease the critical current and to first initiate a thermal runaway on this position.

Test bench The set-up described in subsection 3.3.1 is used to characterize the tape. The fault current set-up is the AC circuit with the parameters given in Table 5.5 at a liquid nitrogen bath temperature equals to 77 K. Nevertheless, the synchronization between the electrical measurements and the optical observation was not effective at the time of this characterization. As a consequence, the time given for each one of these results is not the same.

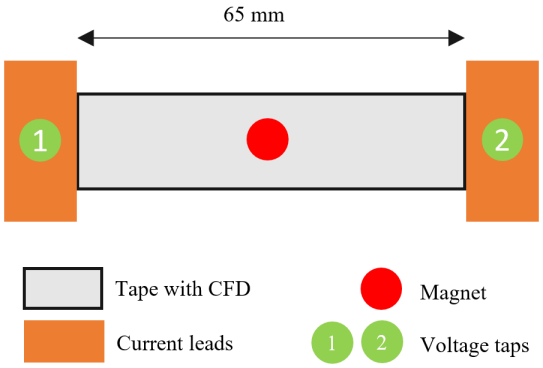

Figure 5.21: Scheme of the tape with a CFD tested. One voltage tap is positioned on each current lead.

V_{source} (V)	Δt (ms)	R_{fault} (Ω)	T_{bath} (K)
6.5	50	0	77

Table 5.5: Parameters of the set-up used to characterize the CFD sample.

5.2.1.2 Experimental results

Figure 5.22 shows the electric field and the current as a function of the time and the images are shown in figure 5.23. The time given on the pictures is the time after the apparition of the first bubble, appearing in the center of the sample at the position of the magnet. At 0.32 ms, the bubble generation occurs on the edges of the sample while the center portion of the width remains mainly without bubble. The propagation in the center portion of the width is observed at 1.27 ms. These images clearly highlight the existence of the CFD effect with the difference of dissipation between the edges of the tape and the center of the width.

The size of the dissipation column as a function of time is recognized using the image processing described in subsection 4.2.2 (see figure 5.24). The complete dissipation of the sample is established in 5 ms. The slight decrease of the size of the dissipation column at the end of the test comes from the image processing. The NZPV is in the range of 12 m/s. This value has to be carefully considered because during this test, the prospective current was high (I_{pros} = 1500 A), with the possibility to initiate a thermal runaway everywhere. For this reason, the NZPV is not compared with existing values. A prospective current slightly overstepping the lowest critical current would have been more interesting. This test highlights the existence of the CFD effect with a very inhomogeneous dissipation over the width of the sample, especially focused on the edges where the current can transfer from the superconducting layer to the stabilizer. A way to quantitatively qualify the CFD effect with the high-speed imaging system would have been to use the DC circuit with the same parameters given in Table 4.1 leading to a prospective current in the range of

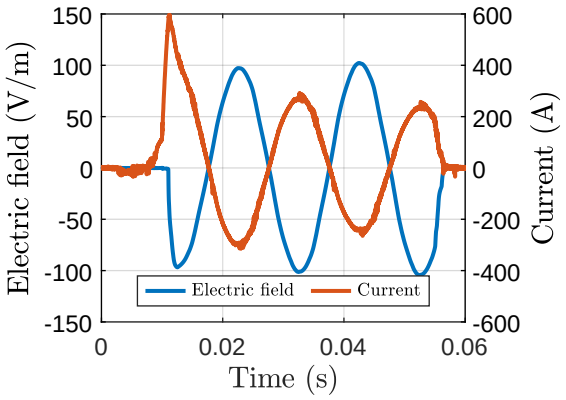

Figure 5.22: Electric field and current as a function of time measured on the CFD sample manufactured by ICMAB.

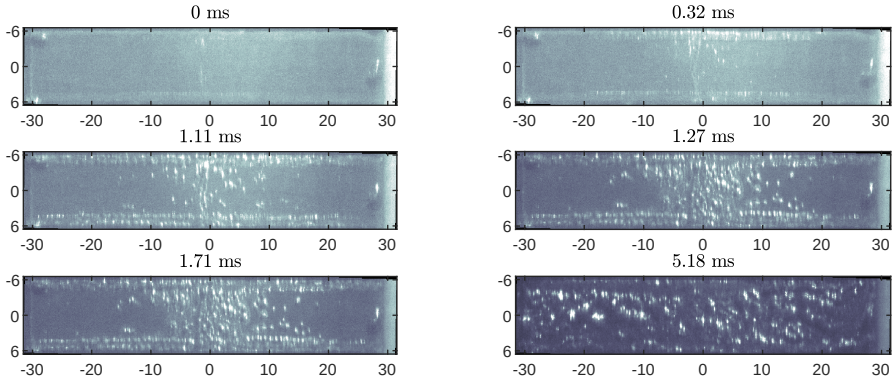

Figure 5.23: Images of the sample showing a CFD recorded with the high-speed camera. The time given is the time after the first picture.

the I_c of the weakest portion of the sample and compared the evolution of the size of the dissipative column with the data given in figure 4.10.

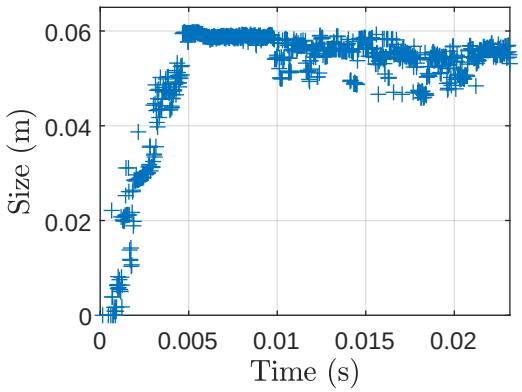

Figure 5.24: Size of the bubble generation spot at the middle of the width of the sample as a function of time on the CFD sample.

5.2.1.3 Assessment of the cost-effectiveness

In principle, tapes with a CFD effect could have a NZPV which can be two orders of magnitude higher than regular commercial 2G HTS tapes [103]. With the same simulation framework developed in subsection 5.1.1.2, figure 5.25 presents the maximum temperature of the conductor over its operation range. The CFD effect can be modeled in a simple way by an enhanced heat conductivity of the tape as it is done in [57]. In such case, multiplying the heat conductivity by a factor of 100 makes it possible to lower the shunt thickness to 400 µm without exceeding a maximum temperature of 400 K in hot-spot regime.

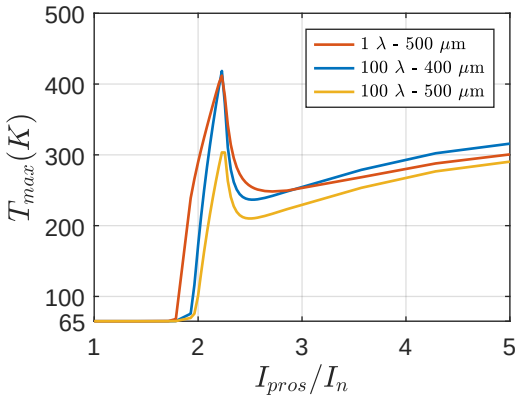

Figure 5.25: Maximum temperature as a function of the prospective current normalized by the rated current of the circuit with several combinations of shunt thicknesses coupled with enhanced heat conductivity.

The resistivity of the CFD sample tested in subsection 5.2.1.2 is very similar to the resistivity of the Fastgrid conductor. Indeed, the addition of the CFD to a commercial tape increases its resistivity. As a consequence, the performances in limitation regime are very similar. In hot-spot regime, the addition of the CFD lowers the thickness of the shunt to solder to a commercial 2G HTS tape. However, it is not sufficient to completely suppress this shunt which would significantly impact the cost of the conductor. One benefit could be an easier winding of the conductor to realize the module of a R-SFCL due to a lower conductor thickness.

5.2.2 Sapphire-Based R-SFCL Conductor

This work was entirely carried out in collaboration with Amir Saraf from Tel-Aviv University in the framework of the FASTGRID project.

In subsection 2.4.3.2, the Sapphire-Based 2G HTS conductor was introduced as a way to mitigate the hot-spot regime. The conductor tested here shows a critical current small enough (around 40 A at 77 K) not to risk any damage in hot-spot regime (2.23). The large interest of the conductor developed by Tel-Aviv University is the possibility to withstand very high electric field due to its thin gold stabilizer layer.

5.2.2.1 Experimental details

Sample The superconductivity group of Tel-Aviv University (TAU), in collaboration with ICMAB, achieved the epitaxial growth of the superconducting layer on a long length substrate of sapphire not requiring any polishing through the use of the edge-defined process [85][107]. This is a step forward in the development of Sapphire-Based conductor because the polishing of the sapphire generally required to grow the REBCO layer is a very expensive process. The YBCO layer grows on this substrate after depositing an Yttrium stabilized Zirconia buffer layer. The HTS layer is protected with a very thin 100 nm thick gold layer. Figure 5.26 shows a picture where the substrate and Sapphire-Based SFCL conductor are presented. A sample is tested in fault condition in a sample-holder where the inner length between the current leads is 50 mm. The nature of the material makes it very brittle and the high rugosity of the sample surface makes the contacts challenging to realize. In order to minimize the damage, the contacts are lightly tightened at ambient temperature and sufficiently tightened at liquid nitrogen temperature. One voltage tap is connected to each current lead to measure the voltage on the sample.

Test bench The sample is connected to the AC circuit described in subsection 3.1.1.3 but without the transformer to have more voltage available. The voltage is 90 V and the switch is on for 50 ms. The sample is positioned in the cryostat shown in figure 3.8b where the bath temperature is 65 K to increase the critical current of the sample.

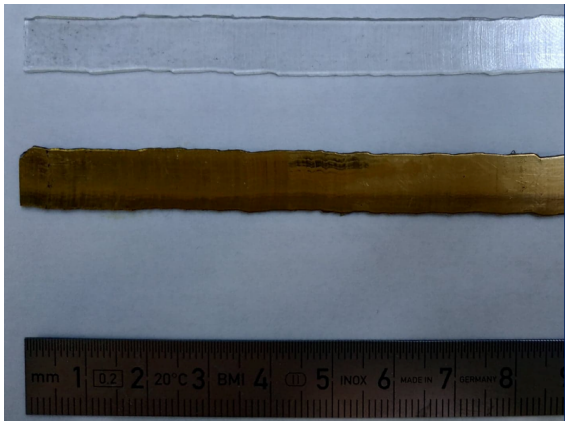

Figure 5.26: Picture of the Sapphire substrate (top) and of the Sapphire-Based SFCL conductor (bottom).

5.2.2.2 Experimental results

Figure 5.28 shows that the electric field withstood by the sample is very high with a maximum instantaneous value of 1500 V/m. Figure 5.28 shows that the electric field frankly increases when the current exceeds 123 A in operation at 65 K.

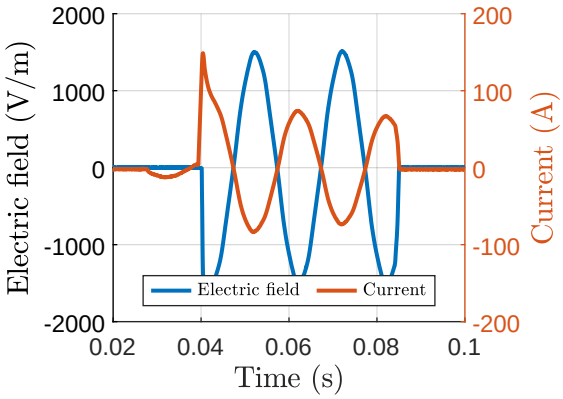

Figure 5.27: Electric field and current as a function of time measured on the Sapphire-Based SFCL conductor produced by TAU at 65 K.

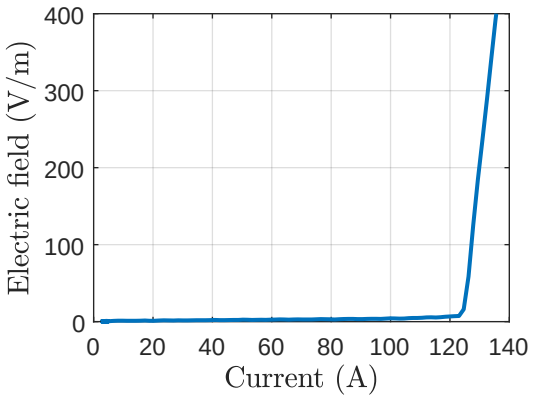

Figure 5.28: Electric field as a function of the current during its first increase when the fault occurs.

Using the expression introduced in subsection 3.2.3, the mean temperature is computed assuming that the conductor is entirely made with sapphire ($c_{p,v}$ of sapphire is given in figure B.2b in Appendix B). The temperature, shown in figure 5.29, is far from 400 K which means that the electric field withstood by the sample could be higher not risking any damage due to excessive heating.

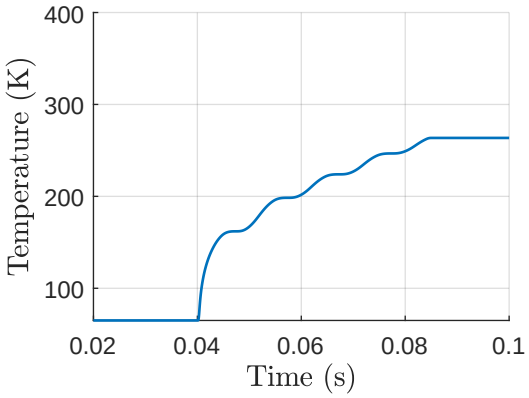

Figure 5.29: Mean temperature of the sample as a function of time.

5.2.2.3 Assessment of the cost-effectiveness

The Sapphire-Based SFCL conductor, manufactured by TAU, shows an outstanding electric field. It reached a rms value of 1060 V/m for 50 ms and this value could be, at least multiplied, by a factor of 1.5 not risking overheating. The electric field is about ten times higher than the electric field of the Fastgrid conductor.

However, the critical current remains very low. The critical current per unit width is about 50 A at 77 K, about ten times smaller than the one of the Fastgrid conductor. All the benefits obtained with the very high electric field are mitigated by the poor critical current. It is not meaningful to compare the cost of the Sapphire-Based R-SFCL conductor with the Fastgrid conductor because the level of industrial maturation is very different. It is possible to be hopeful for the future. The manufacturers made large progresses to increase their I_c in the recent years. This could also occur for this technology. In that case, it would become a total game changer. The shape of the R-SFCL should be however redesigned due to the impossible winding of this conductor.

5.3 Towards other conductors with high performances

5.3.1 Conceptual designs in limitation regime

The analytic expression of the electric field of a conductor is given by (5.2), expressed from (2.24). This expression highlights that adopting solutions similar to the Fastgrid conductor, the ultimate electric field is reached if the resistivity of the conductor is equal to the resistivity of pure Hastelloy® C276. With (5.2), it is 170 V/m considering $c_{p,v}$ the heat capacity per volume unit of the Hastelloy® C276 at ambient temperature ($3.7 * 10^6$ J/Km^3), ΔT a temperature elevation of 330 K, a clearing fault time Δt of 50 ms and ρ the resistivity of the Hastelloy® C276 at ambient temperature ($1.25 * 10^{-6}$ Ωm). As a consequence, to reach higher performances, new concepts should be developed.

$$E_{sc} = \sqrt{\frac{c_{p,v}\rho\Delta T}{\Delta t}} \tag{5.2}$$

If a conductor refers to a tape bonded to a shunt, electrically in parallel and thermally connected, from the application of an energy balance with an isothermal cross-section, E_{tape} the electric field withstood by the tape is expressed by (5.3) with e the thickness, $c_{p,v}$ the heat capacity per volume unit, l the length, w the width and ρ the resistivity. The index *tape* and *shunt* refer to the dimensions or properties of the tape and shunt, respectively. The details of the this expression are given in appendix C.

$$E_{tape}^2\Delta t = \int_{T_c}^{T_{max}} \frac{e_{tape}c_{p,v}^{tape}(T) + \frac{l_{shunt}}{l_{tape}}\frac{w_{shunt}}{w_{tape}}e_{shunt}c_{p,v}^{shunt}(T)}{\frac{e_{tape}}{\rho_{tape}(T)} + \frac{e_{shunt}}{\rho_{shunt}(T)}\frac{w_{shunt}}{w_{tape}}\frac{l_{tape}}{l_{shunt}}}dT \tag{5.3}$$

From this expression, P. Tixador in [108] proposes several ways to increase the electric field through:

- An increase of the ratio $\frac{l_{shunt}}{l_{tape}}$
- The use of a tape and a shunt with high electrical resistivities

First concept: the use of an insulated shunt modifies (5.3) in (5.4) assuming an identical length and width between the tape and the shunt. The electric field increase is possible through the increase of the conductor thickness assuming that the material used as an insulated shunt shows a high thermal conductivity. This concept is different from the Sapphire-Based R-SFCL conductor from TAU because here the idea is to use the shunt as a tool to drain the heat from the tape while the conductor from TAU is based on a high tape resistivity.

$$E_{tape}^2\Delta t = \int_{T_c}^{T_{max}} \frac{e_{tape}c_{p,v}^{tape}(T) + e_{shunt}c_{p,v}^{shunt}(T)}{\frac{e_{tape}}{\rho_{tape}(T)}}dT \tag{5.4}$$

Second concept: the increase of the ratio $\frac{l_{shunt}}{l_{tape}}$ thanks to the bonding of a corrugated shunt in Hastelloy® C276 on the tape. Expression (5.3) becomes (5.5).

$$E_{tape}^2\Delta t = \int_{T_c}^{T_{max}} \frac{e_{tape}c_{p,v}^{tape}(T) + \frac{l_{shunt}}{l_{tape}}e_{shunt}c_{p,v}^{shunt}(T)}{\frac{e_{tape}}{\rho_{tape}(T)} + \frac{e_{shunt}}{\rho_{shunt}(T)}\frac{l_{tape}}{l_{shunt}}}dT \tag{5.5}$$

5.3.2 2G HTS tape associated to an insulated shunt

The work described in this section was achieved jointly with Pedro Barusco from ICMAB in Barcelona, in the framework of the Fastgrid project.

5.3.2.1 Material and structure

The use of an insulated shunt was already explored in the past. Authors in [109] used Aluminium nitride while reference [110] proposed to study various composites showing a high heat capacity. Here, the structure is a tape associated to an insulated shunt showing identical lengths and widths. In addition to the absence of electrical conductivity, the shunt has to present a very high thermal conductivity (hypothesis of homogeneous temperature in the cross-section) and withstand thermal variations from the liquid nitrogen temperature to several hundreds of degrees.

Trials were first realized with copper covered by several µm thick parylene layer as an insulating layer but it did not work experimentally due to the destruction of the parylene layer when the tape was associated to this shunt. Sapphire is an electrical insulator (10^{14} Ωcm [111]) and shows a high thermal conductivity at low temperature (see figure B.3b in appendix B). The mechanical expansion differences between the sapphire and the tape are only considered experimentally through the development of dedicated current leads. To ensure good thermal contacts at low temperatures, Apiezon N grease is used between the shunt and the tape. To increase the surface of contact, one shunt is positioned on the top and another one on the bottom of the tape. The structure studied is presented in figure 5.30.

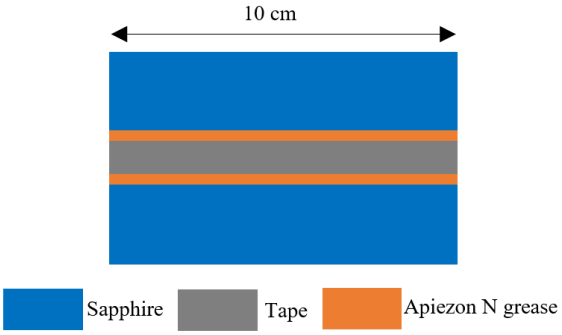

Figure 5.30: Scheme of the cross-section on the longitudinal direction of the conductor using two insulated shunts.

5.3.2.2 Simulation of the structure

With the expression (5.4), it is possible to quantify the benefits of an increase of the conductor thickness on the possible maximum electric field assuming a homogeneous cross-section. However, this expression does not consider the thermal resistance of the Apiezon N grease. Modeling effort is required to estimate the importance of this parameter.

Modeling of the conductor

Geometry and material The structure described in figure 5.30 is modeled in 2D on COMSOL 5.4. The width (12 mm) is not represented and the length is 10 cm. Each sapphire piece is 1 mm thick like the thickness of the actual pieces used in experiment. The tape thickness is 105 µm and there is no need to neither consider the superconducting properties of the tape nor its layered structure because only the heat diffusion is studied in limitation regime. The element modeling the tape presents the resistivity of the SuperOx tape given, in figure B.1b in appendix B and the thermal properties of the Hastelloy® C276 given in [79]. The thermal properties of sapphire come from [78]. The heat capacity per volume unit of the Apiezon N grease is given in [112], its mass per volume unit and its heat conductivity are given by a linear regression done with the data from [113][114] .

Three modules of Comsol are used : electrical circuit, electric currents and heat transfer in solids.

COMSOL Multiphysics modules In the electrical problem, only the tape can conduct the current which is injected through each extremity of the tape connected to the electrical circuit described in figure 4.14 where $L_{circuit}$ is 5 µH and $R_{circuit}$ is set to observe the conductor operation in limitation regime (5.6) with $I_n = 700$ A. In the thermal problem, all the layers are considered, the tape is the heating source.

$$R_{circuit} = \frac{V_{circuit}}{20 I_n} \tag{5.6}$$

The thickness of the Apiezon layers and the voltage over the structure are the parameters of the study. The maximum temperature of the structure should not exceed 400 K. The conductor behavior is simulated for 50 ms.

Simulation results Figure 5.31 shows that the thickness of the Apiezon N grease as to be as small as possible to reach a high electric field without exceeding a maximum temperature of 400 K. This result allows to characterize this conductor in experiment due to the possibility to realize a small thickness of Apiezon N grease, in the range of a few micrometers. If the results demonstrated the need of a lower thickness, the experiment would have not been tried.

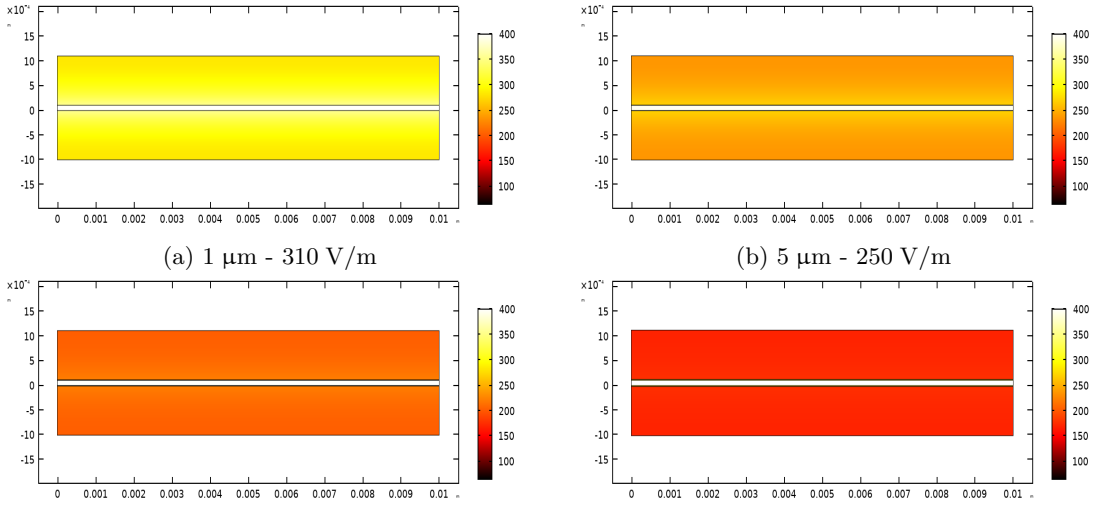

(a) 1 µm - 310 V/m

(b) 5 µm - 250 V/m

(c) 10 µm - 210 V/m

(d) 20 µm - 170 V/m

Figure 5.31: Temperature on the longitudinal cross-section of the tape with several combinations of Apiezon N grease thicknesses and electric fields. The tape (in white) is at 400 K at the end of the numerical simulation.

5.3.2.3 Characterization of the conductor

Experimental details Figure 5.32 shows a sample from SuperOx on its sample holder connected to the rest of the electrical circuit thanks to pressed contact. The inner length of tape between the two current leads is 15 cm. The 10 cm inner portion of the sample is covered by two 1 mm thick and 13 mm wide sapphire pieces. Apiezon N grease is used to have good thermal contacts and an external mechanical support is used to decrease its thickness pressing together the whole structure. The extremities of the sample are electroplated with copper to release the high mechanical stresses which would have occurred in the case of sapphire directly in contact with the current leads. This copper addition decreases the resistivity of the tape not to limit the current.

The sample is cooled in a liquid nitrogen bath at 77 K and connected to the DC electrical circuit described in subsection 3.1.1.4 with $R_{circuit}$ equals to 14 mΩ and $L_{circuit}$ equals to 3 µH. The switch is on for 25 ms. One sample is prepared with the afore mentioned procedure and another one follows this procedure but without using the sapphire pieces. The voltage is set to obtain a similar temperature between both samples at the end of the experiment. In such case, the voltage over the part of the tape covered with sapphire is 36 V while it is set to 25 V in the case where there is no sapphire.

Experimental results Figure 5.33 shows that the electric field in the case where the sapphire is present is 230 V/m while it is 170 V/m without sapphire. Both temperatures shown in figure 5.34 are about 500 K at the end of the test meaning that the sapphire pieces remove the heat from the tape because the electric field withstood by the sample

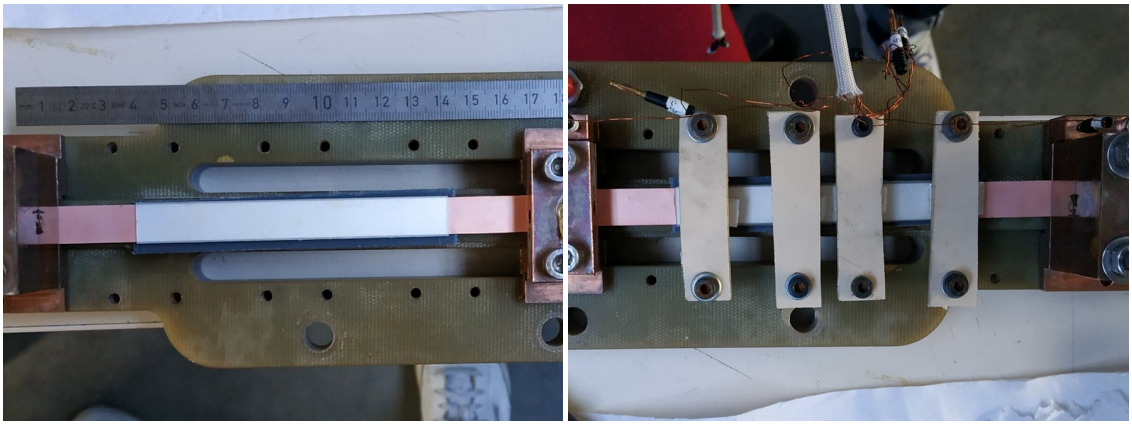

Figure 5.32: Sample-holder with the sample where 10 cm of the inner portion is covered by two pieces of sapphire (a) without and (b) with the support used to press together the sapphire pieces with the sample.

with the sapphire is higher than the sample without.

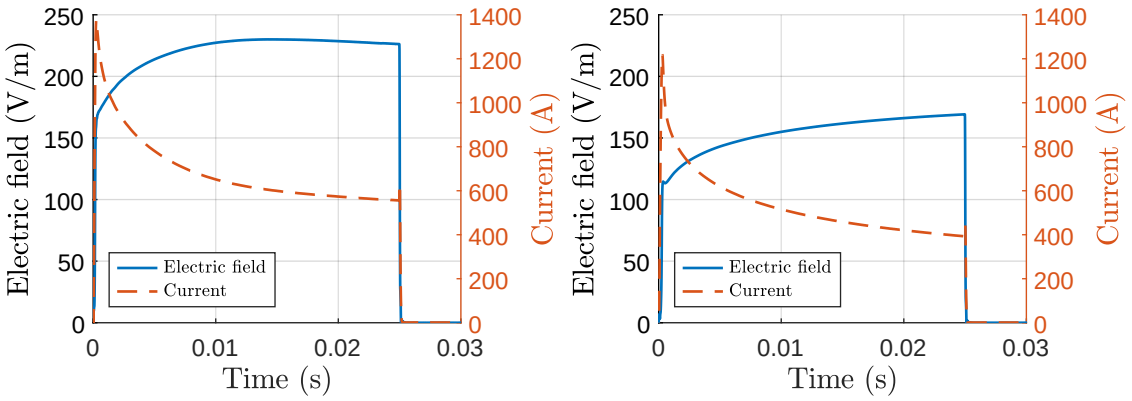

(a) With sapphire pieces.

(b) Without sapphire pieces.

Figure 5.33: Electric field and current as a function of time obtained with the innovative structure and with the witness sample.

It can also be noted that the temperature of the sample with sapphire pieces almost reaches a plateau at the end of the test (also observed in [109]). It may come from the presence of the Apiezon N grease acting as a thermal resistance and delaying the heat transfer from the sample to the sapphire. Then, when the heat propagates through the Apiezon N grease, an equilibrium may be reached between the heat produced by the Joule losses and the heat removed by the shunt.

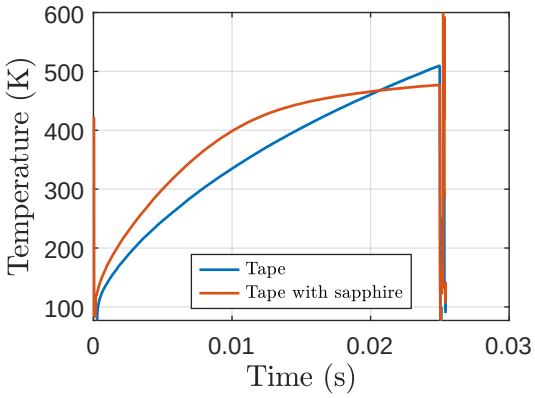

Figure 5.34: Temperature as a function of time obtained with the innovative structure and with the witness sample.

5.3.2.4 Assessment and further developments

It is rather difficult to propose an assessment of the cost-effectiveness of this structure. The study appears more as a proof of concept about the possibility to extract heat thanks to an insulated shunt with a high thermal conductivity. Indeed, the development of this structure as a conductor for R-SFCL appears almost impossible due to the high cost of the sapphire and the difficult realization of the structure on longer lengths. Investigations could be realized with other materials as alumina.

5.3.3 2G HTS tape associated to a metallic corrugated shunt

5.3.3.1 Structure and material

One other way to reach a higher electric field is to increase the ratio of the length of the shunt over the length of the tape. In such case, it is still important to have a highly resistive shunt. One concept presented by P. Tixador in [108] is to associate a metallic corrugated shunt in Hastelloy® C276 on each surface side of the tape. Figure 5.35 shows a scheme of the structure where the positions of the corrugations of both shunts are shifted with an angle of 180° to always present a large thickness to operate safely in hot-spot regime (see (2.23)) and it avoids mechanical stresses by placing the 2G HTS tape on the neutral fiber in wounding.

5.3.3.2 Simulation of the structure

Modeling of the conductor

Geometry The structure displayed in figure 5.35 is modeled in COMSOL 5.4 Multiphysics in two dimensions considering no variation in the width of the conductor. The number of free dimensions is decreased to simplify the study. It is considered that:

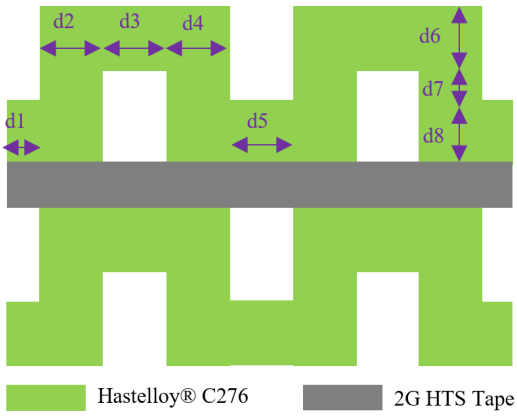

Figure 5.35: Scheme of the association of corrugated shunts with a HTS tape.

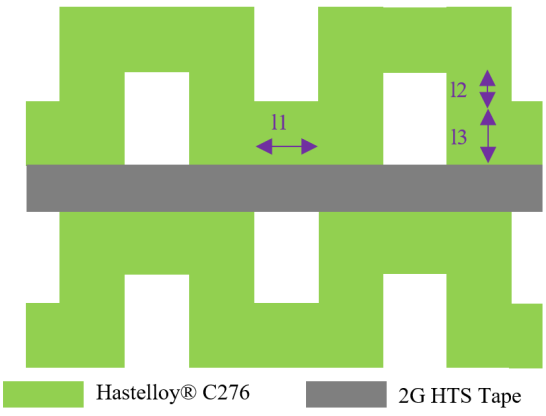

Figure 5.36: Scheme of the conductor presenting the dimensions to optimize.

- the shunt was originally a straight blade wounded to obtain the corrugations so $d_2 = d_4 = d_6 = d_8$
- the size of all corrugations are identical $2d_1 = d_3 = d_5$
- the smallest dimension is 100 µm to enable the manufacturing

It remains three dimensions presented in figure 5.36. The tape is 105 µm thick.

COMSOL Multiphysics modules In the thermal problem, all the elements can conduct the heat. The thermal properties of the Hastelloy® C276 given in [79] are attributed to the tape and the shunt.

The electrical problem is different depending on the regime of operation considered:

- Limitation regime - Similarly to subsection 5.3.2.2, neither the superconducting properties nor the layered structure of the tape are considered, it is a homogeneous element with the resistivity of the SuperOx tape (see figure B.1b in Appendix B). The shunt shows the resistivity of the Hastelloy® C276.
- Hot-spot regime - The layered structure as well as the superconducting properties are considered to observe the heat propagation in the longitudinal axis of the conductor. The model is very similar to the 3D model developed in subsection 4.3.1. A smaller I_c is defined in the center of the tape and the current is chosen to initiate a thermal runaway at this position.

The same electrical circuit described in subsection 5.3.2.2 is used. In limitation regime, the resistance $R_{circuit}$ is equal to the expression given by (5.6) while in hot-spot regime the resistance is set to obtain $I_c(65K) = 1400$ A. In the thermal problem, all the elements can conduct the current.

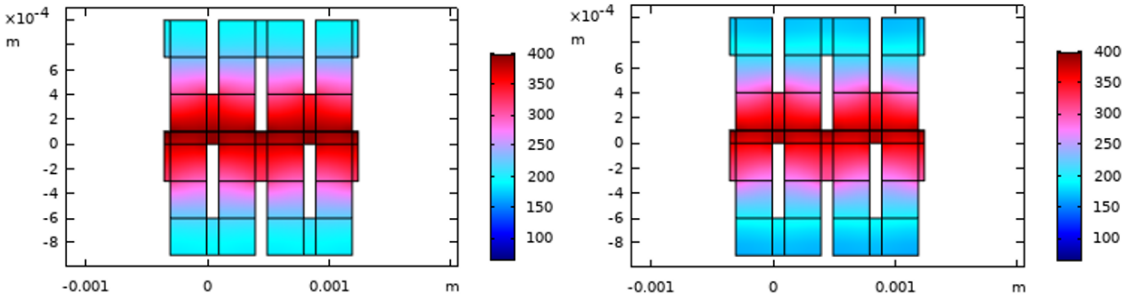

(a) Limitation regime

(b) Hot-spot regime

Figure 5.37: Temperature along the longitudinal axis of the conductor at the end of the simulation at 50 ms.

Simulation results A parametric analysis simulating the conductor operation for 50 ms with combinations of all parameters between [0.0001 m 0.0002 m 0.0003 m 0.0004 m] is realized, without formal optimization, to determine the dimensions giving the highest electric field without exceeding 400 K. The values $l_1 = 100$ µm, $l_2 = 300$ µm and $l_3 = 300$ µm gives the highest electric field equals to 190 V/m. Figure 5.37a shows that the temperature is highest close to the tape, where the resistivity is the lowest and then decreases on the shunt. The temperature gradient could be a problem due to different thermal expansions inside a same material. In hot-spot regime, figure 5.37b shows that the temperature is lower than 400 K ensuring a safe operation but the gradient of temperature is also elevate.

5.3.3.3 Assessment and further developments

The simulation results valid the possibility to increase the electric field with the increase of the ratio between the length of the tape and the shunt. The study was conducted with dimensions constraint and not optimized, it is likely possible to reach even higher electric field with an optimization. This concept appears very difficult to realize practically. First, two solders showing a different melting temperature should be used not to unsolder the first shunt while soldering the second one. In addition, no solder excess should occur to avoid the solder to overlap a corrugation and create a short-circuit. Second, the cost of the shunt would be expensive due to the realization of the corrugations. To finish, the gradient of temperature in the height of the conductor is a matter due to possible differential thermal expansions. This preliminary study is pessimistic on the interest of this conductor, further studies taking into account practical constraints are necessary.

5.4 Conclusion

This chapter presents the contribution of this PhD work to the development of advanced high performances conductors. It presented characterization results of a conductor with a high TRL as well as proofs of concept of advanced conductors.

The design of the Fastgrid conductor was validated on its all operation range. It appears as a very good comprise between high performances and simplicity of realization despite the fact that the manufacturing process to produce long lengths of this conductor experienced difficulties. This architecture could divide the cost of the conductor compared with its predecessor (Eccoflow) by a factor of 10. Ways to continue to increase the electric field still exist (diminution of the thickness of the stabilizer layer or the use of a stabilizer with degraded electrical conductivity) but with that kind of technology, the maximum electric field is limited to 170 V/m using Hastelloy® C276.

Alternative structures were studied during Fastgrid. The Sapphire-Based SFCL conductor developed by TAU showed an outstanding electric field in limitation (around 1000 V/m for 50 ms) due to its very thin stabilizer layer. With these performances, the quantity of conductor would be significantly decrease in a R-SFCL. Nevertheless, its critical current remains very low and it drastically mitigates the benefits just mentioned. To become a game changer, the critical current of this conductor should be significantly improved. The other structure characterized within Fastgrid focuses on the operation in hot-spot regime. In collaboration with ICMAB, the CFD effect was observed using the high-speed imaging system on a sample from ICMAB. The heat propagation appears very inhomogeneous in the width with a clear bubble generation on the edges.

Another way to reach a higher electric field is the use of an insulated shunt. It was experimentally proven that it can act as a heat sink to drain the heat from the tape while withstanding the high electric field. An alternative option would be the increase of the ratio between the length of the shunt and the length of tape. In simulation, a higher electric field was obtained. The development of these two concepts requires further efforts, the material (sapphire) or the manufacturing (corrugations) of the shunt remain expensive. Some ways exist to tackle these issues as the use of alumina instead of sapphire and a proper optimization to determine easy dimensions to realize for the corrugated shunt.

In this chapter, the design of the Fastgrid conductor is based on a very particular critical current distribution. The use of a single defect comes from the observation realized in chapter 4 showing that $I_c(z)$ does not describe the local dissipation phenomena, so it is considered to consider the worst case scenario. The following chapter will justify the choice of the distribution length. It will also investigate the representativeness of the characterizations performed on small samples to validate the design of a conductor. Indeed, the hot-spot regime comes from the inhomogeneities in the REBCO layer and they are not identical along the tape length.

CHAPTER 6

Effect of the conductor length on the hot-spot regime for R-SFCL applications

As it was introduced in chapter 2 using a 1D electro-thermal model, the design of the conductor of a R-SFCL using 2G HTS tapes is driven by two operation regimes. The architecture is adapted to withstand a high electric field in limitation regime and to obtain a non-destructive value of the maximum temperature in hot-spot regime. The last-mentioned regime comes from the consideration of I_c variations and it was mentioned in subsection 1.2.4 that they follow statistical laws. This chapter aims to qualify if trends arise from the fact that I_c variations follow statistical distribution on the evolution of the maximum temperature in hot-spot regime. The size of a I_c distribution is directly linked to the length of the conductor, assuming a constant spatial measurement resolution. As a consequence, the impact of an increasing length is particularly assessed.
The minimum critical current tends to decrease when the conductor length increases. This behavior can be modeled by a Weibull distribution assuming a minimum critical current different from zero with an infinite length of conductor. To assess the impact of such statistical distribution on the hot-spot regime, the deterministic 1D model of 2G HTS conductor is used considering a large number of I_c variations scenarii as input to simulate a R-SFCL behavior. It appears that the longer the conductor, the higher is the maximum temperature in hot-spot regime. Moreover, the fact that two I_c measurements corresponding to a same length of conductor present different maximum temperatures in hot-spot regime leads to present a method to design large-scale conductors of a desired length, robust to survive hot-spot regime due to any I_c variations corresponding to this length.

This chapter aims to study the influence of the conductor length on the hot-spot regime. It uses $I_c(z)$ as the input of the 1D model. It was shown in the previous chapters that this is not appropriate to describe inhomogeneous dissipation, the positions of the inhomogeneities in the REBCO layer is a better indicator. However, this last-mentioned data is not an easy accessible data. As a consequence, it is assumed that the inhomo-

geneities follow statistical distribution and in particular, Weibull distribution, and the use of $I_c(z)$ will give, at least, qualitative trends. s

The main part of this work was published in "Effect of the Conductor Length on the Hot-Spot Regime for Resistive-Type Superconducting Fault Current Limiter Applications," [115].

6.1 Motivation

To predict the peak of maximum temperature in hot-spot regime, $T_{max,peak}$, using the model described in section 2.2, the I_c variations along the length of the conductor are considered. $T_{max,peak}$ is a key element to design conductor as it was introduced in subsection 2.4.1. As it has already been described in subsection 1.2.4, I_c follows statistical law distributions, Gaussian or Weibull. I_c variations are not the same of course in two different tapes even if they have the same length. As $I_c(z)$ is an input of the model of the R-SFCL, $T_{max,peak}$ will also be different in those cases. In the end the question is about the representativity of one simulation using one I_c distribution for the design of any conductor of any length. In addition, it is interesting to question about the confidence it is possible to have in design margins considering the spread of performances of the conductor (i.e. the I_c variations).

In chapter 4, it was concluded that heterogeneous quench are not well described by $I_c(z)$, it is much better to determine the positions of the inhomogeneities in the REBCO layer through SHPM. However, such precise analysis is dedicated to small lengths of tape. To study the influence of the length of the tape on the hot-spot regime, the hypothesis adopted in this manuscript is to consider that the variations of the inhomogeneities are similar to the variations of $I_c(z)$. As a consequence, it is chosen to use $I_c(z)$ as an input, knowing that it is not the appropriate tool to describe local dissipation phenomena but considering that it is the best tool available to characterize tapes.

6.2 Analysis of the I_c variations as a function of the conductor length

The 1D model of 2G HTS conductor used in this PhD work to compute $T_{max,peak}$ requires local I_c data as input. To assess the influence of the conductor length on this key element, an analysis of the length impact on the I_c variations is first carried out.

6.2.1 Effect of the conductor length on the minimum I_c

The I_c measurements of two 100 m long 2G HTS tapes, manufactured by THEVA and SuperOx, performed with a spatial resolution of 1.1 mm and obtained with similar Tapestar® continuous measurement machines, are displayed in figure 6.1a. The probability density functions of these two measurements are also plotted (see figure 6.1b) and shapes of Weibull distributions are recognized with these data from two different manufacturers using two different manufacturing processes. These results were already studied in the past by other groups [55][116]. Looking on the I_c measurements in figure 6.1a, it is visible that the difference between the lowest values and the mean I_c is higher than the difference between the highest values and the mean value. This is found on the shape of the Weibull distribution with a peak of probability not perfectly centered in the middle of the existing I_c in figure 6.1b. In the following work, the study is limited to I_c measurements following

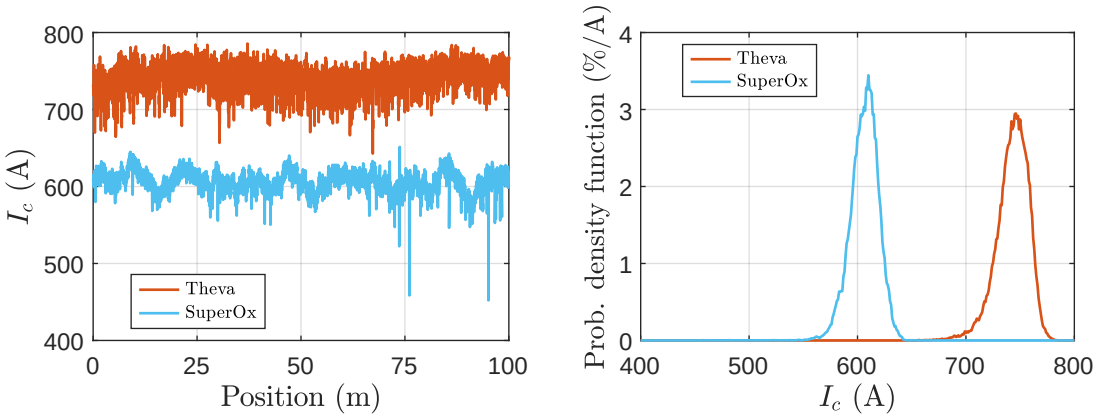

Figure 6.1: (a). I_c over position and (b) probability density functions of I_c. Data (TapeStar, 77 K, self-field) are from THEVA (red line) and SuperOx (blue line).

Weibull distribution. It has the particularity to admit a minimum value considering an infinite distribution. Reference [56] interprets that as a minimum I_c considering an infinite length of tape.

The cumulative distribution function, given by (6.1), is plotted with the I_c values corresponding to 0.1 m, 1 m, 10 m (starting from the beginning) and the full-length of the measurements (see figure 6.2). It appears that $I_{c,min}$ decreases when the conductor length increases. Another way to observe this behavior is to plot $I_{c,min}$ as a function of the sample length. Figure 6.3 shows this evolution for ten I_c measurements extracted from each long-length measurement from THEVA and SuperOx. The averages of these evolutions show that $I_{c,min}$ decreases non linearly with a strong decrease when the length is between 0.1 m and 1 m. It tends to saturate beyond 1 m.

$$P(I_c \leq x) = f(x) \tag{6.1}$$

6.2.2 Description of a I_c measurement with a Weibull distribution

Probability density functions showing Weibull shapes can be analytically described by (6.2). The Weibull parameters are $I_{c,0}$ the scale parameter, M the shape parameter and I_c^* the minimum critical current considering an infinite length of tape [56]. Equation (6.2) only holds for I_c above I_c^*.

$$g(I_c) = \frac{M}{I_{c,0}}\left(\frac{I_c - I_c^*}{I_{c,0}}\right)^{M-1} e^{-\left(\frac{I_c - I_c^*}{I_{c,0}}\right)^M} \tag{6.2}$$

The Weibull parameters of the first meter of the THEVA I_c measurement are determined (see figure 6.4). To determine I_c^*, the linearization (6.4) of the cumulative distri-

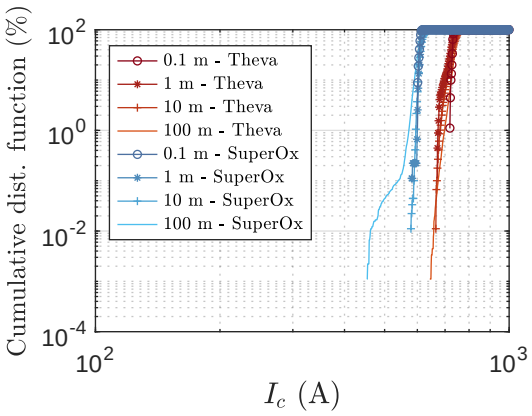

Figure 6.2: Cumulative distribution functions for several samples of I_c measurements (TapeStar, 77 K, self-field) from THEVA (red lines) & SuperOx (blue lines).

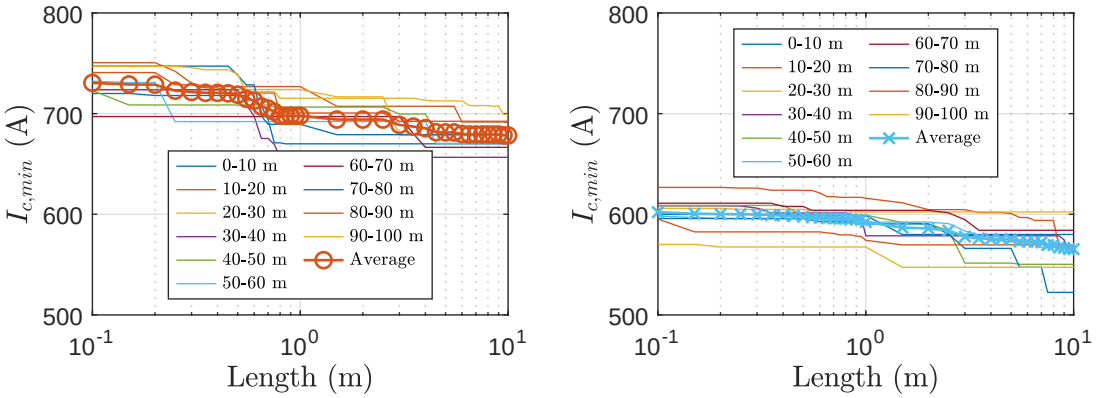

(a) Theva

(b) SuperOx

Figure 6.3: Minimum critical current (TapeStar, 77 K, self-field) as a function of the sample length for ten I_c measurements coming from the 100 m long measurement from (a) THEVA (average values represented by the red line with circles) and from (b) SuperOx (average values represented by the blue line with crosses).

bution function of a Weibull distribution (6.3), is plotted for I_c^* varying from 1 to the $I_{c,min}$ of the original data. The best linearization gives I_c^* with its slope equals to M and its intercept to $Mln(I_{c,0})$ (see figure 6.5). The Weibull parameters in Table 6.1 are used to plot on figure 6.4 the probability density function (6.2) with I_c varying from the real extremum values of the original data.

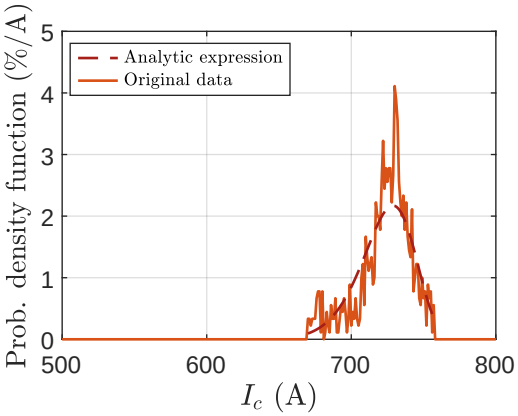

Figure 6.4: Probability density function of the first meter of the I_c measurement from THEVA (TapeStar, 77 K, self-field) (plain red line) and analytic expression of this probability density function (dotted red line).

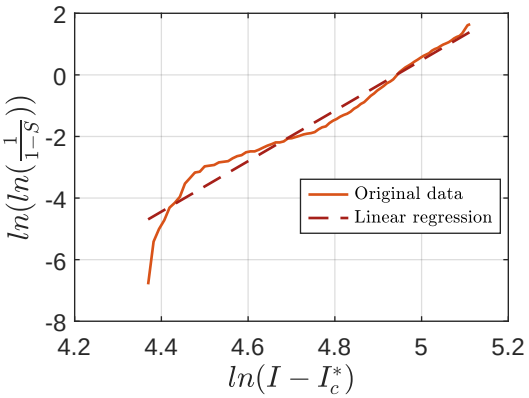

Figure 6.5: Linearization of the cumulative distribution function plotted with original data (plain red line) and linear regression offering the best linearization (dotted red line).

$$S(I_c) = 1 - e^{-(\frac{I_c - I_c^*}{I_{c,0}})^M} \tag{6.3}$$

$$\ln(ln(\frac{1}{1 - S(I_c}})) = Mln(I_c - I_c^*) - Mln(I_{c,0}) \tag{6.4}$$

I_c^*	$I_{c,0}$	M
591	140	8.2

Table 6.1: Weibull Parameters determined with the values of the first meter of the I_c measurement from Theva (Tapestar, 77 K, self-field) given in figure 6.1a.

The I_c measurements considered here highlight the decrease of $I_{c,min}$ when the length of the conductor increases. The description by a Weibull distribution makes it possible to identify an absolute minimum critical current. The influence of these considerations on the maximum temperature in hot-spot regime are studied in the next section.

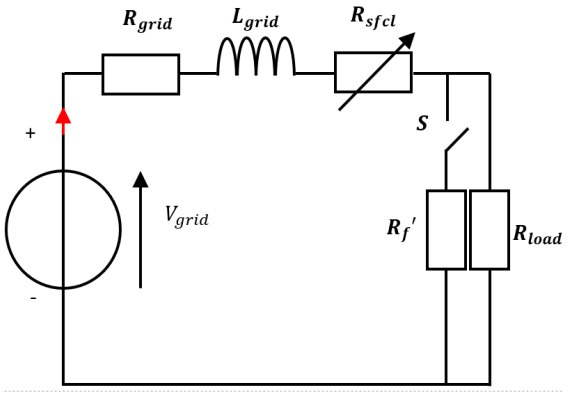

Figure 6.6: DC circuit used to simulate the behavior of the R-SFCL.

6.3 Evolution of the maximum temperature in hot-spot regime when considering large-scale conductors

The consideration of the variations of I_c along the length of a conductor highlights the existence of the hot-spot regime, as it was demonstrated in section 2.4. The 1D model of a 2G HTS conductor is now used to conduct transient R-SFCL behavior simulation to obtain $T_{max,peak}$ for variable input sizes coming from the two long length I_c measurements shown in figure 6.1a.

6.3.1 Simulation framework

To investigate how the conductor length lg affects the hot-spot regime, the maximum temperature of the conductor T_{max} is computed over a large range of prospective currents for multiple lg. Figure 6.6 shows the DC circuit where the R-SFCL is integrated. It is considered that the limiter operates at 65 K, the average I_c at this temperature almost doubles compared to 77 K (around 1400 A) and the rated current I_n is 700 A. I_{pros} can vary from I_n to the maximum prospective current occurring in the event of a zero-impedance fault chosen equals to 20 I_n (6.5). To compare a variable length of conductor but whose conductor in the same conditions, it is necessary to adapt the voltage V to lg (6.6) while the electric field E is constant (150 V/m). R_{grid} is determined by the zero-impedance short-circuit (6.7). L_{grid} is designed with the circuit time constant $\tau = 0.005$ s (6.8) with τ a constant. R_f is the equivalent resistance of R'_f in parallel with R_{load}. R_f varies to obtain the desired range of I_{pros} (6.9). This model makes the comparison of various conductor lengths possible while E, I_{pros} and τ do not change.

$$I_{pros} = [1...20]I_n \tag{6.5}$$

$$V = Elg \tag{6.6}$$

$$R_{grid} = \frac{V}{20 I_n} \tag{6.7}$$

$$L_{grid} = \tau R_{grid} \tag{6.8}$$

$$R_f = \frac{V}{[1 \ldots 20] I_n} - R_{grid} \tag{6.9}$$

Two structures are simulated for 0.05 ms. They are "bare" tapes from THEVA and SuperOx on which a thick Hastelloy® C276 shunt is added (see Table 6.2). Thermal and electrical properties come from [78] for the stabilizer, MgO, tin and nickel while it comes from [79] for the Hastelloy® C276. A homogeneous temperature in the conductor cross-section is justified because the characteristic diffusion time (40 ms) is smaller than the simulation time (50 ms).

Layers	Thickness (µm) (THEVA)	Thickness (µm) (SuperOx)
Substrate	100	100
Buffer stack	3.1	0.3
REBCO	3.5	1.5
Silver	3.2	3
Tin	10	10
Nickel	1	1
Hastelloy® C276 shunt	500	500

Table 6.2: Description of the two conductors.

6.3.2 T_{max} over I_{pros} for 0.1 m, 1 m and 10 m long samples

The I_c measurements from figure 6.2 are used as inputs for the model. The simulation gives the maximum temperature over I_{pros}, shown in figure 6.7, where the hot-spot regime is recognized. The prospective current, for which one $T_{max,peak}$ occurs, is noted $I_{pros,peak}$.

These simulation results show that $T_{max,peak}$ increases with an increasing conductor length on both structures using inputs from two different manufacturers. The hot-spot regime appears more severe with the inputs from THEVA due to a higher I_c in the tapes from this manufacturer.

6.3.3 Evolution of $T_{max,peak}$ as a function of the conductor length

It was shown on a few cases that $T_{max,peak}$ increases with an increasing length of conductor. In order to qualify this dependence T_{max} over I_{pros} is computed several times in figure 6.8 using as input samples varying from 0.1 m to 10 m from the first ten meters of the I_c measurement from THEVA (see figure 6.1a). In figure 6.9, $T_{max,peak}$ as a function of the

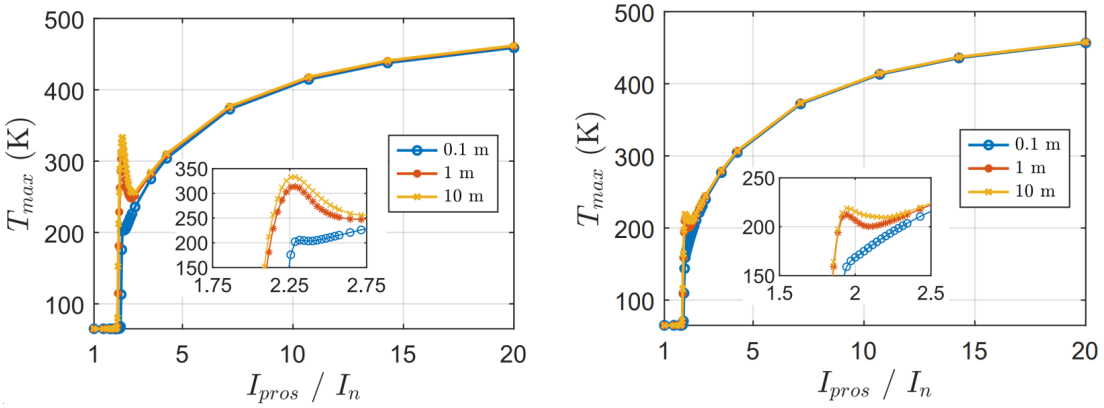

(a) Theva (b) SuperOx

Figure 6.7: T_{max} over I_{pros} normalized by I_n with I_c measurements from (a) THEVA and (b) SuperOx. The simulation lasts 0.05 s and the conductor is operating at 65 K.

sample length is plotted. The peak of maximum temperature increases significantly when the conductor length increases from 0.1 m to 1 m and it seems to saturate beyond 1 m.

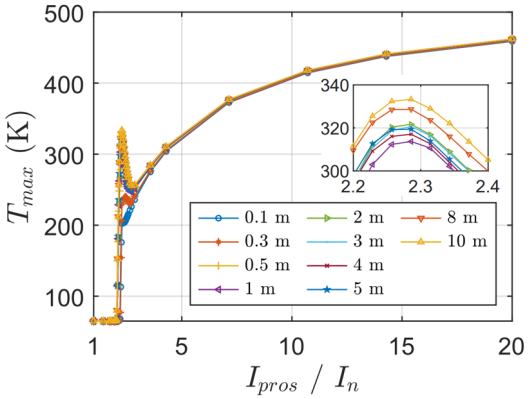

Figure 6.8: T_{max} over I_{pros} normalized by I_n for several I_c measurements. These results come from the simulation for 0.05 s at 65 K of a conductor with a THEVA structure using I_c values from THEVA (TapeStar, 77 K, self-field).

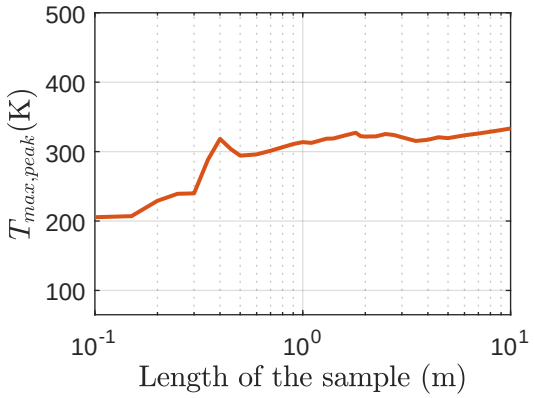

Figure 6.9: $T_{max,peak}$ as function of the conductor length. These results come from the simulation for 0.05 s at 65 K of a conductor with a THEVA structure using I_c values from THEVA (TapeStar, 77 K, self-field).

Figure 6.10 presents the evolution as a function of the conductor length of $I_{c,min}$ at 65 K, $I_{pros,peak}$ and the RMS value of the current in the circuit I_{rms} when $T_{max,peak}$ occurs (6.10) where Δt is the simulation time. Two elements from this figure help to explain the evolution of $T_{max,peak}$. When the conductor length increases, first, $I_{c,min}$ is lower and considering a similar current in the grid, the dissipative state is reached faster (due to the power law) and the heating is longer. Second, I_{rms} increases which means that the current

limitation becomes slightly less efficient. The ratio between the length of the dissipative parts of the conductor and its total length seems to decrease with an increasing length for a given $I_{pros,peak}$.

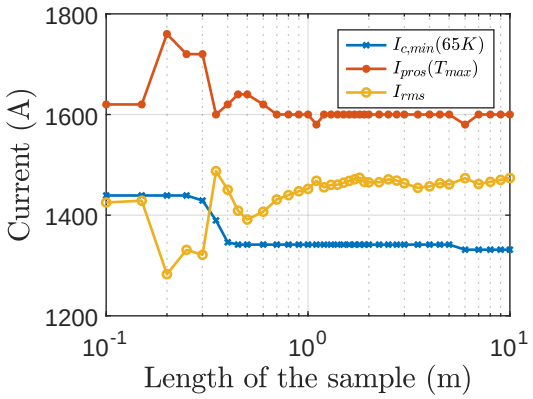

Figure 6.10: $I_{c,min}$ at 65 K, $I_{pros,peak}$ and I_{rms} as a function of the conductor length. These results come from the simulation for 0.05 s at 65 K of a conductor with a THEVA structure and using I_c values from THEVA (Tapestar, 77 K, self-field).

$$I_{rms} = \sqrt{\frac{1}{\Delta t}\int_{t_0}^{t_0+\Delta t} i(t)^2 dt} \tag{6.10}$$

6.3.4 From specific results to general case: a probabilistic approach

A study similar to the work described in the previous section is carried out to assess if $T_{max,peak}$ follows a trend arising from the description of I_c variations by a Weibull distribution. To develop a probabilistic approach, the deterministic model is used considering in input twenty 10 m long I_c measurements used in figure 6.3. Figure 6.11 confirms the previous results with a non linear increase of $T_{max,peak}$ when the conductor length increases. It starts to saturate beyond 1 m. The average $T_{max,peak}$ is not continuous below 1 m for SuperOx because for some inputs, no hot-spot regime is observed. These results show that a hot-spot regime is more likely to be observed at the industrial scale, few meters long conductors than at the scale of the lab, few centimeters samples. This result has a lot of importance from an experimental point of view. Indeed, on one hand, the characterization of a sample of few centimeters is not representative of the behavior of a long length conductor. But, on the other hand, it is not necessary to invest in a large and expensive high voltage set-up to characterize a conductor of few dozens of meters as its behavior starts to be representative for a 1 m long conductor, considering a reasonable margin. These results also show that two same length samples do not present the same $T_{max,peak}$.

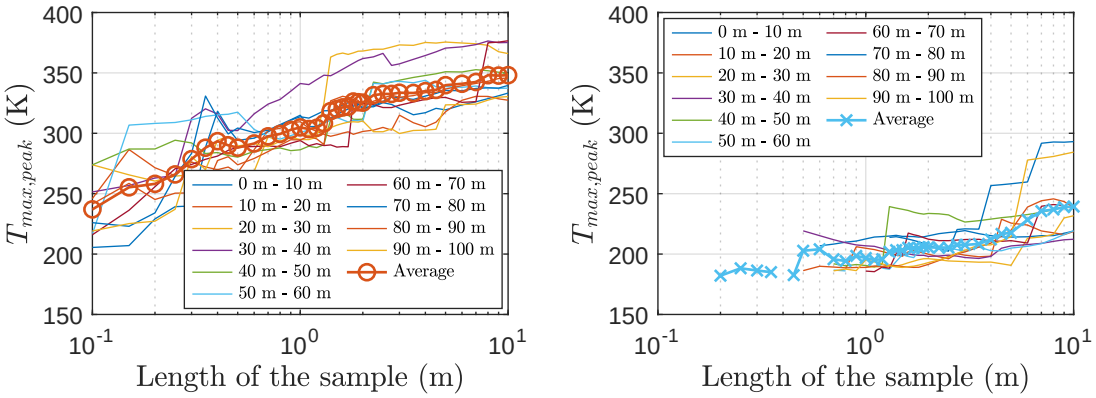

(a) Theva

(b) SuperOx

Figure 6.11: $T_{max,peak}$ as a function of the conductor length using as input ten samples coming from I_c measurements from (a) THEVA and (b) SuperOx used to plot figure 6.3. An average evolution is also computed for each manufacturer. These results come from the simulation for 0.05 s at 65 K of conductors with a THEVA structure (a) and a SuperOx structure (b) using I_c values from THEVA (a) and SuperOx (b) (TapeStar, 77 K, self-field).

6.4 Prediction of an upper bound temperature in hot-spot regime when considering large-scale conductors

It is established that knowing the $I_c(z)$ over the full length of conductor makes the precise evaluation of the maximum temperature T_{max} of a R-SFCL for any prospective current possible. However, the designer may not have such detailed characterization available, and in any case, redesigning the R-SFCL structure for each $I_c(z)$ corresponding to a length L of conductor is impractical.

The conductor follows a behavior that can be estimated due to the fact that I_c distributions follow statistical laws. The determination of an upper bound of $T_{max,peak}$ for the design of a conductor of a desired length L would be practical. How is it possible to identify this upper bound with reasonable margins ? It will be shown that the only value $I_{c,min}$ along the length L is required to give an upper bound of $T_{max,peak}$. $I_{c,min}$ of the desired length L is extracted from the I_c measurement on a short length (1 m) assuming that the critical current follows a Weibull distribution. Such a $I_c(z)$ on 1 m long tape is available during the design phase. An example is detailed by first creating a I_c distribution for L equals to 20 m. Reference [117] states that it is also possible to extract the minimum I_c of a desired length L from transport measurements on a reduced length.

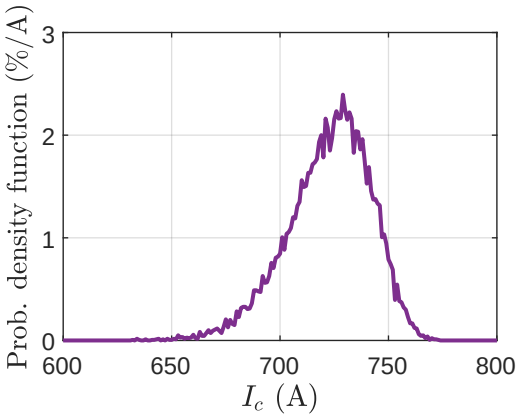

Figure 6.12: Probability density function of a fictive 20 m long I_c distribution. The values are generated with (6.11) using the Weibull parameters from Table 6.1.

6.4.1 Creation of a fictive I_c distribution corresponding to a long length conductor

In subsection 6.2.2, the Weibull parameters of a 1 m long I_c distribution from THEVA were determined (see Table 6.1). The measurement of I_c was given with a spatial resolution of 1.1 mm. The original 1 m long tape contains 900 values. The generation of I_c values to create a fictive I_c distribution is possible using (6.11) expressed from (6.3) considering that $S(I_c)$ is a uniformly distributed random number between 0 and 1. For a 20 m long tape, 18000 values given by (6.11) are required. The I_c probability density distribution corresponding to this fictive 20 m long tape is plotted in figure 6.12. This I_c distribution is specific and another distribution corresponding to the same length with the same Weibull parameters would give a different $T_{max,peak}$ in simulation. It does not give an upper bound.

$$I_c = I_c^* + I_{c,0}(\ln(\frac{1}{1-S(I_c)})^{\frac{1}{M}} \tag{6.11}$$

However, in section 6.3, the increase of $T_{max,peak}$ with an increasing conductor length is explained by the simultaneous decrease of $I_{c,min}$ and a limitation becoming weaker. The worst scenario giving the highest $T_{max,peak}$ would be obtained with a constant I_c along the conductor length holding a single defect equals to $I_{c,min}$. A comparison is carried out between a real 1 m long I_c measurement and this worst scenario (see figure 6.13). The fictive 1 m long I_c measurement is equal to the mean value of the real 1 m long $I_c(z)$ except one value equals to the minimum value of the original data. The size of this element is not important as the current limitation due to the transition of this small portion has a very reduced impact compared with the total length of the conductor. Figure 6.14 shows that $T_{max,peak}$ of the worst scenario is higher than $T_{max,peak}$ computed with the real I_c measurement. This behavior has already been studied in the past [105]. The large advantage of considering this worst scenario, which is unlikely to exist, is that it covers

all the plausible I_c variations for a given length of conductor and it gives an upper bound value of $T_{max,peak}$ without presenting a too large error ($T_{max,peak}$ is 335 K for the fictive I_c input and 314 K for the original I_c input).

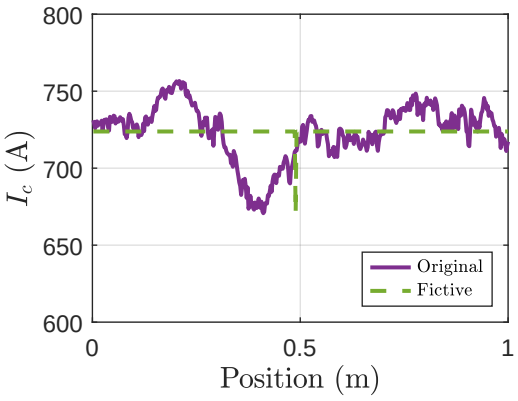

Figure 6.13: I_c measurement from THEVA (TapeStar, 77 K, self-field) (plain violet line) and fictive I_c distribution (dotted green line) created with the mean and minimum values of the original I_c values.

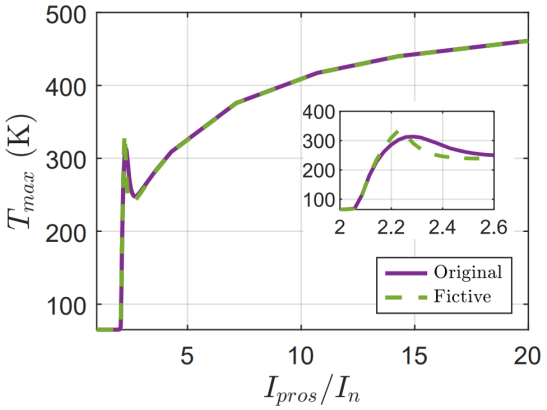

Figure 6.14: T_{max} over I_{pros} normalized by I_n computed with the original (plain violet line) and fictive I_c values (dotted green line). The simulation lasts 50 ms and the structure is a THEVA conductor operating at 65 K.

This method is adopted to predict the upper bound of $T_{max,peak}$ of the 20 m long conductor made with the same tape used to determine the Weibull parameters of Table 6.1. The minimum and mean critical current of the distribution in figure 6.12 are used to compute the fictive I_c over position in figure 6.15.

6.4.2 Prediction of the upper bound of $T_{max,peak}$ of a 20 m long conductor

The fictive I_c variations shown in figure 6.15 are used to simulate for 0.05 s the behavior of a conductor showing a THEVA structure and operating at 65 K. It gives T_{max} over I_{pros} displayed in figure 6.16. The maximum temperature in hot-spot regime is 380 K. This value is an upper bound for all the plausible I_c distributions corresponding to the same length of conductor due to the considerations of the most adverse scenario of I_c variations.

Thanks to this value, the designer may adapt the structure of the conductor of the R-SFCL to obtain a non-destructive temperature value, the shunt thickness to solder to a superconducting tape for example. It offers to the designer of R-SFCL, a way to design a long length conductor, without having the full I_c measurement of the corresponding length and working for all same length tapes.

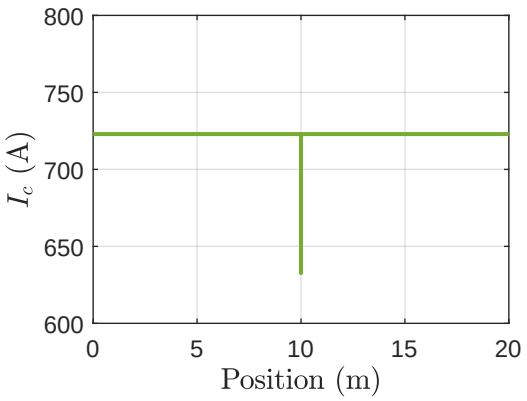

Figure 6.15: I_c over position of a fictive 20 m long conductor built from Weibull parameters of a real 1 m long I_c measurement from THEVA (TapeStar, 77 K, self-field).

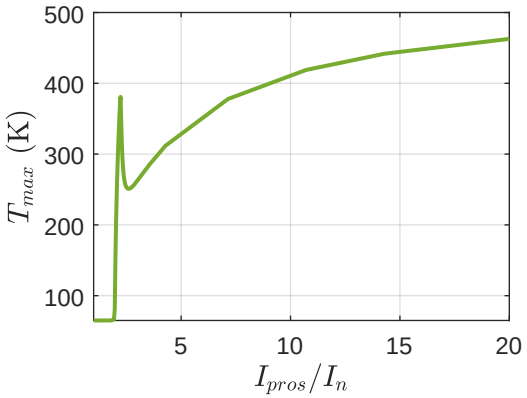

Figure 6.16: T_{max} over I_{pros} normalized by I_n computed using the fictive I_c over position as input. It gives an upper bound of the maximum temperature in hot-spot regime. These results come from the simulation for 0.05 s at 65 K of a conductor with a THEVA structure.

6.5 Conclusion

The effect of the length of the conductor with realistic distributions of I_c for R-SFCL applications was studied. The analysis of $I_c(z)$ of two tapes corroborates previous results. They can be described by Weibull distribution. The longer the tape, the lower the minimum I_c is but it exists a minimum value considering an infinite length. Considering devices with similar conditions of operation, the total length of conductor that is used plays an important part for the so called "hot-spot" regime. Thanks to a 1D model of 2G HTS conductor, it was shown that the maximum temperature in hot-spot regime increases when the conductor length increases. The important outcome is that this increase of $T_{max,peak}$ is not linear. It increases significantly with a conductor length increasing from 0.01 m to 1 m and it starts to saturate beyond. This result shows the interest to experimentally characterize at least 1 m long samples to obtain representative results of what could be expected for real R-SFCL devices.

The study made it clear that the maximum temperature in hot-spot regime is not identical for several conductors presenting the same length. It means that the conductor design should be adapted to each I_c distribution but this approach is not feasible for a commercial product. In response, a method resulting from the synthesis of the previous results was presented. Thanks to the determination of the Weibull parameters of the I_c measurement of a small tape, it is possible to predict the average and minimum values of a fictive critical current distribution corresponding to a given length to determine an upper bound of the maximum temperature in hot-spot regime. This value is reasonably higher than the values which would have been obtained with all plausible real I_c scenarii of the desired length without injecting a too large error. As a consequence, the design

of the conductor can be adapted to this value and will be robust to any I_c distributions of the desired length to survive the hot-spot regime, without significant oversizing of the conductor.

In subsection 5.1.1, the design of the Fastgrid conductor is based on this approach. The I_c distribution corresponds to a length of 1 m and it holds one single defect.

Conclusions and Perspectives

The R-SFCL was introduced in chapter 1 as a technology providing concrete solutions to some of today's pressing needs of power grids such as the increase of the fault current levels. The use of 2G HTS tapes as the base to develop R-SFCL conductors is particularly interesting thanks to their high performances. Nevertheless, the R-SFCL remains rare in the grids despite recent successes. The high cost of the tapes and the reluctance of the utilities to adopt such a breakthrough technology were identified as barriers to its development. This PhD work was within this framework, focusing on the conductor itself more than on the complete solution (the R-SFCL as a system). The two axis of research were:

- The consolidation of the understanding of the behavior of the 2G HTS tapes to increase the confidence level in the conductor design approach and to use their full performances.
- The development of cost-effective conductors with high performances to decrease the cost of the R-SFCL.

The approach adopted throughout this PhD work was to study the conductor at a large scale (chapter 2) giving the basic elements of its design, then to tighten the focus on the local thermo-electrical behavior of the 2G HTS tapes (chapters 3 and 4) where the design route just presented was validated but suggesting changes in the considerations of the superconducting properties and to zoom out and come back to the design of conductors with the development of optimized architectures (chapters 5 and 6).

The chapter 2 was the base of the approach just mentioned to answer the two main objectives of this PhD work. The 2G HTS conductor operation was simulated using a 1D thermo-electrical model on a large range of prospective currents. The study of the maximum temperature of the conductor over this range enabled the extraction of two extreme cases: the limitation regime and the hot-spot regime. The temperature elevation during these two regimes represents a crucial step to design R-SFCL conductors with

high performances. The existence of the hot-spot regime was highlighted through the consideration of the I_c variations of the 2G HTS tapes. It refers to the regime where the tape is almost not limiting the current due to localized quenches on its length. The first axis of research of this PhD work particularly focused on the local behavior of these tapes during inhomogeneous quenches throughout chapters 3 and 4 to get a better understanding of their operation.

The development of a dedicated set-up, introduced in chapter 3, to study the hot-spot regime led to the particularly rare experimental observation of a temperature elevation occurring when prospective currents were in the range of the I_c variations of the 2G HTS tape sample. The set-up also featured a high-speed imaging system enabling the observation of the bubble generation on the surface of the sample. It showed that whatever the prospective current, the quench is first inhomogeneous: bubbles appear in very localized positions and propagate in the width. Then, they propagate along the length of the tape leading to a complete quench. The higher the prospective current, the more initial dissipation spots are numerous and the faster the total quench of the tape. These observations raised a semantic issue. The use of "hot-spot regime" is not appropriate at a small scale because when looking to the local behavior of the tape, the inhomogeneous and homogeneous dissipation are successive behaviors occurring for any prospective current while in the conductor design approach, "hot-spot regime" refers to a partial quench of the tape. In that sense, the use of this denomination should be dedicated to the design of a conductor.

These observations stressed the need to continue the study of the quench mechanism: additional experiments and simulations were therefore carried out. A collaboration with TU Wien was initiated to determine why the bubble generation is very localized at the onset of a quench. Thanks to Hall Scan Probe Microscopy and observations of the tape with Scanning Electron Microscopy, it was highlighted that the positions of bubble generation match the positions of non-epitaxial growth of the REBCO layer. The $I_c(z)$ measurement given by traditional measurement machines such as TapeStar is not the appropriate indicator to describe the dissipation phenomena occurring at the surface of the tape even if its use in simulation helped to predict the hot-spot regime. The existence of this regime was experimentally confirmed with a temperature elevation occurring for prospective currents in the range of $I_c(z)$. Then, it was proposed to adapt the design approach of the conductors by considering the worst scenario of superconducting properties which is a constant I_c distribution with an unique weak defect instead of an actual I_c measurement.

Using a 3D FEM model developed by colleagues from Ecole Polytechnique de Montréal, the defects in the REBCO layer were emulated as areas of poor critical current density. Such an approach allowed to recreate the quench mechanism in simulation. It showed that the propagation first occurs in the width due to an increase of the current density in the direct vicinity of these defects, leading to dissipation and thus reducing the available cross-section of the superconducting layer. When the dissipation is fully developed in the width, it then propagates along the length. The current shares between the conductive layers at the level of the dissipative column. The comparison of experimental and simulation results

enabled the observation of the non equipotential cross-section of 2G HTS tapes during inhomogeneous quenches. This was explained by a larger current transfer length between the superconducting layer and the bottom silver layer than between the superconducting layer and the top stabilizer layer. As a consequence, even if the current in the top stabilizer layer is bigger than the current in the bottom stabilizer layer, it circulates in a larger portion on the bottom stabilizer layer, in the vicinity of a dissipation column.

The first focus of this PhD was to improve the current knowledge on the operation of 2G HTS tapes which was successfully performed by using appropriate simulations and experiments often in collaboration with other institutions. In the perspective of future developments, some directions could be explored:

- The 3D FEM model works well to recreate the local behavior observed on the 2G HTS tapes thanks to high-speed imaging. However, it is based on a strong hypothesis which is the non consideration of the self-field, i.e. the current distribution inside the superconducting layer. It would be interesting to assess the influence of the magnetic problem on this mechanism.

- It was highlighted that the I_c is not the appropriate indicator to describe the local behaviors occurring in 2G HTS tapes. It would be interesting to question about which data is the most adapted and should be furnished to the users of commercial tapes to qualify the local behaviors on these tapes.

- The propagation of the heat in the width of the 2G HTS tape is explained thanks to simulation results. A dedicated experimental set-up would be very useful to confirm the simulation results. In particular, measuring the voltage in the width of the 2G HTS tape would be a first step in this direction.

The second axis of research of this PhD work was to contribute to the development of conductors with high performances in order to decrease the total cost of the R-SFCL. The chapters 5 and 6 fall in this direction. Several conductor architectures proposed within Fastgrid were studied coupling both numerical simulations and characterizations. The main output was the validation of the Fastgrid conductor design on a small length. This conductor showed an electric field of 120 V/m for 50 ms and no damage in hot-spot regime at 65 K, demonstrating once again experimentally the existence of this regime. With these performances, the cost of the conductor in a R-SFCL may be decreased by a factor of ten compared to the conductor used in the predecessor of the Fastgrid project (Eccoflow). Two other architectures from this project, with a lower level of industrial maturation, were studied. One of them was a tape with a CFD, characterized in collaboration with ICMAB and EPM. The use of a high-speed imaging system to observe dissipation on its surface clearly showed that the bubble generation was active on the edges of the sample while the main portion of the width was not generating bubbles, highlighting the existence of the CFD effect by an optical observation. The second structure was a Sapphire-based substrate HTS tape from Tel-Aviv University on which it was possible to reach an electric

field exceeding 1000 V/m for 50 ms. However, the critical current remains poor (around 50 A at 77 K). Two alternative architectures were introduced in order to reach a higher electric field than the one observed with the Fastgrid conductor. Their concepts were validated in experiments or in simulations but the cost-effectiveness of these structures did however not appear interesting at this stage.

Between these five innovative architectures, the Fastgrid conductor appeared as the best comprise between high performances and simplicity of implementation. With a significant increase of its critical current, the Sapphire-Based substrate could become a total game changer.

The design of the Fastgrid conductor was based on a very specific I_c distribution considering a 1 m long constant I_c with a single defect at the center. The choice of this length was based on the work developed in chapter 6. This chapter questioned the representativeness of the characterization of a conductor considering one specific distribution for any device of any length. Using a probabilistic approach on the 1D model of conductor, a probabilistic understanding of the simulation results showed that the peak of maximum temperature occurring in hot-spot regime increases with an increasing length of conductor. In other words, the longer the conductor, the more severe the hot-spot regime is but this trend saturates when the conductor length is beyond 1 m. Two conductors with a different length do not present the same behavior in hot-spot regime neither two conductors with the same length. Indeed, I_c variations are not identical from one conductor to another one. A method to design conductors with long lengths was proposed. The idea is to give an upper bond of the peak of maximum temperature in hot-spot regime for a conductor with a given length and working with all I_c variations corresponding to this same length. The architecture of the conductor can be adapted to this upper bond as it was done with the Fastgrid conductor in chapter 5. It implies reasonable margins and it tends to an universal design of a given conductor length considering the spread of performances of the tapes.

Regarding the second axis of research of this thesis, in the perspective of future developments, some directions could be investigated:

- The electric field of the Fastgrid conductor is linked to its resistivity. Reducing the silver layer thickness or using a less conductive stabilizer could lead to a higher electric field.
- The industrialization of the manufacturing process of the Fastgrid conductor remains difficult due to the delicate bonding of the tape and the shunt. Once this issue is solved, a large step forward would be the test of an actual R-SFCL module with such technology. This would demonstrate to utilities the cost-effectiveness of the solution.
- An elevation of the critical current of the Sapphire-based substrate R-SFCL conductor might occur. Indeed, the critical current of commercial tapes largely increased

in the recent years. Assuming a higher critical current, this technology would be a total breakthrough and the design of the R-SFCL with this conductor would be very challenging.

- The study of the evolution of the peak of maximum temperature in hot-spot regime is limited to conductor with a length of 10 m in this study. Nevertheless, this length reaches tens of meters in a full R-SFCL device. It would be interesting to continue this study with longer lengths and in the meantime optimize the model in order to reduce the computation time.

To finish, even though these results come from an effort to develop advanced superconducting conductors for R-SFCL, they can be useful for other large-scale applications, especially the thermo-electrical mechanism of quench onset described in chapter 4.

APPENDIX A

Schemes of Superconducting Fault Current Limiters

The schemes of the circuits presented in this appendix correspond to the structures introduced in 1.1.3. In the schemes, V_{grid}, R_{grid}, L_{grid} and Z_{load} represent a power grid.

SFCL - Non-based on the quench

DC Biased iron core-type SFCL

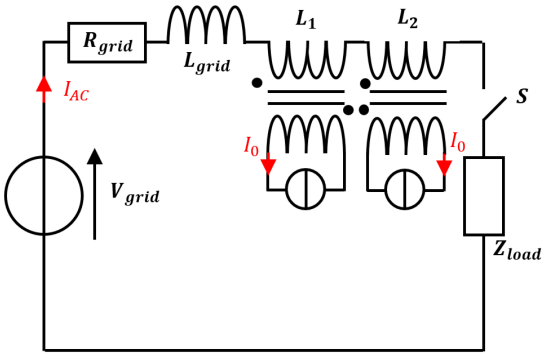

Figure A.1: Structure of the DC Diased iron-core-type SFCL. L_1 and L_2 represent two windings of the grid transmission around two iron cores. One superconducting coil loaded with a current I_0 is used to saturate the iron cores.

Bridge-type SFCL

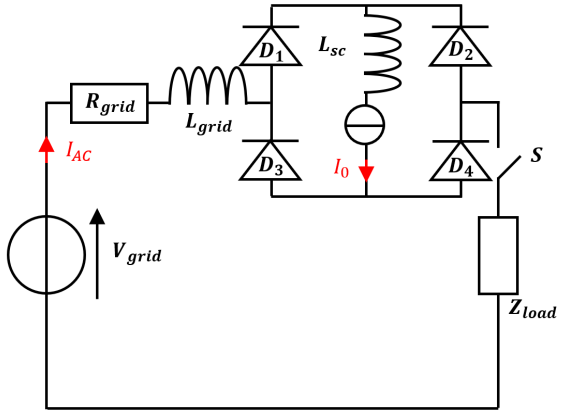

Figure A.2: Structure of the bridge type SFCL. A rectifier is inserted in a power grid. A superconducting coil is used to feed the semi-conductors with a permanent current I_0.

The currents in the diodes are :

$$\begin{cases} D_1 \quad \& \quad D_4 : I_1 = I_4 = I_0/2 + Icos(wt + \phi)/2 \\ D_2 \quad \& \quad D_3 : I_2 = I_3 = I_0/2 - Icos(wt + \phi)/2 \end{cases} \tag{A.1}$$

Superconducting Fault Current Controller Limiter - SFCCL

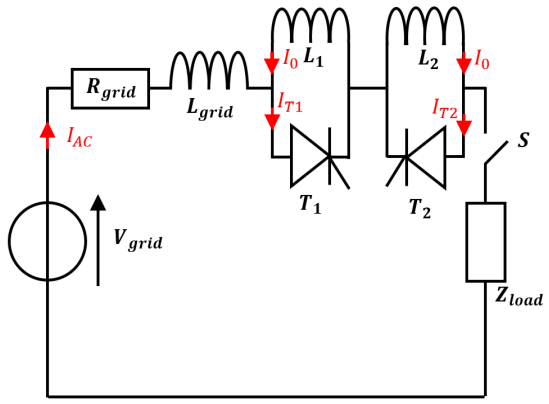

Figure A.3: Structure of the Superconducting Fault Current Controller Limiter. Two superconducting coils are each associated to a semi-conductor to ensure the circulation of a permanent current I_0.

The currents in the thyristors are :

$$\begin{cases} I_{T1} = I_0 + I_{AC}cos(wt + \phi) \\ I_{T2} = I_0 - I_{AC}cos(wt + \phi) \end{cases} \tag{A.2}$$

SFCL - Based on the quench

Resistive-type SFCL

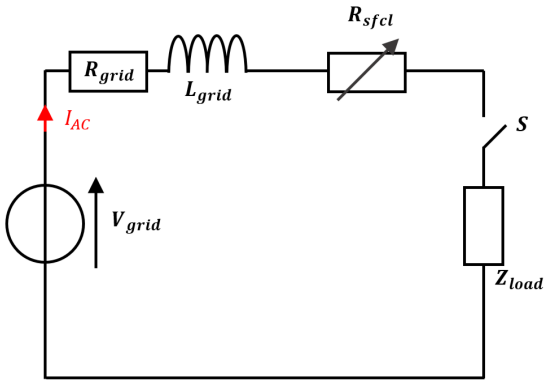

Figure A.4: Structure of the Resistive-type SFCL. A superconducting non-inductive coil R_{sfcl} is inserted in the power grid.

Shielded iron-core-type SFCL

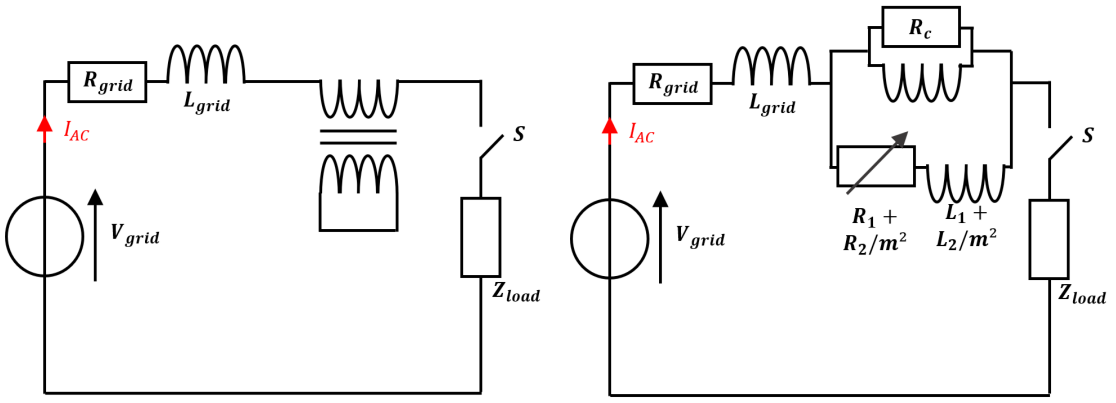

(a) (b)

Figure A.5: (a) Structure of the shielded iron core SFCL. A transformer made with the grid transmission on the primary side and with a superconducting wire on the secondary side. The transformer shows a ratio m (b) Practical representation of the shielded iron core SFCL.

APPENDIX B

Data of selected materials

Resistance per length unit as a function of temperature

The resistance per length unit as a function of the temperature is used to compute the maximum temperature of a conductor thanks to electrical measurements. Values under T_c and above the ambient temperature are necessary to compute T_{max}.

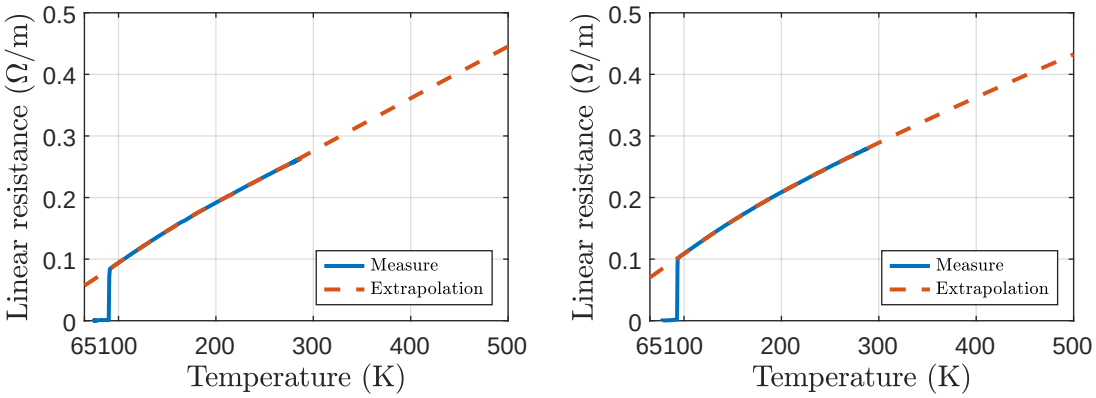

(a) Superpower

(b) SuperOx

Figure B.1: Resistance per length unit as a function of temperature of a (a) Superpower tape and a (b) SuperOx tape obtained with measurements (plain blue line) and their extrapolations on a larger range of temperatures (dotted red line).

Specific heat capacity per volume unit as a function of temperature

The heat capacity per volume unit as a function of temperature is another important element to compute the maximum temperature T_{max} or the mean temperature T_{mean} of a conductor.

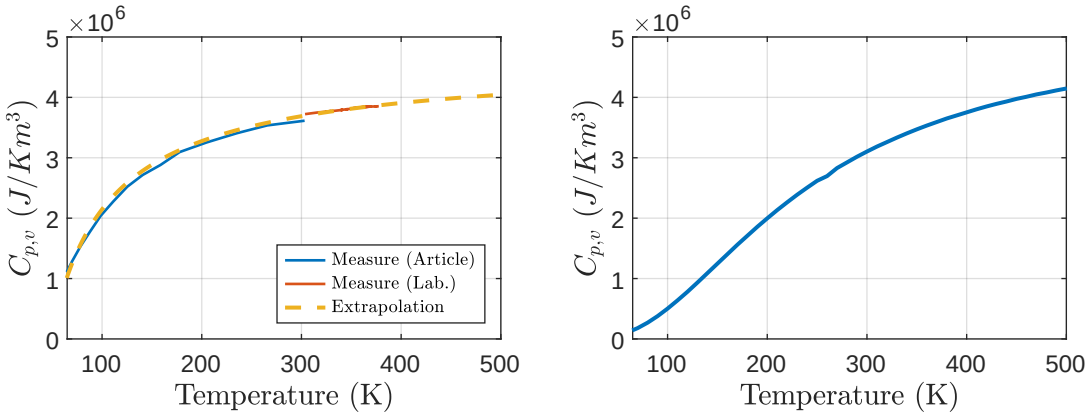

(a) Hastelloy® C276

(b) Sapphire

Figure B.2: Heat capacity per volume unit of (a) Hastelloy® C276 with data from [79] and additional measures carried out in Neel Institute and (b) Sapphire from [78]. Extrapolation on a wider range of temperatures is given for the Hastelloy® C276.

Heat conductivity as a function of the temperature

The heat conductivity is important to compute the temperature diffusion.

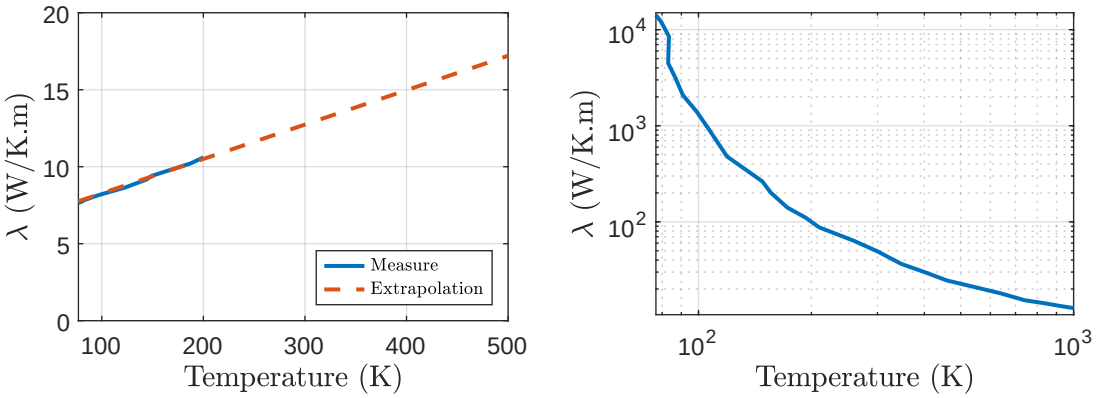

(a) Hastelloy® C276

(b) Sapphire

Figure B.3: Thermal conductivity of (a) Hastelloy®C276 with data from [79] and of (b) Sapphire from [78]. Extrapolation on a wider range of temperatures is given for the Hastelloy ®C276.

APPENDIX C

Description of the boiling heat transfer

The author warmly thanks S.Siedel for its kind help in understanding the boiling phenomenon in liquid nitrogen.

A short introduction about the boiling mechanism is given to understand why bubble generation will be observed on the surface of the tape. In 1966, Nukiyama [89] used an experimental apparatus where a Platinum wire is fed by a power-controlled heating system in saturated water. The temperature on its surface is known using the measure of the resistance per length unit which is temperature dependent. In such case, the independent parameter is the heat flux transfer to the liquid, in the y-axis of figure C.1 and the dependent variable is ΔT, the difference of temperature between the surface of the wire and the saturated water far from the sample.

A saturated liquid, i.e a liquid at the thermodynamic equilibrium under the ambient pressure, is considered in which a heater is immersed. The heater power is increased slowly enough that quasi-static behavior is obtained. The following regimes can be observed :

- A to B: No bubble exists, this regime is called the free convection boiling.
- B to C: At point B, bubbles start to appear, this is the Onset of Boiling. This improvement of the heat transfer thanks to bubble nucleation leads to a transient temperature fall to point C.
- C to E: The nucleate boiling regime is established from C to E with a distinction between C and D where only isolated bubbles exist and D to E where the boiling is fully developed. The point E is called the critical heat flux.
- E to F: From point E, if the power received by the Platinum exceeds the critical heat flux, a transient temperature increase occurs until it reaches point F. The film boiling is established from point F.

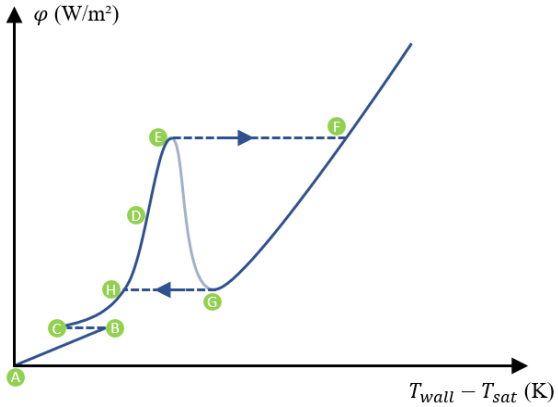

Figure C.1: Power per surface unit transfers to the bath as a function of the difference between the temperature of the tape and the temperature of the bath.

When the power received by the element decreases, a similar path is followed until point F. Then, the temperature, instead of transiently decreasing until point E, keeps decreasing with the heat flux until it reaches point G, the Leidenfrost point. A small decrease of the power in point G leads to a sudden temperature drop until point H.

The portion of the Nukiyama curve between E and G is obtained only in temperature-controlled mode.

APPENDIX D

Expression of the electric field over a conductor

This appendix was mainly written by P. Tixador in [108].

This appendix brings elements to design a conductor in limitation regime. A conductor refers to a superconducting tape bonded to a shunt. These two elements are electrically in parallel and thermally connected. An energy balance is applied in limitation regime on the conductor assuming adiabatic conditions and an isothermal cross section of the conductor. This is questionable even in case of a metallic shunt but mandatory to get analytic expressions to study the relevant parameters. It gives (D.1) where v is the instantaneous voltage, R_{cond} the resistance of the conductor and $c_{p,v}^{cond}$ the specific heat per volume unit of the conductor.

$$\frac{v(t)^2}{R_{cond}(T)}dt = V_{cond}c_{p,v}^{cond}(T)dT \tag{D.1}$$

The tape and the shunt being electrically in parallel the equation becomes:

$$v(t)^2(\frac{1}{R_{tape}(T)} + \frac{1}{R_{shunt}(T)})dt = (V_{tape}c_{p,v}^{tape}(T) + V_{shunt}c_{p,v}^{shunt}(T))dT \tag{D.2}$$

The tape and the shunt do not have necessarily the same lengths (l_{tape} and l_{shunt}) nor the same widths (w_{tape} and w_{shunt}). e_{tape} and e_{shunt} are the thicknesses of the tape and shunt.

$$\frac{v(t)}{l_{tape}}^2 dt = \frac{e_{tape}c_{p,v}^{tape}(T) + \frac{l_{shunt}}{l_{tape}}\frac{w_{shunt}}{w_{tape}}e_{shunt}c_{p,v}^{shunt}(T)}{\frac{e_{tape}}{\rho_{tape}(T)} + \frac{e_{shunt}}{\rho_{shunt}(T)}\frac{w_{shunt}}{w_{tape}}\frac{l_{tape}}{l_{shunt}}}dT \tag{D.3}$$

ρ_{tape} and ρ_{shunt} are the resistivity of the tape and shunt, respectively. One only has to integrate to get the maximum temperature (T_{max}) when the R-SFCL is electrically isolated after Δt (clearing time). The starting temperature is not the initial one (T_0) but the critical one (T_c) so that the regime under T_c where the resistivity of the tape depends on the current is neglected. This has a very limited impact on the results while simplifying greatly the calculations. The only consequence is that the maximum temperature is slightly overestimated.

$$E_{tape}^2 \delta t = \int_{T_c}^{T_{max}} \frac{e_{tape} c_{p,v}^{tape}(T) + \frac{l_{shunt}}{l_{tape}} \frac{w_{shunt}}{w_{tape}} e_{shunt} c_{p,v}^{shunt}(T)}{\frac{e_{tape}}{\rho_{tape}(T)} + \frac{e_{shunt}}{\rho_{shunt}(T)} \frac{w_{shunt}}{w_{tape}} \frac{l_{tape}}{l_{shunt}}} dT \tag{D.4}$$

Bibliography

[1] I. E. Agency, "IEA, World total final consumption by source, 1973-2018," tech. rep.

[2] I. E. Agency, "Net Zero by 2050 - A Roadmap for the Global Energy Sector," June 2021.

[3] G. Migliavacca, ed., *Advanced Technologies for Future Transmission Grids*. Power Systems, London: Springer London, 2013.

[4] X. Obradors and T. Puig, "Coated conductors for power applications: materials challenges," *Supercond. Sci. Technol.*, p. 18, 2014.

[5] A. Hobl, S. Krämer, S. Elschner, C. Jänke, J. Bock, and J. Schramm, "Superconducting fault current limiters — A new tool for the "Grid of the future"," in *CIRED 2012 Workshop: Integration of Renewables into the Distribution Grid*, pp. 1–4, May 2012.

[6] M. Moyzykh, D. Gorbunova, P. Ustyuzhanin, D. Sotnikov, K. Baburin, A. Maklakov, E. Magommedov, A. Shumkov, A. Telnova, V. Shcherbakov, D. Kumarov, L. Sabirov, M. Medovik, A. Kadyrbaev, S. Alexandrov, I. Mikoyan, S. Samoilenkov, and A. Vavilov, "First Russian 220 kV superconducting fault current limiter (SFCL) for application in city grid," p. 6.

[7] S. Furtner, R. Nemetschek, R. Semerad, G. Sigl, and W. Prusseit, "Reel-to-reel critical current measurement of coated conductors," *Superconductor Science and Technology*, vol. 17, pp. S281–S284, May 2004.

[8] S. Electric, "Guide de la protection," tech. rep., France, 2006.

[9] A. Hobl, W. Goldacker, B. Dutoit, L. Martini, A. Petermann, and P. Tixador, "Design and Production of the ECCOFLOW Resistive Fault Current Limiter," *IEEE Transactions on Applied Superconductivity*, vol. 23, pp. 5601804–5601804, June 2013.

[10] S. Dai, T. Ma, C. Xue, L. Zhao, Y. Huang, L. Hu, B. Wang, T. Zhang, X. Xu, L. Cai, and H. Chen, "Development and test of a 220 kV/1.5 kA resistive type superconducting fault current limiter," *Physica C: Superconductivity and its Applications*, vol. 565, p. 1253501, Oct. 2019.

[11] Y. Han, S. Yang, H. Kim, B. Park, J. Yu, H. Kim, S. In, Y. Hong, and H. Yeom, "Development and Long-Term Test of a Compact 154-kV SFCL," *IEEE Transactions on Applied Superconductivity*, vol. 29, pp. 1–6, June 2019.

[12] Conseil international des grands réseaux électriques and Comité d'études A3, *Application and feasibility of fault current limiters in powers systems*. Paris: CIGRÉ, 2012. OCLC: 798408394.

[13] C. W. G. A3.10, "Fault Current Limiters in electrical Medium and High voltage systems," tech. rep., Dec. 2003.

[14] S. Eckroad, "Survey of Fault Current Limiter (FCL) Technologies – Update," p. 54, 2008.

[15] K.-H. Hartung and V. Schmidt, "Limitation of short circuit current by an IS-limiter," in *2009 10th International Conference on Electrical Power Quality and Utilisation*, pp. 1–4, Sept. 2009. ISSN: 2150-6655.

[16] M. Noe and M. Steurer, "High-temperature superconductor fault current limiters: concepts, applications, and development status," *Superconductor Science and Technology*, vol. 20, pp. R15–R29, Jan. 2007.

[17] H. Wu, X. Li, M. Zhang, D. Stade, and H. Schau, "Analysis of a Liquid Metal Current Limiter," *IEEE Transactions on Components and Packaging Technologies*, vol. 32, pp. 572–577, Sept. 2009.

[18] R. Strumpler, J. Skindhoj, J. Glatz-Reichenbach, J. H. W. Kuhlefelt, and F. Perdoncin, "Novel medium voltage fault current limiter based on polymer PTC resistors," *IEEE Transactions on Power Delivery*, vol. 14, pp. 425–430, Apr. 1999.

[19] C. Gandioli, *Du dimensionnement à l'intégration dans le réseau électrique du limiteur de courant supraconducteur*. PhD thesis, 2013.

[20] N. T. Nguyen, *Mise en oeuvre et intégration des matériaux supraconducteurs dans les dispositifs de puissance*. PhD thesis, 2009.

[21] B. P. Raju, K. C. Parton, and T. C. Bartram, "A Current Limiting Device Using Superconducting D.C. Bias Applications and Prospects," *IEEE Transactions on Power Apparatus and Systems*, vol. PAS-101, pp. 3173–3177, Sept. 1982.

[22] Y. Xin, W. Z. Gong, Y. W. Sun, J. B. Cui, H. Hong, X. Y. Niu, H. Z. Wang, L. Z. Wang, Q. Li, J. Y. Zhang, Z. Q. Wei, L. Liu, H. Yang, and X. H. Zhu, "Factory and Field Tests of a 220 kV/300 MVA Statured Iron-Core Superconducting Fault Current

Limiter," *IEEE Transactions on Applied Superconductivity*, vol. 23, pp. 5602305–5602305, June 2013.

[23] J. Zhang, S. Dai, Y. Teng, D. Zhang, N. Song, Z. Zhu, X. Xu, T. Ma, Z. Zhang, Z. Gao, Q. Bao, H. Li, F. Zhang, L. Lin, and L. Xiao, "Development, Updating and Long-Term Operations of a 10.5 kV HTS Fault Current Limiter," *Journal of Superconductivity and Novel Magnetism*, vol. 27, pp. 2195–2203, Oct. 2014.

[24] K. J. G.Kuperman, "Current limiter with electric valves for limiting the short-circuit current in an electric power circuit."

[25] C.-H. Bonnard, *Méthodes d'évaluation du comportement des limiteurs de courant de court-circuit supraconducteurs résistifs intégrés dans des simulateurs de réseaux électriques*. PhD thesis, 2017.

[26] Y. Cointe, *Limiteur supraconducteur de courant continu*. PhD thesis, 2008.

[27] A. Safaei, M. Zolfaghari, M. Gilvanejad, and G. B. Gharehpetian, "A survey on fault current limiters: Development and technical aspects," *International Journal of Electrical Power & Energy Systems*, vol. 118, p. 105729, June 2020.

[28] P. Mangin and R. Kahn, *Superconductivity*. Cham: Springer International Publishing, 2017.

[29] K. van der Beek and F. Lévy-Bertrand, "Les vortex dans les supraconducteurs: Une matière molle au sein de la matière dure," *Reflets de la physique*, pp. 4–9, Mar. 2012.

[30] A. C. Rose-Innes and E. H. Rhoderick, *Introduction to superconductivity*. No. 6 in International series in solid state physics, Oxford: Pergamon Press, 2. ed., reprinted with corr ed., 1994. OCLC: 833025412.

[31] A. P. Smith, M. J. Raine, E. Surrey, S. Awaji, T. Okada, and D. P. Hampshire, "3-D Properties in (RE)BCO Tapes Measured in Fields up to 35T," *IEEE Transactions on Applied Superconductivity*, vol. 29, pp. 1–5, Aug. 2019. Conference Name: IEEE Transactions on Applied Superconductivity.

[32] C. Böhmer, G. Brandstätter, and H. W. Weber, "The lower critical field of high-temperature superconductors," *Superconductor Science and Technology*, vol. 10, pp. A1–A10, July 1997.

[33] C. P. Bean, "Magnetization of High-Field Superconductors," *Reviews of Modern Physics*, vol. 36, pp. 31–39, Jan. 1964.

[34] P. W. Anderson, "Theory of Flux Creep in Hard Superconductors," *Physical Review Letters*, vol. 9, pp. 309–311, Oct. 1962.

[35] J. Rhyner, "Magnetic properties and AC-losses of superconductors with power law current—voltage characteristics," *Physica C: Superconductivity*, vol. 212, pp. 292–300, July 1993.

[36] G. Nishijima, Y. Tsuchiya, H. Kitaguchi, T. Nishimura, and T. Kato, "Ic - B - T Evaluation for High-Tc Superconductors in Pressurized/Depressurized Liquid Nitrogen," *IEEE Transactions on Applied Superconductivity*, vol. 23, pp. 8000703–8000703, June 2013.

[37] M. Chudy, Z. Zhong, M. Eisterer, and T. Coombs, "n -Values of commercial YBCO tapes before and after irradiation by fast neutrons," *Superconductor Science and Technology*, vol. 28, p. 035008, Mar. 2015.

[38] J. Duron, F. Grilli, B. Dutoit, and S. Stavrev, "Modelling the E–J relation of high-Tc superconductors in an arbitrary current range," *Physica C: Superconductivity*, vol. 401, pp. 231–235, Jan. 2004.

[39] P. Tixador, "Supraconductivité : quoi de neuf 100 ans après sa découverte?," 2013.

[40] J. G. Bednorz and A. Müller, "Possible High Tc Superconductivity in the Ba - La-Cu- 0 System," *Z. Physik B - Condensed Matter*, 1986.

[41] M. K. Wu, J. R. Ashburn, C. J. Torng, P. H. Hor, R. L. Meng, L. Gao, Z. J. Huang, Y. Q. Wang, and C. W. Chu, "Superconductivity at 93 K in a new mixed-phase Y-Ba-Cu-O compound system at ambient pressure," *Physical Review Letters*, vol. 58, pp. 908–910, Mar. 1987.

[42] Y. Kamihara, H. Hiramatsu, M. Hirano, R. Kawamura, H. Yanagi, T. Kamiya, and H. Hosono, "Iron-Based Layered Superconductor: LaOFeP," *Journal of the American Chemical Society*, vol. 128, pp. 10012–10013, Aug. 2006.

[43] G. Dilasser, *Experimental and numerical study of screening currents in REBCO high temperature superconducting magnets*. PhD thesis, 2018.

[44] S. Elschner, J. Bock, X. Obradors, T. Puig, and J. Granados, "Superconducting Materials for SFCL," in *Superconducting Fault Current Limiter: Innovation for the Electric Grids*, vol. 03, pp. 61–76, WORLD SCIENTIFIC, Dec. 2018.

[45] D. Dimos, P. Chaudhari, J. Mannhart, and F. K. LeGoues, "Orientation Dependence of Grain-Boundary Critical Currents in Y Ba 2 Cu 3 O 7 - Bicrystals," *Physical Review Letters*, vol. 61, pp. 219–222, July 1988.

[46] A. Girard, *Nouveaux substrats métalliques à texture biaxiale pour câbles supraconducteurs à haute température critique*. PhD thesis, 2006.

[47] P. Tixador, *Matériaux Supraconducteurs*. Electronique - Génie électrique - Microsystème, hermes science ed., 2003.

[48] T. D. GmbH, "General properties - THEVA PRO-LINE HTS WIRE," Mar. 2020.

[49] S. Lee, V. Petrykin, A. Molodyk, S. Samoilenkov, A. Kaul, A. Vavilov, V. Vysotsky, and S. Fetisov, "Development and production of second generation high T_c superconducting tapes at SuperOx and first tests of model cables," *Superconductor Science and Technology*, vol. 27, p. 044022, Apr. 2014.

[50] V. Selvamanickam, Y. Chen, X. Xiong, Y. Y. Xie, J. L. Reeves, X. Zhang, Y. Qiao, K. P. Lenseth, R. M. Schmidt, A. Rar, D. W. Hazelton, and K. Tekletsadik, "Recent Progress in Second-Generation HTS Conductor Scale-Up at SuperPower," *IEEE Transactions on Applied Superconductivity*, vol. 17, pp. 3231–3234, June 2007.

[51] M. Eisterer, S. Haindl, M. Zehetmayer, R. Gonzalez-Arrabal, H. W. Weber, D. Litzkendorf, M. Zeisberger, T. Habisreuther, W. Gawalek, L. Shlyk, and G. Krabbes, "Limitations for the trapped field in large grain YBCO superconductors," *Superconductor Science and Technology*, vol. 19, pp. S530–S536, July 2006.

[52] X. Hu, L. Rossi, A. Stangl, J. W. Sinclair, F. Kametani, D. Abraimov, A. Polyanskii, J. Y. Coulter, J. Jaroszynski, and D. C. Larbalestier, "An Experimental and Analytical Study of Periodic and Aperiodic Fluctuations in the Critical Current of Long Coated Conductors," *IEEE Transactions on Applied Superconductivity*, vol. 27, pp. 1–5, June 2017.

[53] C. Senatore, C. Barth, M. Bonura, M. Kulich, and G. Mondonico, "Field and temperature scaling of the critical current density in commercial REBCO coated conductors," *Superconductor Science and Technology*, vol. 29, p. 014002, Jan. 2016.

[54] G. Angeli, "Measurement of Ic as a function of the temperature," 2019. Document intern to Fastgrid.

[55] T. Kiss, M. Inoue, K. Higashikawa, T. Suzuki, L. Lyu, K. Takasaki, K. Imamura, Y. Onodera, D. Uetsuhara, A. Ibi, T. Izumi, and H. Kitaguchi, "Comparison between Bi-2223 tape and RE-123 coated conductor from the view point of current transport properties influencing thermal stability," *Cryogenics*, vol. 80, pp. 221–228, Dec. 2016.

[56] T. Kiss, "Numerical modeling: Remarks from the view point of materials characterization," 2015. Presented at EUCAS'15.

[57] P. Tixador, M. Bauer, C. Bruzek, A. Calleja, G. Deutscher, B. Dutoit, F. Gomory, L. Martini, M. Noe, X. Obradors, M. Pekarčíková, and F. Sirois, "Status of the European Union Project FASTGRID," *IEEE Transactions on Applied Superconductivity*, vol. 29, pp. 1–5, Aug. 2019.

[58] P. Tixador and A. Badel, "Resistive SFCL Design," in *Superconducting Fault Current Limiter: Innovation for the Electric Grids*, vol. 03, pp. 85–115, WORLD SCIENTIFIC, Dec. 2018.

[59] P. Tixador, "Limiteur supraconducteur de courant de défaut Superconducting fault current limiteur," p. 28, 2013.

[60] H.-P. Kraemer, W. Schmidt, H. Cai, B. Gamble, D. Madura, T. MacDonald, J. McNamara, W. Romanosky, G. Snitchler, N. Lallouet, F. Schmidt, and S. Ahmed, "Superconducting Fault Current Limiter for Transmission Voltage," *Physics Procedia*, vol. 36, pp. 921–926, 2012.

[61] S. Elschner, A. Kudymow, J. Brand, S. Fink, W. Goldacker, F. Grilli, M. Noe, M. Vojenciak, A. Hobl, M. Bludau, C. Jänke, S. Krämer, and J. Bock, "ENSYSTROB – Design, manufacturing and test of a 3-phase resistive fault current limiter based on coated conductors for medium voltage application," *Physica C: Superconductivity and its Applications*, vol. 482, pp. 98–104, Nov. 2012.

[62] M. Song, C. Sheng, T. Ma, Y. Huang, C. Yang, Y. Xin, H. Jin, T. Yang, J. Xiong, C. Li, Q. Li, C. Wang, B. Li, L. Xiao, and P. Luo, "Current limiting tests of a prototype 160 kV/1 kA resistive DC superconducting fault current limiter," *Superconductor Science and Technology*, vol. 34, p. 014002, Jan. 2021.

[63] J. Sun, J. Du, Y. Li, S. Mo, Y. Cai, W. Yuan, and T. Ma, "Design and Performance Test of a 20-kV DC Superconducting Fault Current Limiter," *IEEE Transactions on Applied Superconductivity*, vol. 30, pp. 1–5, Mar. 2020. Conference Name: IEEE Transactions on Applied Superconductivity.

[64] J. Bock, A. Hobl, J. Schramm, S. Krämer, and C. Jänke, "Resistive Superconducting Fault Current Limiters Are Becoming a Mature Technology," *IEEE Transactions on Applied Superconductivity*, vol. 25, pp. 1–4, June 2015.

[65] B. G. Marchionini, Y. Yamada, L. Martini, and H. Ohsaki, "High-Temperature Superconductivity: A Roadmap for Electric Power Sector Applications, 2015–2030," *IEEE Transactions on Applied Superconductivity*, vol. 27, pp. 1–7, June 2017.

[66] W. R. L. Garcia, P. Tixador, B. Raison, A. Bertinato, B. Luscan, and C. Creusot, "Technical and Economic Analysis of the R-Type SFCL for HVDC Grids Protection," *IEEE Transactions on Applied Superconductivity*, vol. 27, pp. 1–9, Oct. 2017.

[67] P. Tixador and A. Badel, "SuperConducting Fault Current Limiter optimized design," *Physica C*, p. 4, 2015.

[68] A. Badel, B. Rozier, B. Ramdane, G. Meunier, and P. Tixador, "Modeling of 'quench' or the occurrence and propagation of dissipative zones in REBCO high temperature superconducting coils," *Superconductor Science and Technology*, vol. 32, p. 094001, Sept. 2019.

[69] S. Elschner, A. Hobl, and J. Bock, "SFCL Developments at Nexans," in *Superconducting Fault Current Limiter: Innovation for the Electric Grids*, vol. 03, pp. 237–271, WORLD SCIENTIFIC, Dec. 2018.

[70] "https://www.fastgrid-h2020.eu/."

[71] M. Lindmayer and H. Mosebach, "Current limiting properties of YBCO-films on sapphire substrates," *IEEE Transactions on Appiled Superconductivity*, vol. 9, pp. 1369–1372, June 1999.

[72] D. Colangelo and B. Dutoit, "Inhomogeneity effects in HTS coated conductors used as resistive FCLs in medium voltage grids," *Superconductor Science and Technology*, vol. 25, p. 095005, Sept. 2012.

[73] W. T. B. d. Sousa, A. Polasek, F. A. Silva, R. Dias, A. R. Jurelo, and R. d. Andrade, "Simulations and Tests of MCP-BSCCO-2212 Superconducting Fault Current Limiters," *IEEE Transactions on Applied Superconductivity*, vol. 22, pp. 5600106–5600106, Apr. 2012.

[74] P. Tixador, T. Nguyen-Nhat, H. G. Okada-Vieira, and R. Ponceau, "Impact of Conductor Inhomogeneity on FCL Transient Performance," *IEEE Transactions on Applied Superconductivity*, vol. 21, pp. 1194–1197, June 2011.

[75] C. Gandioli, P. Tixador, and G. B. Mariani, "Tests and Simulations of Different YBCO Tapes for FCL," *IEEE Transactions on Applied Superconductivity*, vol. 22, pp. 5603104–5603104, June 2012.

[76] A. Badel, G. Escamez, and P. Tixador, "REBCO FCL Modelling: Influence of Local Critical Current Non-Uniformities on Overall Behavior for Various Tape Architectures," *IEEE Transactions on Applied Superconductivity*, vol. 25, pp. 1–4, June 2015.

[77] J. Vialle, "Contribution aux limiteurs supraconducteurs de courant de défaut." Master Thesis, 2018.

[78] L. David, *Crc handbook of chemistry and physics: a ready reference of chemical and physical data 74th ed.* Journal of the American Chemical Society, 1993.

[79] J. Lu, E. S. Choi, and H. D. Zhou, "Physical properties of Hastelloy ® C-276™ at cryogenic temperatures," *Journal of Applied Physics*, vol. 103, p. 064908, Mar. 2008.

[80] M. Noe, A. Hobl, P. Tixador, L. Martini, and B. Dutoit, "Conceptual Design of a 24 kV, 1 kA Resistive Superconducting Fault Current Limiter," *IEEE Transactions on Applied Superconductivity*, vol. 22, pp. 5600304–5600304, June 2012.

[81] M. Casali, M. Breschi, and P. L. Ribani, "Two-Dimensional Anisotropic Model of YBCO Coated Conductors," *IEEE Transactions on Applied Superconductivity*, vol. 25, pp. 1–12, Feb. 2015.

[82] C. Lacroix and F. Sirois, "Concept of a current flow diverter for accelerating the normal zone propagation velocity in 2G HTS coated conductors," *Superconductor Science and Technology*, vol. 27, p. 035003, Mar. 2014.

[83] H.-P. Kraemer, W. Schmidt, B. Utz, and H.-W. Neumueller, "Switching behavior of YBCO thin film conductors in resistive fault current limiters," *IEEE Transactions on Applied Superconductivity*, vol. 13, pp. 2044–2047, June 2003. Conference Name: IEEE Transactions on Applied Superconductivity.

[84] L. Antognazza, M. Therasse, M. Decroux, F. Roy, B. Dutoit, M. Abplanalp, and y. Fischer, "Comparison Between the Behavior of HTS Thin Film Grown on Sapphire and Coated Conductors for Fault Current Limiter Applications," *IEEE Transactions on Applied Superconductivity*, vol. 19, pp. 1960–1963, June 2009.

[85] G. Deutscher, "High-Voltage Superconducting Fault Current Limiters Based on High-Diffusivity Dielectric Substrates," *Journal of Superconductivity and Novel Magnetism*, vol. 31, pp. 1961–1963, July 2018.

[86] "https://encyclopedia.airliquide.com."

[87] N. T. Nguyen and P. Tixador, "A YBCO-coated conductor for a fault current limiter: architecture influences and optical study," *Superconductor Science and Technology*, vol. 23, p. 025008, Feb. 2010.

[88] R. Gyuráki, F. Sirois, and F. Grilli, "High-speed fluorescent thermal imaging of quench propagation in high temperature superconductor tapes," *Superconductor Science and Technology*, vol. 31, p. 034003, July 2018.

[89] S. Nukiyama, "The maximum and minimum values of the heat Q transmitted from metal to boiling water under stmospheric pressure," *International journal of Heat and Mass transfer*, 1966.

[90] P. Tixador, Y. Cointe, N. T. Nguyen, and C. Villard, "Electrothermal Phenomena About Current Limitation With Coated Conductors," *IEEE Transactions on Applied Superconductivity*, vol. 19, pp. 1938–1941, June 2009.

[91] "https://www.superpower-inc.com."

[92] F. Liang, W. Yuan, M. Zhang, Z. Zhang, S. Venuturumilli, and J. Patel, "The Impact of Critical Current Inhomogeneity in HTS Coated Conductors on the Quench Process for SFCL Application," *IEEE Transactions on Applied Superconductivity*, vol. 26, pp. 1–5, Apr. 2016.

[93] A. Kudymow, S. Elschner, S. Frink, W. Goldacker, A. Hobl, J. Schramm, and J. Brand, "2g hts material selection, insulation, optimization, and the resulting component design of the eccofow resistive fault current limiter."

[94] A. Zampa, S. Holleis, A. Badel, P. Tixador, J. Bernardi, and M. Eisterer, "Influence of local inhomogeneities in the REBCO layer on the quench mechanism of 2G HTS tapes," *Submitted in Augut 2021.*

[95] M. Lao, J. Hecher, P. Pahlke, M. Sieger, R. Hühne, and M. Eisterer, "Magnetic granularity in pulsed laser deposited YBCO films on technical templates at 5 K," *Superconductor Science and Technology*, vol. 30, p. 104003, Oct. 2017.

[96] B. Rozier, *Contribution to electromagnetic and thermal modelling of High Temperature Superconducting REBCO coils for protection purpose.* PhD thesis, 2019.

[97] F. Hengstberger, M. Eisterer, M. Zehetmayer, and H. W. Weber, "Assessing the spatial and field dependence of the critical current density in YBCO bulk superconductors by scanning Hall probes," *Superconductor Science and Technology*, vol. 22, p. 025011, Feb. 2009.

[98] R. Duckworth, J. Lue, D. Lee, R. Grabovickic, and M. Gouge, "The role of nickel substrates in the quench dynamics of silver coated YBCO tapes," *IEEE Transactions on Appiled Superconductivity*, vol. 13, pp. 1768–1771, June 2003.

[99] "https://www.amsc.com/."

[100] X. Wang, A. Caruso, M. Breschi, G. Zhang, U. Trociewitz, H. Weijers, and J. Schwartz, "Normal Zone Initiation and Propagation in Y-Ba-Cu-O Coated Conductors With Cu Stabilizer," *IEEE Transactions on Appiled Superconductivity*, vol. 15, pp. 2586–2589, June 2005.

[101] A. Sakurai, M. Shiotsu, and K. Hata, "Effect of System Pressure on Minimum Film Boiling Temperature for Various Liquids," *Experimental Thermal and Fluid Science*, vol. 3, p. 8, 1990.

[102] M. Breschi, P. L. Ribani, X. Wang, and J. Schwartz, "Theoretical explanation of the non-equipotential quench behaviour in Y–Ba–Cu–O coated conductors," *Superconductor Science and Technology*, vol. 20, pp. L9–L11, Apr. 2007.

[103] C. Lacroix, F. Sirois, and J.-H. F. Lupien, "Engineering of second generation HTS coated conductor architecture to enhance the normal zone propagation velocity in various operating conditions," *Superconductor Science and Technology*, vol. 30, p. 064004, June 2017.

[104] P. Krajewski, G. Piwowarski, J. Buraś, W. Krajewski, P. Rutkowski, and D. Szeliga, "Thermo-Physical Properties of Selected Inconel," *Archives of Metallurgy and Materials*, vol. 59, pp. 1055–1058, Oct. 2014.

[105] P. Tixador, J. Vialle, and A. Badel, "Operation of an SCFCL at 65 K," *IEEE Transactions on Applied Superconductivity*, vol. 28, pp. 1–5, June 2018.

[106] M. Mošať, J. Šouc, M. Vojenčiak, M. Solovyov, M. Búran, and F. Gömöry, "Influence of Current Change Rate During DC Current Limitation on the Coated Conductor Degradation," *IEEE Transactions on Applied Superconductivity*, vol. 31, pp. 1–5, Aug. 2021. Conference Name: IEEE Transactions on Applied Superconductivity.

[107] A. Saraf, B. Almog, M. Azoulay, and G. Deutscher, "Sapphire-Based SFCL Conductors," in *Superconducting Fault Current Limiter: Innovation for the Electric Grids*, vol. 03, pp. 357–372, WORLD SCIENTIFIC, Dec. 2018.

[108] P. Tixador, J. Vialle, A. Zampa, and A. Badel, "Shunts for REBCO Conductors for High Performance SFCL," *Submitted in June 2021.*

[109] M. Vojenčiak, B. Dutoit, J. Šouc, and F. Gömöry, "Can Resistive-Type Fault Current Limiter Operate in Cryogen-Free Environment?," *IEEE Transactions on Applied Superconductivity*, vol. 26, pp. 1–4, Apr. 2016.

[110] M. Pekarčíková, J. Mišík, M. Drienovský, J. Krajčovič, M. Vojenčiak, M. Búran, M. Mošať, T. Húlan, M. Skarba, E. Cuninková, and F. Gömöry, "Composite Heat Sink Material for Superconducting Tape in Fault Current Limiter Applications," *Materials*, vol. 13, p. 1832, Apr. 2020.

[111] "https://www.goodfellow-ceramics.com/white-papers/saphir-synthetique-ultra-performance-wp-fr.pdf."

[112] W. Schnelle, J. Engelhardt, and E. Gmelin, "Specific heat capacity of Apiezon N high vacuum grease and of Duran borosilicate glass," *Cryogenics*, vol. 39, pp. 271–275, Mar. 1999.

[113] M. Kreitman and J. Callahan, "Thermal conductivity of apiezon N grease at liquid helium temperatures," *Cryogenics*, vol. 10, pp. 155–159, Apr. 1970.

[114] "https://static.mimaterials.com/."

[115] A. Zampa, P. Tixador, and A. Badel, "Effect of the Conductor Length on the Hot-Spot Regime for Resistive-Type Superconducting Fault Current Limiter Applications," *IEEE Transactions on Applied Superconductivity*, vol. 31, pp. 1–11, Sept. 2021. Conference Name: IEEE Transactions on Applied Superconductivity.

[116] S. Ochiai, D. Doko, H. Okuda, S. S. Oh, and D. W. Ha, "Distribution of local critical current along sample length and its relation to overall current in a long Bi2223/Ag superconducting composite tape," *Superconductor Science and Technology*, vol. 19, pp. 1097–1103, Nov. 2006.

[117] J. J. Gannon, A. P. Malozemoff, R. C. Diehl, P. Antaya, and A. Mori, "Effect of Length Scale on Critical Current Measurement in High Temperature Superconductor Wires," *IEEE Transactions on Applied Superconductivity*, vol. 23, pp. 8002005–8002005, June 2013.

Etude expérimentale et numérique des rubans REBCO dans le but de développer des conducteurs de limiteur supraconducteur de courants de défaut de type résistif avec de grandes performances

Résumé Malgré les avantages certains du limiteur supraconducteur de courants de défaut de type résistif (R-SFCL) utilisant des rubans REBCO pour protéger le réseau contre les courants de court-circuit, le nombre de dispositifs installés sur les réseaux électriques reste faible. Le coût du ruban REBCO est identifié comme étant le frein majeur au développement commercial de cette technologie. De plus, les performances importantes de ces rubans ne sont généralement pas pleinement utilisées. Cette thèse de doctorat, menée en partie au sein du projet européen Fastgrid, s'inscrit dans ce cadre. Les objectifs sont, d'une part, de contribuer à une meilleure connaissance du comportement de ces rubans lors d'une phase essentielle de leur fonctionnement, la transition, et d'autre part, de développer des conducteurs avec de grandes performances pour diminuer la quantité requise dans un R-SFCL.

Une approche couplant simulations numériques (1D et 3D) et expériences menées dans un environnement cryogénique permet d'aboutir à la proposition d'un mécanisme macroscopique thermo-électrique de la transition ainsi qu'à la conception et à la caractérisation de plusieurs architectures innovantes de conducteurs de R-SFCL. Une partie importante de ces résultats a été obtenue à travers plusieurs collaborations avec des institutions internationales.

Mots-clés Rubans REBCO, R-SFCL, modélisation thermo-électrique, transition, imagerie très rapide

---

Experimental and numerical study of 2G HTS tapes to develop high-performance R-SFCL conductors

Abstract Despite the large benefits of the resistive-type Superconducting Fault Current Limiter (R-SFCL) using 2G HTS tapes to protect the grid against fault currents, the number of devices currently installed in the power grids remains small. The high cost of the REBCO tape is identified as the main obstacle to the commercial development of this dispositive. In addition, the high performances of these tapes are generally not fully used. This PhD work, carried out in the European project Fastgrid, falls within this framework. The objectives are, on one hand, to contribute to a better understanding of the operation of these tapes during the quench and, on the other hand, to develop R-SFCL conductors showing high performances in order to decrease the quantity required in a full device.

An approach coupling numerical simulations (1D and 3D) and experiments, carried out in a cryogenics environment, leads to the proposition of a macroscopic thermo-electrical mechanism of the quench as well as to the design and the characterization of several innovative architectures of R-SFCL conductors. A significant part of these results was obtained through collaborations with international institutions.

Keywords REBCO tapes, R-SFCL, thermo-electrical modelling, quench, high-speed imaging